



Università degli Studi Roma Tre

DIPARTIMENTO DI MATEMATICA E FISICA
Corso di Dottorato di Ricerca in Fisica
XXXII Ciclo

Measurement of Higgs-boson self-coupling with single-Higgs and double-Higgs production channels

Eleonora Rossi

Supervisore:
Prof. Biagio Di Micco

Coordinatore:
Prof. Giuseppe Degrassi

Abstract

One of the most important targets of the LHC is to improve the experimental results of the Run 1 and the complete exploration of the properties of the Higgs boson, in particular the Higgs-boson self-coupling. The self-coupling is very loosely constrained by electroweak precision measurements therefore new physics effects could induce large deviations from its Standard Model expectation. The trilinear self-coupling can be measured directly using the Higgs-boson-pair production cross section, or indirectly through the measurement of single-Higgs-boson production and decay modes. In fact, at next-to-leading order in electroweak interaction, the Higgs-decay partial widths and the cross sections of the main single-Higgs production processes depend on the Higgs-boson self-coupling via weak loops. Measurements of κ_λ , i.e. the rescaling of the trilinear Higgs self-coupling, are presented in this dissertation. Results are obtained exploiting proton-proton collision data from the Large Hadron Collider at a centre-of-mass energy of 13 TeV recorded by the ATLAS detector in 2015, 2016 and 2017, corresponding to a luminosity of up to 80 fb^{-1} .

Constraints on the Higgs self-coupling are presented considering the most sensitive double-Higgs channels (HH), $b\bar{b}\tau^+\tau^-$, $b\bar{b}\gamma\gamma$ and $b\bar{b}b\bar{b}$, considering single-Higgs (H) production modes, ggF , VBF , ZH , WH and $t\bar{t}H$, together with WW^* , ZZ^* , $\tau^+\tau^-$, $\gamma\gamma$ and $b\bar{b}$ decay channels, and combining the aforementioned analyses (H+HH) to improve the sensitivity on κ_λ .

Under the assumption that new physics affects only the Higgs-boson self-coupling, the combined H+HH best-fit value of the coupling modifier is: $\kappa_\lambda = 4.6_{-3.8}^{+3.2}$, excluding values outside the interval $-2.3 < \kappa_\lambda < 10.3$ at 95% confidence level.

Results with less stringent assumptions are also provided, decoupling the Higgs self-coupling and the other Standard Model couplings.

The final results of this thesis provide the most stringent constraint on κ_λ from experimental measurements.

Contents

Introduction	4
1 The Standard Model of Particle Physics	7
1.1 Fundamental Interactions in the Standard Model	7
1.1.1 Quantum Electrodynamics	11
1.1.2 Quantum Chromodynamics	12
1.1.3 Weak Interactions and Unified Electroweak (EW) Model	14
1.2 A Spontaneous Symmetry Breaking (SSB): the Higgs Mechanism	17
1.3 The Standard Model Higgs Boson	20
1.3.1 Higgs-Boson Production	20
1.3.2 Higgs-Boson Decays	23
1.4 Higgs-Boson Property Measurements	29
1.4.1 Higgs self-coupling	35
1.5 The Standard Model: successes and open issues	37
2 The Large Hadron Collider	39
2.1 Accelerator Complex	39
2.2 The LHC Experiments	41
2.3 Luminosity	42
2.4 LHC Operation	45
3 The ATLAS Experiment at the Large Hadron Collider	47
3.1 Detector Sub-Systems	48
3.2 Coordinate System	50
3.3 Magnet System	51
3.4 Inner Detector	53
3.4.1 The Insertable B-Layer (IBL)	55
3.4.2 The Pixel Detector	56
3.4.3 The SemiConductor Tracker (SCT)	56
3.4.4 The Transition Radiation Tracker (TRT)	57
3.5 Calorimeters	57
3.5.1 The Electromagnetic Calorimeter	59
3.5.2 The Hadronic Calorimeter	60
3.5.3 Forward Calorimeter	60
3.6 Muon Spectrometer	61
3.6.1 Tracking Chambers	62
3.6.2 Triggering Chambers	64

3.7	Trigger and Data Acquisition System	65
3.8	Luminosity Detectors	67
4	Reconstruction of physics objects	68
4.1	Reconstruction of tracks and vertices	69
4.2	Electron and photon reconstruction and identification	71
4.2.1	Electron identification and isolation	72
4.2.2	Photon identification and isolation	76
4.3	Jet and b -jet reconstruction	76
4.3.1	b -tagging algorithms	79
4.4	Muon reconstruction and identification	80
4.5	Tau reconstruction	83
4.6	Missing transverse momentum	85
5	Statistical Treatment	87
5.1	Profile-likelihood technique	87
5.2	Sensitivity and p – value	89
5.3	Asymptotic limit and Asimov Dataset	91
5.4	Neyman’s confidence intervals	91
6	Probing the Higgs self-coupling	93
6.1	Higgs self-coupling through direct Higgs-boson pair searches	93
6.2	HL-LHC projections for double-Higgs processes	95
6.3	Higgs self-coupling through loop corrections of single-Higgs production and decay modes	97
6.4	HL-LHC projections for single-Higgs processes	103
7	Constraints on the Higgs-boson self-coupling from double-Higgs production and decay measurements	106
7.1	Data and input measurements	106
7.2	Simulation of signal samples	109
7.3	Implementation of the theoretical model	109
7.4	Statistical model	111
7.4.1	Systematic uncertainties	113
7.5	Validation of double-Higgs results	119
7.6	Results of fits to κ_λ from individual channels	120
7.7	Results of fits to κ_λ from the combination of double-Higgs channels	125
8	Constraints on the Higgs-boson self-coupling from single-Higgs production and decay measurements	133
8.1	Data and input measurements	133
8.2	Implementation of the theoretical model	139
8.3	Statistical model	145
8.3.1	Systematic uncertainties	146
8.4	Results of fit to κ_λ	151
8.5	Results of fit to κ_λ and either κ_F or κ_V	156
8.5.1	Cross-check on the validity of the theoretical approximations	158

8.6	HL-LHC projections	161
9	Constraining the Higgs-boson self-coupling combining single- and double-Higgs production and decay measurements	163
9.1	Data and input measurements	163
9.2	Theoretical model	164
9.3	Statistical model	164
9.3.1	Correlation scheme between single- and double-Higgs analyses . . .	165
9.4	Overlap studies	169
9.4.1	$HH \rightarrow b\bar{b}\gamma\gamma$ and $H \rightarrow \gamma\gamma$ overlap	169
9.4.2	$HH \rightarrow b\bar{b}\tau^+\tau^-$ overlap with $H \rightarrow \tau^+\tau^-$, $t\bar{t}H \rightarrow b\bar{b}$, $t\bar{t}H$ multilepton, $VH \rightarrow b\bar{b}$	173
9.4.3	$HH \rightarrow b\bar{b}b\bar{b}$ and $t\bar{t}H \rightarrow b\bar{b}$ overlap	175
9.4.4	Signal contamination in double-Higgs and single-Higgs channels . .	175
9.5	Validation of single- and double-Higgs inputs	175
9.5.1	Single-Higgs input validation	175
9.5.2	Double-Higgs input validation	178
9.6	Results of fit to κ_λ	179
9.7	Results of fit to κ_λ and κ_t	187
9.8	Results of fit to more generic models	189
	Conclusion	195
	Appendices	207
	A Correlations between double-Higgs analyses	207
	B Correlations between single- and double-Higgs analyses	209

Introduction

The Standard Model (SM) of particle physics is the theory that, as of today, best describes matter in terms of elementary particles and interactions, and has been validated with an excellent level of accuracy, thus constituting one of the most successful achievements in modern physics. Among the successes of the SM, it has to be underlined that all the particles the SM predicted have been observed, including the W and Z bosons, the top and bottom quarks, and the Higgs boson, the particle responsible of the Higgs mechanism that allows bosons and fermions to acquire mass in the electroweak gauge theory. The search for the Higgs boson has lasted for decades. More than 20 years after the formulation of the Higgs mechanism had to pass until a significant mass range could be probed first with the Large Electron Positron collider (LEP) at CERN and then with the Tevatron proton-antiproton collider. In 2010, the Large Hadron Collider (LHC), a proton-proton and heavy-ion collider, started to take data at unprecedented centre-of-mass energies with the primary goal of searching for this boson.

Thus, in July 2012, the announcement of the discovery of a particle compatible with the SM Higgs boson by the ATLAS and CMS experiments at the LHC, represented a great milestone in the history of particle physics. After the discovery of the Higgs boson, a new era in understanding the nature of electroweak symmetry breaking, possibly completing the SM and constraining effects from new physics (NP), has opened. One of the main targets of particle physics, and of ATLAS and CMS physics analyses at the LHC, is the precision measurement of the properties of the Higgs boson including spin-parity, couplings and evidence for production mechanisms, which are essential tests of the SM. The complete exploration of the properties of the Higgs boson includes the interactions of the Higgs boson with itself, known as the Higgs-boson self-couplings. The self-couplings determine the shape of the potential which is connected to the phase transition of the early universe from the unbroken to the broken electroweak symmetry and are very loosely constrained by electroweak precision measurements, therefore NP effects could induce large deviations from their SM expectation.

The trilinear Higgs self-coupling can be probed directly in searches for multi-Higgs final states and indirectly via its effects on precision observables or loop corrections to single-Higgs processes, while the quartic self-coupling, being further suppressed with respect to the trilinear self-coupling, is currently not accessible at hadron colliders.

The results presented in this dissertation are obtained using proton-proton collision data from the LHC at a centre-of-mass energy of 13 TeV recorded by the ATLAS detector in 2015, 2016 and 2017.

A description of the Standard Model theoretical framework is reported in Chapter 1, ranging from a summary of the fundamental particles and their properties, to the introduction of the Higgs mechanism, a simple mechanism for the breaking of the electroweak

symmetry. Furthermore, this chapter reports a detailed description of the Higgs-boson phenomenology and latest measurements, from production and decay modes to properties like the mass, the couplings and the self-coupling of the Higgs boson itself. Chapter 2 describes the LHC accelerator complex and the basic concepts of proton-proton collisions, together with the experiments housed in the ring and the periods of operation of the accelerator, while Chapter 3 presents the ATLAS experiment, giving details on the sub-detectors composing ATLAS and on the interaction of different particles with the detector materials.

A general overview of the reconstruction of physics objects, consists of combining and interpreting information collected from the sub-detectors described in Chapter 3, is provided in Chapter 4. Basics concepts of the statistical model used to extract the results of this dissertation are reported in Chapter 5.

The work presented in this thesis has the target of probing the sector of the SM that is responsible for electroweak symmetry breaking, focusing on the Higgs potential and on the trilinear Higgs self-coupling. The theoretical models on the basis of which the results of the thesis have been produced are summarised in Chapter 6 for both double- and single-Higgs productions.

The results coming from the extraction of limits on the rescaling of the trilinear Higgs self-coupling, κ_λ , considering the $gg \rightarrow HH$ production process and the most sensitive double-Higgs channels, $b\bar{b}\tau^+\tau^-$, $b\bar{b}\gamma\gamma$ and $b\bar{b}b\bar{b}$, and exploiting the dependence of the double-Higgs cross section and kinematics on both the coupling of the Higgs boson to the top quark and the Higgs self-coupling, are reported in Chapter 7.

Chapter 8 exploits the complementary approach to constrain the Higgs self-coupling described in Chapter 6, applying next-to-leading order electroweak corrections depending on κ_λ to single-Higgs processes, combining information from ggF , VBF , ZH , WH and $t\bar{t}H$ production modes together with WW^* , ZZ^* , $\tau^+\tau^-$, $\gamma\gamma$ and $b\bar{b}$ decay channels; the limits extracted using this approach are probed to be competitive with double-Higgs limits.

The final results of this dissertation, providing the most stringent constraints on κ_λ from experimental measurements through the combination of the aforementioned double- and single-Higgs analyses, whose details have been described in Chapters 7 and 8, are reported in Chapter 9.

Chapter 1

The Standard Model of Particle Physics

A description of the Standard Model (SM) of particle physics is presented in this chapter. Section 1.1 introduces the SM as a gauge theory that, currently, is the most accurate theory covering the foundations of particle physics and describes three of the four known fundamental forces. Section 1.2 presents the Higgs mechanism, i.e. a simple mechanism for the breaking of the electroweak symmetry as a consequence of the introduction of an additional scalar field in the SM. An overview of the Higgs-boson phenomenology, focusing on production and decay channels together with the current status of the couplings of the Higgs boson with other SM particles are reported in Sections 1.3 and 1.4. Finally Section 1.5 is devoted to a brief description of the successes of this theory making more room to remaining open questions of this great even though incomplete model.

The results reported in this thesis represent validations of this theory, looking for deviation of the predicted SM values as possible hints of new physics (NP).

Throughout this chapter, natural units have been used, i.e. the speed of light in vacuum, c , and the reduced Planck constant, \hbar , have been set to $c = \hbar = 1$ and the unit of energy is the GeV.

1.1 Fundamental Interactions in the Standard Model

The Standard Model [1–7] is currently the quantum field theory, i.e. a theory having quantum fields as fundamental objects, that better describes the matter in terms of elementary particles and interactions, and constitutes one of the most successful achievements in modern physics; only the gravitational interaction is not included in the theory. According to the SM, matter is composed of 12 fundamental *fermions*, 4 *vector gauge bosons* (spin = 1), and one *scalar Higgs boson* (spin = 0); fermions are half-integer spin particles obeying Fermi-Dirac statistics and satisfying the Pauli exclusion principle while bosons have integer spin and obey Bose-Einstein statistics. The spin is a quantum number, i.e. a property describing the values of conserved quantities under transformations of quantum systems, that, in the case of the spin, are rotations.

Fermions are classified in *leptons* and *quarks*, depending on the interaction they are subject to:

- leptons interact through the electromagnetic and weak forces;
- neutrinos interact only via the weak force;
- quarks interact through the electromagnetic, weak and strong forces, thus having an additional quantum number with respect to leptons, related to the strong interaction, the colour charge (*red*, *green* and *blue*).

The main experimental difference between leptons and quarks is that quarks cannot be observed as isolated particles as they are confined in colour charge singlets with integer charge, namely hadrons, such as protons and neutrons. Quarks and leptons are further divided into three families, or generations, of increasing mass:

$$\begin{pmatrix} e^- \\ \nu_e \end{pmatrix} \quad \begin{pmatrix} \mu^- \\ \nu_\mu \end{pmatrix} \quad \begin{pmatrix} \tau^- \\ \nu_\tau \end{pmatrix} \quad \begin{pmatrix} u \\ d \end{pmatrix} \quad \begin{pmatrix} c \\ s \end{pmatrix} \quad \begin{pmatrix} t \\ b \end{pmatrix}.$$

The electron is the only stable charged lepton while both muon and tau are unstable; three neutrino flavours match the flavour of the corresponding charged lepton, i.e. electron, muon, and tau, as indicated by the subscript, for example ν_μ matches the muon μ ; within the Standard Model, neutrinos are neutral massless leptons, in contrast with the experimental evidence of their oscillation, which requires a mass different from zero. Each fermion has an anti-particle with identical mass and opposite quantum numbers. This statement is not yet verified for neutrinos, as they might be Majorana particles, namely $\nu = \bar{\nu}$.

Lepton/quark	Q/e	mass [GeV]
electron (e)	-1	0.511×10^{-3}
electron neutrino (ν_e)	0	$< 2 \times 10^{-9}$
muon (μ)	-1	0.106
muon neutrino (ν_μ)	0	$< 0.19 \times 10^{-3}$
tau (τ)	-1	1.777
tau neutrino (ν_τ)	0	$< 18.2 \times 10^{-3}$
up (u)	$\frac{2}{3}$	$2.2^{+0.5}_{-0.3} \times 10^{-3}$
down (d)	$-\frac{1}{3}$	$4.7^{+0.5}_{-0.2} \times 10^{-3}$
charm (c)	$\frac{2}{3}$	1.27 ± 0.02
strange (s)	$-\frac{1}{3}$	$93^{+11}_{-5} \times 10^{-3}$
top (t)	$\frac{2}{3}$	172.9 ± 0.4
bottom (b)	$-\frac{1}{3}$	$4.18^{+0.03}_{-0.02}$

Table 1.1: Properties of leptons and quarks: the electric charge Q , in units of the electron charge e , and the mass (or mass limit), in GeV, are reported [8]. The uncertainties on the mass of charged leptons are omitted, due to the fact that they are several orders of magnitude smaller than the precision adopted in the table.

Thus the SM has 24 fermion fields: 18 of them are quarks, i.e. 6 types, known as flavours, of quarks, (*down*, *up*, *strange*, *charm*, *bottom* and *top*) times 3 colours (*red*, *green* and *blue*), while 6 of them are leptons, 3 charged leptons (electron, muon and tau) and the corresponding neutrinos. Table 1.1 reports a summary of the aforementioned fermions, along with their charge expressed in units of the electron charge, e , and mass (or mass limit): all leptons except for neutrinos have a charge $|Q/e| = 1$; hadrons can be composed of three quarks, called *baryons* and being half-integer spin, or of a quark-antiquark pair, called *mesons* and being integer-spin; quarks have a fractional charge, $|Q/e| = 2/3$ or $1/3$. In addition to the direct limits on the masses of neutrinos reported in Table 1.1, cosmological observations allowed to set an upper limit on the sum of neutrino masses of 0.12 eV at 95% confidence level [9]. Fermions interact through the exchange of force-carrying particles (mediators), referred to as “gauge bosons”:

- the photon, γ , is the spin-1 massless mediator of the electromagnetic interaction between charged particles;
- the W and Z bosons are the spin-1 massive mediators of the weak interaction, responsible of processes like nuclear decays and processes involving neutrinos; their masses are of order of 100 times the mass of the proton;
- the gluons, g , are the spin-1 massless mediators of the strong interaction, responsible of holding together both quarks in neutrons and protons, and neutrons and protons within nuclei;
- the graviton, G , is the hypothetical, not existing in the SM neither predicted by a complete quantum field theory, spin-2 massless gauge boson carrying the gravitational interaction, the weakest among the interactions.

The fundamental properties of the bosons, i.e. their charge, mass, spin and the respective force, are reported in Table 1.2.

Boson	Q/e	mass [GeV]	spin	force
photon (γ)	0	$< 10^{-27}$	1	electromagnetic
W boson (W)	± 1	80.379 ± 0.012	1	weak
Z boson (Z)	0	91.1876 ± 0.0021	1	weak
gluon (g)	0	$\leq 10^{-3}$	1	strong
graviton (G)	0	$< 6 \times 10^{-41}$	2	gravitational

Table 1.2: Properties of the gauge bosons mediating the four fundamental forces: the electric charge Q , in units of the electron charge e , the mass (or mass limit), in GeV, the spin and the type of force are reported [8]; the graviton, G , is the hypothetical, not existing in the SM neither predicted by a complete quantum field theory, gauge boson carrying the gravitational force.

Finally, the Higgs boson is a neutral fundamental scalar particle introduced in the Standard Model in order to generate the masses of the gauge bosons and of all the other

elementary particles considered in the theory, as explained in Section 1.2.

Figure 1.1 shows a summary of the SM particles and fundamental interactions.

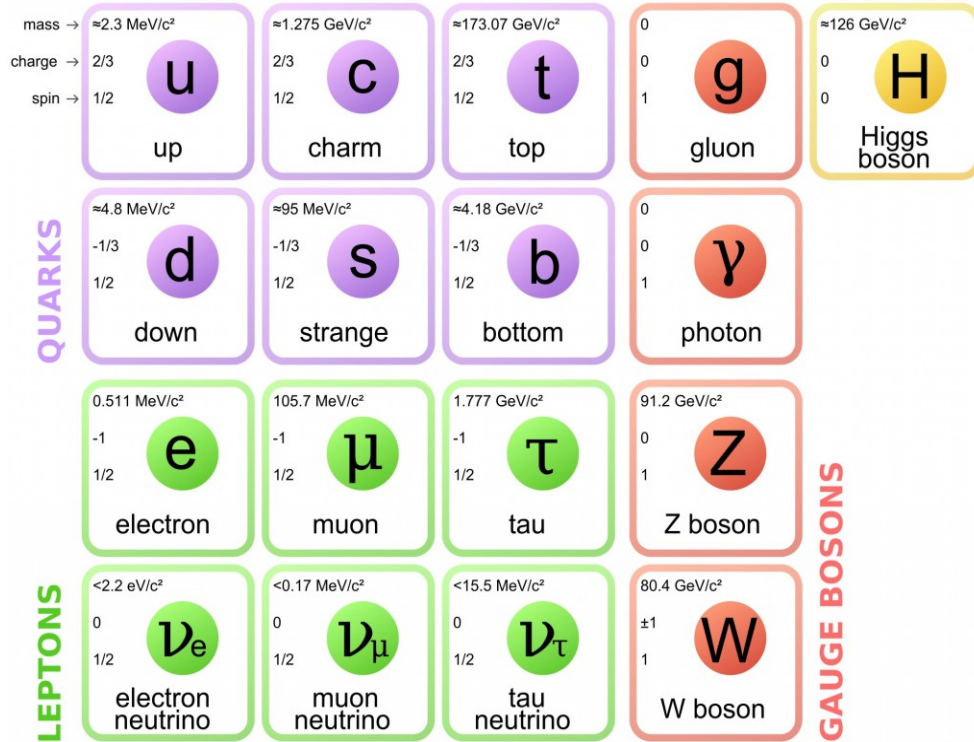


Figure 1.1: Standard Model particles and interaction mediators.

The construction of the Standard Model has been guided by principles of symmetry: Noether’s theorem [10] implies that, if an action is invariant under some group of transformations (symmetry), these symmetries are associated with one or several conserved quantities at the point where the interaction occurs, like the charge and the colour.

Local symmetries, i.e. when actions are invariant under transformation of parameters depending on the space-time coordinates, are the ones on top of which the SM is defined.

The mathematics of symmetry is provided by group theory; thus the SM is based on three symmetry groups: $SU(3)_C \otimes SU(2)_L \otimes U(1)_Y$, where:

- $SU(3)_C$ reflects the symmetry of the strong interaction, described by Quantum Chromodynamics (QCD); it represents the non-abelian, i.e. non-commutative, gauge group, with 8 gauge bosons (gluons); the “C” letter stands for the colour;
- $SU(2)_L \otimes U(1)_Y$ indicates the electroweak symmetry group, which unifies electromagnetic and weak interactions in the so-called “electroweak theory”; the “L” letter stands for “left”, involving only left-handed fermion fields while the “Y” letter stands for the weak hypercharge.

The foundations of quantum electrodynamics and chromodynamics will be the starting point of the next paragraphs.

1.1.1 Quantum Electrodynamics

Quantum Electrodynamics (QED) is a major success of quantum field theory (QFT) describing the interaction between electrically charged particles and the mediator of the electromagnetic interaction, i.e. the photon. Mathematically, it is an abelian gauge theory, symmetric with respect to gauge rotations of U(1) group, while the gauge field is the electromagnetic field.

For a free Dirac fermion of mass m , the Lagrangian is:

$$\mathcal{L} = \bar{\psi}(i\cancel{\partial} - m)\psi \quad (1.1)$$

where ψ represents the fermion field, $\bar{\psi} = \psi^\dagger \gamma^0$, $\cancel{\partial} = \gamma^\mu \partial_\mu$ and γ^μ are the Dirac matrices. The Lagrangian described in Equation 1.1 is invariant under global U(1) transformations:

$$\psi \xrightarrow{\text{U(1)}} \psi' = e^{i\vartheta} \psi$$

where the phase ϑ is “global”, i.e. it does not vary for every point in space-time ($\frac{\partial \vartheta}{\partial x} = 0$). However, if the phase transformation depends on the space time coordinate, i.e. $\vartheta = \vartheta(x)$, the free Lagrangian is no longer invariant. In order to ensure the local invariance of the Lagrangian, additional terms should be considered, consisting of a gauge field A_μ transforming as:

$$A_\mu \xrightarrow{\text{U(1)}} A'_\mu = A_\mu + \frac{1}{e} \partial_\mu \vartheta(x) \quad (1.2)$$

and the corresponding covariant derivative through the minimal coupling e :

$$D_\mu = \partial_\mu - ieA_\mu. \quad (1.3)$$

The Lagrangian for a free gauge field A_μ is described by:

$$\mathcal{L} = -\frac{1}{4} F_{\mu\nu} F^{\mu\nu} \quad (1.4)$$

where $F_{\mu\nu} = (\partial_\mu A_\nu - \partial_\nu A_\mu)$ is the electromagnetic field strength; a hypothetical mass for the gauge field A_μ is forbidden because it would violate the local U(1) gauge invariance. After the introduction of the gauge field A_μ , the QED Lagrangian is written as:

$$\mathcal{L}_{QED} = -\bar{\psi}(\gamma^\mu \partial_\mu + m)\psi - \frac{1}{4} F_{\mu\nu} F^{\mu\nu} + ieA_\mu \bar{\psi} \gamma^\mu \psi \quad (1.5)$$

where the first term describes the free propagation of the ψ fermion field (charged particles), the second term describes the free propagation of the A_μ field (photons) while the third term describes the interaction of electrons and positrons (ψ) with photons (A_μ). The interaction between the Dirac fermions and the A_μ gauge field is described, at the lowest order of perturbation theory, by the Feynman diagram shown in Figure 1.2.

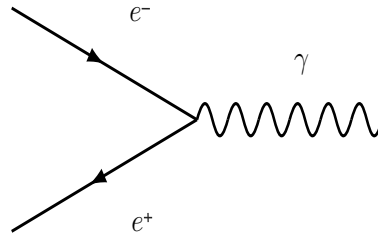


Figure 1.2: Example of an interaction vertex for the QED Lagrangian, showing electron-positron annihilation.

The electromagnetic coupling constant is the fine structure constant, α , expressed at low energies as:

$$\alpha = \frac{e^2}{4\pi\epsilon_0\hbar c} = \frac{1}{137} \quad (1.6)$$

where $e = 1.602176 \times 10^{-19}$ C is the electron charge, $\epsilon_0 = 8.854187 \times 10^{12}$ F \cdot m $^{-1}$ is the vacuum dielectric constant, $c = 299792458$ m \cdot s $^{-1}$ is the speed of light in vacuum and $\hbar = h/2\pi = 1.054571 \times 10^{-34}$ J \cdot s, h being the Planck constant. The renormalisation of the photon field brings, as a consequence, the fact that the QED coupling constant is not a real constant but a “running constant” depending on the energy scale and decreasing at large distances given the “screening effect” of virtual particles in vacuum.

1.1.2 Quantum Chromodynamics

Quantum Chromodynamics (QCD) describes the interaction between quarks and the mediators of the strong interaction, i.e. the gluons. Mathematically, it is a non-abelian gauge theory, symmetric with respect to gauge rotation of the $SU(3)_C$ group having 8 gauge fields, the gluons. The non-abelian nature of the theory leads to the fact that gluons, having the colour charge unlike photons that are neutral, interact not only with quarks but also among themselves, thus leading to three- or four-gluon vertices.

The free Lagrangian for a quark field of flavour f is [11]:

$$\mathcal{L} = \sum_f \bar{q}_f (i\gamma^\mu \partial_\mu - m_f) q_f. \quad (1.7)$$

The Lagrangian is invariant under global $SU(3)_C$ transformations:

$$q_f^\alpha \xrightarrow{SU(3)} (q_f^\alpha)' = U_\beta^\alpha q_f^\beta \quad \text{being} \quad U = e^{i\frac{\lambda^a}{2}\vartheta_a} \quad (1.8)$$

where the indices α and β run over the colour quantum numbers, the $\frac{1}{2}\lambda^a$ ($a = 1, \dots, 8$) denotes the generators of the fundamental representation of the $SU(3)_C$ algebra and ϑ_a are arbitrary parameters. The matrices λ^a satisfy the commutation relations:

$$\left[\frac{\lambda^a}{2}, \frac{\lambda^b}{2} \right] = if^{abc} \frac{\lambda^c}{2} \quad (1.9)$$

with f^{abc} being the $SU(3)_C$ structure constants. The covariant derivative introduced in order to guarantee the local invariance under $SU(3)_C$ transformations, i.e. $\vartheta_a = \vartheta_a(x)$, including as additional terms eight different gauge bosons $G_a^\mu(x)$, the gluons, reads:

$$D_\mu = [\partial_\mu - ig \frac{\lambda^a}{2} G_a^\mu(x)] = [\partial_\mu - ig G^\mu(x)] \quad (1.10)$$

where g is the coupling constant of QCD and $G^\mu(x) \equiv (\frac{\lambda^a}{2} G_a^\mu(x))$. The field strengths can be generalised for a non-abelian Lie group as:

$$G_a^{\mu\nu}(x) = \partial^\mu G_a^\nu - \partial^\nu G_a^\mu - gf^{abc} G_b^\mu G_c^\nu \quad (1.11)$$

where the last term generates the cubic and quartic gluon self-interactions as a consequence of the non-abelian nature of $SU(3)_C$.

After the introduction of the gauge fields, the $SU(3)_C$ invariant QCD Lagrangian can be written as:

$$\mathcal{L}_{QCD} = -\frac{1}{4} G_a^{\mu\nu} G_{\mu\nu}^a + \sum_f \bar{q}_f (i\gamma^\mu D_\mu - m_f) q_f \quad (1.12)$$

where the index f runs over the quark flavour and the index a runs over the colour charge; the first term of the Lagrangian is the gauge boson kinetic term giving rise to three- and four-gluon vertices. Similarly to the QED Lagrangian, the $SU(3)_C$ symmetry forbids to add mass terms for the gluon fields, explaining why the gluons are massless bosons in the SM. Interactions between quarks and gluons are shown in the diagrams of Figure 1.3.

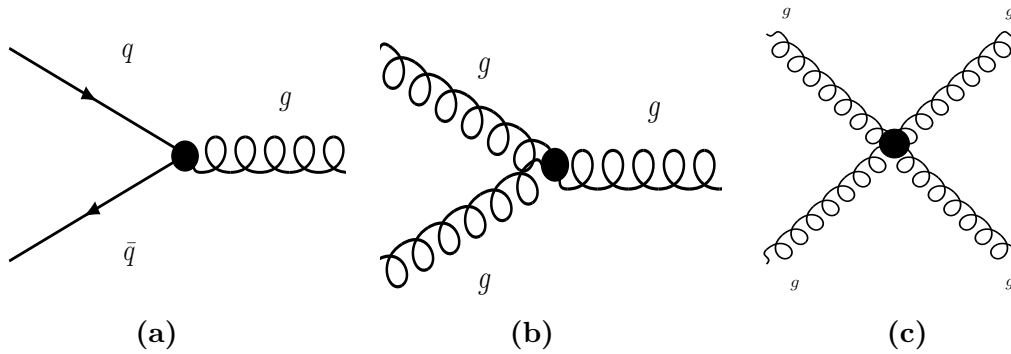


Figure 1.3: Interaction vertices for the QCD Lagrangian: (a) quark-gluon interaction; (b) three-gluon vertex; (c) four-gluon vertex.

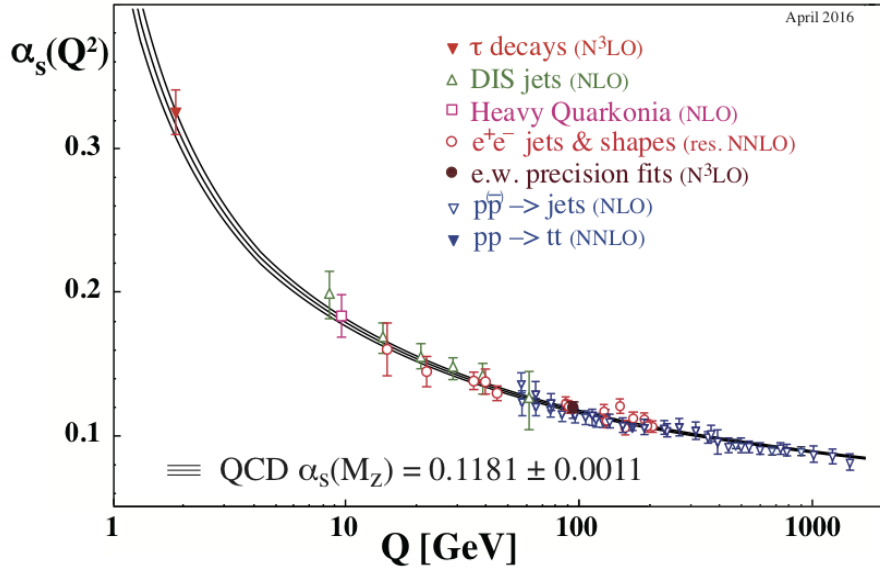


Figure 1.4: Summary of measurements of α_S as a function of the energy scale Q . The respective degree of QCD perturbation theory used in the extraction of α_S is indicated within brackets (NLO: next-to-leading order; NNLO: next-to-next-to leading order; res. NNLO: NNLO matched with resummed next-to-leading logs; N3LO: next-to-NNLO) [12].

The running coupling constant $\alpha_S(Q^2)$ as a function of the energy scale Q , exploiting a first order perturbative QCD calculation, strictly valid only if $\alpha_S \ll 1$, is given by:

$$\alpha_s(Q^2) = \frac{12\pi}{(33 - 2n_f) \ln \frac{Q^2}{\Lambda_{QCD}^2}} \quad (1.13)$$

where Q represents the energy transferred in the interaction, n_f is the number of quark flavours and Λ_{QCD} is the energy scale at which the perturbative QCD coupling diverges, $\Lambda_{QCD} \sim 0.2 \text{ GeV}/c$.

An opposite effect, compared to the QED case, is present due to vacuum polarisation, thus leading to an “anti-screening effect” generated by gluon self-interactions. For a short distance, i.e. when $Q^2 \rightarrow \infty$, the coupling between quarks decreases leading to the famous property of QCD known as asymptotic freedom, i.e. quarks behaving as free particles; on the other hand, for large distances, the coupling constant increases thus making impossible the detachment of quarks from hadrons, a property known as confinement.

The trend of the running coupling constant as a function of the energy scale Q is shown in Figure 1.4.

1.1.3 Weak Interactions and Unified Electroweak (EW) Model

In 1932 Enrico Fermi suggested a simple model [13] to explain the β decay, e.g. $n \rightarrow pe^- + \bar{\nu}_e$, an interaction experienced by all SM fermions and characterised by a much smaller intensity with respect to the strong or electromagnetic interactions. The “weakness” of this interaction can be quantified looking at the lifetimes of the particles weakly decaying that are inversely related to the coupling strengths: the longer muon

lifetime $\sim 10^{-6}$ with respect to $\sim 10^{-23}$ or $\sim 10^{-16}$ as examples of the strong and electromagnetic interaction typically lifetimes, respectively, reflects a much weaker strength of the interaction.

This interaction was originally explained by Fermi as an effective point-like vectorial current interaction (V) between four fermions involving a contact force with no range; Fermi's theory was valid at low energy but did not explain important features of this interaction, like the massive mediators and the parity violation. Driven by the observation that weak interactions violate parity, Fermi's theory was extended introducing to the model an axial (A) term which conserves its sign under parity transformations, while the violation of parity arises from the $V - A$ interaction term [14, 15]. Figure 1.5 shows the Fermi four-fermion interaction describing the β decay.

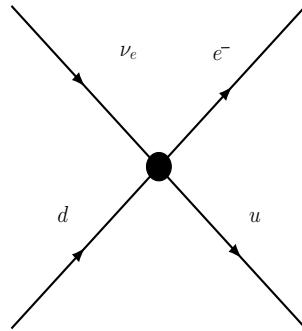


Figure 1.5: Four-fermion interaction describing the β decay.

Particles exist in two helicity states: left-handed or right-handed. Weak interactions are found to involve only left-handed particles or right-handed anti-particles, which are defined as:

$$\psi_L = \frac{1}{2}(1 - \gamma_5)\psi \quad \psi_R = \frac{1}{2}(1 + \gamma_5)\psi$$

where $\gamma_5 = i\gamma^0\gamma^1\gamma^2\gamma^3$. The weak interaction field is invariant under $SU(2)_L$ transformations, where the subscript “L” means that only left-handed particles participate to these interactions. Two types of weak interactions exist, depending on the charge of the interaction mediator: the charged-current interaction mediated by W^+ or W^- bosons, carrying an electric charge, and the neutral-current interaction mediated by the Z^0 boson.

The weak interaction allows quarks to change their flavour; the transition probability for a quark to change its flavour is proportional to the square of the Cabibbo-Kobayashi-Maskawa (CKM) matrix elements [16]:

$$V_{CKM} = \begin{pmatrix} V_{ud} & V_{us} & V_{ub} \\ V_{cd} & V_{cs} & V_{cb} \\ V_{td} & V_{ts} & V_{tb} \end{pmatrix} =$$

$$= \begin{pmatrix} 0.97446 \pm 0.00010 & 0.22452 \pm 0.00044 & 0.00365 \pm 0.00012 \\ 0.22438 \pm 0.00044 & 0.97359^{+0.00010}_{-0.00011} & 0.04214 \pm 0.00076 \\ 0.00896^{+0.00024}_{-0.00023} & 0.04133 \pm 0.00074 & 0.999105 \pm 0.000032 \end{pmatrix}.$$

During the 1960's, Weinberg, Salam and Glashow started to work on the unification of the electromagnetic and weak theory [1–3]. In order to develop a unified theory, a

symmetry group needs to be identified.

QED is invariant under local gauge transformations of the $U(1)$ symmetry group; instead of the electric charge for QED, a quantum number called hypercharge, Y , is introduced, being related to the electric charge, Q , through:

$$Q = T^3 + \frac{Y}{2} \quad (1.14)$$

where T^3 is the third component of the weak isospin, generating the $SU(2)$ algebra.

The gauge fields of the $SU(2)_L \otimes U(1)_Y$ gauge symmetry group correspond to the four bosons W^\pm , Z^0 and γ : they are four massless mediating bosons, organised in a weak isospin triplet W^1, W^2, W^3 ($SU(2)_L$) and a weak hypercharge singlet B ($U(1)_Y$).

The free Lagrangian for massless fermions is then written as:

$$\mathcal{L} = i\bar{u}(x)\gamma^\mu\partial_\mu u(x) + i\bar{d}(x)\gamma^\mu\partial_\mu d(x) = \sum_{j=1}^3 i\bar{\psi}_j(x)\gamma^\mu\partial_\mu\psi_j(x). \quad (1.15)$$

Following the same procedure used for the QED and QCD theories, the EW theory has to be invariant under global and local $SU(2)_L \otimes U(1)_Y$ transformations, thus the ∂_μ derivative has to be replaced with a covariant derivative, that is:

$$D_\mu = \partial_\mu + ig'\frac{Y}{2}B_\mu(x) + ig\frac{\sigma_a}{2}W_\mu^a(x) \quad (1.16)$$

where g' and g are the coupling constants for $U(1)_Y$ and $SU(2)_L$, while W_μ^a and B_μ are the gauge bosons of the $SU(2)_L$ and $U(1)_Y$ groups, respectively. The Pauli matrices σ_a ($a = 1, 2, 3$) and the hypercharge Y represent the generators of such groups.

The electric charge is related to the coupling constants of $SU(2)_L$ and $U(1)_Y$ by the equation:

$$g\sin\theta_W = g'\cos\theta_W = e \quad (1.17)$$

where θ_W is the weak-mixing angle, also called Weinberg angle, with $\sin^2\theta_W = 0.23122 \pm 0.00017$ [8]. The boson field strengths, necessary to build the gauge-invariant kinetic term for the gauge fields are the following:

$$B_{\mu\nu} \equiv \partial_\mu B_\nu - \partial_\nu B_\mu \quad (1.18)$$

$$W_{\mu\nu}^i \equiv \partial_\mu W_\nu^i - \partial_\nu W_\mu^i - g\epsilon^{ijk}W_\mu^j W_\nu^k \quad (1.19)$$

where ϵ^{ijk} is the Levi-Civita tensor. Thus the kinetic Lagrangian of the gauge fields becomes:

$$\mathcal{L}_{Kin} = -\frac{1}{4}B_{\mu\nu}B^{\mu\nu} - \frac{1}{4}W_{\mu\nu}^i W_i^{\mu\nu} \quad (1.20)$$

and the resulting electroweak Lagrangian is:

$$\mathcal{L}_{EW} = \sum_{j=1}^3 i\bar{\psi}_j(x)\gamma^\mu D_\mu\psi_j(x) - \frac{1}{4}B_{\mu\nu}B^{\mu\nu} - \frac{1}{4}W_{\mu\nu}^a W_a^{\mu\nu} \quad (1.21)$$

where the first term describes fermion propagation and fermion interaction, while the last two terms describe EW free field propagation with the kinetic part for both W_μ and

B_μ fields and the self-coupling of the W_μ field. Since the field strengths, $W_{\mu\nu}^a$, contain a quadratic term, the Lagrangian gives rise to cubic and quartic self-interactions among gauge fields. The gauge symmetry forbids again to write mass terms for the gauge bosons. The experimental evidences of massive gauge bosons represent one of the elements suggesting the existence of a mechanism which must give mass to these particles (Higgs mechanism, Section 1.2).

Fermionic masses are also forbidden, because they would produce an explicit breaking of the gauge symmetry. The electromagnetic interaction and the neutral weak current interaction arise from a mixing of the W^3 and B fields, i.e.:

$$\begin{pmatrix} A_\mu \\ Z_\mu^0 \end{pmatrix} = \begin{pmatrix} \cos\theta_W & \sin\theta_W \\ -\sin\theta_W & \cos\theta_W \end{pmatrix} \cdot \begin{pmatrix} B_\mu \\ W_\mu^3 \end{pmatrix}. \quad (1.22)$$

Furthermore, the W^\pm bosons are linear combinations of W^1 and W^2 :

$$W^\pm = \frac{1}{\sqrt{2}}(W^1 \mp iW^2). \quad (1.23)$$

1.2 A Spontaneous Symmetry Breaking (SSB): the Higgs Mechanism

The Lagrangian for a complex scalar field $\phi(x)$ reads [11]:

$$\mathcal{L} \equiv T - V = \frac{1}{2}(\partial_\mu\phi)^2 - \left(\mu^2\phi^\dagger\phi + \lambda(\phi^\dagger\phi)^2\right) \quad (1.24)$$

where $\lambda > 0$ and the Lagrangian is invariant under the global phase transformations of the scalar field (U(1)) already defined. The potential has two possible shapes, depending on the sign of μ^2 , as shown in Figure 1.6:

1. if $\mu^2 > 0$, the potential has only the trivial minimum or ground state, identified by $\phi = 0$; this case describes a scalar field with mass μ and quartic coupling λ ;
2. if $\mu^2 < 0$, the potential has an infinite number of degenerate states of minimum energy satisfying:

$$|\phi_0| = \sqrt{\frac{-\mu^2}{2\lambda}} \equiv \frac{\nu}{\sqrt{2}} \quad (1.25)$$

where ϕ_0 is the vacuum mean value of the field ϕ , also called the vacuum expectation value (vev).

For a specific ground state, the original symmetry gets spontaneously broken; in fact, if the perturbation of the ground state is parameterised in terms of ϕ_1 and ϕ_2 , where ϕ_1 and ϕ_2 are real fields, as:

$$\phi(x) = \nu + \frac{1}{\sqrt{2}}(\phi_1(x) + i\phi_2(x)), \quad (1.26)$$

the potential becomes:

$$V(\phi) = V(\phi_0) - \mu^2\phi_1^2 + \lambda\nu\phi_1(\phi_1^2 + \phi_2^2) + \frac{\lambda}{4}(\phi_1^2 + \phi_2^2)^2. \quad (1.27)$$

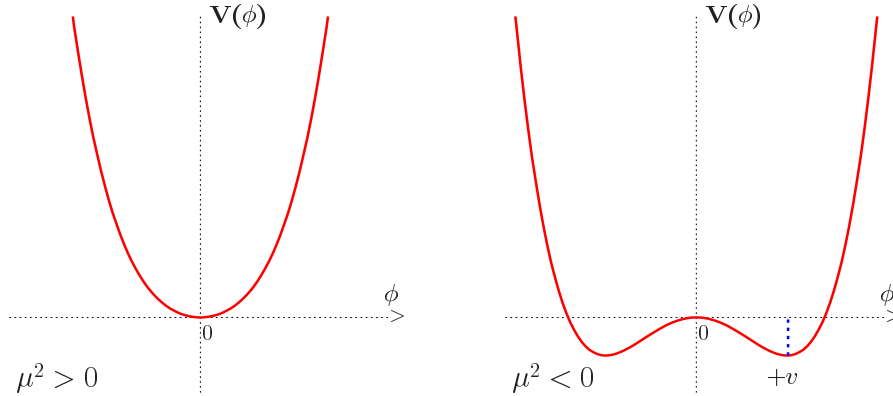


Figure 1.6: The potential V of the scalar field ϕ in the case $\mu^2 > 0$ (left) and $\mu^2 < 0$ (right) [17].

Thus the ϕ_1 describes a state with mass $m_{\phi_1}^2 = 2\lambda\nu^2 = -2\mu^2$ while ϕ_2 describes a massless state: the Lagrangian does not possess the original symmetry. This is the simplest example of spontaneously broken symmetry.

The fact that massless particles appear when a global symmetry is spontaneously broken is known as the Goldstone theorem [18, 19]: given a Lagrangian that is invariant under a group of continuous transformations with N generators, if M of N generators are spontaneously broken, in the particle spectrum of the theory, developed around the vacuum expectation value, there will be M massless particles.

This approach has to be extended to the non-abelian case of the SM, where masses for the three gauge bosons W^\pm and Z have to be generated, while the photon should remain massless: the resulting theory must still include QED with its unbroken $U(1)$ symmetry. The Higgs mechanism is used in order to introduce the mass terms [5–7]; first of all, a $SU(2)$ doublet of complex scalar field is introduced:

$$\phi = \begin{pmatrix} \phi^+ \\ \phi^0 \end{pmatrix} = \frac{1}{\sqrt{2}} \begin{pmatrix} \phi_1 + i\phi_2 \\ \phi_3 + i\phi_4 \end{pmatrix} \quad (1.28)$$

with the corresponding Lagrangian being:

$$\mathcal{L}_{scalar} = (D_\mu \phi)^\dagger (D^\mu \phi) - V(\phi) \quad (1.29)$$

where D_μ is the covariant derivative associated to $SU(2)_L \otimes U(1)_Y$ and $V(\phi)$:

$$V(\phi) = \mu^2(\phi^\dagger \phi) + \lambda(\phi^\dagger \phi)^2 \quad (1.30)$$

is the quartic potential associated to the new scalar field. The parameter λ of the potential is assumed to be positive.

When $\mu^2 < 0$, there is not a single vacuum located at 0, but the two minima in one dimension correspond to a continuum of minimum values in $SU(2)$. The canonical solution for the Higgs potential ground state is:

$$\phi_1 = \phi_2 = \phi_4 = 0, \quad \phi_3 = -\frac{\mu^2}{\lambda} = \nu, \quad \text{being} \quad \nu = \left(\frac{-\mu^2}{\lambda} \right)^{\frac{1}{2}} \quad (1.31)$$

and the corresponding vacuum state is:

$$\phi_0 = \frac{1}{\sqrt{2}} \begin{pmatrix} 0 \\ \nu \end{pmatrix}. \quad (1.32)$$

The ϕ field can be expanded around the vacuum expectation value by a perturbation:

$$\phi(x) = \frac{1}{\sqrt{2}} \begin{pmatrix} 0 \\ \nu + H(x) \end{pmatrix} \quad (1.33)$$

where $H(x)$ is a physical scalar Higgs field and the unitarity gauge is chosen in order to set the Goldstone boson components in the scalar field to zero.

The scalar Lagrangian can be expanded including the gauge Lagrangian expressed in terms of the physical gauge fields:

$$\begin{aligned} \mathcal{L}_{Higgs} = & \frac{1}{2} \partial_\mu H \partial^\mu H + \frac{g^2}{4} (\nu + H)^2 \left(W_\mu^+ W^{\mu-} + \frac{1}{2 \cos^2 \theta_W} Z_\mu Z^\mu \right) \\ & + \mu^2 H^2 - \lambda_{HHH} \nu H^3 - \frac{\lambda_{HHHH}}{4} H^4 \end{aligned} \quad (1.34)$$

where the first three terms describe the kinetic and the mass terms of the W and Z fields together with the interaction between these fields and the Higgs field. The last two terms describe the self-couplings of the Higgs scalar field. Writing explicitly the Lagrangian, the W and Z boson masses and the self-interactions of the Higgs boson can be expressed as:

- $M_W = g\nu/2$
- $M_Z = g\nu/2\cos\theta_W$
- $\nu = (\sqrt{2}G_F)^{-1/2} \sim 246 \text{ GeV}$
- $\lambda_{HHH} = 3M_H^2/\nu$ and $\lambda_{HHHH} = 3M_H^2/\nu^2$.

The Higgs mass is given by $M_H = \sqrt{-2\mu^2} = \sqrt{2\lambda\nu}$: even though ν is known, λ is a free parameter of the theory, thus the SM does not predict the Higgs-boson mass value.

A fermionic mass term, $m\bar{\psi}\psi$, is prohibited since it would break the gauge symmetry. Thus new terms, involving the so-called *Yukawa coupling*, need to be added to the Lagrangian in order to generate the masses of charged leptons:

$$\mathcal{L}_{Yukawa}^{Leptons} = -y_t (\bar{\psi}_L \phi \psi_R + \bar{\psi}_R \phi^\dagger \psi_L) \quad (1.35)$$

where y_t is the Yukawa coupling. After spontaneous symmetry breaking, the Yukawa Lagrangian becomes:

$$\mathcal{L}_{Yukawa}^{Leptons} = -\frac{y_t}{\sqrt{2}} \nu (\bar{\ell}_L \ell_R + \bar{\ell}_R \ell_L) - \frac{y_t}{\sqrt{2}} \nu (\bar{\ell}_L \ell_R + \bar{\ell}_R \ell_L) H \quad (1.36)$$

where lepton masses of value $M_\ell = y_t \nu / \sqrt{2}$ are generated. The Higgs interaction with quarks can be described by:

$$\mathcal{L}_{Yukawa}^{Quarks} = -y_d \bar{Q}_L \phi d_R - y_u \bar{Q}_L \tilde{\phi}^c u_R + h.c. \quad (1.37)$$

where $Q_L = \begin{pmatrix} u \\ d \end{pmatrix}_L$, $\tilde{\phi}^c \equiv i\sigma_2\phi^*$, i.e. the \mathcal{C} -conjugate scalar field, $y_{u,d}$, i.e. the Yukawa couplings, are matrices introducing the mixing between different quark flavours and $M_{u,d} = y_{u,d}\nu/\sqrt{2}$. The generic form of the Yukawa Lagrangian reads:

$$\mathcal{L}_{Yukawa} = - \left(1 + \frac{H}{\nu}\right) m_f \bar{f} f. \quad (1.38)$$

The total SM Lagrangian is represented by the sum of the following terms:

$$\mathcal{L}_{SM} = \mathcal{L}_{QCD} + \mathcal{L}_{EW} + \mathcal{L}_{Higgs} + \mathcal{L}_{Yukawa}. \quad (1.39)$$

It is important to note that lepton and quark masses are free parameters of the theory; moreover, neutrinos, that do not have right-handed states, remain massless. Following experimental evidences, the three right-handed neutrinos with the corresponding mass terms can be added in a minimal extension of the Standard Model.

The coupling of the Higgs boson to fermions is proportional to the mass, thus leading to very different values of the strengths of these couplings, given the huge mass range considered.

1.3 The Standard Model Higgs Boson

The search for the particle responsible of the Higgs mechanism, the Higgs boson, has lasted for decades. More than 20 years after the formulation of the Higgs mechanism had to pass until a significant mass range could be probed first with the Large Electron Positron Collider (LEP) at CERN [20] and then with the Tevatron [21] proton-antiproton collider.

In 2010 the Large Hadron Collider (LHC) [22], whose main features are summarised in Chapter 2, started to take data at unprecedented centre-of-mass energies with the primary goal of confirming the existence of this boson.

Finally, in July 2012, the discovery of a particle compatible with the SM Higgs boson by the ATLAS [23, 24] and CMS [25, 26] experiments at the LHC represented a great milestone in the history of particle physics. After the discovery of the Higgs boson, a new era in understanding the nature of electroweak symmetry breaking, possibly completing the SM and constraining effects from NP, has opened. One of the main focus of ATLAS and CMS physics analyses is the precision measurement of the properties of the Higgs boson including spin-parity, couplings and evidence for production mechanisms, which are essential tests of the SM.

In the following sections, these properties, ranging from the main production modes and main decay channels in proton-proton collisions, to the mass and width of this particle, are described.

1.3.1 Higgs-Boson Production

The main mechanisms to produce the Higgs boson are the following: through the fusion of gluons (gluon-fusion, or ggF); through the fusion of weak vector bosons (VBF); in association with a W or a Z boson (WH or ZH , VH to identify both WH and ZH), or in association with one or more top quarks ($t\bar{t}H + tH$). The size of the respective cross

sections depends both on the type of colliding hadrons and on the collision energy; the ranking of different mechanisms at the LHC is shown in Figure 1.7 as a function of the Higgs-boson mass (*a*) and as a function of LHC centre-of-mass energy (*b*).

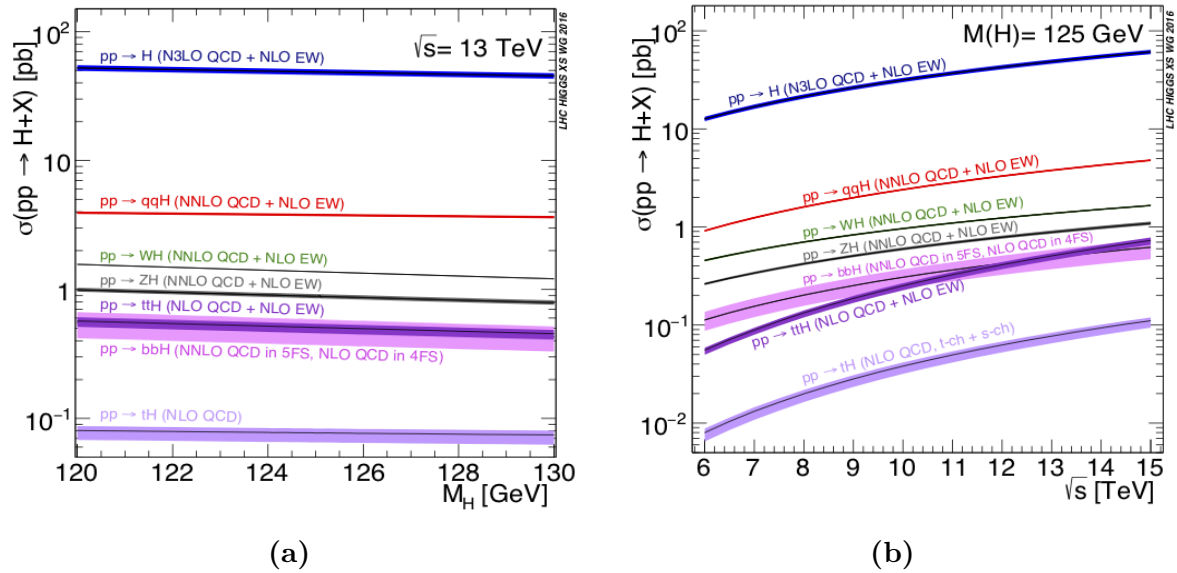


Figure 1.7: The SM Higgs-boson production cross section at $\sqrt{s} = 13$ TeV in proton-proton collisions as a function of the Higgs-boson mass (a) and as a function of the LHC centre-of-mass energy (b) [27].

The gluon-fusion production mode

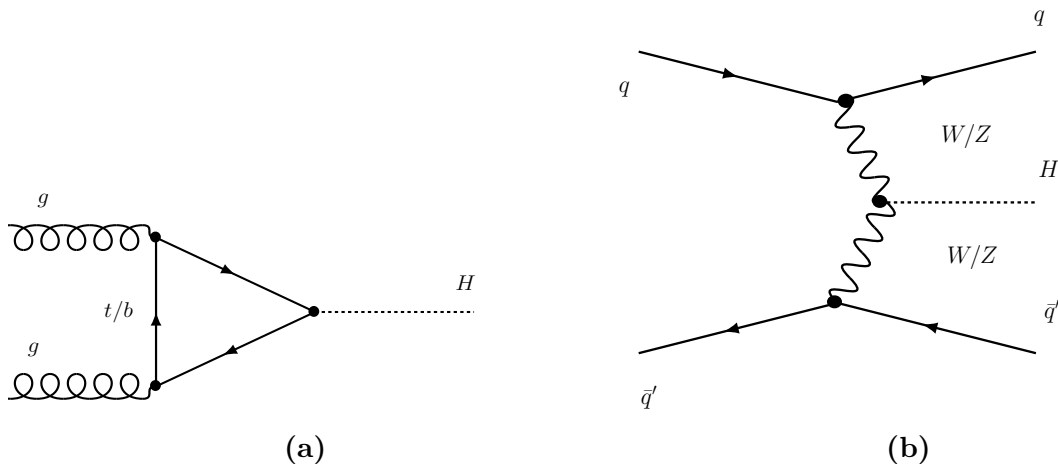


Figure 1.8: Leading-order diagrams for the gluon fusion (a) and vector-boson fusion (b) initiated production of the SM Higgs boson.

Due to the high flux of gluons in high-energy proton-proton collisions, the gluon-fusion process is the production mode having the largest cross-section at the LHC: two gluons combine mediated by a loop of virtual quarks. Due to the dependence of the Higgs-boson

couplings to quarks on the square of the quark mass, this process is more likely for heavier quarks, thus it is sufficient to consider virtual top and bottom loops. When the Higgs boson is produced through this production mode, there are no additional particles in the final state except for the products of the decays of the Higgs boson itself other than any additional QCD radiation.

The current best prediction for the inclusive ggF cross section of a Higgs boson with a mass $M_H = 125$ GeV at the LHC for a centre-of-mass energy of $\sqrt{s} = 13$ TeV, is [27]:

$$\sigma_{ggF} = 48.6 \text{ pb}^{+2.2 \text{ pb}(+4.6\%)}_{+3.3 \text{ pb}(+6.7\%)} \text{ (theory)} \pm 1.6 \text{ pb} (3.2\%) \text{ (PDF} + \alpha_S) \quad (1.40)$$

where the total uncertainty is divided into contributions from theoretical uncertainties, “theory”, and from parametric uncertainties due to parton-distribution-function (PDF) uncertainties and α_S computation uncertainties, “PDF + α_S ”.

This cross section is at least an order of magnitude larger than the other production cross sections. Figure 1.8 (a) shows the leading-order (LO) diagram for the gluon-fusion production mode.

The vector-boson-fusion production mode

The Higgs-boson production mode with the second largest cross section at the LHC is vector-boson fusion. It proceeds through the scattering of two quarks or anti-quarks mediated by the exchange of a virtual W or Z boson, which radiates the Higgs boson. This production mode has a clear signature consisting in two energetic jets, coming from the fragmentation of the quarks, that appear in the forward region of the detector close to the beam pipe, in addition to the products of the Higgs-boson decay. It represents $\sim 10\%$ of the total production cross section for a Higgs boson with a mass $M_H = 125$ GeV. The leading-order diagram for VBF is shown in Figure 1.8 (b).

Higgs-strahlung: WH and ZH associated production mechanism

The next most relevant Higgs-boson production mechanism is the associated production with an electroweak vector boson W or Z , also called Higgs-strahlung. Most of the contribution to this production mode comes from the annihilation of quarks even if, for the ZH production, there are also gluon-gluon contributions that produce the Higgs and the Z bosons through a top-quark loop. Figure 1.9 shows Feynman diagrams for qq - and gg -initiated VH processes.

Higgs production in association with top quarks

Finally, the Higgs production in association with top quarks represents one of the rarest Higgs-boson production modes. Nevertheless, this production mode can provide important information on the Yukawa coupling and its relative sign (tH), since it involves the direct coupling of the Higgs boson to the top quark. As can be seen from the set of Feynman diagrams shown in Figure 1.10, the $t\bar{t}H$ and tH processes have very complex final states, thus increasing the experimental challenge of isolating them. The presence of other tagging objects (either b -jets, jets or leptons) in addition to the Higgs-boson decay products allows to reduce the background, reaching a good sensitivity despite the low cross section of this process.

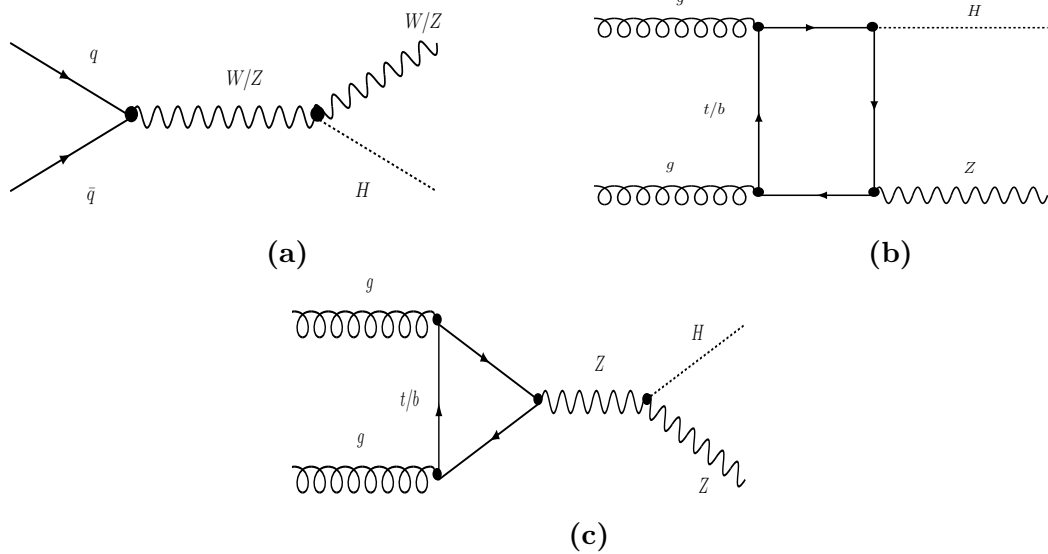


Figure 1.9: Leading-order diagrams for the production of a Higgs boson in association with a vector boson.

1.3.2 Higgs-Boson Decays

The branching fraction of a certain final state f is defined as the fraction of the time that a particle decays into that certain final state; it is related to the partial and the total width through:

$$BR(H \rightarrow X_f) = \frac{\Gamma(H \rightarrow X_f)}{\sum_f \Gamma(H \rightarrow X_f)}. \quad (1.41)$$

The SM prediction for the branching fractions of the different decay modes of the Higgs boson depends on the value of the Higgs-boson mass as it is shown in Figure 1.11. The branching fractions are reported as a function of the Higgs-boson mass over an extended mass range from 80 to 200 GeV (a) and in a zoomed range 5 GeV within the best-fit measured mass (b), 120 – 130 GeV. Table 1.3 reports the branching fractions for a SM Higgs boson with $M_H = 125.09$ GeV, i.e. Run 1 ATLAS+CMS best-fit combined result [28]. As a general rule, like it was made explicit in previous sections, the Higgs boson is more likely to decay into heavy fermions than light fermions, because of the fact that the strength of fermion interaction with the Higgs boson is proportional to fermion mass. In case of a Higgs boson heavier than the one that was discovered in 2012 with a mass of ~ 125 GeV, the most common decay should be into a pair of W or Z bosons. However, given the measured mass, the SM predicts that the most common decay is into a $b\bar{b}$ pair ($H \rightarrow b\bar{b}$), accounting for $\sim 58\%$ of the total decays. Due to the large QCD background, the gluon fusion production mode is really difficult to be detected but other production modes, like VH , can be used to achieve the evidence for this decay channel. $H \rightarrow WW^*$ represents the second most common decay mode, with a branching fraction of $\sim 21\%$. The W bosons subsequently decay into a quark and an antiquark or into a charged lepton and a high transverse momentum neutrino; the decays into quarks are difficult to distinguish from the background and the decays into leptons cannot be fully reconstructed due to the presence of neutrinos. A cleaner signal is given by the decay into a pair of Z bosons when each of the bosons subsequently decays into a pair of charged leptons (electrons or

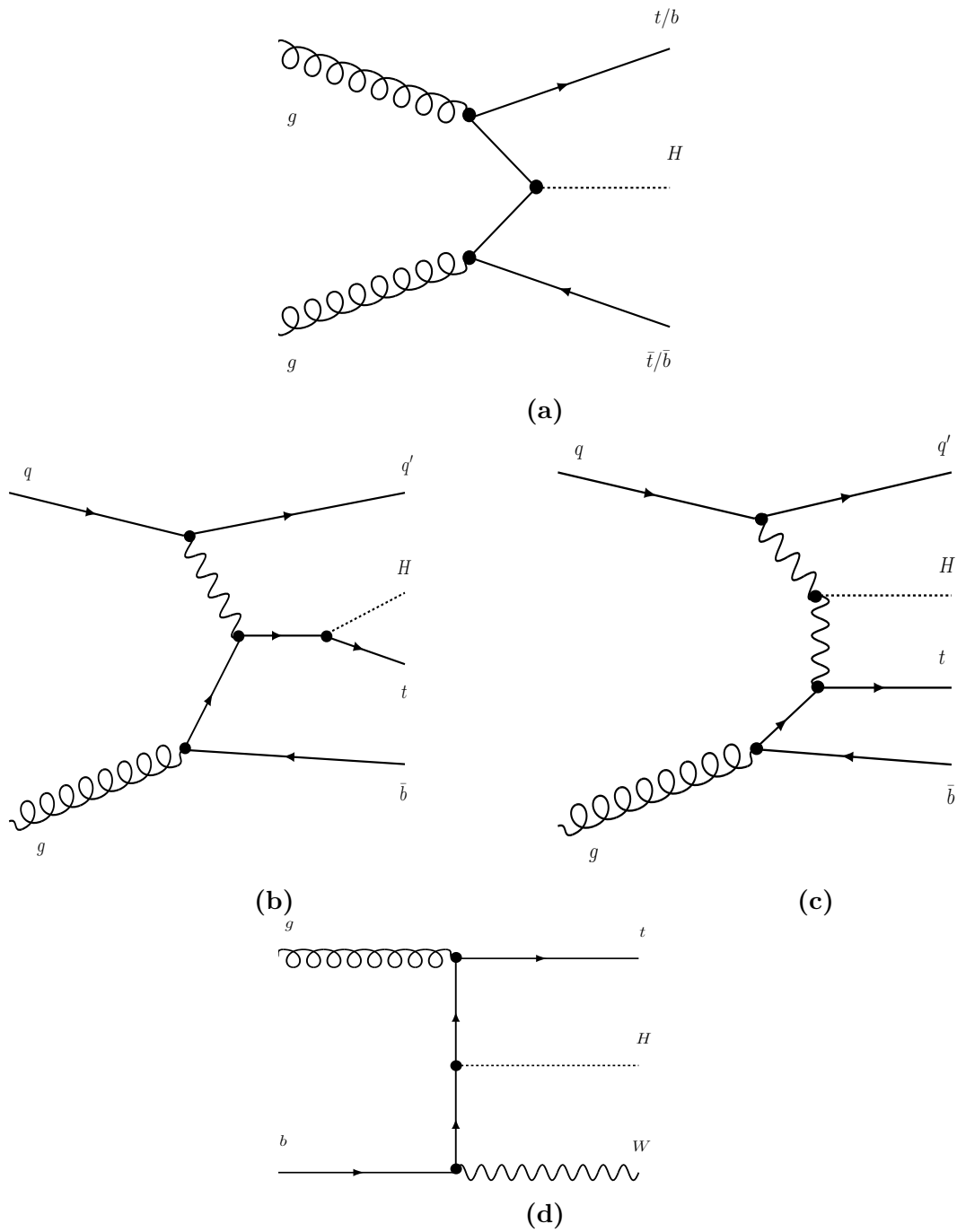


Figure 1.10: Leading-order diagrams for the production of a Higgs boson in association with top quarks.

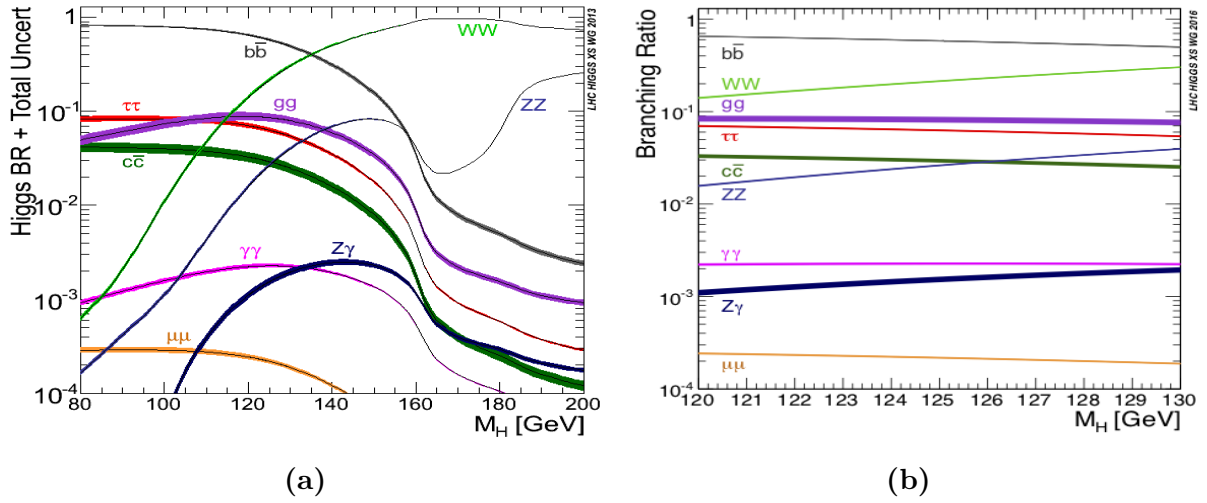


Figure 1.11: The SM Higgs-boson branching fractions as a function of the Higgs-boson mass over an extended mass range from 80 to 200 GeV (a) and in a zoomed range 5 GeV within the best-fit measured mass (b), 120 – 130 GeV [27].

muons) that are easy to be detected and result in almost no background contributions; even if the production rate is really low, it is the so-called “golden channel”, as it has the clearest and cleanest signature among all the possible decay modes and has a good invariant mass resolution (1-2%).

Decay channel	Branching fraction
$H \rightarrow b\bar{b}$	5.81×10^{-1}
$H \rightarrow W^+W^-$	2.15×10^{-1}
$H \rightarrow gg$	8.18×10^{-2}
$H \rightarrow \tau^+\tau^-$	6.26×10^{-2}
$H \rightarrow ZZ$	2.64×10^{-2}
$H \rightarrow \gamma\gamma$	2.27×10^{-3}
$H \rightarrow Z\gamma$	1.54×10^{-3}
$H \rightarrow \mu^+\mu^-$	2.17×10^{-4}

Table 1.3: Branching fractions for a SM Higgs boson with $M_H = 125.09$ GeV [29].

Decays into massless gauge bosons (i.e. gluons or photons) are also possible, but require intermediate loop of virtual heavy quarks (top or bottom), for gluons and photons, and massive gauge bosons (W^\pm loops) for photons. The most common process is the decay into a pair of gluons through a loop of virtual heavy particles occurring $\sim 9\%$ of the times; it is really difficult to distinguish such a decay from the QCD background, typical of a hadron collider.

The decay into a pair of photons, proceeding via loop diagrams with main contributions

from W boson and top quark loops, has a small branching fraction, $\sim 0.23\%$, but provides the highest signal sensitivity to a SM Higgs boson signal followed by the ZZ^* and WW^* channels, due to two high energetic photons that form a very narrow invariant mass peak; it has a good mass resolution (1-2%).

Double-Higgs production

The main interest in the double-Higgs production comes from the fact that it provides information on the Higgs potential; in particular, it gives direct access to the Higgs cubic self-interaction and to the quartic couplings among two Higgs bosons and a pair of gauge bosons or of top quarks. At hadron colliders, double-Higgs pairs are dominantly produced via the following processes: gluon fusion (ggF), vector-boson fusion (VBF), associated production of Higgs pairs with a W or a Z boson (VHH) and $t\bar{t}HH$ associated production. While searches in the ggF production mode are more sensitive to deviations in the Higgs self-interactions, the VBF production mode is particularly sensitive to c_{2V} , i.e. the quartic coupling between the Higgs bosons and vector bosons (di-vector-boson di-Higgs-boson $VVHH$). The c_{2V} coupling is significantly constrained by ATLAS excluding a region that corresponds to $c_{2V} < -1.02$ and $c_{2V} > 2.71$ thanks to a search for double-Higgs production via vector-boson fusion (VBF) in the $b\bar{b}b\bar{b}$ final state [30].

The most relevant production is gluon fusion $gg \rightarrow HH$, accounting for more than 90% of the total Higgs-boson pair production cross section and proceeding via virtual top and bottom quarks, i.e. box and triangle diagrams, as shown in Figure 1.12, like single-Higgs ggF production.

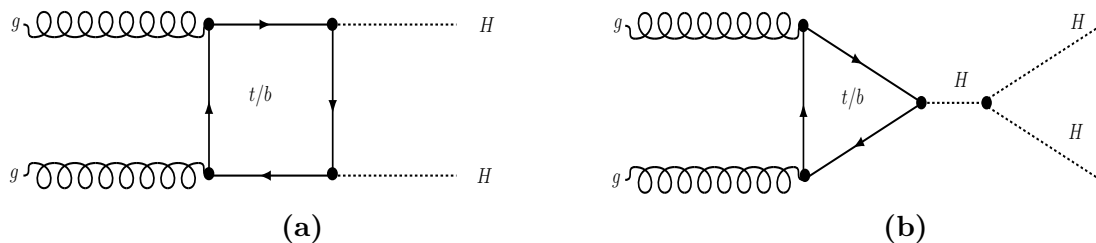


Figure 1.12: Feynman diagrams for box (a) and triangle (b) topologies contributing to Higgs boson pair production via gluon fusion at leading order.

The interference between the diagrams leads to the small cross-section value which is a thousand times smaller than the single-Higgs cross section as shown in Figure 1.13 (a) reporting the cross sections of the different production modes including double-Higgs production. Figure 1.13 (b) shows the current total cross sections for Higgs pair production at a proton-proton collider, including higher-order corrections. The current best prediction for the inclusive ggF cross section for Higgs-boson pair production, considering a Higgs boson with a mass $M_H = 125$ GeV and a centre-of-mass energy of $\sqrt{s} = 13$ TeV, is [31]:

$$\sigma_{pp \rightarrow HH}^{ggF} = 31.05 \text{ fb}_{(-5.0\%)}^{(+2.2\%)} (\text{scale}) \pm 3.0\% (\text{PDF} + \alpha_S) \pm 2.6\% (m_{top} \text{ unc}) \quad (1.42)$$

where “scale” stands for the QCD renormalisation and factorisation scale, “PDF+ α_S ” stands for uncertainties on the PDFs and on the α_S computation and “ m_{top} unc” represents the uncertainties related to missing finite top-quark mass effects [32].

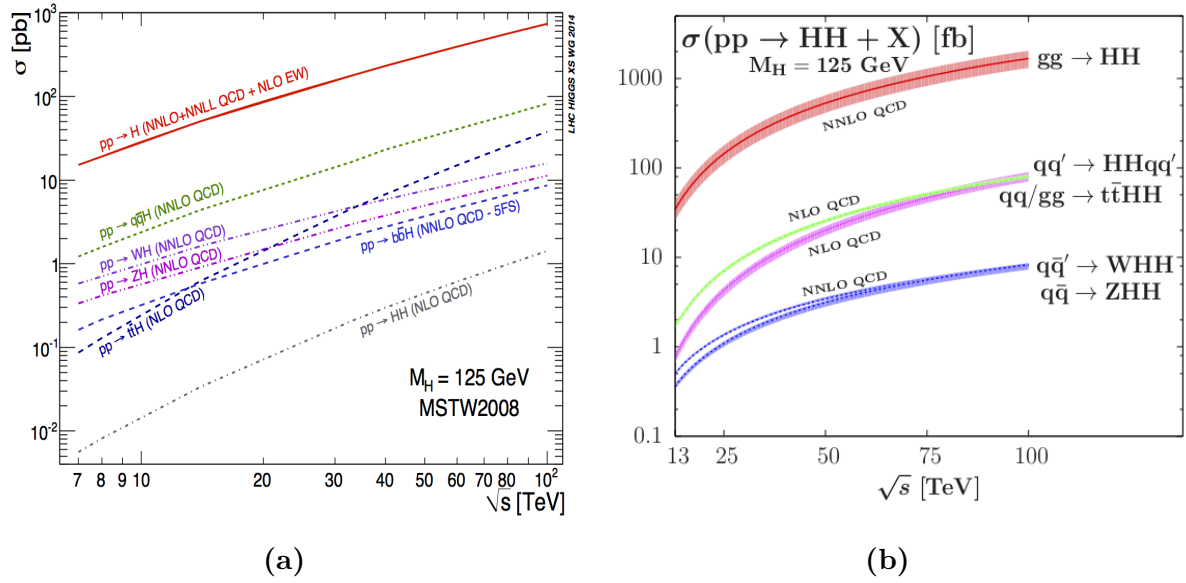


Figure 1.13: Higgs-boson production cross sections as a function of centre-of-mass energies with $M_H = 125$ GeV including double-Higgs production [29] (a); total cross sections for Higgs-pair production at a proton-proton collider in the main production channels as a function of the centre-of-mass energy with $M_H = 125$ GeV, including higher-order corrections [33] (b).

Table 1.4 reports the branching fractions for the leading double-Higgs final states. The largest contribution comes from the $b\bar{b}b\bar{b}$ decay channel, accounting for $\sim 34\%$ of the total decays but affected by a large QCD background.

Decay channel	Branching fraction
$HH \rightarrow b\bar{b}b\bar{b}$	3.37×10^{-1}
$HH \rightarrow b\bar{b}W^+W^-$	2.50×10^{-1}
$HH \rightarrow b\bar{b}\tau^+\tau^-$	7.27×10^{-2}
$HH \rightarrow W^+W^-W^+W^-$	4.63×10^{-2}
$HH \rightarrow b\bar{b}\gamma\gamma$	2.64×10^{-3}
$HH \rightarrow W^+W^-\gamma\gamma$	9.77×10^{-4}

Table 1.4: Double-Higgs branching fractions considering a Higgs boson with $M_H = 125.09$ GeV.

The most sensitive channels involve one Higgs boson decaying into a pair of b -quarks and one decaying into either two tau-leptons ($HH \rightarrow b\bar{b}\tau^+\tau^-$), another pair of b -quarks ($HH \rightarrow b\bar{b}b\bar{b}$) or two photons ($HH \rightarrow b\bar{b}\gamma\gamma$). Despite the low branching fraction, $\sim 0.26\%$, the sensitivity of the $b\bar{b}\gamma\gamma$ final state arises from the fact that it has a clean signal and an excellent diphoton mass resolution due to the small background. Thus the most sensitive final states are chosen according to a compromise between the largeness of the Higgs branching fractions and their cleanliness with respect to the backgrounds [34].

Latest results from the ATLAS experiment setting limits on the gluon fusion $gg \rightarrow HH$

production process exploiting up to 36.1 fb^{-1} of proton-proton collision data, have been produced combining six analyses searching for Higgs boson pairs in the $b\bar{b}b\bar{b}$, $b\bar{b}W^+W^-$, $b\bar{b}\tau^+\tau^-$, $W^+W^-W^+W^-$, $b\bar{b}\gamma\gamma$ and $W^+W^-\gamma\gamma$ final states. Upper limits at the 95% confidence level are shown in Figure 1.14. The combined observed (expected) limit at 95% confidence level on the non-resonant Higgs-boson pair production cross section is 6.9 (10) times the predicted SM cross section.

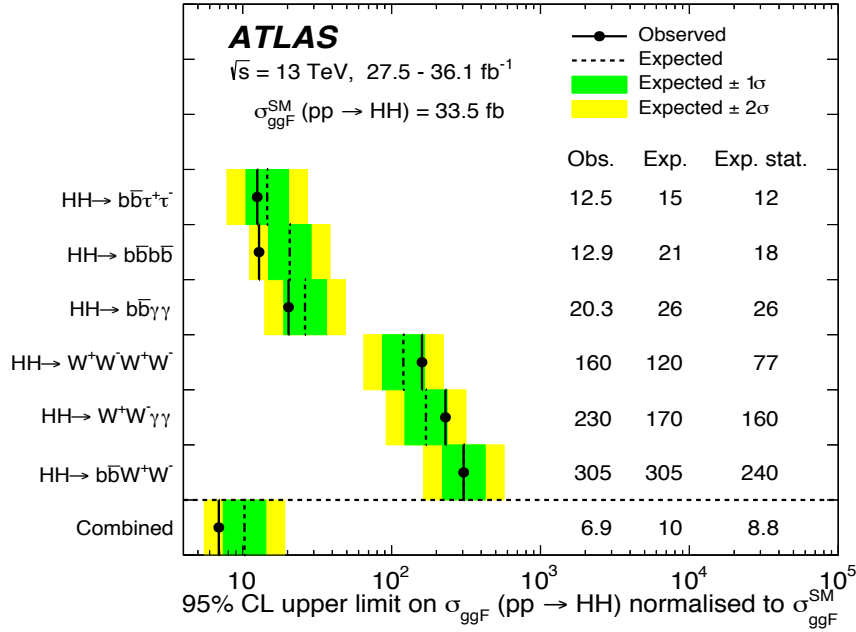


Figure 1.14: Upper limits at 95% CL on the cross section of the ggF SM HH production normalised to its SM expectation $\sigma_{SM}^{ggF}(pp \rightarrow HH)$ from the $b\bar{b}b\bar{b}$, $b\bar{b}W^+W^-$, $b\bar{b}\tau^+\tau^-$, $W^+W^-W^+W^-$, $b\bar{b}\gamma\gamma$ and $W^+W^-\gamma\gamma$ searches, and their statistical combination. The column “Obs.” lists the observed limits, “Exp.” the expected limits with all statistical and systematic uncertainties, and “Exp. stat.” the expected limits obtained including only statistical uncertainties in the fit [35].

1.4 Higgs-Boson Property Measurements

Higgs-boson mass measurements

In order to measure the mass of the Higgs boson, ATLAS and CMS experiments rely on the two high mass resolution and sensitive channels, $\gamma\gamma$ and ZZ^* , with a typical resolution of 1-2%, while the other channels have significantly worse resolutions up to $\sim 20\%$. The results from each of the four individual measurements, as well as various combinations, along with the LHC Run 1 result, are summarised in Figure 1.15 for both ATLAS and CMS experiments.

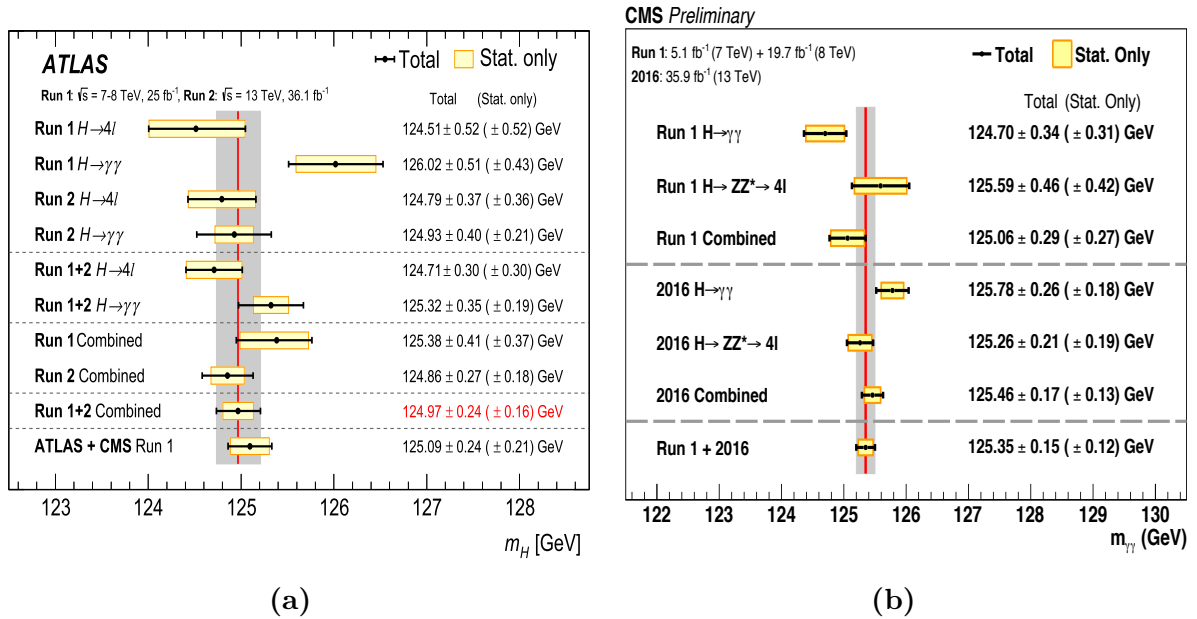


Figure 1.15: Summary of the Higgs-boson mass measurements from the individual and combined analyses, compared to the combined Run 1 measurement by ATLAS and CMS. The statistical-only (horizontal yellow-shaded bands) and total (black error bars) uncertainties are indicated. The (red) vertical line and corresponding (grey) shaded column indicate the central value and the total uncertainty of the combined ATLAS Run 1+2 measurement (a) and CMS Run 1+2 measurement (b) [36, 37].

The combination of CMS Run 1 and Run 2 measurements leads to a mass value [36]:

$$M_H = 125.35 \pm 0.15 \text{ GeV} = 125.35 \pm 0.12 \text{ (stat.)} \pm 0.09 \text{ (syst.) GeV} \quad (1.43)$$

where “stat.” stands for the statistical uncertainty and “syst.” for systematic uncertainties. The combination of the ATLAS Run 1 and Run 2 measurements yields a mass [37]:

$$M_H = 124.97 \pm 0.24 \text{ GeV} = 124.97 \pm 0.16 \text{ (stat.)} \pm 0.18 \text{ (syst.) GeV} . \quad (1.44)$$

The CMS mass measurements represent the most precise M_H to date.

Higgs-boson width measurements

In the Standard Model, the Higgs-boson width is very precisely predicted once the Higgs-boson mass is known. For a Higgs boson with a mass of 125 GeV, the width is

4.1 MeV [27]. It is dominated by the fermionic decay partial width at approximately 75%, while the vector-boson modes are suppressed and contribute at 25% only.

Direct on-shell measurements of the Higgs-boson width are limited by detector resolution and have errors much larger than the expected SM width with a sensitivity of ~ 1 GeV. Indirect measurements exploiting off-shell production of the Higgs boson have a substantial cross section at the LHC, due to the increased phase space as the vector bosons ($V = W, Z$) and top-quark decay products become on-shell with the increasing energy scale [38]. Both ATLAS and CMS have exploited the combination of on- and off-shell measurements to set the best limits on the Higgs-boson width. The ATLAS limits, determined using $ZZ^* \rightarrow 4\ell$ and $ZZ^* \rightarrow 2\ell 2\nu$ final states using data corresponding to an integrated luminosity of 36.1 fb^{-1} , are [38]:

$$\Gamma_H < 14.4 \text{ MeV} . \quad (1.45)$$

The CMS limits for the Higgs-boson width from on-shell and off-shell Higgs boson production in the four-lepton final state using an integrated luminosity of 80.2 fb^{-1} , under the assumption of SM-like couplings, are [39]:

$$0.08 < \Gamma_H < 9.16 \text{ MeV} . \quad (1.46)$$

The CMS lower bound on the Higgs width comes from the different fit procedure that has been used with respect to ATLAS measurement, i.e. profile-likelihood technique vs CLs method, respectively, explained in Chapter 5.

Higgs-boson coupling and signal-strength measurements

The Higgs-boson cross sections and branching fractions are often presented in terms of the modifier μ , defined as the ratio of the measured Higgs-boson yield, i.e. the total cross section times the branching fraction, to its SM expectation value:

$$\mu = \frac{\sigma \times BR}{\sigma_{SM} \times BR_{SM}} . \quad (1.47)$$

For a specific production mode i and decay final state f , the signal strengths μ_{if} are defined as:

$$\mu_{if} = \frac{\sigma_i}{\sigma_i^{SM}} \times \frac{BR_f}{BR_f^{SM}} \quad (1.48)$$

where $i=ggF, VBF, WH, ZH, t\bar{t}H$ production modes and $f = \gamma\gamma, ZZ^*, WW^*, \tau^+\tau^-, b\bar{b}$ decay channels. In the SM hypothesis, $\mu_i = \mu_f = 1$.

The best-fit value of the global signal strength obtained by ATLAS and CMS with the full Run 1 dataset is [40]:

$$\mu = 1.09_{-0.10}^{+0.11} = 1.09_{-0.07}^{+0.07} (\text{stat.})_{-0.04}^{+0.04} (\text{exp.})_{-0.06}^{+0.07} (\text{sig. th.})_{-0.03}^{+0.03} (\text{bkg. th.}) \quad (1.49)$$

where “stat.” stands for the statistical uncertainty, “sig. th.” and “bkg. th.” account for signal theory and background theory uncertainties, respectively. Finally, “exp.” contains the contributions of all the experimental systematic uncertainties.

Figure 1.16 shows the best-fit results for the production (a) and decay (b) signal strengths for the Run 1 combination of ATLAS and CMS data.

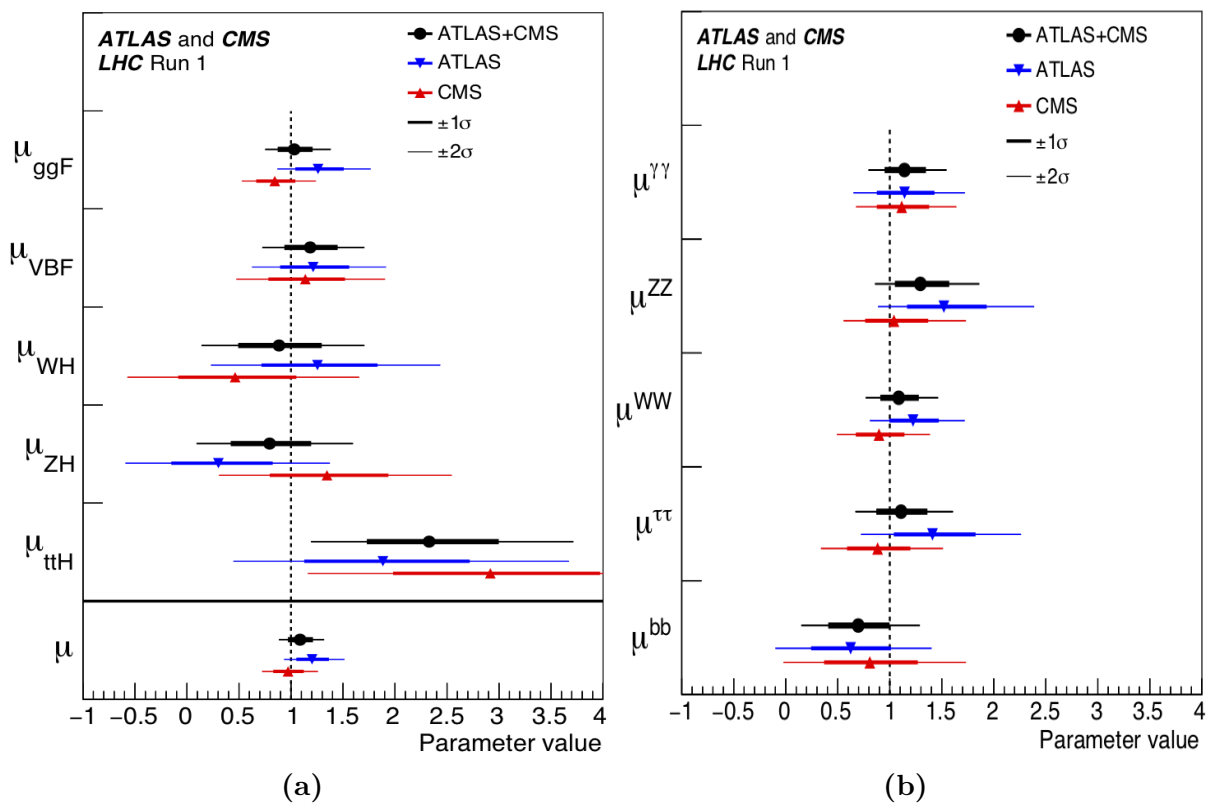


Figure 1.16: Best-fit results for the production (a) and decay (b) signal strengths for the combination of ATLAS and CMS Run 1 data. Results from each experiment together with the global signal strength μ are also shown. The error bars indicate the 1σ (thick lines) and 2σ (thin lines) intervals [40].

Preliminary Run 2 measurements of Higgs-boson production cross sections and branching fractions have been performed using up to 79.8 fb^{-1} of proton-proton collision data produced by the LHC at a centre-of-mass energy $\sqrt{s} = 13 \text{ TeV}$ and recorded by the ATLAS detector. The best-fit value of the global signal strength obtained by ATLAS is:

$$\mu = 1.11^{+0.09}_{-0.08} = 1.11^{+0.05}_{-0.05} (\text{stat.})^{+0.05}_{-0.04} (\text{exp.})^{+0.05}_{-0.04} (\text{sig. th.})^{+0.03}_{-0.03} (\text{bkg. th.}), \quad (1.50)$$

thus the standalone ATLAS measurement with the partial Run 2 dataset is already better than the combined ATLAS and CMS Run 1 result, mainly due to the reduction of statistical uncertainties. Figure 1.17 shows the signal strengths μ_{if} with $i=ggF, VBF, VH$ and $t\bar{t}H + tH$ production in each relevant decay mode $f = \gamma\gamma, ZZ^*, WW^*, \tau^+\tau^-, b\bar{b}$ using a luminosity of up to 80 fb^{-1} recorded with the ATLAS detector. The values are obtained from a simultaneous fit to all channels. No significant deviation from the Standard Model predictions is observed.

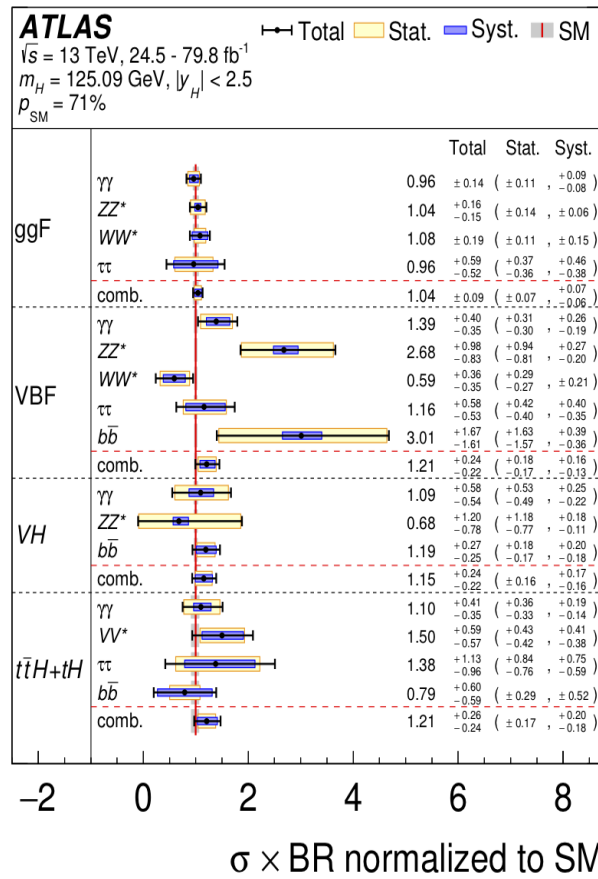


Figure 1.17: Cross sections times branching fraction for ggF , VBF , VH and $t\bar{t}H + tH$ production in each relevant decay mode, normalised to their SM predictions for the ATLAS experiment. The values are obtained from a simultaneous fit to all channels. The cross sections of the ggF , $H \rightarrow b\bar{b}$, VH , $H \rightarrow WW^*$ and VH , $H \rightarrow \tau^+\tau^-$ processes are fixed to their SM predictions. Combined results for each production mode are also shown, assuming SM values for the branching fractions into each decay mode [41].

In order to parameterise the Higgs coupling deviations from the SM, a simple parameterisation (the so called κ -framework) has been introduced in Reference [42], based on the leading-order contributions to each production and decay modes; using the zero-width approximation, the signal cross section can be decomposed in the following way for all channels:

$$(\sigma \cdot BR)(i\bar{i} \rightarrow H \rightarrow f\bar{f}) = \frac{\sigma_{i\bar{i}} \cdot \Gamma_{f\bar{f}}}{\Gamma_H} \quad (1.51)$$

where $\sigma_{i\bar{i}}$ is the production cross section through the initial state $i\bar{i}$, $\Gamma_{f\bar{f}}$ the partial decay width into the final state $f\bar{f}$ and Γ_H the total width of the Higgs boson. Higgs-boson production cross sections and decay rates for each process are thus parameterised via coupling-strength modifiers κ in the following way:

$$\kappa_i^2 = \frac{\sigma_{i\bar{i}}}{\sigma_{i\bar{i}}^{SM}} \quad \text{or} \quad \kappa_f^2 = \frac{\Gamma_{f\bar{f}}}{\Gamma_{f\bar{f}}^{SM}}. \quad (1.52)$$

The SM expectation corresponds by definition to $\kappa_i = \kappa_f = 1$.

Leading-order-coupling-scale-factor relations for Higgs-boson cross sections and partial-decay widths, relative to the SM and used in the results reported in this thesis, are reported in Table 1.5. The ratio of the observed couplings to the SM expectation is conventionally indicated by κ_V for vectors and κ_F for fermions.

Figure 1.18 shows the results of the combined fit in the (κ_V, κ_F) plane as well as the contributions of the individual decay modes. Both coupling modifiers, κ_V and κ_F , have been measured to be compatible with the SM expectation.

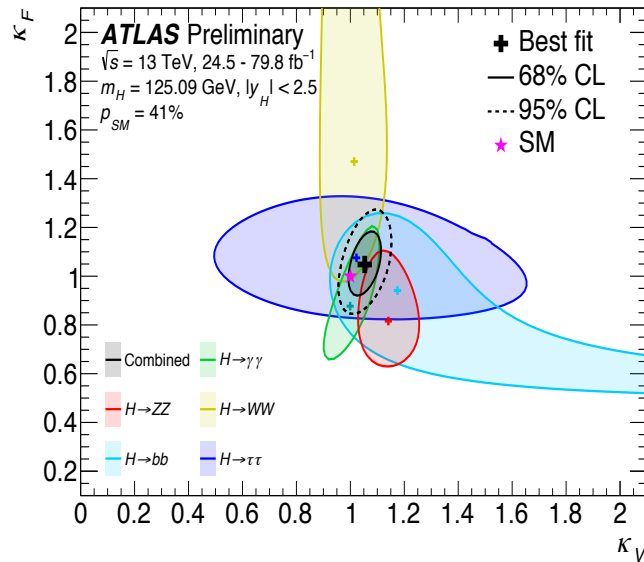


Figure 1.18: Negative log-likelihood contours at 68% and 95% confidence level in the (κ_V^f, κ_F^f) plane for the individual decay modes and their combination (black) assuming the coupling strengths to fermions and vector bosons to be positive. No contributions from invisible or undetected Higgs boson decays are assumed. The best-fit value for each measurement is indicated by a cross while the SM hypothesis is indicated by a star [41].

Production Mode	Resolved modifiers
$\sigma(ggF)$	$1.04 \kappa_t^2 + 0.002 \kappa_b^2 - 0.04 \kappa_t \kappa_b$
$\sigma(VBF)$	$0.73 \kappa_W^2 + 0.27 \kappa_Z^2$
$\sigma(qq/qg \rightarrow ZH)$	κ_Z^2
$\sigma(gg \rightarrow ZH)$	$2.46 \kappa_Z^2 + 0.46 \kappa_t^2 - 1.90 \kappa_Z \kappa_t$
$\sigma(WH)$	κ_W^2
$\sigma(t\bar{t}H)$	κ_t^2
$\sigma(tHW)$	$2.91 \kappa_t^2 + 2.31 \kappa_W^2 - 4.22 \kappa_t \kappa_W$
$\sigma(tHq)$	$2.63 \kappa_t^2 + 3.58 \kappa_W^2 - 5.21 \kappa_t \kappa_W$
$\sigma(b\bar{b}H)$	κ_b^2
Partial decay width	Resolved modifiers
Γ^{bb}	κ_b^2
Γ^{WW}	κ_W^2
Γ^{gg}	$1.11 \kappa_t^2 + 0.01 \kappa_b^2 - 0.12 \kappa_t \kappa_b$
$\Gamma^{\tau\tau}$	κ_b^2
Γ^{ZZ}	κ_Z^2
Γ^{cc}	$\kappa_c^2 (= \kappa_t^2)$
$\Gamma^{\gamma\gamma}$	$1.59 \kappa_W^2 + 0.07 \kappa_t^2 - 0.67 \kappa_W \kappa_t$
$\Gamma^{Z\gamma}$	$1.12 \kappa_W^2 - 0.12 \kappa_W \kappa_t$
Γ^{ss}	$\kappa_s^2 (= \kappa_b^2)$
$\Gamma^{\mu\mu}$	κ_μ^2

Table 1.5: Parameterisations of Higgs-boson production cross sections σ_i and partial decay widths Γ_f , normalised to their SM values, as functions of the coupling-strength modifiers κ [41].

1.4.1 Higgs self-coupling

One of the most important targets of the LHC is to improve the experimental results of the Run 1 and the complete exploration of the properties of the Higgs boson, in particular the self-interactions. This is the only way to reconstruct the scalar potential of the Higgs doublet field ϕ , that is responsible for spontaneous electroweak symmetry breaking,

$$V_H = \mu^2 \phi^\dagger \phi + \frac{1}{2} \lambda (\phi^\dagger \phi)^2 \quad \lambda = \frac{M_H^2}{v^2} \quad \mu^2 = -\frac{1}{2} M_H^2 \quad (1.53)$$

with $v = 246$ GeV. In the SM, the potential is fully determined by only two parameters, the vacuum expectation value, $v = (\sqrt{2}G_F)^{-1/2}$, and the coefficient of the $(\Phi^\dagger \Phi)^2$ interaction, λ . Considering the Standard Model an effective theory, λ stands for two otherwise free parameters, the trilinear (λ_{HHH}) and the quartic (λ_{HHHH}) self-couplings:

$$\lambda_{HHH} \text{ (or } \lambda_3) = \frac{3M_H^2}{v}, \quad \lambda_{HHHH} \text{ (or } \lambda_4) = \frac{3M_H^2}{v^2}. \quad (1.54)$$

The self-couplings determine the shape of the potential which is connected to the phase transition of the early universe from the unbroken to the broken electroweak symmetry. Large deviations of the trilinear and quartic couplings, λ_3 and λ_4 , are possible in scenarios beyond the SM predictions (BSM). For example, in two-Higgs doublet models where the lightest Higgs boson is forced to have SM-like couplings to vector bosons, quantum corrections may increase the trilinear Higgs-boson coupling by up to 100% [43]. Examples of two-Higgs doublet models modifying the value of the trilinear Higgs coupling are the Gildener-S.Weinberg (GW) [44] models of electroweak symmetry breaking, based on an extension of Coleman-Weinberg [45] theory of radiative corrections as the origin of spontaneous symmetry breaking, and involving a broken scale symmetry to generate a light Higgs boson in addition to a number of heavy bosons. The scalar couplings can acquire values larger than in the Standard Model at one-loop level of the Coleman-E.Weinberg expansion. In a two-Higgs doublet model of the GW mechanism, the trilinear Higgs self-coupling λ_{HHH} is typically 1.5 – 3.0 times its SM value [46].

Anomalous Higgs-boson self-couplings also appear in other BSM scenarios, such as models with a composite Higgs boson [47], or in Little-Higgs models [48–50].

The trilinear Higgs self-coupling can be probed directly in searches for multi-Higgs final states and indirectly via its effect on precision observables or loop corrections to single-Higgs production; the quartic self-coupling instead, being further suppressed by a power of v compared to the trilinear self-coupling, is currently not accessible at hadron colliders [51].

Preliminary Run 2 results of the Higgs self-coupling from direct searches for Higgs pairs of the ATLAS and CMS collaborations have been performed using up to 36.1 fb^{-1} and 35.9 fb^{-1} of proton-proton collision data produced by the LHC at a centre-of-mass energy $\sqrt{s} = 13$ TeV and recorded by the ATLAS and CMS detectors, respectively. Results are reported in terms of the ratio of the Higgs-boson self-coupling to its SM expectation, i.e. $\kappa_\lambda = \lambda_{HHH}/\lambda_{HHH}^{SM}$. Latest constraints coming from the combination of the most sensitive final states, i.e. $b\bar{b}\tau^+\tau^-$, $b\bar{b}b\bar{b}$ and $b\bar{b}\gamma\gamma$ (and $b\bar{b}VV$ for CMS), are shown in Figure 1.19 and Table 1.6 where the limits from single channels are reported.

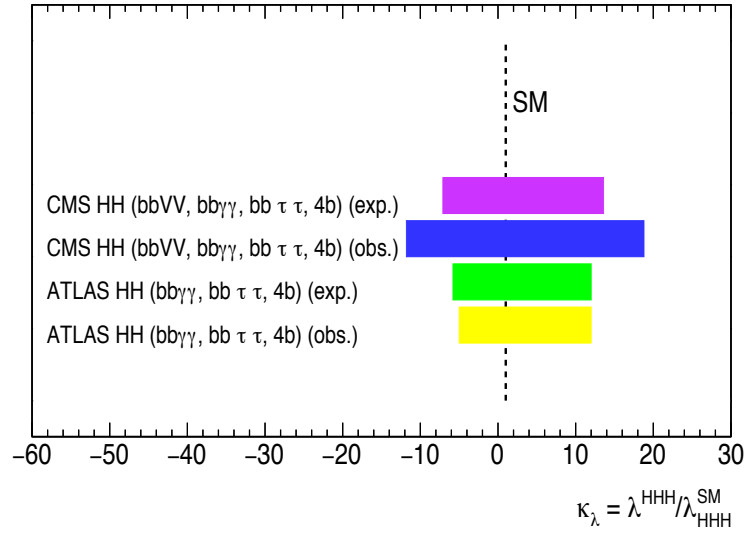


Figure 1.19: Summary of recent constraints on the Higgs self-coupling by the ATLAS and CMS experiments [35, 52].

Details on the channels used in the ATLAS combination and the methodology exploited in order to extract κ_λ intervals are reported in Chapter 7. The best final states for the κ_λ limit are the $b\bar{b}\tau^+\tau^-$ and $b\bar{b}\gamma\gamma$ channels for ATLAS and CMS, respectively. Differences between ATLAS and CMS sensitivities in each channel come from different optimisations of the analysis strategies.

Channels	Collaboration	κ_λ [95% CL] (obs.)	κ_λ [95% CL] (exp.)
$HH \rightarrow b\bar{b}\tau^+\tau^-$	ATLAS [35]	$[-7.4, 15.7]$	$[-8.9, 16.8]$
	CMS [34]	$[-18, 26]$	$[-14, 22]$
$HH \rightarrow b\bar{b}b\bar{b}$	ATLAS [35]	$[-10.9, 20.1]$	$[-11.6, 18.8]$
	CMS [34]	$[-23, 30]$	$[-15, 23]$
$HH \rightarrow b\bar{b}\gamma\gamma$	ATLAS [35]	$[-8.1, 13.1]$	$[-8.1, 13.1]$
	CMS [34]	$[-11, 17]$	$[-8.0, 11.4]$
Combination	ATLAS [35]	$[-5.0, 12.0]$	$[-5.8, 12.0]$
	CMS [52]	$[-11.8, 18.8]$	$[-7.1, 13.6]$

Table 1.6: Allowed κ_λ intervals at 95% CL for the $b\bar{b}\tau^+\tau^-$, $b\bar{b}b\bar{b}$ and $b\bar{b}\gamma\gamma$ final states and their combination for both ATLAS and CMS experiments. The column “obs.” lists the observed results while the column “exp.” reports the expected results obtained including all statistical and systematic uncertainties in the fit [34, 35, 52].

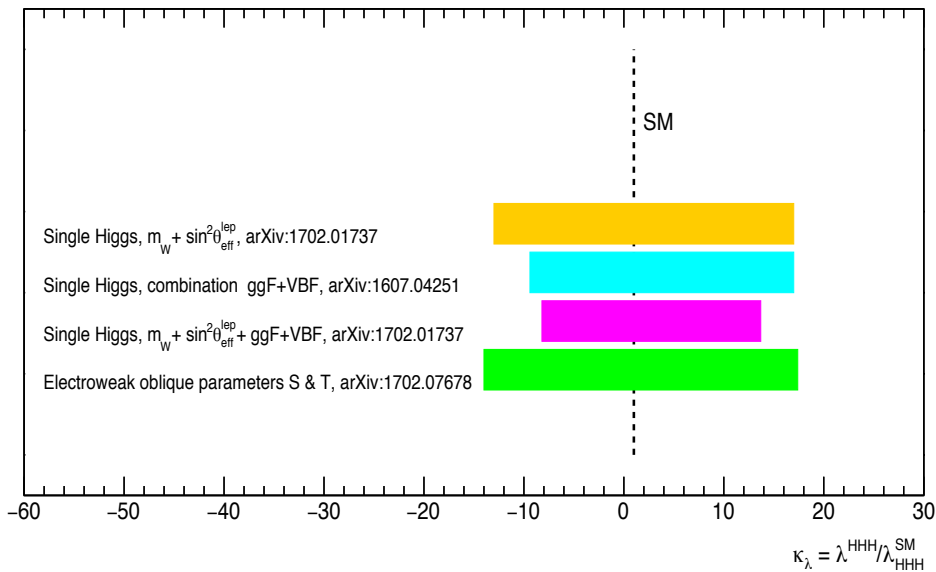


Figure 1.20: Summary of constraints on the Higgs self-coupling from precise observable measurements [53–55].

Constraints on the trilinear Higgs self-coupling from precision observables, like the mass of the W boson, m_W , the effective Weinberg angle, $\sin^2 \theta_{\text{eff}}^{\text{lep}}$ [53], the electroweak oblique parameters [54], and loop corrections to single-Higgs production, the best κ_λ interval coming from the combination of ggF and VBF production mode [55], are shown in Figure 1.20. Theoretical models describing the extraction of the Higgs self-coupling either from double-Higgs production measurements or from single-Higgs production measurements are reported in Chapter 6.

This thesis is dedicated to the improvement of experimental constraints on the Higgs-boson self-coupling with the ATLAS detector. These results are presented in Chapters 7, 8, 9.

1.5 The Standard Model: successes and open issues

The discovery of the Higgs boson by the ATLAS [24] and CMS [26] experiments in 2012 is considered as the last milestone in the long history of the Standard Model of particle physics, a highly predictive and rigorously tested model that has been validated with an excellent level of accuracy throughout the years and shows an impressive agreement between theory prediction and experimental measurements. Among the successes of the SM, it has to be underlined that all the particles the SM predicted have been observed, including the W and Z bosons, the top and bottom quarks and the Higgs boson. Furthermore, other successes are related to predictions of particle properties, like the electron “anomalous” magnetic dipole moment, which is one of the most accurately measured properties of an elementary particle, and one of the properties of a particle that

can be most accurately predicted by the SM.

However, at the same time, there are several indications of the incompleteness of the SM, indications that cannot be explained in terms of minor deviations of some measured observables from their theory predictions due to insufficient precision of the measurements or of the theoretical calculations. Here a list of the main issues remaining opened in particle physics:

- According to the SM, neutrinos are massless particles; however, there are experimental evidences, i.e. neutrino oscillations, predicted by Pontecorvo in 1957 and observed for the first time in 1998, that prove the fact that neutrinos do have mass. Neutrino mass terms can be added introducing at least nine more parameters: three neutrino masses, three real mixing angles, and three CP-violating phases.
- The SM does not explain why fundamental particles are divided in three generations of leptons and three of quarks with properties that are very similar to the first generation, as well as it does not explain the hierarchy of the Yukawa couplings.
- The SM has 18 free parameters, i.e. 3 lepton masses, 6 quark masses, 3 CKM angles and 1 CKM CP-violation phase, 3 gauge couplings, the Higgs mass and the Higgs vacuum expectation value, that are not predicted by the theory but are numerically established by the experiments.
- The hierarchy problem [56] in the SM arises from the fact that the electroweak symmetry breaking scale (~ 100 GeV) and the Planck scale ($\sim 10^{19}$ GeV) are separated by many orders of magnitude. The Higgs mass is modified by one-loop radiative corrections coming from its couplings to gauge bosons, from Yukawa couplings to fermions and from its self-couplings, resulting in a quadratic sensitivity to the ultraviolet cutoff, i.e. the scale below which QFTs are valid. For the Standard Model, this scale can go to the Planck scale, and so the QFT expectation for the Higgs mass is much higher than the experimental result.
- The SM does not include the gravitational interaction, one of the four fundamental forces; this inclusion would require the gravity to be quantised. Since the gravity strength is much smaller than the other strengths, quantum gravitational effects would become important at length scales near the Planck scale, i.e. 10^{19} GeV, not accessible at any experimental facilities.
- The SM does not explain the matter-antimatter asymmetry in the universe, i.e. the imbalance between baryonic and antibaryonic matter; in fact, the measured CP violation and deviation from equilibrium during electroweak symmetry breaking are both too small, thus making unlikely that baryogenesis, i.e. the physical process that could produce baryonic asymmetry, is possible within the SM theoretical framework [57].
- The SM describes the ordinary matter surrounding us that accounts just for the 5% of the mass/energy content of the universe; it does not fully describe the nature of dark matter or dark energy, even if, from cosmological observations, they contribute to approximately 27% and to 68% of this content, respectively.

Chapter 2

The Large Hadron Collider

The **L**arge **H**adron **C**ollider (**LHC**) [22] is a two-ring hadron accelerator and collider with superconducting magnets built by the European Organisation for Nuclear Research (CERN); it was installed in the existing 26.7 km tunnel that was constructed between 1984 and 1989 for the CERN LEP machine, situated at a mean depth of 100 m underground. Beams of particles travel in opposite directions, kept separated in two ultra-high vacuum pipes and bent in the accelerator ring by a magnetic field of up to 8.33 T produced by superconducting electromagnets which operate at the temperature of 1.9 K.

The LHC was designed to reach the highest energy ever explored in particle physics, i.e. centre-of-mass collision energies of up to 14 TeV with the primary purpose of discovering new particles, like the Higgs boson, as well as revealing physics beyond the Standard Model (BSM). To this end several detectors were placed in the accelerator ring. The four largest experiments at the LHC are ALICE [58], ATLAS [23], CMS [25] and LHCb [59]. In this Chapter, Sections 2.1 and 2.2 report details on the accelerator complex and the LHC experiments placed along the beam line, respectively. The most important beam and machine parameters are summarised in Section 2.3 while Section 2.4 describes the scheduled periods of operation and shutdown.

2.1 Accelerator Complex

The LHC is the last accelerator in a complex chain of machines, a scheme of which is shown in Figure 2.1. The primary proton source is a bottle of hydrogen gas connected to a metal cylinder that strips off the electrons leaving just protons.

Before being injected in the LHC, protons are accelerated through a series of accelerators that gradually increases their energy:

- **Linac2**: is a linear accelerator that uses radiofrequency cavities to charge cylindrical conductors and small quadrupole magnets to focus protons in a tight beam, accelerating them to an energy of 50 MeV;
- **Proton Synchrotron Booster (PSB)**: is made of four superimposed synchrotron rings that receive beams of protons at 50 MeV and accelerate them to 1.4 GeV;
- **Proton Synchrotron (PS)**: is CERN's first synchrotron and has 277 conventional electromagnets, including 100 dipoles to bend the beams round the ring; it pushes

the beam to 25 GeV;

- **Super Proton Synchrotron (SPS)**: is the second largest machine in CERN's accelerator complex measuring nearly 7 km in circumference; it has 1317 conventional electromagnets, including 744 dipoles to bend the beams round the ring, and it operates at up to 450 GeV.

Protons are finally injected into the LHC beam pipes, with beam circulating both clockwise and anticlockwise.

CERN's Accelerator Complex

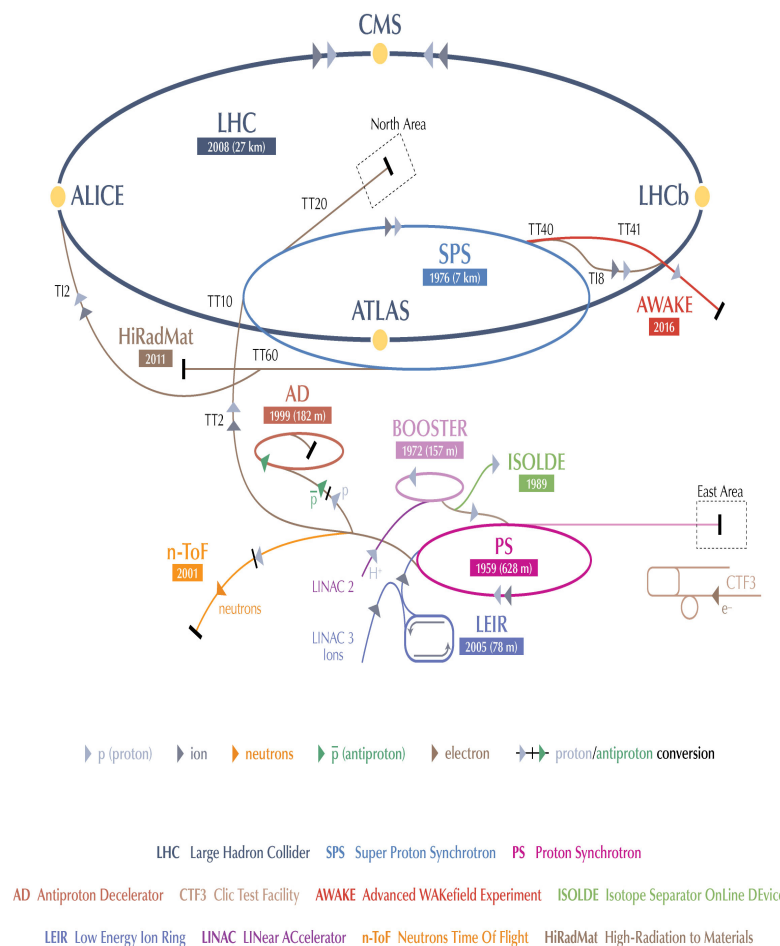


Figure 2.1: Accelerator Complex and Experiments [60].

2.2 The LHC Experiments

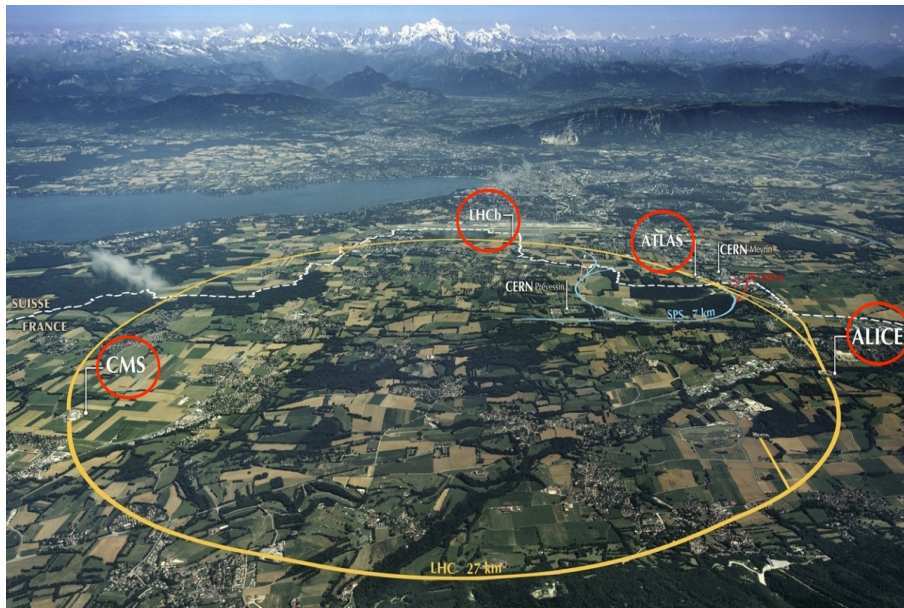


Figure 2.2: The LHC ring and its main experiments around the IPs.

The experiments located around the IPs are:

- **ALICE** [58] (A Large Ion Collider Experiment), a general-purpose, heavy-ion detector which is designed to address the physics of strongly interacting matter and the quark-gluon plasma;
- **ATLAS** [23] (A Toroidal LHC ApparatuS), the largest, multi-purpose particle detector experiment designed to explore a wide range of physics processes;
- **CMS** [25] (Compact Muon Solenoid), a general-purpose detector designed to target the same processes of ATLAS while using different and complementary technologies;
- **LHCb** [59] (Large Hadron Collider beauty experiment), an experiment dedicated to heavy flavour physics; its primary goal is to look for indirect evidence of new physics in CP violation and rare decays of beauty and charm hadrons.

Two additional experiments, TOTEM and LHCf, are much smaller in size. They are designed to focus on “forward particles” (protons or heavy ions):

- **TOTEM** [61] is an experiment that studies forward particles and is focused on physics that is not accessible to the general-purpose experiments; it measures the total pp cross section with the luminosity-independent method and studies elastic and diffractive scattering at the LHC;
- **LHCf** [62] is an experiment dedicated to the measurement of neutral particles emitted in the very forward region of LHC collisions. The physics goal is to provide data for calibrating the hadron interaction models that are used in the study of extremely high-energy cosmic rays.

2.3 Luminosity

In the LHC collisions, the rate of produced events (R_{event}), i.e. the number of events produced per second, is given by:

$$R_{event} = \frac{dN_{event}}{dt} = \mathcal{L} \cdot \sigma_{event} \quad (2.1)$$

where \mathcal{L} is the instantaneous luminosity of the accelerator (machine luminosity) and σ_{event} is the cross section of the corresponding physics process. Thus, in order to produce a significant amount of interesting/rare physics events and increase the discovery opportunity, high luminosity is a crucial achievement.

In the case of two Gaussian beams colliding head-on, the machine luminosity [$\text{cm}^{-2}\text{s}^{-1}$] can be expressed in terms of the beam parameters as [22]:

$$\mathcal{L} = \frac{N_b^2 n_b f_{rev} \gamma_r}{4\pi \epsilon_n \beta^*} F \quad (2.2)$$

where:

- N_b is the number of particles per bunch: protons do not flow as a continuous beam inside the machine but are packed into bunches;
- n_b is the number of bunches per beam;
- f_{rev} is the revolution frequency;
- γ_r is the relativistic gamma factor of the protons;
- ϵ_n is the normalised transverse beam emittance, that is a measure of the average spread of particles in the beam;
- β^* is the beta function at the collision point relating the beam size to the emittance, $\beta = \pi\sigma^2/\epsilon$, determined by the accelerator magnet configuration (basically, the quadrupole magnet arrangement) and powering;
- F is the geometric luminosity reduction factor due to the crossing angle at the interaction point (IP).

The geometric reduction factor F , assuming round beams and equal beam parameters for both beams, is in turn expressed in terms of θ_c , the full crossing angle at the IP, σ_z , the RMS bunch length, and σ^* , the transverse RMS beam size at the IP, as:

$$F = \left(1 + \left(\frac{\theta_c \sigma_z}{2\sigma^*} \right)^2 \right)^{-1/2}. \quad (2.3)$$

The nominal LHC peak luminosity $\mathcal{L} = 10^{34}\text{cm}^{-2}\text{s}^{-1}$ corresponds to a nominal bunch spacing of 25 ns, $\beta^* = 0.55$ m, a full crossing angle $\theta_c = 300$ μrad , and bunch population, $N_b = 1.1 \times 10^{11}$, while the RMS beam size and the geometric reduction factor are $\sigma^* = 16.7$ μm and $F = 0.836$, respectively [63].

Parameter	2015	2016	2017	2018
Maximum number of colliding bunch pairs (n_b)	2232	2208	2544/1909	2544
Bunch spacing (ns)	25	25	25/8b4e	25
Typical bunch population (10^{11} protons)	1.1	1.1	1.1/1.2	1.1
β^* (m)	0.8	0.4	0.3	0.3-0.25
Peak luminosity \mathcal{L}_{peak} (10^{33} cm $^{-2}$ s $^{-1}$)	5	13	16	19
Peak number of inelastic interactions/crossing ($\langle \mu \rangle$)	~ 16	~ 41	$\sim 45/60$	~ 55
Luminosity-weighted mean inelastic interactions/crossing	13	25	38	36
Total delivered integrated luminosity (fb $^{-1}$)	4.0	38.5	50.2	63.4

Table 2.1: Selected LHC parameters for pp collisions at $\sqrt{s} = 13$ TeV in 2015–2018. The values shown are representative of the best accelerator performance during normal physics operation [64].

The instantaneous luminosity is not constant over a physics run, indeed the peak luminosity is achieved at the beginning of stable beams, i.e. the phase of actual physics data taking in the LHC cycle, but decreases due to the degradation of the intensities of the circulating beams, according to the following law:

$$\mathcal{L}(t) = \frac{\mathcal{L}_0}{(1 + t/\tau_{nuclear})^2} \quad \text{with} \quad \tau_{nuclear} = \frac{N_{tot,0}}{\mathcal{L}_0 \sigma_{tot} k}, \quad (2.4)$$

where:

- $\tau_{nuclear}$ is the initial decay time of the bunch intensity due to the beam loss from collisions;
- $N_{tot,0}$ is the initial beam intensity;
- \mathcal{L}_0 is the initial luminosity;
- σ_{tot} is the total cross section ($\sigma_{tot} = 10^{-25}$ cm 2 at 13 TeV);
- k is the number of IPs with luminosity \mathcal{L}_0 .

Further contributions to beam losses come from a blow-up of the transverse emittance related to the intra-beam scattering, to synchrotron radiation and noise effects and from particle-particle collisions within a bunch.

Assuming the LHC nominal parameters and combining the different contributions, the length of a luminosity run is estimated as $\tau_L \sim 15$ h.

Typical values of the most important beam and machine parameters are reported in Table 2.1 [64]; the design machine luminosity of $\mathcal{L} = 10^{34}$ cm $^{-2}$ s $^{-1}$ has already been surpassed in 2016 when the instantaneous luminosity has reached the value of $\mathcal{L} = 1.3 \times 10^{34}$ cm $^{-2}$ s $^{-1}$. Considering a luminosity of $\mathcal{L} = 10^{34}$ cm $^{-2}$ s $^{-1}$ and an inelastic cross section of ~ 80 mb [65], an estimation of the expected rate of events at the LHC can be made, thus leading to $R_{event} = \mathcal{L} \sigma_{event} \sim 8 \times 10^8$ events/s. The actual figure of merit of the luminosity is the so-called integrated luminosity which directly relates the number of events to the cross section; it is defined integrating the instantaneous luminosity over the time of operation T :

$$L = \frac{\text{number of events of interest}}{\sigma_{event}} = \int_0^T \mathcal{L} dt. \quad (2.5)$$

The results presented in this thesis are based on data collected by the ATLAS detector at $\sqrt{s} = 13$ TeV, corresponding to an integrated luminosity of up to 80 fb^{-1} .

Figure 2.3 shows, for the ATLAS detector, the delivered luminosity, defined as the luminosity made available by the LHC machine, and the recorded luminosity, defined as the luminosity recorded by the detector.

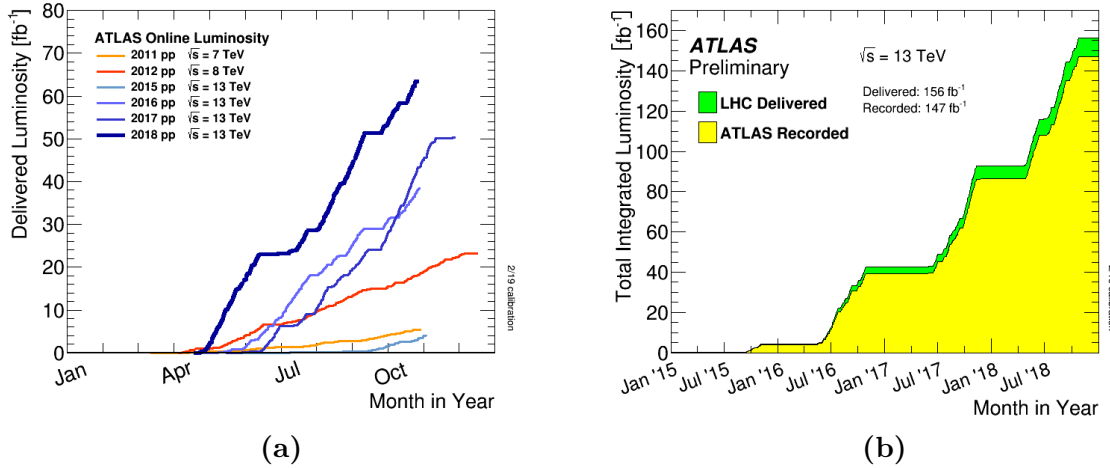


Figure 2.3: (a) Cumulative luminosity versus time delivered to ATLAS for high energy pp collisions and (b) cumulative luminosity versus time delivered to ATLAS (green) and recorded by ATLAS (yellow) during stable beams for pp collisions at 13 TeV centre-of-mass energy in LHC Run 2 [66].

ATLAS and CMS are the high-luminosity LHC experiments, both designed to aim at a peak luminosity of $\mathcal{L} = 10^{34} \text{ cm}^{-2}\text{s}^{-1}$ for proton operation; moreover, two low-luminosity experiments are present: LHCb aiming at a peak luminosity of $\mathcal{L} = 10^{32} \text{ cm}^{-2}\text{s}^{-1}$, and TOTEM aiming at a peak luminosity of $\mathcal{L} = 2 \times 10^{29} \text{ cm}^{-2}\text{s}^{-1}$.

The LHC has also one dedicated heavy-ion experiment ($p - Pb$ or $Pb - Pb$), ALICE, aiming at a peak luminosity of $\mathcal{L} = 10^{27} \text{ cm}^{-2}\text{s}^{-1}$ [22].

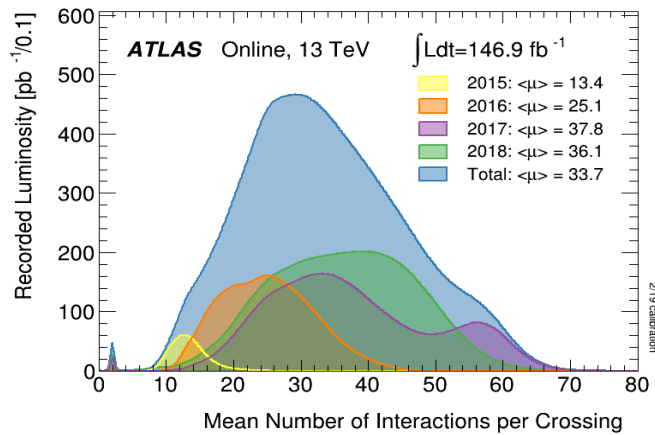


Figure 2.4: Luminosity-weighted distribution of the mean number of interactions per crossing for the 2015–2017 pp collision data at 13 TeV centre-of-mass energy [66].

The average number of interactions per bunch crossing, whose distribution is shown in Figure 2.4 for the 2015, 2016, 2017 and 2018 data, is given by the pile-up $\langle\mu\rangle$ which is related to the instantaneous luminosity through the following formula:

$$\langle\mu\rangle = \frac{\mathcal{L}\sigma_{tot}}{f_{rev}n_b}. \quad (2.6)$$

The pile-up is therefore proportional to the luminosity and constitutes a challenge from the detector side for resolving the individual collisions and thus a limit to the increase of luminosity of a collider. The peak value for the pile-up in 2016 data taking has been $\mu \sim 50$, considering a total cross section $\sigma_{tot} = 10^{-25} \text{ cm}^2$ at 13 TeV, a peak luminosity $\mathcal{L} = 1.3 \times 10^{34} \text{ cm}^{-2}\text{s}^{-1}$, a number of bunches $n_b \sim 2200$ and a revolution frequency $f_{rev} = 11.245 \text{ kHz}$.

2.4 LHC Operation

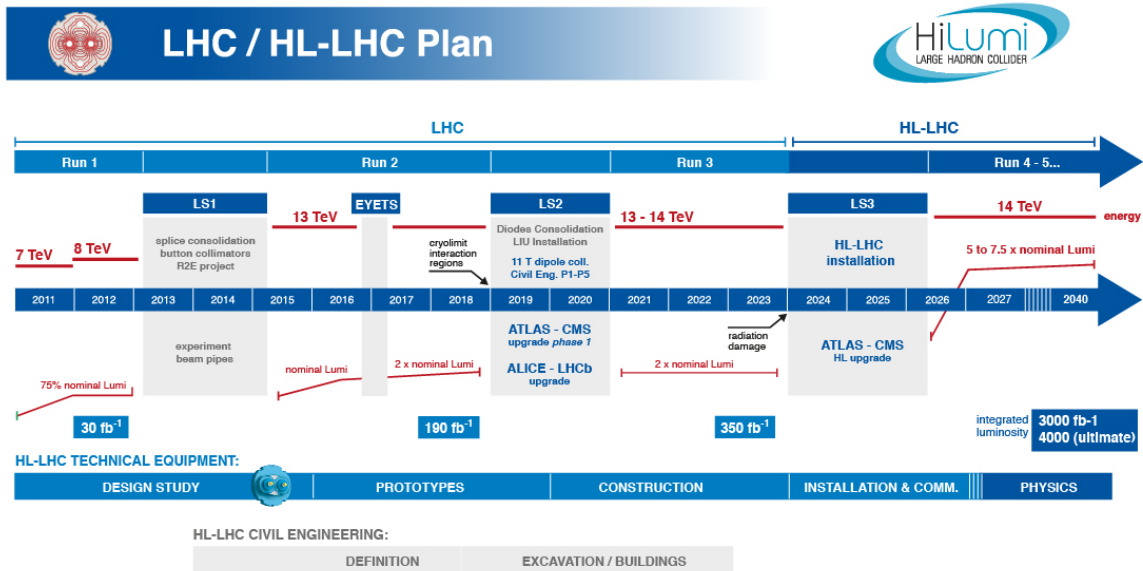


Figure 2.5: Time schedule of LHC, involving active periods and technical shutdown, from Run 1 to last upgrade to High-Luminosity LHC [67].

The scheduled periods of operations of the LHC and the shutdown periods are shown in Figure 2.5, together with future developments and upgrades [67].

The LHC began operation for data taking in 2009, with the first operational run called “Run 1”: beams were injected in both rings and stable beam collisions were performed at 450 GeV (900 GeV centre-of-mass energy). By the end of the year, beams were accelerated to 1.18 TeV (2.36 TeV centre-of-mass energy) per beam.

In 2010 the centre-of-mass energy was successfully increased to 7 TeV and the LHC continued to run during 2010 and 2011 at $\sqrt{s} = 7 \text{ TeV}$, delivering a cumulative luminosity of 5.46 fb^{-1} , corresponding to a recorded luminosity, for the ATLAS experiment, of 5.08 fb^{-1} . During 2012, an increase in beam energy from 3.5 to 4 TeV per beam, corresponding to

$\sqrt{s}=8$ TeV was made, thus leading to a total recorded integrated luminosity of 22.8 fb^{-1} . The first operational run therefore collected $\sim 25 \text{ fb}^{-1}$ of “good for physics” data [68].

After a long shutdown, necessary to upgrade the magnet interconnects and safety systems for a centre-of-mass energy of 13 TeV, the second operational run of the LHC, called “Run 2”, started in 2015 and ended in 2018; LHC accelerated protons up to an energy of 6.5 TeV, corresponding to a centre-of-mass energy of 13 TeV. The peak instantaneous luminosity achieved was $2.1 \times 10^{34} \text{ cm}^{-2} \text{ s}^{-1}$. The total integrated luminosity delivered to ATLAS during the second run was 156 fb^{-1} , corresponding to $\sim 140 \text{ fb}^{-1}$ of data good for physics analyses.

The 2015–2017 ATLAS data-taking period, corresponding to an integrated luminosity of up to $\sim 80 \text{ fb}^{-1}$, has been exploited for the results presented in this thesis.

A long shutdown period, LS2, has just started (2019); this period will be devoted to the consolidation and the upgrades of the detectors and to start testing some new systems and technologies that will be essential to further pushing the LHC machine beyond its limits.

After 2020, the statistical gain in running the accelerator without a significant luminosity increase will become marginal.

A key element for further increasing the luminosity is a new linear accelerator, the Linac4, that is replacing the Linac2 in providing protons to the LHC, accelerating them to an energy of 160 MeV.

Furthermore, the LHC will undergo a major upgrade, Phase-2 Upgrade, to a High-Luminosity LHC (HL-LHC) expected to start operations in 2026, after collecting a total dataset of approximately 400 fb^{-1} by the end of Run 3 (in 2023).

The two main goals of the HL-LHC project will be the following [67]:

- a peak luminosity from 5 to $7 \times 10^{34} \text{ cm}^{-2} \text{ s}^{-1}$ with levelling, allowing:
- an integrated luminosity of $300/350 \text{ fb}^{-1}$ per year with an ultimate goal of 4000 fb^{-1} within twelve years. This integrated luminosity is about ten times the expected luminosity reach of the first twelve years of the LHC lifetime.

Chapter 3

The ATLAS Experiment at the Large Hadron Collider

ATLAS (A Toroidal LHC ApparatuS) [69, 70] is a general-purpose detector, i.e. a detector capable of addressing a huge range of physics processes and observing all possible decay products of the pp interactions; furthermore, it is the largest-volume detector ever built for a particle collider. The ATLAS detector is forward-backward symmetric with respect to the interaction point, covering almost the entire 4π solid angle with a cylindrical shape. It is 44 m long and 25 m high; it weighs over 7000 tons and it sits in a cavern ~ 100 m underground placed at Point 1 (one of the LHC Interaction Points). Figure 3.1 shows a schematic representation of the ATLAS detector.

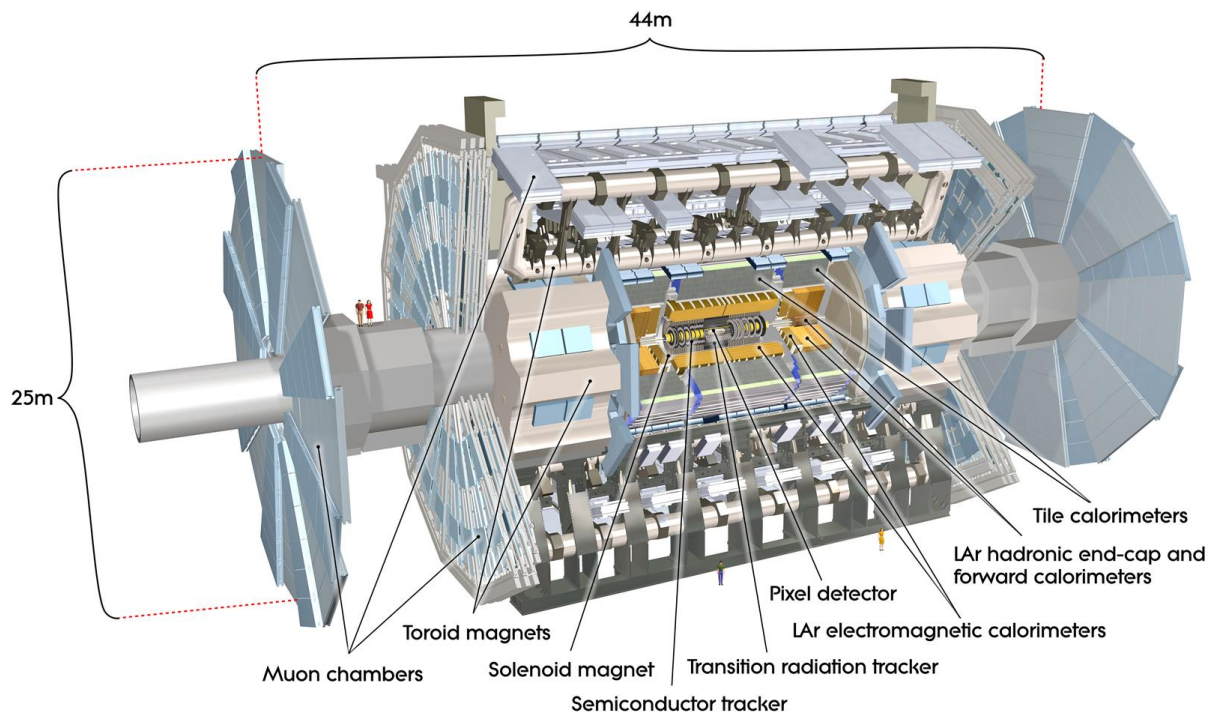


Figure 3.1: Cut-away view of the whole ATLAS detector and its sub-systems [23].

The high luminosity and high centre-of-mass energy of the LHC pp collisions allow to explore physics at the TeV scale and are needed because of the small cross sections expected for many of the following processes, the ATLAS detector has been designed to target:

- the Higgs-boson search and the measurement of its fundamental properties;
- high precision tests of QCD, electroweak interactions, and flavour physics;
- exotic searches, e.g. searches for new heavy gauge bosons or extra dimensions;
- precision measurements of the top-quark properties, like its mass, coupling and spin;
- the search for supersymmetry-like extensions of the SM.

In order to handle a high rate of events, $\sim 6 \times 10^8$ events/s for inelastic pp interactions, as discussed in Chapter 2, as well as a high rate of bunch crossing, ~ 40 MHz, the ATLAS detector was designed to fulfil these general requirements [23]:

- fast, radiation-hard electronics and sensor elements together with a high detector granularity needed to handle particle fluxes and to reduce the influence of overlapping events;
- large acceptance in pseudorapidity with almost full azimuthal angle coverage;
- accurate tracking of charged-particle, i.e. good momentum resolution and reconstruction efficiency in the inner tracker as well as precise reconstruction of secondary vertices in order to identify τ -leptons and b -jets;
- accurate electromagnetic calorimetry to identify electrons and photons, complemented by full-coverage hadronic calorimetry for precise jet and missing transverse energy measurements;
- good muon identification and momentum resolution over a wide range of momenta.

The detector is constituted by a central part, barrel, and two side parts, end-caps. In this Chapter, ATLAS sub-detectors and coordinate system are introduced in Sections 3.1 and 3.2, respectively. Section 3.3 describes the magnet system, necessary to make accurate track reconstruction and momentum measurement. A comprehensive description of each sub-detector is reported in Sections 3.4, 3.5, 3.6 and 3.8. The Trigger and Data Acquisition System is described in Section 3.7.

3.1 Detector Sub-Systems

ATLAS is composed by different sub-detectors that are arranged in an onion-like layered structure to provide an angular uniform coverage around the beam pipe; going from the closest to the beam pipe to the external one, it is composed by the **Inner Detector** [71], the **Electromagnetic Calorimeter**, the **Hadronic Calorimeter**, the **Forward Calorimeter** [72, 73], the **Muon Spectrometer** [74] and the **luminosity detectors** [75]:

- the Inner Detector is immersed in a 2 T magnetic field parallel to the beam axis; it measures the direction, momentum, and charge of electrically-charged particles and reconstructs the interaction vertices;
- the Calorimeters absorb photons, electrons and hadrons and measure their energy; they are able to stop most known particles except muons and neutrinos;
- the Muon Spectrometer is the outermost part of the ATLAS detector and measures the energy and trajectory of the muons with high accuracy. To this end, the particles are deflected in a strong magnetic field, which is generated by superconducting magnetic coils;
- the forward detectors LUCID (Luminosity measurement Using Cherenkov Detectors), followed by ZDC (Zero Degree Calorimeter) and ALFA (Absolute Luminosity For ATLAS), measure the online luminosity.

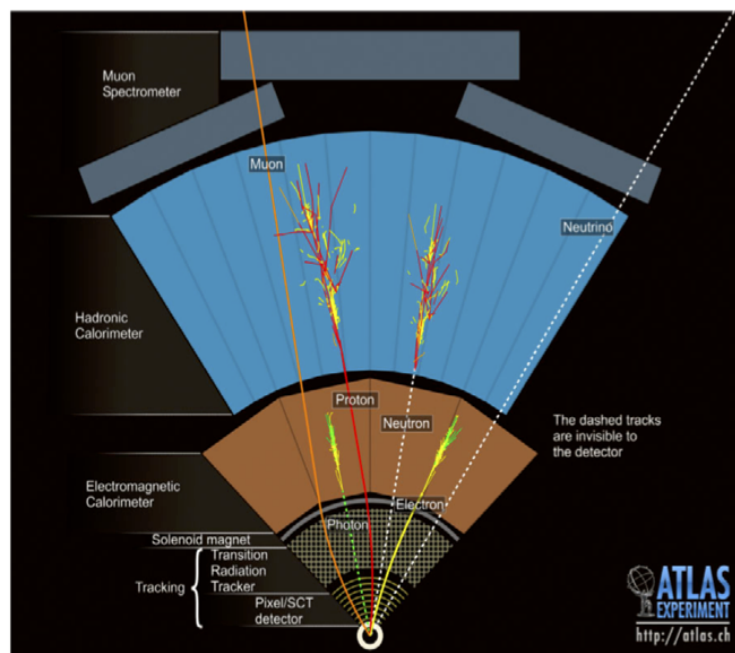


Figure 3.2: Sketch representing how different particles interact with different layers and subsystems of the detector [76].

Particles are reconstructed according to their interactions with the detector materials. A complete representation of the particles reconstructed and identified in the ATLAS detector is shown Figure 3.2. Charged particles leave ionisation signatures in the innermost part of ATLAS where the Inner Detector is present, whereas neutral particles such as neutrons are invisible to it. A magnetic field bends charged particles and allows to reconstruct their momentum and measure their charge according to the direction they bend towards. All particles (bar neutrinos) deposit a fraction (or all) of their energy in the Electromagnetic and Hadronic Calorimeters, the former targeting photons and electrons

and the latter hadrons; photons, electrons, protons and neutrons create showers in the calorimeters and are stopped there. Muons cross all the sub-systems depositing only a small fraction of their energy throughout their path before being stopped in the Muon Spectrometer. Neutrinos, due to their really elusive nature and small interaction cross section, can't be detected by ATLAS; their presence is deduced by looking for missing momentum in the momentum balance of the event.

A comprehensive description of particle reconstruction is given in Chapter 4, while details on the different sub-detectors are reported in the following sections.

The main performance goals of the detector sub-systems are listed in Table 3.1.

Detector component	Required resolution	η coverage	
		Measurements	Trigger
Tracking	$\sigma_{p_T}/p_T = 0.05\%/p_T \oplus 0.01\%$	± 2.5	
EM calorimetry	$\sigma_E/E = 10\%/\sqrt{E} \oplus 0.7\%$	± 3.2	± 2.5
Hadronic calorimetry (jets)			
	barrel and end-cap	$\sigma_E/E = 50\%/\sqrt{E} \oplus 3\%$	± 3.2
forward	$\sigma_E/E = 100\%/\sqrt{E} \oplus 10\%$	$3.1 < \eta < 4.9$	$3.1 < \eta < 4.9$
Muon spectrometer	$\sigma_{p_T}/p_T = 10\%$ at $p_T = 1 \text{ TeV}$	± 2.7	± 2.4

Table 3.1: General performances of the various components of the ATLAS detector [23].

3.2 Coordinate System

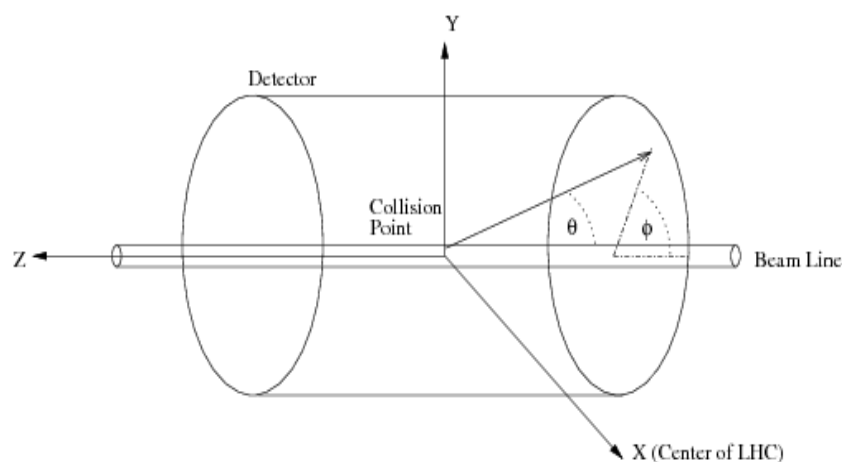


Figure 3.3: ATLAS and CMS coordinate system [77].

ATLAS uses a right-handed coordinate system with the origin in the nominal interaction point while the beam direction defines the z -axis; the x -axis points to the centre of

the LHC ring and the y -axis points vertically upwards, thus the $x - y$ plane is transverse to the beam, as shown in the sketch of Figure 3.3. Given the symmetry of the detector, a system of cylindrical coordinates (R, ϕ, θ) can be used, where $R = \sqrt{x^2 + y^2}$, the polar angle θ is the angle from the beam axis and ϕ is the azimuthal angle measured around the beam (z) axis. The rapidity y is defined as:

$$y = \frac{1}{2} \ln \left(\frac{E + p_z}{E - p_z} \right) \quad (3.1)$$

where E and p_z are the energy and the z -axis momentum component of the particle. Differences in rapidity are invariant under Lorentz transformations along the z -axis.

In case of particles with a mass negligible with respect to the energy, y corresponds to the pseudorapidity η , shown graphically in Figure 3.4 and often used to measure angular distances:

$$\eta = -\ln \left(\tan \frac{\theta}{2} \right). \quad (3.2)$$

Transverse momentum and transverse energy are defined in the $x - y$ plane as $p_T = \sqrt{p_x^2 + p_y^2}$ and $E_T = E \sin \theta$, respectively.

ΔR is the distance in the $(\eta - \phi)$ space between particles defined as:

$$\Delta R = \sqrt{\Delta \eta^2 + \Delta \Phi^2} \quad (3.3)$$

where $\Delta \eta$ and $\Delta \phi$ are the differences in pseudorapidity and azimuthal angles between the particles.

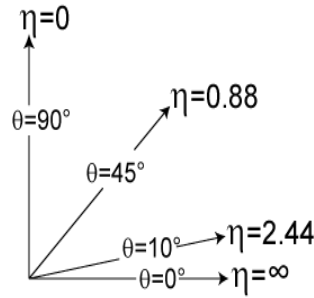


Figure 3.4: Pseudorapidity η and corresponding θ values.

3.3 Magnet System

A strong magnetic field represents the key element to provide sufficient bending power to make accurate track reconstruction and momentum measurement. The radius of curvature ρ of a particle with charge q and momentum p entering perpendicularly a magnetic field B , follows from the Lorentz force:

$$\rho = \frac{p}{q \cdot B}. \quad (3.4)$$

Thus, in order to determine the momentum of a charged particle, the curvature of its trajectory through the tracking detectors, placed in magnetic fields, is measured.

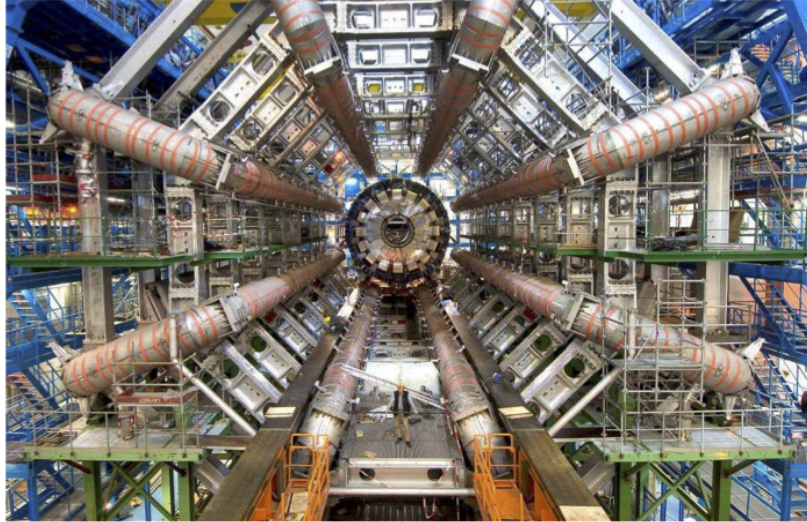


Figure 3.5: Barrel toroid as installed in the underground cavern [23].

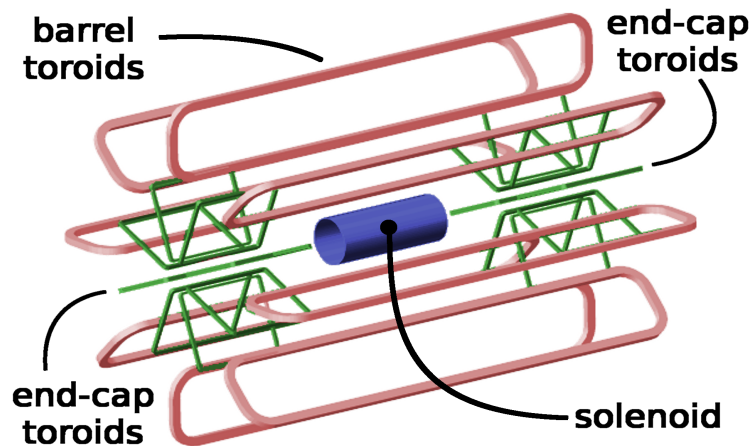


Figure 3.6: Layout of the ATLAS Magnet System.

Differently from CMS, which uses a single solenoid magnet to provide a 4 T magnetic field, the ATLAS design includes two separate magnetic systems [78] composed by the following four large superconducting magnets:

- a Central Solenoid (CS), which is aligned on the beam axis and is located between the Inner Detector and the Electromagnetic Calorimeter; it has a diameter of 2.4 m and a length of 5.3 m and provides a 2 T axial magnetic field for the inner detector, while minimising the radiative thickness in front of the barrel electromagnetic calorimeter;
- a Barrel Toroid (BT), shown in Figure 3.5, 25 m long (inner core 9.4 m, outer diameter 20.1 m), and two End-Cap Toroids (ECT), 5 m long (inner core 1.64 m,

outer diameter 10.7 m), which produce a toroidal magnetic field of 4 T in the Muon Spectrometer volume mostly orthogonal to muon trajectories.

The ATLAS magnet system layout is shown in Figure 3.6. The whole magnetic system is cooled at liquid helium temperature (~ 4.8 K).

3.4 Inner Detector

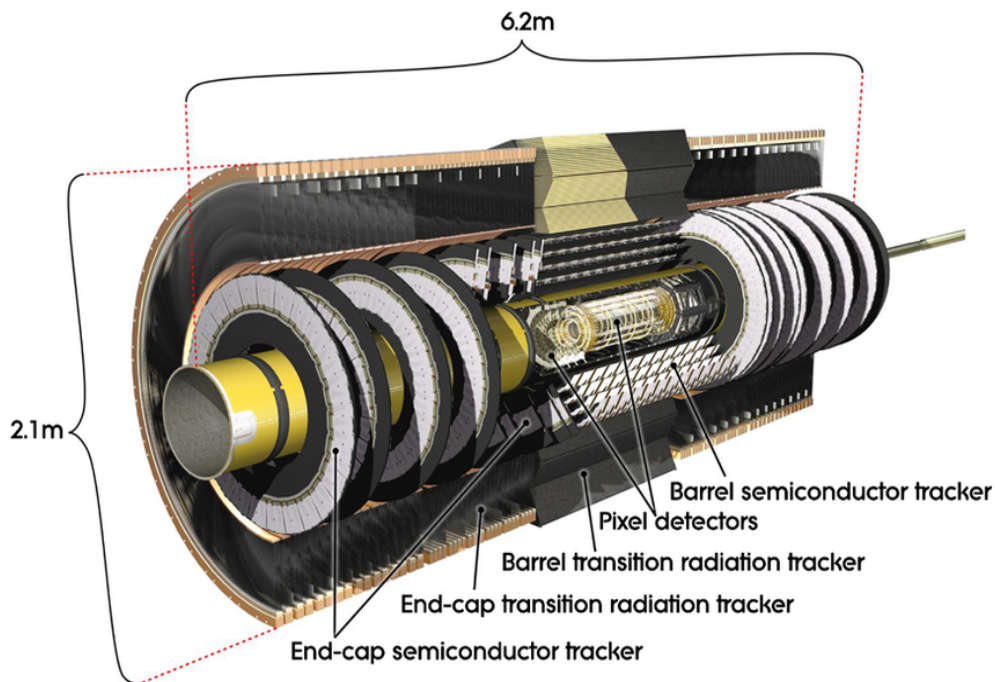


Figure 3.7: Cut-away view of the ATLAS Inner Detector [23].

The ATLAS Inner Detector (ID), shown in Figure 3.7, has been designed to provide hermetic and robust pattern recognition, excellent momentum resolution and both primary and secondary vertex measurements for charged tracks, thus contributing, together with the calorimeter and muon systems, to the electron, photon and muon identification. The ID is composed of concentric layers of detecting material, divided into a barrel and two end-caps, and its acceptance covers the pseudorapidity range $|\eta| < 2.5$.

It is immersed in a 2 T solenoidal magnetic field, has a total radius of 1.1 m and length of 6.2 m, and it is constituted of high granularity detectors, needed to perform high-precision track parameter measurements and event vertex reconstruction. The ID consists of several independent but complementary sub-detectors going from layers of high resolution silicon detectors at inner radii to gaseous tracking detectors at higher radii; starting from the inner layer and following the sketch shown in Figure 3.8, they are: the Insertable B-Layer, the Pixel and the Silicon microstrip of the Semi Conductor Trackers, used in conjunction with the Transition Radiation Tracker.

The magnetic field is essential to measure the charge and the momentum of particles from their bendings.

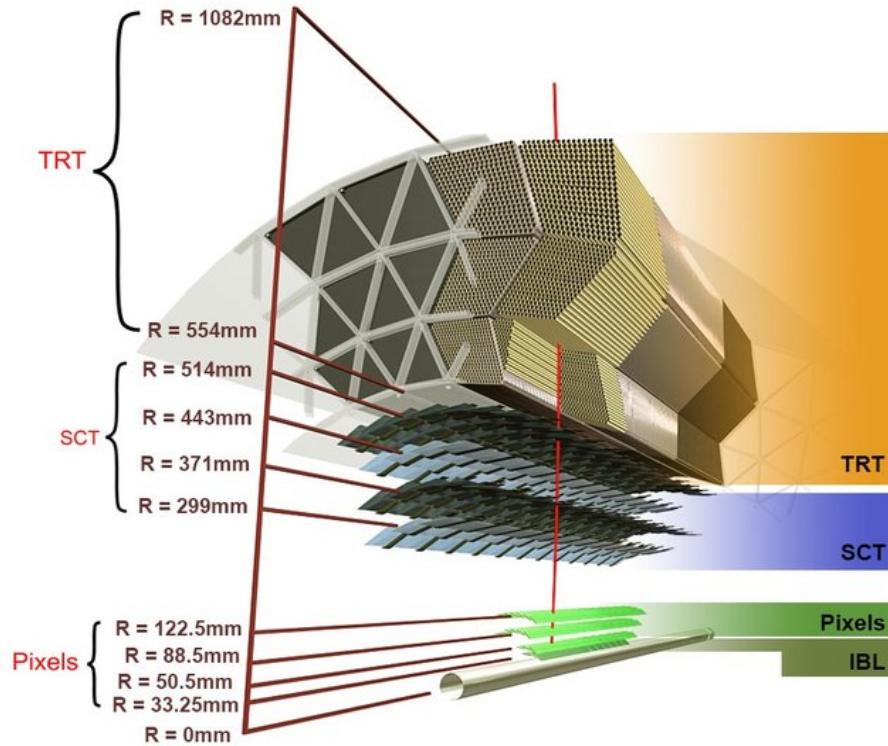


Figure 3.8: A sketch of a segment of the ATLAS ID barrel modules, showing the radial layout of the detection sub-systems. The central grey cylinder is the LHC beam-pipe. Visible is the IBL pixel layer, that has been added for Run 2.

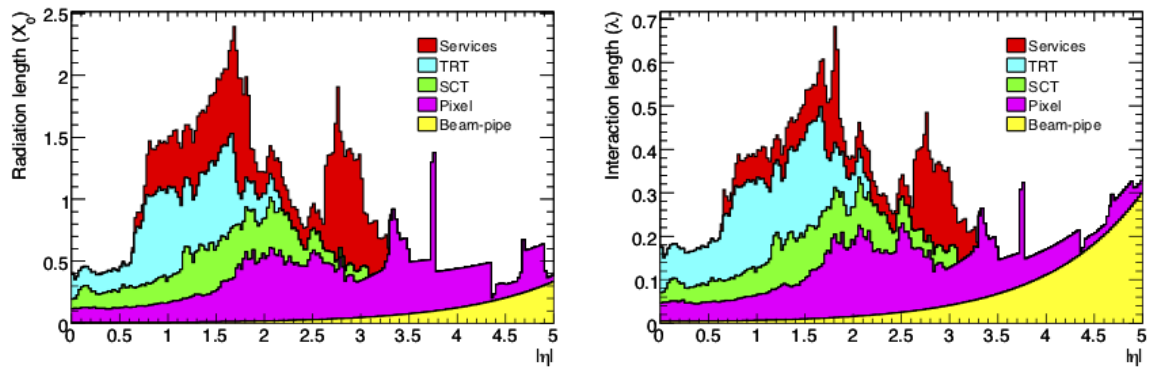


Figure 3.9: Material distribution (X_0, λ) at the exit of the ID envelope, including the services and thermal enclosures. The distribution is shown as a function of $|\eta|$ and averaged over ϕ [23].

The performance requirements of the ATLAS ID are more stringent than any tracking detector built so far for operation at a hadron collider. In order to achieve high granularity and include readout and cooling system, it is necessary to introduce a significant amount of material in the ID, as it is shown in Figure 3.9 in terms of radiation length X_0 , where X_0 represents the average path the particle needs to travel to reduce its initial energy

Sub-detector	Element size [μm]	Intrinsic resolution [μm]	Radius of the barrel layers [mm]
IBL	50×250	8×40	33.2
Pixel	50×400	10×115	50.5, 88.5, 122.5
SCT	80	17	299, 371, 443, 514
TRT	4000	130	554 - 1082

Table 3.2: Summary of the main features of the ID sub-detectors. The intrinsic resolution of the IBL and the Pixel is reported along $R - \phi$ and z and for SCT and TRT along $R - \phi$. For SCT and TRT the element sizes refer to the spacing of the readout strips and the diameter of the straw tubes, respectively [71].

by a factor $1/e$, and nuclear interaction length λ , defined as the mean free path between interactions; due to this material budget, photons may convert into electron-positron pairs before reaching the electromagnetic calorimeter and electrons may lose part of their energy through bremsstrahlung emissions affecting the resolution of the energy measured by the calorimeter system.

Table 3.2 summarises the main feature of ID sub-detectors, i.e. the element size and resolution of each sub-system as well as the radii of the barrel layers.

3.4.1 The Insertable B-Layer (IBL)

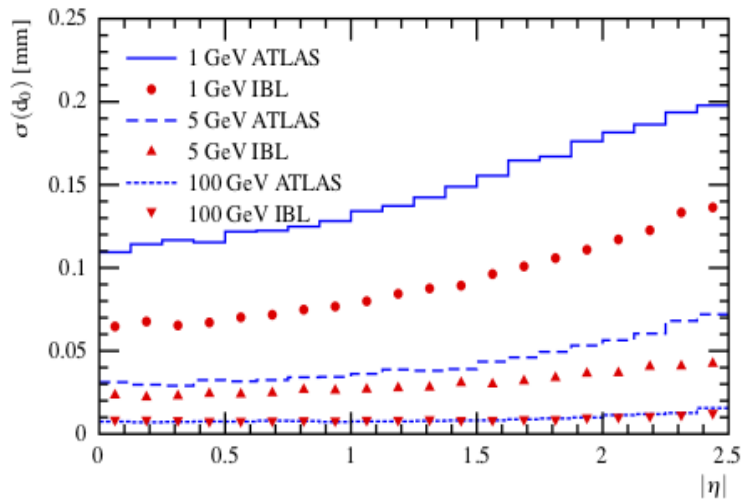


Figure 3.10: Track parameter resolution of the impact parameter d_0 for single muons at 1, 5 and 100 GeV as a function of η for the original ID and for the ID with IBL [79].

The Insertable B-Layer (IBL) [79] is the ATLAS sub-detector closest to the beam pipe, being on average 33.2 mm away. One of the main concerns before Run 2 was that significant radiation damage to the ID could occur, increasing luminosity; this would lead to a loss in tracking efficiency, especially affecting b -tagging. To cope with this issue, the IBL has been added to the ATLAS detector. It was installed before the start of Run 2

data taking, between a new beryllium beam pipe with a reduced inner diameter (47 mm instead of 59 mm) to fit inside the IBL and the first layer of the original Pixel detector. It consists of a cylindrical layer 3.5 m long. Due to its position close to the beam pipe, the IBL pixel sensors have a small size ($50 \times 250 \mu\text{m}$) to reduce occupancy at high luminosity, and are radiation hard. It also provides a full ϕ coverage.

The biggest contribution of the IBL to the precision of the measurement, is the improvement, shown in Figure 3.10, of the resolution of the impact parameter d_0 , that is defined as the distance in the $x - y$ plane between the track closest point to the z axis and the z axis itself and it also the crucial parameter that affects the b -tagging performance. The significant gains are due to the additional layer at smaller radius, and to the smaller z pitch of the IBL compared to the present Pixel detector. The contribution from the IBL to the measurement of the track curvature is small as the overall track length is nearly unchanged. The IBL improves also the quality of the vertex reconstruction and of the b -tagging performance.

3.4.2 The Pixel Detector

The Pixel Detector provides critical tracking information for pattern recognition near the collision point, measuring the particle impact parameter resolution, and largely determines the ability of the Inner Detector to find secondary vertices. The system provides three or more precision measurements points for tracks with pseudorapidity $|\eta| < 2.5$ and it has a full ϕ coverage. Due to its position close to the barrel, where the particle density is at its highest, this system has to achieve a high granularity. It is composed by three barrel layers placed at the radii of 51 mm, 89 mm, and 123 mm respectively, centred around the beam axis (z) and two end-caps, each end-cap having three disk layers at $|z|=495$, 580 and 650 mm; the silicon pixel sensors have a minimum pixel size in $(R - \phi \times z)$ of $50 \mu\text{m} \times 400 \mu\text{m}$ in both the barrel and the end-cap positions. The dimensions are chosen in order to maximise the probability that a particle crossing one layer will cross also the other two. The intrinsic precisions in the barrel are $10 \mu\text{m}$ ($R - \phi$) and $115 \mu\text{m}$ (z) and in the disks are $10 \mu\text{m}$ ($R - \phi$) and $115 \mu\text{m}$ (R). The pixel detector has approximately 80.4 million readout channels.

3.4.3 The SemiConductor Tracker (SCT)

The SemiConductor Tracker (SCT) is placed in the intermediate range of the ID and employs the same semiconductor technology used by the Pixel detector, providing the pseudorapidity coverage in the range $|\eta| < 2.5$ replacing pixels with silicon microstrips having a $120 \text{ mm} \times 60 \text{ mm}$ size in $\phi \times z$ and completing the precision tracking of the Pixel detector in the measurement of momentum, impact parameter and vertex position. The SCT is composed by four layers in the barrel ($299 \text{ mm} < R < 514 \text{ mm}$) and nine in each end-cap ($850 \text{ mm} < z < 2730 \text{ mm}$).

It is arranged in twenty-two layers: four cylindrical barrel layers and eighteen disk layers, nine on each of the end-caps. The barrel layers are organised in 4 cylinders made of two layers of sensors, placed at approximate radial distances of 30, 37, 44 and 51 cm from the interaction point, to provide 4 additional space points for each tracks in the $R - \phi$ and z coordinates. Each layer is made of $p - n$ silicon semiconductor modules of nominal size

6.36 cm \times 6.40 cm with 780 readout strips. Each strip is 12 cm long and has a constant pitch of 80 μm . The end-cap modules have a very similar structure, but exploit tapered strips, where one set is aligned radially. The SCT has a total of 6.3 million readout channels. The intrinsic measurement precisions per module are 17 μm for the $R - \phi$ plane and 580 μm for the $z(R)$ -coordinate in both the barrel and the end-caps.

3.4.4 The Transition Radiation Tracker (TRT)

The Transition Radiation Tracker (TRT) is placed in the outermost part of the ID; it is a combination of a tracker (based on straw tubes) working as a drift chamber measuring the charge drift time, and a Transition Radiation detector for the pattern recognition; the Transition Radiation detector allows to discriminate between light and heavy particles: in fact, particles emit transition radiation according to the speed they have passing through several layers of material with different refraction indices. High relativistic particles (typically electrons) have a higher probability of emitting transition radiation photons with respect to the other particles.

A single TRT component is made of Polyamide straw tubes of 4 mm diameter and long up to 144 cm in the barrel region; at the centre of each straw tube, there is a 31 μm diameter tungsten wire, the anode, directly connected to the front-end electronics and kept at ground potential. The gap between the straw and the wire is filled by a mixture of gases. The passage of ionising particles induces a low amplitude signal on the anodes. At the same time, some particles crossing polypropylene fibres cause transition radiation emission, absorbed by the Xenon present in the gas mixture; this last process leads to a high amplitude signal in the TRT electronics that can be distinguished from low amplitude ionisation signal.

The TRT only provides $R - \phi$ information, for which it has an intrinsic measurement accuracy of 130 μm per straw.

3.5 Calorimeters

The ATLAS calorimetry system consists of the Electromagnetic Calorimeter (ECal) that covers the pseudorapidity range $|\eta| < 3.2$, the Hadronic Calorimeter (HCal) which covers the pseudorapidity range $|\eta| < 3.9$ and the Forward Calorimeter (FCal) covering the pseudorapidity range $3.1 < |\eta| < 4.9$; it is structured in three cryostats, one barrel and two end-caps, is finely segmented in η and ϕ and covers the full azimuthal range, as shown in Figure 3.11.

The calorimeters' main purpose is to fully contain and measure destructively the energy and direction of incident electrons and photons, producing electromagnetic showers in the ECal and FCal electromagnetic part, and hadrons, interacting via the strong force in the HCal and FCal hadronic parts; particles that can interact either electromagnetically (other than the muon) or strongly, deposit their energy in all calorimeters. The system gives also a fundamental contribution in measuring the missing transverse energy.

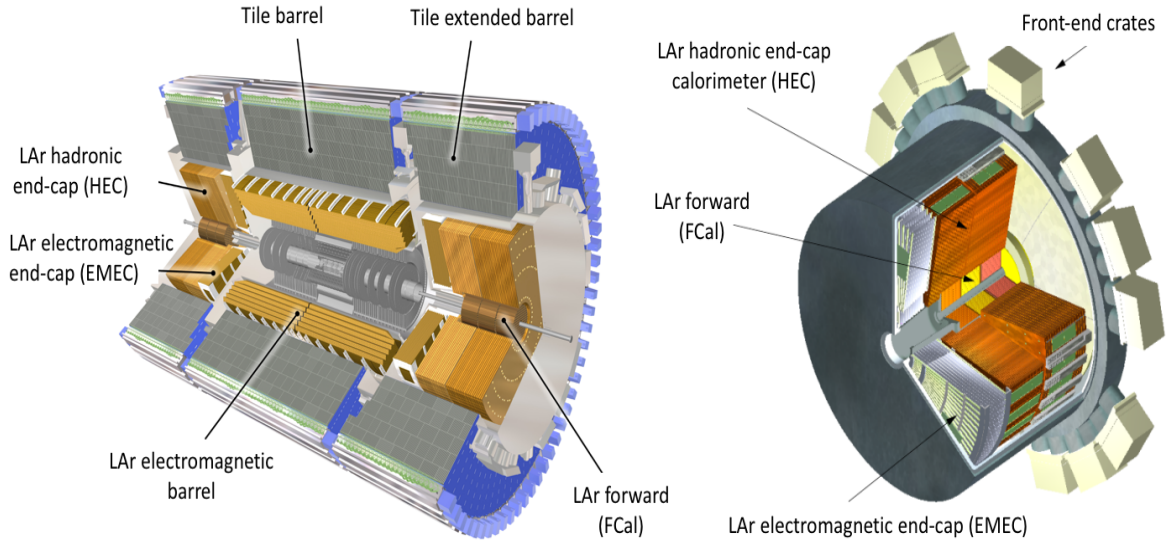


Figure 3.11: Left: sketch showing the sub-systems of the ATLAS calorimeter; right: cut-away view of an end-cap cryostat showing the positions of the three end-cap calorimeters. The outer radius of the cylindrical cryostat vessel is 2.25 m and the length of the cryostat is 3.17 m [23].

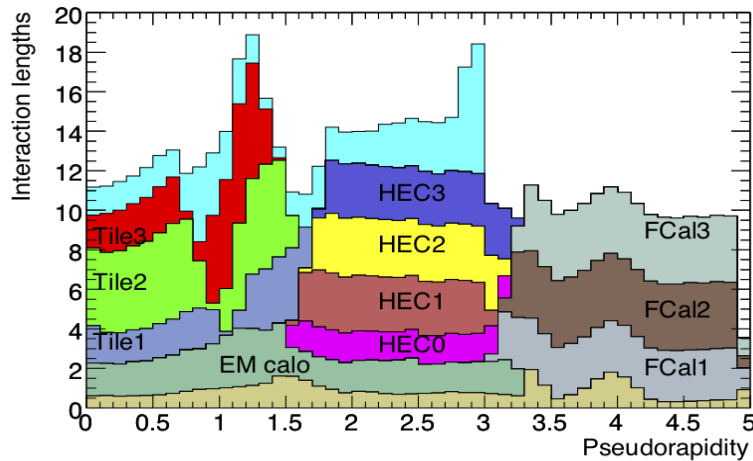


Figure 3.12: Cumulative amount of material, in units of interaction length λ , as a function of the pseudorapidity, in front of the electromagnetic calorimeters themselves, in each hadronic layer, and total amount of material at the end of the active calorimetry. The total amount of material in front of the first active layer of the muon spectrometer (up to $|\eta| < 3.0$) is also shown [23].

The ATLAS calorimeters are sampling calorimeters, i.e. they are made of alternating layers of “passive” material that degrades the particle energy and “active material” that provides a measurable signal and collects the energy of particles via ionisation or scintillation; lead (Pb), copper, or iron are used as passive materials and Liquid Argon (LAr)

or polystyrene scintillator as active materials.

The total thickness of the electromagnetic calorimeter is more than $22 X_0$ in the barrel and more than $24 X_0$ in the end-caps. The total interaction length λ of the entire system is $\sim 10 \lambda$, adequate to provide good resolution for high-energy jets. The numbers of interaction lengths as a function of the pseudorapidity in front of and in the ECal, HCal and FCal are shown in Figure 3.12, while the main features of the calorimeters are described in the following sections.

3.5.1 The Electromagnetic Calorimeter

The ATLAS Electromagnetic Calorimeter is 6.65 m long and has an outer radius of 2.25 m. The main part of the ATLAS ECal is a lead-Liquid Argon (LAr) detector with accordion-shaped Kapton electrodes and lead absorber plates over its full coverage, as shown in Figure 3.13. The LAr serves as the active material and was chosen due to its intrinsic linear behaviour, its stability of response over time and its intrinsic radiation-hardness; the lead absorber plates act as the passive material.

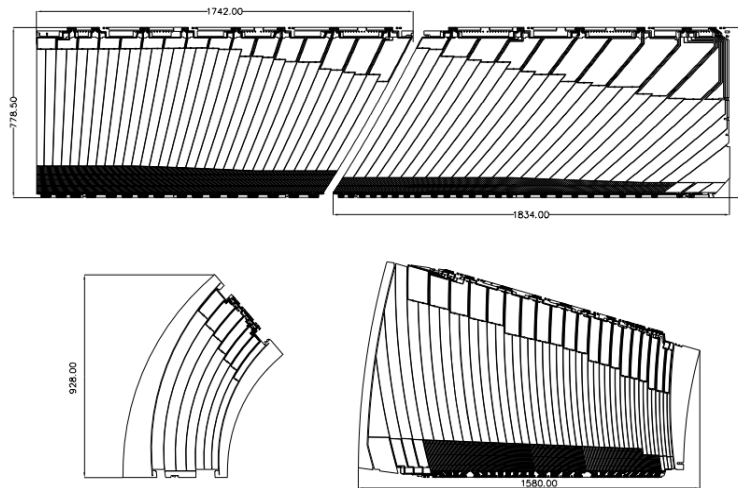


Figure 3.13: Layout of the signal layer for the four different types of electrodes before folding. The two top electrodes are for the barrel and the two bottom electrodes are for the end-cap inner (left) and outer (right) wheels. Dimensions are in millimetres. The drawings are all at the same scale [23].

The accordion geometry provides complete ϕ symmetry without azimuthal cracks. The ECal is divided into a barrel part (EMB) ($|\eta| < 1.475$) and two end-cap components (EMEC) ($1.375 < |\eta| < 3.2$). The overall segmentation allows for high precision spatial measurements, providing a geometry that helps in identifying photons coming from a primary vertex. In order to contain completely the electromagnetic shower, the EM calorimeter has a thickness of more than $22 X_0$ in the barrel and more than $24 X_0$ in the end-caps.

The nominal Electromagnetic Calorimeter resolution is:

$$\frac{\sigma(E)}{E} = \frac{10\%}{\sqrt{E}} \oplus 0.7\% \quad (3.5)$$

where E is expressed in GeV.

3.5.2 The Hadronic Calorimeter

The Hadronic Calorimeter is placed directly outside the ECal and it is composed by a barrel and two end-caps; it is 6.10 m long and has an external radius of 4.25 m. The central barrel region, called Tile Calorimeter, is a sampling calorimeter using iron as passive material and scintillating tiles as active material; it covers the pseudorapidity range $|\eta| < 1.7$ and is divided in cells of size $\Delta\eta \times \Delta\phi = 0.1 \times 0.1$. The Hadronic End-Cap Calorimeter (HEC), covering the range $1.5 < |\eta| < 3.2$, uses LAr as active medium and consists of two independent wheels per end-cap, located directly behind the end-cap ECal and sharing the same LAr cryostats; its cells have a granularity of $\Delta\eta \times \Delta\phi = 0.1 \times 0.1$ or 0.2×0.2 depending on η . The overall thickness of the HCal is 11λ for $\eta = 0$. The nominal energy resolution for hadronic jets (combined with the ECal) is:

$$\frac{\sigma(E)}{E} = \frac{50\%}{\sqrt{E}} \oplus 3\%. \quad (3.6)$$

3.5.3 Forward Calorimeter

The Forward Calorimeter is an electromagnetic and hadronic calorimeter, with a total thickness of 10λ . The FCal modules are located at high η , at a distance of approximately 4.7 m from the interaction point, so they are exposed to high particle fluxes; the positioning of these systems results in a quite hermetic design, which minimises energy losses in cracks between the calorimeter systems and also limits the backgrounds that reach the muon system. Each FCal is split into three 45 cm deep modules: one electromagnetic module (FCal1) and two hadronic modules (FCal2 and FCal3). Both the electromagnetic part and the hadronic parts use LAr as active material while copper and tungsten are used as passive materials. To optimise the resolution and the heat removal, copper was chosen as the absorber for FCal1, while mainly tungsten was used in FCal2 and FCal3, to provide containment and minimise the lateral spread of hadronic showers. The FCal provides a measurement of both electromagnetic and hadronic showers. The typical energy resolution of the FCal is:

$$\frac{\sigma(E)}{E} = \frac{100\%}{\sqrt{E}} \oplus 10\%. \quad (3.7)$$

3.6 Muon Spectrometer

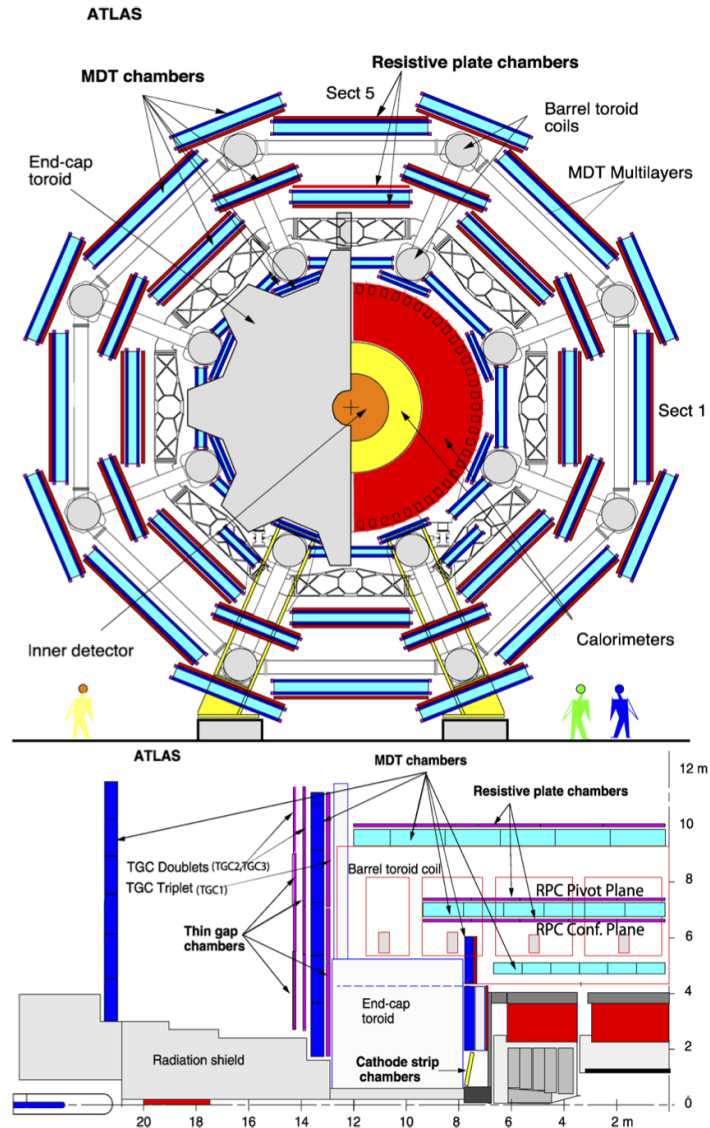


Figure 3.14: Schematic view of the Muon Spectrometer in the $x-y$ (top) and $z-y$ (bottom) projections [80].

The choice for the Muon Spectrometer (MS) to be the outermost part of the ATLAS detector comes from the fact that muons travel in the detector much more than the other charged particles generated in the collisions, losing just few MeV/mm in calorimeter electromagnetic interactions, since they have a low interaction cross section with the materials, they radiate bremsstrahlung far less than the electrons due to the larger mass and are long-lived particles. All other particles, except neutrinos, are expected to not escape the hadronic calorimeters.

The MS is designed to reconstruct muons and measure their momentum in the pseudorapidity range $|\eta| < 2.7$ as well as trigger on these particles in the pseudorapidity range $|\eta| < 2.4$; the toroidal magnets surrounding the calorimeters generate a magnetic field

perpendicular to the beam and orthogonal to the solenoid field in the ID, causing muons to bend in the $R - z$ plane. Thus muons are reconstructed by exploiting the combination of information obtained both from the ID and from the MS that makes an independent measurement of the momentum.

Precision chambers, the Monitored Drift Tubes (MDT) and the Cathode Strip Chambers (CSC), are used to reconstruct the trajectory of the muons.

An essential design criterion of the muon system is the capability to trigger on muon tracks. The precision-tracking chambers have therefore been complemented by a system of fast trigger chambers capable of delivering track information within a few tens of nanoseconds after the passage of the particle. Trigger chambers are fast muon momentum measurement detectors consisting of the Resistive Plate Chambers (RPC) and the Thin Gap Chambers (TGC).

A schematic layout of the MS in the $x - y$ and $z - y$ projections is shown in Figure 3.14. Most important parameters regarding MS sub-detectors are reported in Table 3.3.

Type	Function	Chamber resolution in			Measurements/track		Number of	
		z/R	ϕ	time	barrel	end-cap	chambers	channels
MDT	tracking	$35 \mu\text{m} (z)$	—	—	20	20	1150	354k
CSC	tracking	$40 \mu\text{m} (R)$	5 mm	7 ns	—	4	32	30.7k
RPC	trigger	10 mm (z)	10 mm	1.5 ns	6	—	606	373k
TGC	trigger	2 – 6 mm (R)	3-7 mm	4 ns	—	9	3588	318k

Table 3.3: Parameters of the four sub-systems of the muon detector. The quoted spatial resolution (columns 3, 4) does not include chamber-alignment uncertainties. Column 5 lists the intrinsic time resolution of each chamber type, to which contributions from signal-propagation and electronics contributions need to be added [23].

3.6.1 Tracking Chambers

A brief description of the muon tracking chambers is reported in the following lines.

- The **Monitored Drift Tubes** (MDT) measure only the z coordinate in the barrel region and in the end-cap region up to $|\eta| < 2.7$ except for the innermost layer where they are replaced by the CSC. The basic elements of the MDT chambers are pressurised drift tubes, that act as the cathode, with a diameter of 30 mm, operating with Ar/CO₂ gas (93/7, i.e. 93% Ar and 7% CO₂) at 3 bar and central tungsten-rhenium wires, which act as the anode, with a diameter of $50 \mu\text{m}$, at a potential of ~ 3 kV. Muons ionise the gas mixture in the tubes to create electrons (which are attracted to the wire) and positive ions (which drift towards the cathode), as shown in Figure 3.15. Each MDT chamber is made of 3 – 8 layers of drift tubes, has an average resolution of $80 \mu\text{m}$ per tube and $35 \mu\text{m}$ per chamber; the limiting factor at high luminosity is a typical drift time of 700 ns.
- The **Cathode Strip Chambers** (CSC) are multi-wire proportional chambers consisting of arrays of positively-charged “anode” wires oriented in the radial direction crossed with negatively-charged copper “cathode” strips measuring muon momentum in the forward region, i.e. in the pseudorapidity range $2 < |\eta| < 2.7$. The wires

are kept at a voltage of 1.9 kV and the space enclosing the wires is filled with a gas mixture of Ar/CO₂ (80/20). The CSC combine high spatial, time and double track resolution with high-rate capability and low neutron sensitivity. The whole CSC system consists of two disks each with eight chambers (eight small and eight large), each chamber containing four CSC planes. This design provides a resolution of 60 μm in the bending plane and 4 mm in the transverse plane while the time resolution is about 7 ns. A sketch of the gas gap in a CSC is shown in Figure 3.16.

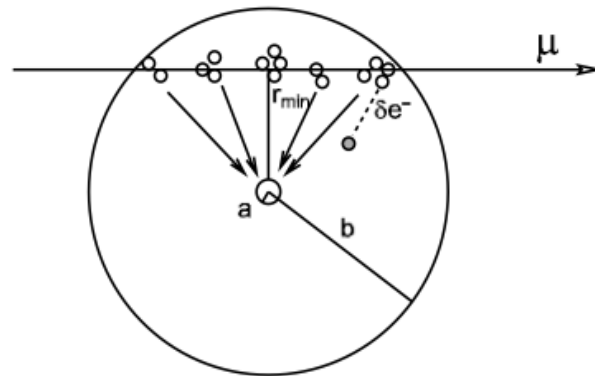


Figure 3.15: Cross section of a charged particle passing through a drift tube. The charged particle ionises electrons in the gas which drift to the anode wire at the centre of the tube [23].

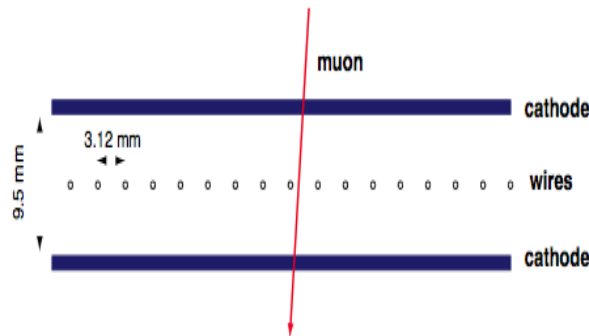


Figure 3.16: Diagram of the gas gap in a Cathode Strip Chamber.

The precision of the momentum measurement for a high- p_T muon track depends on the resolution of the sagitta, namely the deviation in the $R-z$ plane with respect to a straight line. For a high-momentum track ($p_T \sim 1$ TeV), the typical sagitta is around 500 μm . The ATLAS muon system, in particular the MDTs, provides a momentum measurement with a σ_{p_T}/p_T resolution between 2 – 3% and $\sim 10\%$ in the p_T range between 10 GeV and 1 TeV.

3.6.2 Triggering Chambers

The trigger chambers of the muon system provide fast information on muon tracks traversing the detector, allowing the trigger logic to recognise their multiplicity and approximate energy range. Details on the trigger system are reported in the next section. A brief description of the muon trigger system is reported in the following lines.

- The **Resistive Plate Chambers** (RPC) are fast gaseous detectors and consist of two parallel plates, a positively-charged anode and a negatively-charged cathode, both made of a very high resistivity plastic material and separated by a gas volume, as shown in Figure 3.17; each plate is read by two orthogonal series of strips: the η -strips are parallel to the MDT wires and provide the bending view of the trigger detector, the ϕ -strips are orthogonal to the MDT wires and provide the second-coordinate measurement. The resistive plates are kept at a potential difference of 9.8 kV and the chamber is filled with a gas mixture of $C_2H_2F_4$, C_4H_{10} and SF_6 (94.7/5/0.3 respectively). They cover the pseudorapidity range $|\eta| < 1.05$ and combine a good spatial resolution with a time resolution of just 1 ns.

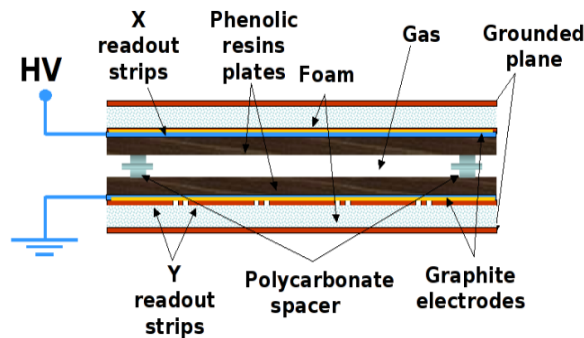


Figure 3.17: Structure of a Resistive Plate Chamber.

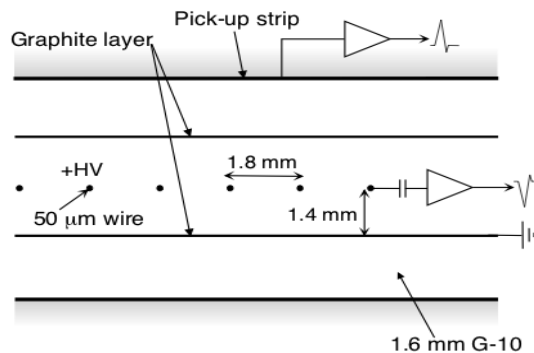


Figure 3.18: TGC structure showing anode wires, graphite cathodes, G-10 layers and a pick-up strip, orthogonal to the wires [23].

- The **Thin Gap Chambers** (TGC) consist of planes of closely spaced wires maintained at positive high voltage, sandwiched between resistive grounded cathode planes covering the pseudorapidity range $1.05 < |\eta| < 2.4$. The operational gas is a mixture of $\text{CO}_2/\text{n-C}_5\text{H}_{12}$ (55/45 respectively) (n-pentane). The anode wires, arranged parallel to the MDT wires, provide trigger signal together with readout strips arranged orthogonal to the wires. The TGC can provide spatial resolution better than $100 \mu\text{m}$. Their spatial resolution is mainly determined by the readout channel granularity: several wires (the number depending on the desired granularity at that η location) are ganged together to provide an anode signal. Furthermore, the TGC provide good time resolution and high rate capability.

3.7 Trigger and Data Acquisition System

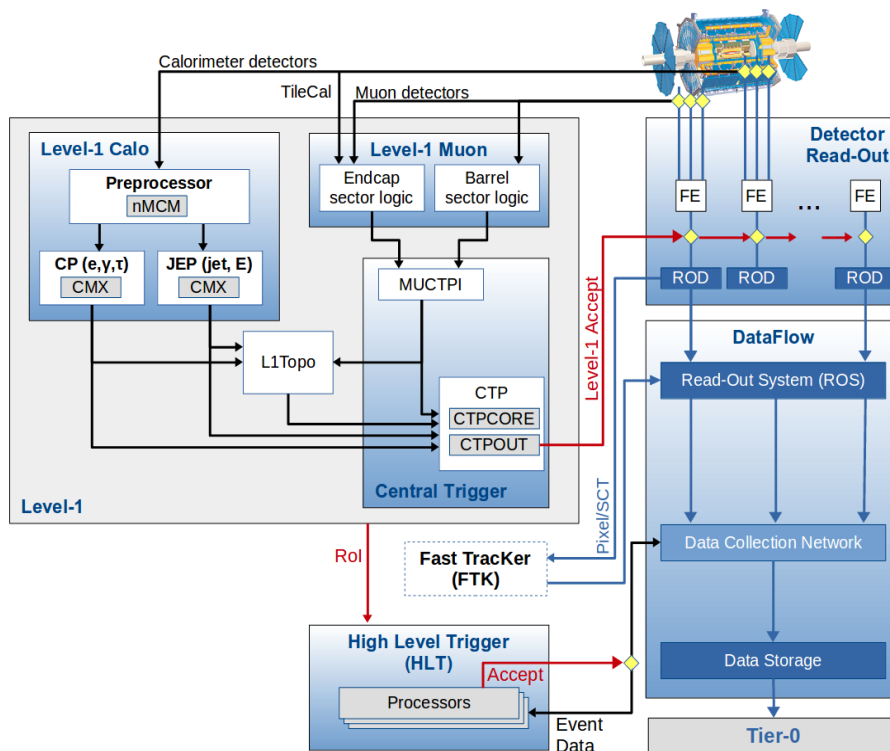


Figure 3.19: Scheme of the ATLAS Trigger and Data Acquisition system in Run 2 with specific focus given to the components of the L1 Trigger system [81].

The Trigger and Data Acquisition system (TDAQ) is an essential component of the ATLAS experiment because it is responsible for deciding whether or not to save a given collision as an interesting physics process for the offline analysis among the large number of data collected. The main challenges this system has to face are the unprecedented rate of events, $R_{event} \sim 8 \times 10^8$ events/s as discussed in Chapter 2, the need to select rare predicted physics processes with high efficiency while rejecting much higher-rate background processes, as well as acquire information from large and complex detectors with huge numbers of channels $O(10^7)$ [23]. The system has to decrease the event rate

from the nominal bunch crossing rate of 40 MHz to a rate of about 1 kHz, that is the maximum reachable rate in order to process data.

Higher luminosity, increased collision energy and higher pile-up have led to an increase of the rates as compared to the Run 1 trigger selections by up to a factor five; therefore, after the LHC long shutdown (2013 – 2014), the ATLAS trigger system was upgraded to reduce the amount of data [82]. Starting from the three levels of Run 1, Level-2 (L2) and Event Filter (EF) triggers have been merged into a single “High Level Trigger” (HLT) farm. The Trigger System in Run 2 consists of a hardware-based First Level Trigger (Level-1) [83] and a software-based High Level Trigger (HLT) [84], as schematically shown in Figure 3.19:

- *Level-1 Trigger*: the initial selection is made by the Level-1 Trigger, which reduces the event rate from the LHC bunch crossing of ~ 40 MHz to ~ 100 kHz, with an overall latency of less than $2.5 \mu\text{s}$; it uses custom electronics to determine Regions-of-Interest (RoIs) in the detector, the size of such regions depending on the type of object being triggered, taking as input coarse granularity calorimeter and muon detector information. There are two types of Level-1 triggers: calorimeter Level-1 and muon Level-1: as an example, the Level-1 muon trigger receives inputs from the RPCs in the barrel region and from the TGCs in the end-caps region;
- *High Level Trigger*: the second stage of the Trigger System, the HLT, further reduces the event rate up to 1 kHz with a processing time of 200 ms; the RoIs formed at Level-1 are sent to the HLT in which sophisticated offline selection and reconstruction algorithms are run using full granularity detector information in either the RoI defined by the L1 trigger or the whole event; it is used to refine the Level-1 decision and it is the responsible for the final physics selection for the following offline analyses.

Figure 3.20 shows an example of HLT trigger rates grouped by trigger signature in a 2017 run with a peak luminosity of $\mathcal{L} = 1.53 \times 10^{34} \text{ cm}^{-2}\text{s}^{-1}$ and a peak pile-up of $\mu = 43$ [85].

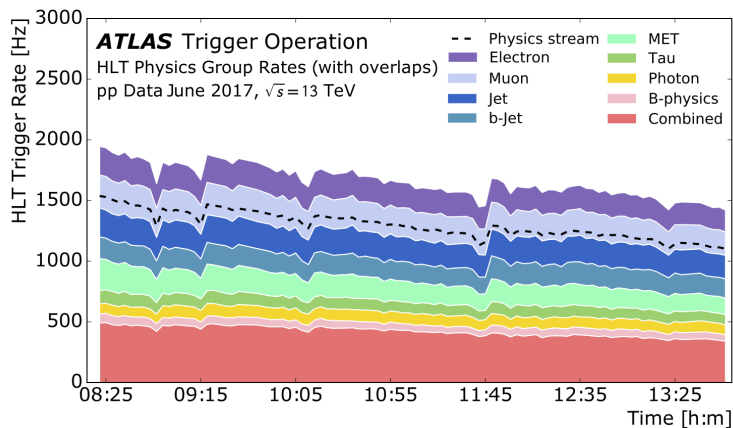


Figure 3.20: Physics trigger group rates at the High Level Trigger (HLT) as a function of time in a fill taken in June 2017 with a peak luminosity of $\mathcal{L} = 1.53 \times 10^{34} \text{ cm}^{-2}\text{s}^{-1}$ and a peak pile-up of $\mu = 43$. Presented are the rates of the individual trigger groups specific to trigger physics objects [85].

3.8 Luminosity Detectors

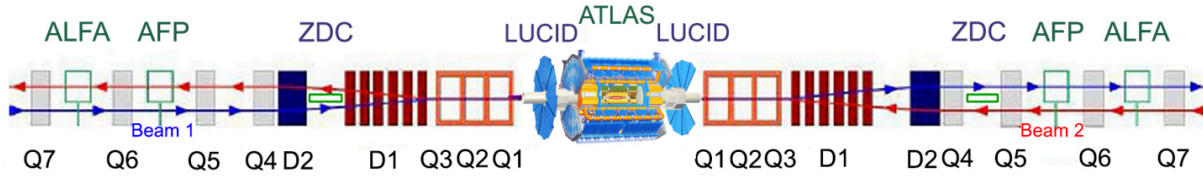


Figure 3.21: ATLAS luminosity detectors [86].

The main target of the ATLAS forward detectors is to extend ATLAS program by detecting particles in the high rapidity region.

The ATLAS strategy to understand and control the systematic uncertainties affecting the luminosity determination is to compare the measurements of several luminosity detectors [75] shown in Figure 3.21:

- **LUCID**, **L**uminosity **M**easurements **U**sing **C**herenkov **I**ntegrating **D**etector, is the official ATLAS luminosity monitor since the beginning of Run 2 and the luminosity detector closest to the IP, located at a distance of ± 17 m from the IP, covering a pseudorapidity range $5.6 < |\eta| < 6$; its main purpose is to monitor inelastic pp scattering rate in the forward direction with sufficient efficiency and low sensitivity to the background, counting the mean number of inelastic pp collisions through the number of charged particles that are produced in each collision within the LUCID acceptance; it can both measure the integrated luminosity and provide online monitoring of the instantaneous luminosity.
- **ZDC**, **Z**ero **D**egree **C**alorimeter is a system of calorimeters designed for relative luminosity measurements during pp and heavy ion runs, placed at a distance of ± 140 m from the IP and covering a pseudorapidity range $8.3 < |\eta|$, about zero degree to the beam; the primary purpose of this system is to detect forward neutrons in heavy-ion collisions and pp collisions.
- **ALFA**, the **A**bsolute **L**uminosity **F**or **A**TLAS is based on scintillator fibers placed in Roman Pots (RP) [87] close to the LHC proton beam at 240 m from the IP, covering a pseudorapidity range $10.6 < |\eta| < 13.5$. Its target is to measure the pp scattering at very small angles in order to determine, at the same time, the absolute luminosity and the total pp cross-section σ_{tot} .

Chapter 4

Reconstruction of physics objects

This chapter presents a general overview of the reconstruction of physics objects, a procedure that consists of combining information collected from the sub-detectors described in Chapter 3 and using it in order to reconstruct interaction vertices (Section 4.1), to identify, from tracks and calorimeter clusters, electrons and photons (Section 4.2), jets (Section 4.3), muons (Section 4.4) and tau leptons (Section 4.5), and to measure the global properties of the event, like the total transverse energy and, through the energy balance, the so-called “missing transverse energy” (Section 4.6) attributed to neutrinos; tau leptons, due to their short lifetime of $2.9 \times 10^{-13} \text{s}^{-1}$ ($c\tau = 87 \mu\text{m}$) decay inside the beam pipe, so they are not identified as tau reconstructed objects, but they are reconstructed and identified through their decay products, from leptonic and hadronic decay modes. Figure 4.1 shows a candidate event display for the $VH \rightarrow b\bar{b}$ channel where the Higgs boson decays to two b -quarks and the W boson to a muon and a neutrino, that leaves the detector without being seen and is thus reconstructed through the missing transverse energy represented by the dashed line.

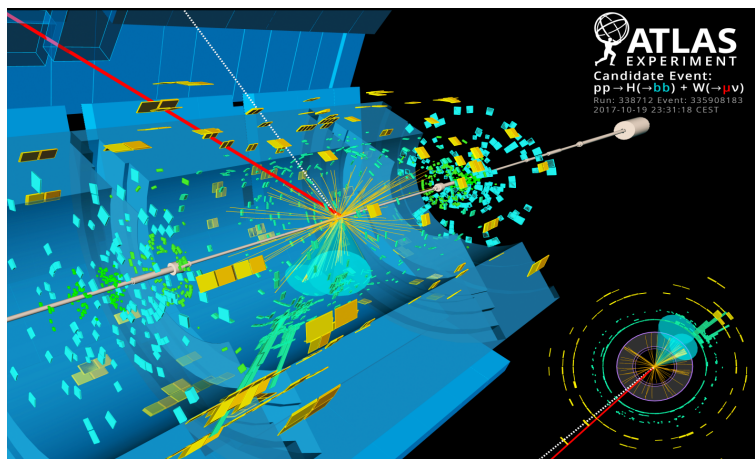


Figure 4.1: A candidate event display for the production of a Higgs boson decaying to two b -quarks (blue cones), in association with a W boson decaying to a muon (red) and a neutrino [88].

All physics analyses need to define their objects of interest; given the fact that the results presented in this thesis come from the combination of many analyses targeting

Higgs-boson decay channels, a brief description of the several types of reconstruction will be reported in the following sections.

4.1 Reconstruction of tracks and vertices

Tracks are used both to identify the particles produced in the collisions and to locate the primary vertex, by extrapolating their path to the beam line; they are reconstructed from individual particle interaction with the detector using a sequence of algorithms [89]:

- Track reconstruction begins with the formation of space-points: the first step consists in exploiting detector information in order to create clusters in the Pixel and SCT, and drift circles in the TRT. Then, clusters and drift circles are transformed into 3D space-points, i.e. three dimensional representations of detector measurements. A space-point corresponds to a hit in the IBL and Pixel detector, while the SCT space-points correspond to hits on both sides of the module. Clusters created by charge deposits from one particle are called single-particle clusters. Clusters created by charge deposits from multiple particles are called merged clusters; the different types of clusters are illustrated in Figure 4.2.

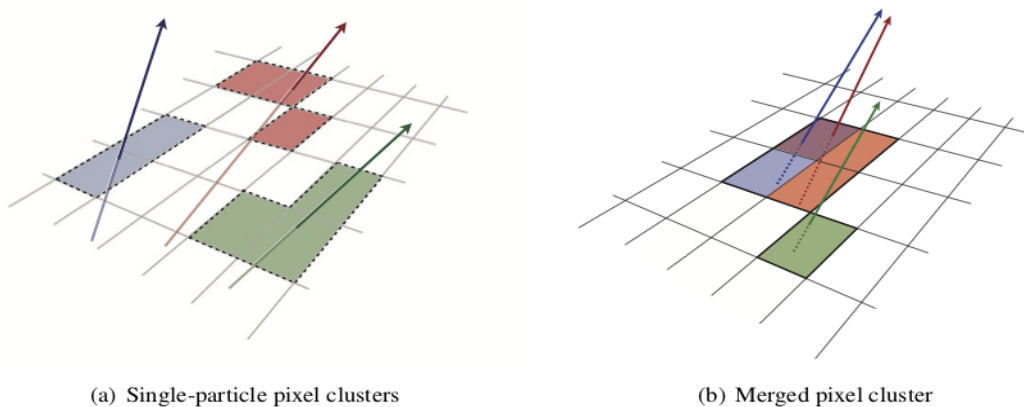


Figure 4.2: Illustration of (a) single-particle pixel clusters on a pixel sensor and (b) a merged pixel cluster due to very collimated charged particles. Different colours represent energy deposits from different charged particles traversing the sensor and the particles trajectories are shown as arrows [89].

- Track seeds are formed from sets of three space-points, either Pixel-only, SCT-only or Mixed seed. Seeds which pass the initial transverse momentum (p_T) and impact parameter resolution cuts are also required to match a fourth space-point that is compatible with the particle's trajectory estimated from the seed. A combinatorial Kalman filter [90] is then used to build track candidates from the chosen seeds by incorporating additional space-points from the remaining layers of the pixel and SCT detectors which are compatible with the preliminary trajectory.

- When all combinations of space-points have been made, there are a number of track candidates where space-points overlap, or have been incorrectly assigned. This necessitates an ambiguity-solving stage: track candidates are ranked based on track score, favouring tracks with a higher score. Track candidates are rejected if they fail to meet basic quality criteria. An artificial neural network (NN) clustering algorithm [91] is trained to identify merged clusters and separate multiple particles within a merged cluster in dense environments.
- Finally, the track candidates selected through this procedure are extended to the TRT if there is a valid set of matching drift circles. Then, a high-resolution fit is performed using all available information. Fitted tracks which pass through the ambiguity solver without modification are added to the final track collection.

The reconstruction of the primary vertex, i.e. the location where the pp interaction takes place, is essential for physics analyses. The correct assignment of charged particle trajectories to their source vertex, together with an accurate reconstruction of the number and positions of interaction vertices, is essential to reconstruct the full kinematic properties of the hard-scatter and separate the effects of additional collisions.

The reconstruction of vertices can be split into two main stages [92]: vertex finding, i.e. the association of reconstructed tracks to a given vertex candidate, and vertex fitting, i.e. the reconstruction of the actual vertex position.

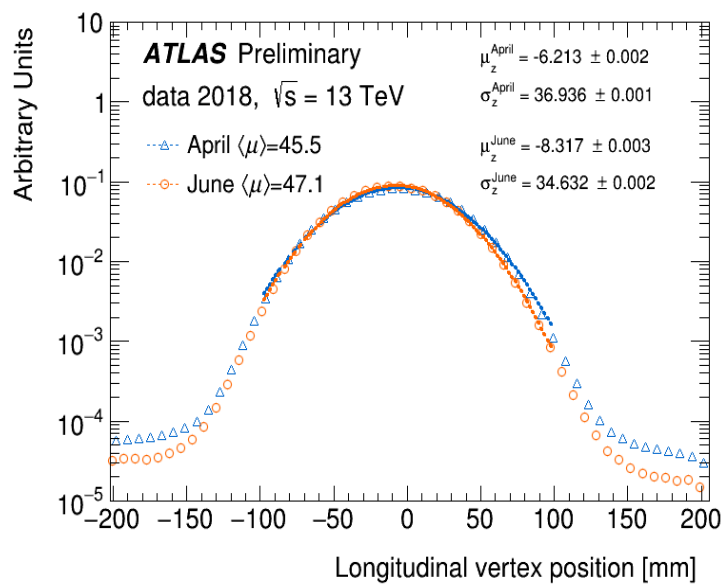


Figure 4.3: Normalised distribution of the longitudinal position of primary vertices in two fills with different average μ taken at different points in 2018. The non-gaussian tails at large values of z are due to fake vertices. Fake vertices, that are expected in normal operation, are due to combinatorics and become relevant in high pile-up environments. A gaussian function is fitted in the range $(-100, 100)$ mm to extract the mean value and the sigma of the distribution [93].

It consists of the following steps [94]:

- a set of tracks passing the vertex selection criteria is defined;

- a seed position for the first vertex is selected;
- the tracks and the seed are used to fit the best-vertex position, exploiting an iterative procedure; in each iteration, less compatible tracks are down-weighted and the vertex position is recomputed;
- after the determination of the vertex position, tracks that are found incompatible with the vertex are removed and are used in the determination of another vertex; vertices are required to have at least two associated tracks;
- this procedure is repeated until no track in the event is left unassociated or no additional vertex can be found in the remaining set of tracks.

The output of the vertex reconstruction algorithm is a set of three dimensional vertex positions. Figure 4.3 shows the normalised distribution of the longitudinal position of primary vertices in two fills with different average μ , taken at different points in 2018. The vertex reconstruction efficiency is determined from data by taking the ratio between events with a reconstructed vertex and events with at least two reconstructed tracks.

4.2 Electron and photon reconstruction and identification

The reconstruction of electrons and photons is based on combining information from the tracking and calorimeter systems. The interactions of photons and electrons with the ATLAS ECal produce similar electromagnetic showers, depositing a significant amount of energy in a restricted number of neighbouring calorimeter cells; thus their reconstruction proceeds in parallel through the following steps [95]:

1. *Topo-cluster reconstruction*: the preparation of the clusters uses a topo-cluster reconstruction algorithm [96, 97] whose first step is the formation of proto-clusters in the electromagnetic and hadronic calorimeters using a set of noise thresholds in which the cell initiating the cluster is required to have significance $|\zeta_{cell}^{EM}| \geq 4$, being the significance defined as:

$$\zeta_{cell}^{EM} = \frac{E_{cell}^{EM}}{\sigma_{noise,cell}^{EM}} \quad (4.1)$$

where E_{cell}^{EM} is the cell energy at the EM scale and $\sigma_{noise,cell}^{EM}$ is the expected cell noise that includes the known electronic noise and an estimation of the pile-up noise corresponding to the average instantaneous luminosity expected for Run 2. In this initial stage, cells from the pre-sampler and the first LAr EM calorimeter layer are excluded from initiating proto-clusters, to suppress the formation of noise clusters. Then the proto-clusters collect neighbouring cells with significance $|\zeta_{cell}^{EM}| \geq 2$; each neighbour cell that passes this threshold becomes a seed cell in the next iteration, collecting each of its cell neighbours in the proto-cluster. After all nearby cells have been collected, a final set of neighbouring cells with $|\zeta_{cell}^{EM}| \geq 0$ is added to the cluster.

2. *Track reconstruction* [98]: topo-clusters are associated to tracks reconstructed in the ID. The track information from the ID is extracted by using both pattern recognition and track fit. The pattern recognition algorithm uses the pion hypothesis for energy loss from interactions of the particle with the detector material, or the electron hypothesis if the track seeds have transverse momentum above 1 GeV and the track seed cannot be extended to a full track (with at least 7 hits) using the pion hypothesis; the modified pattern recognition, designed to better account for energy loss of charged particles in materials, uses an optimised Gaussian-sum filter (GSF) [99] fit while the standard fit uses the ATLAS Global χ^2 Track Fitter [100]. The photon conversion reconstruction proceeds in a similar way [95]: a candidate particle is reconstructed as a photon if there are no tracks with at least four hits in the silicon detector matched to the calorimeter cluster; tracks loosely matched to fixed-size clusters serve as input to the reconstruction of the conversion vertex. Both tracks with silicon hits (denoted Si tracks) and tracks reconstructed only in the TRT (denoted TRT tracks) are used for the conversion reconstruction. Two-track conversion vertices are reconstructed from two opposite-charged tracks forming a vertex consistent with that of a massless particle, while single-track vertices are essentially tracks without hits in the innermost sensitive layers. To increase the converted-photon purity, requirements on the TRT tracks and on double-track Si conversions are applied.
3. *Super-cluster reconstruction*: the reconstruction of electron and photon super-clusters proceeds independently, each in two stages: in the first stage, EM topo-clusters are tested in order to be used as seed cluster candidates, which form the basis of super-clusters; in the second stage, EM topo-clusters near the seed candidates are identified as satellite-cluster candidates, which may emerge from bremsstrahlung radiation or topo-cluster splitting. If satellite clusters satisfy the necessary selection criteria, they are added to the seed candidates to form the final super-clusters. The super-clustering algorithm, shown in the sketch of Figure 4.4, has replaced the sliding-window algorithm [97] to search for cluster “seeds” previously exploited in ATLAS for the reconstruction of fixed-size clusters of calorimeter cells.
4. *Creation of electrons and photons for analysis*: after building electron and photon super-clusters, initial energy calibration and position correction are applied, and tracks are matched to electron super-clusters and conversion vertices to photon super-clusters. The matching is performed in the same way the matching to EM topo-clusters was performed, but using super-clusters. After this matching, analysis-level electrons and photons are built and discriminating variables used to separate electrons or photons from background are added.

4.2.1 Electron identification and isolation

The baseline identification algorithm for electrons is the likelihood-based (LH) method, that is a multivariate technique evaluating signal versus background probability density functions. For each electron candidate, these probabilities are combined into a discrimi-

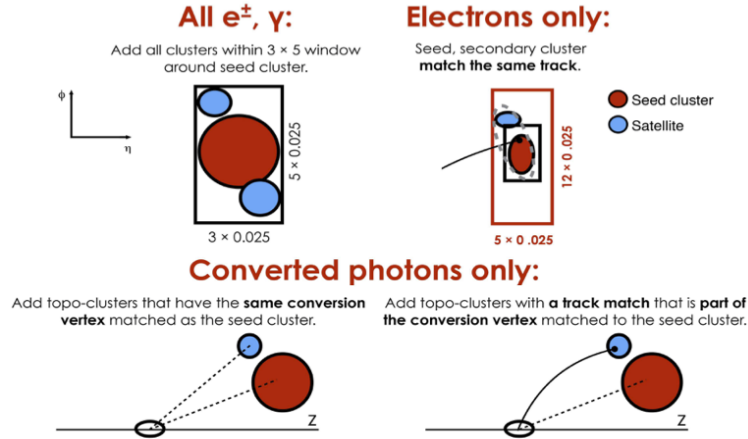


Figure 4.4: Sketch of the super-clustering algorithm for electrons and photons. Seed clusters are shown in red, satellite clusters in blue [95].

nant d_L , defined as:

$$d_L = \frac{L_S}{L_S + L_B} \quad \text{with} \quad L_{S(B)}(\vec{x}) = \prod_{i=1}^n P_{s(b),i}(x_i) \quad (4.2)$$

where:

- \vec{x} is the set of discriminating variables, like track conditions from the ID measurement and track-cluster matching;
- $P_{s(b),i}(x_i)$ are the values of the signal/background pdfs for quantity i at value x_i ;
- $L_{S(B)}(\vec{x})$ are the likelihood functions for signal and background.

Three fixed values of the LH discriminant are used to define three operating points corresponding to increasing thresholds for the LH discriminant; they are referred to as Loose, Medium, and Tight.

In order to further reject hadronic jets misidentified as electrons, most analyses require electrons to pass some isolation requirements in addition to the identification requirements described above, where the isolation is a measurement of the detector activity around a candidate. The two main isolation variables are: calorimeter-based isolation and track-based isolation. The total efficiency ϵ_{total} for a single electron can be factorised as a product of different efficiency terms [98] that can be estimated directly from data using tag-and-probe methods [101, 102]:

$$\begin{aligned} \epsilon_{total} &= \epsilon_{EMclus} \times \epsilon_{reco} \times \epsilon_{id} \times \epsilon_{iso} \times \epsilon_{trig} = \\ &= \left(\frac{N_{cluster}}{N_{all}} \right) \times \left(\frac{N_{reco}}{N_{cluster}} \right) \times \left(\frac{N_{id}}{N_{reco}} \right) \times \left(\frac{N_{iso}}{N_{id}} \right) \times \left(\frac{N_{trig}}{N_{iso}} \right) \end{aligned} \quad (4.3)$$

where:

- the efficiency to reconstruct EM-cluster candidates, ϵ_{EMclus} , is given by the number of reconstructed EM calorimeter clusters, $N_{cluster}$, divided by the number of produced electrons, N_{all} ;

- the reconstruction efficiency, ϵ_{reco} , is given by the number of reconstructed electron candidates, N_{reco} , divided by the number of EM-cluster candidates, $N_{cluster}$;
- the identification efficiency, ϵ_{id} , is given by the number of identified and reconstructed electron candidates, N_{id} , divided by N_{reco} ;
- the isolation efficiency, ϵ_{iso} , is calculated as the number of identified electron candidates satisfying the isolation, identification, and reconstruction requirements, N_{iso} , divided by N_{id} ;
- the trigger efficiency, $\epsilon_{trigger}$, is calculated as the number of triggered (and isolated, identified, reconstructed) electron candidates, N_{trig} , divided by N_{iso} .

The reconstruction efficiency, ϵ_{reco} , is shown in Figure 4.5 as a function of the true (generator) transverse energy E_T for each step of the electron-candidate formation. Figure 4.6 reports electron identification efficiencies as a function of the pseudorapidity for the three operating points in $Z \rightarrow e^+e^-$ events, used to benchmark the expected electron efficiencies and to define the electron identification criteria, exploiting the 2017 ATLAS dataset that corresponds to an integrated luminosity of 43.8 fb^{-1} .

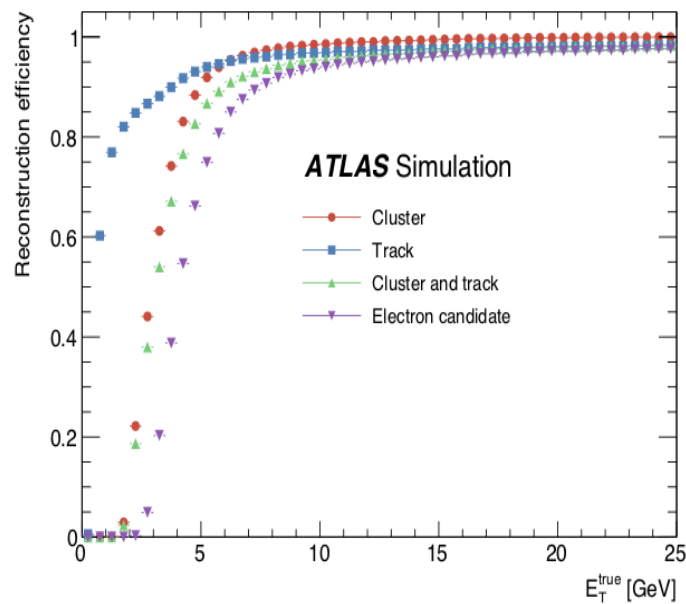


Figure 4.5: Cluster, track, cluster and track, and electron reconstruction efficiencies as a function of the electron E_T [95].

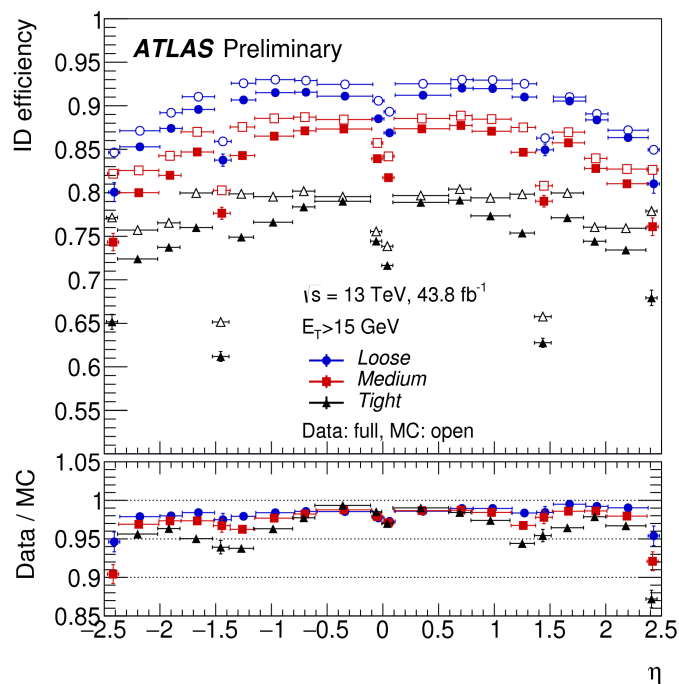


Figure 4.6: Electron identification efficiencies in $Z \rightarrow e^+e^-$ events as a function of pseudo-rapidity η , for electrons with $E_T > 15$ GeV. The efficiencies are shown in data and MC for the three operating points, Loose, Medium and Tight. The data efficiencies are obtained by applying data/MC efficiency ratios that were measured in $J/\Psi \rightarrow e^+e^-$ and $Z \rightarrow e^+e^-$ events to MC simulation. A dataset corresponding to an integrated luminosity of 43.8 fb^{-1} that was recorded by the ATLAS experiment in the year 2017 at a centre-of-mass energy of $\sqrt{s} = 13$ TeV was used. The total statistical and systematic uncertainty is shown [103].

4.2.2 Photon identification and isolation

The photon identification criteria are designed to efficiently select prompt, isolated photons and reject backgrounds from hadronic jets. The photon identification is constructed from one-dimensional selection criteria, or a cut-based selection, using shower shape variables like the lateral and the total shower widths in different EM layers [95]. The variables using the EM first layer play a particularly important role in rejecting π^0 decays into two highly collimated photons.

Three identification selections are identified: the primary one is labelled as Tight, with less restrictive selections called Medium and Loose, which are used for trigger algorithms. In order to better discriminate signal vs background, additional information is exploited quantifying the activity near photons from the tracks of nearby charged particles, or from energy deposits in the calorimeters; requirements on the calorimeter and track isolation variables are applied, and three photon isolation operating points are defined, i.e. FixedCutLoose, FixedCutTight and FixedCutTightCaloOnly operating points.

Figure 4.7 shows the efficiency of the tight identification requirement for unconverted (a) and converted photons (b) from radiative Z decays as a function of the transverse energy E_T using 44.3 fb^{-1} of data recorded by the ATLAS experiment in 2017.

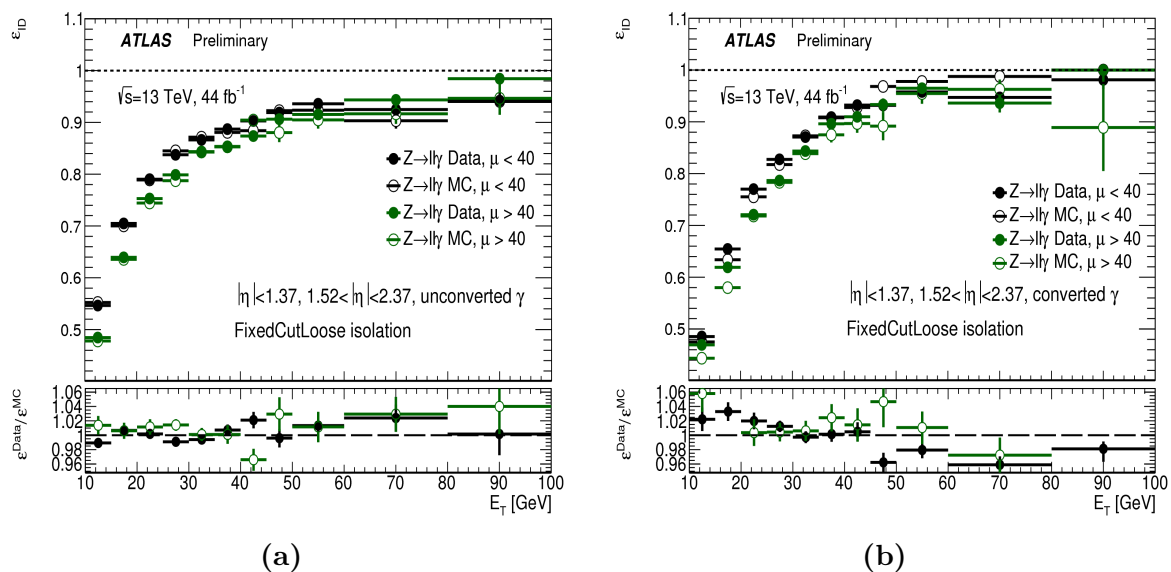


Figure 4.7: Efficiency of the tight identification requirement for unconverted (a) and converted photons (b) from radiative Z decays as a function of the transverse energy E_T , averaged over pseudorapidity. Loose photon isolation requirement is applied. The efficiencies have been measured using 44.3 fb^{-1} of data recorded by the ATLAS experiment in 2017 at $\sqrt{s}=13 \text{ TeV}$ for $\mu < 40$, and are compared to the 2017 data with $\mu > 40$. Only the statistical uncertainties are shown [103].

4.3 Jet and b -jet reconstruction

Hadronic collisions in the ATLAS experiment produce a variety of particles, including quarks or gluons, called “partons”. Due to colour confinement, partons cannot exist

individually and they re-combine, i.e. “hadronise”, with quarks and anti-quarks spontaneously created from the vacuum, in order to form hadrons. A jet can thus be defined as a collimated shower of stable particles arising from fragmentation and hadronisation of a parton (quark or gluon) after a collision. Jet reconstruction algorithms combine calorimeter objects grouping individual clusters in an ordered way. The jets provide a link between the observed colourless stable particles and the underlying physics at the partonic level [104].

Jets can be reconstructed through the following steps [105]:

1. the inputs of the jet reconstruction are topo-clusters, i.e. topologically-grouped noise-suppressed clusters of calorimeter cells. They are formed from seed cells through the procedure already described in Section 4.2. The process concludes by adding all calorimeter cells adjacent to the topo-cluster, irrespective of their energy;
2. a jet finding algorithm is then typically used, and the standard ATLAS solution is the anti- k_t [106] algorithm, whose application is shown in Figure 4.8, that sequentially recombines clusters exploiting the following procedure:

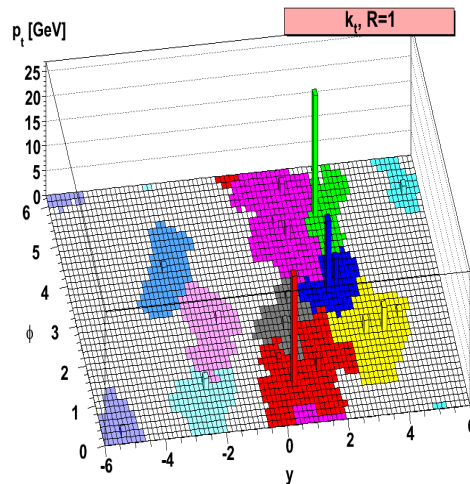


Figure 4.8: A sample parton-level event, together with many random soft “ghosts”, clustered with the anti- k_t algorithm, illustrating the “active” catchment areas of the resulting hard jets [106].

- the distance d_{ij} between entities (particles, pseudo-jets) i and j is evaluated:

$$d_{ij} = \min(k_{ti}^{2p}, k_{tj}^{2p}) \frac{\Delta_{ij}^2}{R^2} \quad (4.4)$$

where $\Delta_{ij} = (y_i - y_j)^2 + (\phi_i - \phi_j)^2$ and y_i , ϕ_i and k_{ti} , are respectively the rapidity, the azimuthal coordinate and the transverse momentum of the i particle, R represents the size of the jet, while p is a parameter of the anti- k_t algorithm fixed equal to -1.

- For each entity i , the distance from the beam is estimated:

$$d_{iB} = k_{ti}^{2p}. \quad (4.5)$$

- The minimum distance between d_{ij} and d_{iB} is identified.
- If d_{ij} is the minimum distance, i and j are combined into a single pseudo-jet and the procedure is repeated from the first step; if this is not the case, i is considered as a final state and is removed from the list of entities; the distances are recalculated and the procedure is repeated until no entities are left.

Two different distance parameters R are typically used: jets representing quarks and gluons are typically called small- R jets, and are reconstructed with $R = 0.4$, while jets representing hadronically decaying massive particles are typically called large- R jets, and are reconstructed with $R = 1.0$.

3. A substantially increased sensitivity to pile-up effects due to the larger fraction of the calorimeter enclosed within the jet volume comes from using large- R jets, that are however necessary to fully contain the hadronic massive particle decays. Additionally, pile-up is randomly distributed so it can obscure the angular structure within the jet that represents the key element in order to identify massive particle decays. To get around these limitations, large- R jets are typically groomed, where grooming is a class of algorithms that take a jet and throw away constituents following a defined strategy, rebuilding the final jet from the remaining constituents.

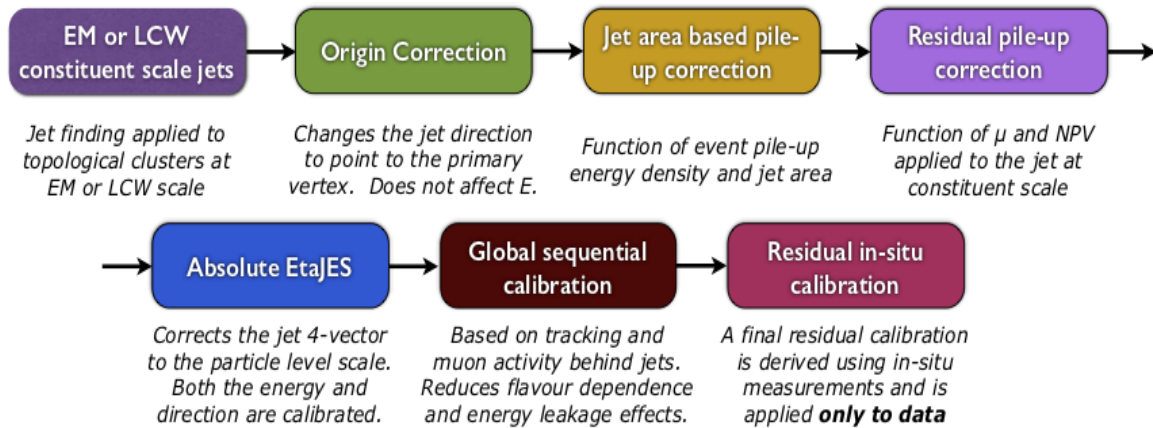


Figure 4.9: Overview of the ATLAS jet calibration scheme [108].

After jets have been built, they have to be calibrated to account for several effects: the energy scale of reconstructed jets does not correspond to the truth-particle jet energy scale (JES), defined as the energy of jets built from all stable Monte Carlo particles from the hard interaction only, including the underlying event activity. A dedicated jet energy calibration is then needed to calibrate, on average, the reconstructed jet energy to that of the corresponding truth-particle jet. The energy scale calibration needs to also correct for pile-up effects, that add energy deposits to the jets from the hard-scatter event and

create additional jets (pile-up jets). Furthermore, the jet energy calibration has to bring the energy scale of jets in data and simulation to the same footing [107]. Figure 4.9 shows an overview of the jet calibration used in the ATLAS experiment.

4.3.1 b -tagging algorithms

The long lifetime of hadrons with b -quarks ($\sim 1.5 \times 10^{-12}$ s) results in a typical decay topology with at least one vertex displaced from the primary vertex coming from the hard-scattering collision as shown in Figure 4.10. The identification of b -quark jets is

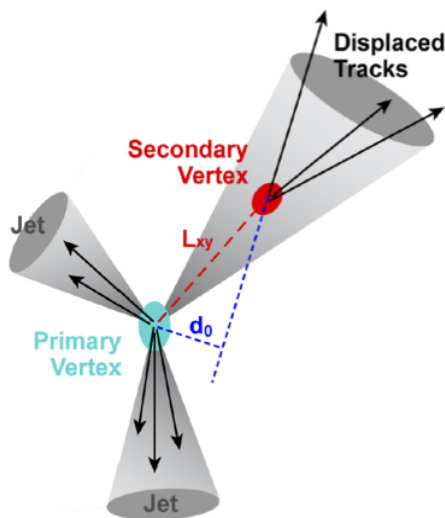


Figure 4.10: Schematic view of a jet containing a secondary vertex and displaced tracks, signature of a b -jet. Tracks are represented by arrows and the circles mark the primary (grey/blue) and secondary (dark grey/red) vertices. The transverse decay length L_{xy} and the transverse impact parameter distance d_0 which characterise the secondary vertex are indicated by dashed lines [110].

important for many physics analyses, including the $H \rightarrow b\bar{b}$ channel and all the double-Higgs channels studied in this thesis, i.e. $b\bar{b}b\bar{b}$, $b\bar{b}\tau^+\tau^-$ and $b\bar{b}\gamma\gamma$; it is based on three fundamental algorithms [109]:

- an impact-parameter-based algorithm;
- an inclusive secondary vertex reconstruction algorithm, based on the reconstruction of the distance of the transverse decay length, L_{xy} , of the b -hadron which is the vector pointing from the primary vertex to the b -hadron decay vertex;
- a decay chain multi-vertex reconstruction algorithm (JetFitter), exploiting the topological features of weak b - and c -hadron decays inside the jet and trying to reconstruct the full b -hadron decay chain.

The outputs of these three algorithms are combined into a Boosted Decision Tree (BDT), i.e. a machine-learning technique combining linear cuts on input discriminant observables in order to maximise the separation between two or more processes, and the multivariate

discriminant tagger is called MV2 [111], capable to provide the best separation between the different jet flavours. The training of the BDT is performed using $t\bar{t}$ events with b -jets as signal, and c -jets and light-flavour jets as background. Different MV2 taggers can be defined, depending on the fraction of c -jets used in the training. Different b -jets efficiency working points are defined, corresponding to different cuts on the BDT output score of the b -tagging algorithm. Since the majority of physics analysis are limited by charm rather than light-flavour jet rejection, the c -jet fraction is set in such a way to enhance charm rejection keeping a good light-flavour rejection as well. The MV2c10 tagger background composition is made of 93% light-flavour jets and 7% c -jets; its output for b -jets, c -jets and light-flavour jets in a $t\bar{t}$ sample is presented in Figure 4.11 (a). The rejection rates for light-flavour jets and c -jets are defined as the inverse of the efficiency for tagging a light-flavour jet or a c -jet as a b -jet, respectively. Figure 4.11 (b) shows the corresponding light-flavour jet and c -jet rejection factors as a function of the b -jet tagging efficiency.

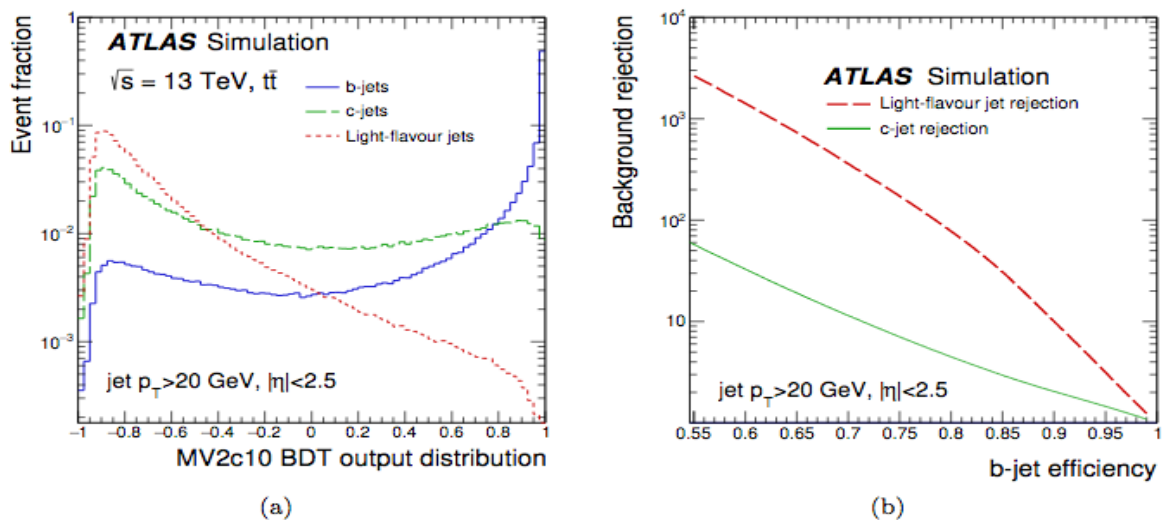


Figure 4.11: The MV2c10 output for b -jets (solid-line), c -jets (dashed line) and light flavour jets (dotted line) in simulated $t\bar{t}$ events; (b) the light-flavour jet (dashed line) and c -jet rejection factors (solid line) as a function of the b -jet tagging efficiency of the MV2c10 b -tagging algorithm [111].

4.4 Muon reconstruction and identification

Muon reconstruction is first performed independently in the ID and in the MS, described in Chapter 3. The information from individual sub-detectors is then combined to form the muon tracks that are used in physics analyses. In the ID, muons are reconstructed following the general track reconstruction described in Section 4.1. In the MS, muon reconstruction starts searching for hit patterns from the MDT and trigger chambers through a Hough transform algorithm [112] to form segments. This algorithm finds at least two seed-segments in the middle layers of the MDT; the muon tracks are reconstructed by performing a straight line fit, which takes seed-segments and hits found in each layer as inputs. The RPC or TGC hits measure the coordinate orthogonal to the

bending plane. In the CSC chambers, segments are built searching in the η and ϕ planes. Muon track candidates are then built by fitting together hits from segments in different layers [113].

The combined information of ID, MS and calorimeter system leads to the definition of four types of reconstructed muons, a sketch of whom is shown in Figure 4.12, depending on the sub-detector used in the reconstruction [114]:

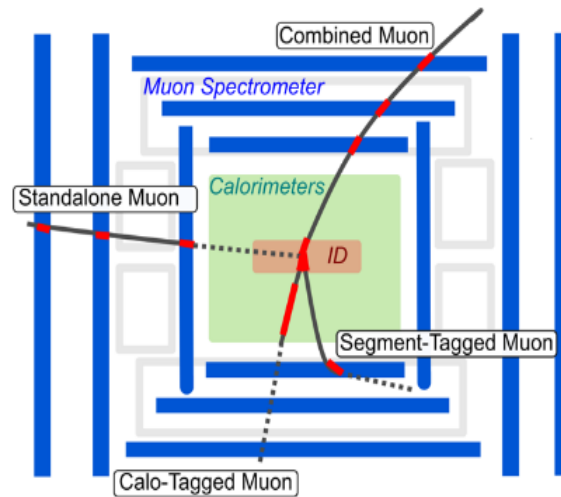


Figure 4.12: Schematic drawing of the detector parts used for muon reconstruction and of the different types of muon reconstruction [115].

1. Stand-Alone (SA) muons: the muon trajectory reconstruction is based only on the MS track and on a loose requirement on compatibility with tracks originating from the IP. In general, the muon has to cross at least two layers of MS chambers to provide a track measurement, but three layers are required in the forward region. SA muons are mainly used to extend the acceptance to the pseudorapidity range $2.5 < |\eta| < 2.7$ which is not covered by the ID.
2. Combined (CB) muons (main type of reconstructed muons): track reconstruction is performed independently in the ID and in the MS, and a combined track is formed through a global fit procedure that uses hits from both ID and MS sub-detectors. In order to maximise the fit quality, MS hits may be added to or removed from the track. The acceptance of CB muons is limited by the ID coverage, i.e. $|\eta| < 2.5$.
3. Segment-tagged (ST) muons: a track in the ID is classified as a muon if, once extrapolated to the MS, it is associated with at least one local track segment in the MDT or CSC chambers. ST muons can be used to increase the acceptance in cases in which the muon has crossed only one layer of MS chambers, either because of its low p_T or because it falls in regions with reduced MS acceptance.
4. Calorimeter-tagged (CT) muons: these muons are reconstructed by matching a track in the ID and an energy deposit in the calorimeter compatible with a minimum

ionising particle. This type of reconstructed muons has the lowest purity of all the muon types but it recovers acceptance in the uninstrumented regions of the MS.

Overlaps between different types of reconstructed muons are resolved in the following way: when two muon types share the same ID track, preference is given to CB muons, then to ST, and finally to CT muons. The overlap with SA muons in the muon system is resolved by analysing the track hit content and selecting the track with better fit quality and larger number of hits.

Muon identification is based on quality requirements suppressing background muons, that come mainly from pion and kaon decays, while selecting prompt muons with high efficiency, ensuring at the same time a precise momentum measurement. The variables, necessary to discriminate between background and prompt muons, are the following [113]:

- q/p significance, defined as the absolute value of the difference between the ratio of the charge and momentum of the muons measured in the ID and in the MS divided by the sum in quadrature of the corresponding uncertainties;
- ρ' , defined as the absolute value of the difference between the transverse momentum measurements in the ID and in the MS divided by the p_T of the combined track;
- the normalised χ^2 of the combined track fit.

In order to provide a robust momentum measurement, additional specific requirements on the number of hits in the ID and in the MS are used.

The four muon identification selections optimised for different physics analyses are: Loose, Medium, Tight, and High- p_T . The muon reconstruction efficiency is obtained with the tag-and-probe method for muons in the region $|\eta| < 2.5$, using $J/\Psi \rightarrow \mu^+\mu^-$ and $Z \rightarrow \mu^+\mu^-$ decays for low- (< 10 GeV) and high- p_T muons, respectively.

The reconstruction efficiencies for signal and background, considering all the identification selections, are reported in Table 4.1 for prompt muons from W decays and hadrons decaying in flight, categorised according to the MC truth information.

Selection	$4 < p_T < 20$ GeV		$20 < p_T < 100$ GeV	
	ϵ_{μ}^{MC} [%]	$\epsilon_{Hadrons}^{MC}$ [%]	ϵ_{μ}^{MC} [%]	$\epsilon_{Hadrons}^{MC}$ [%]
Loose	96.7	0.53	98.1	0.76
Medium	95.5	0.38	96.1	0.17
Tight	89.9	0.19	91.8	0.11
High p_T	78.1	0.26	80.4	0.13

Table 4.1: Efficiency for prompt muons from W decays and hadrons decaying in flight and misidentified as prompt muons computed using a $t\bar{t}$ MC sample. The results are shown for the four identification selection criteria separating low momentum ($4 < p_T < 20$ GeV) and high momentum ($20 < p_T < 100$ GeV) muons for candidates with $|\eta| < 2.5$ [113].

Figure 4.13 shows the reconstruction efficiencies with the full 2016 dataset for the Loose/Medium/Tight identification algorithms measured in $Z \rightarrow \mu^+\mu^-$ events as a function of the muon pseudorapidity for muons with $p_T > 10$ GeV.

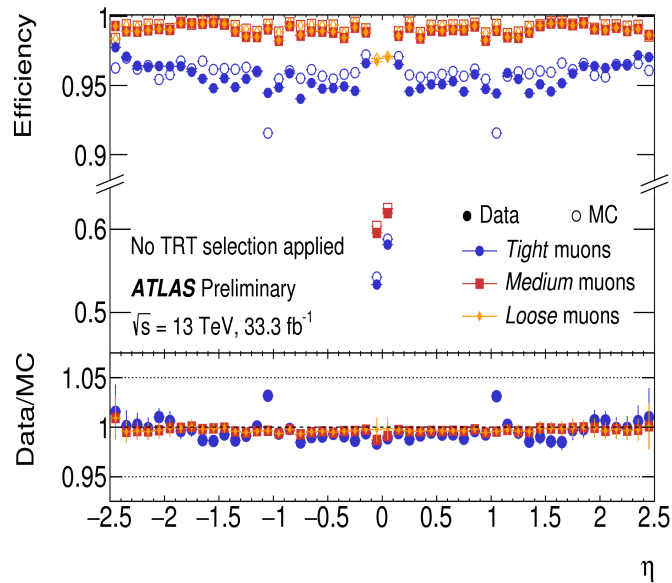


Figure 4.13: Muon reconstruction efficiencies with the full 2016 dataset for the Loose/Medium/Tight identification algorithms measured in $Z \rightarrow \mu^+ \mu^-$ events as a function of the muon pseudorapidity for muons with $p_T > 10$ GeV. The prediction by the detector simulation is depicted as open circles, while filled dots indicate the observation in collision data with statistical errors. The bottom panel shows the ratio between expected and observed efficiencies, i.e. the efficiency scale factor. The errors in the bottom panel represent the quadratic sum of statistical and systematic uncertainties [116].

Another powerful tool that can be exploited in order to reject background, is the measurement of muon isolation. As already mentioned in the electron case, two variables are used to assess the muon isolation: a track-based variable and a calorimeter-based isolation variable.

4.5 Tau reconstruction

The tau lepton is the heaviest lepton and, due to its short lifetime, it decays inside the beam pipe without reaching any detector.

It is the only lepton which decays both leptonically, i.e. $\tau_{lep} \rightarrow l \nu_l \nu_\tau$, $l = e, \mu$ (BR $\sim 35\%$) and hadronically, i.e. $\tau_{had} \rightarrow \text{hadrons} + \nu_\tau$ (BR $\sim 65\%$). Since the leptonic tau decay products are nearly indistinguishable from prompt electrons and muons, they will not be treated in this section.

Most of hadronic tau decays are characterised by one ($\sim 72\%$ of the cases) or three charged pions ($\sim 22\%$ of the cases) together with neutral pions ($\sim 68\%$ of all hadronic decays), thus the typical signature of such a decay is a narrow jet or spray of particles in the calorimeter, associated to one or three tracks in the ID.

The main background comes from jets of energetic hadrons produced via the fragmentation of quarks and gluons that are present both at trigger level and during the event reconstruction. The tau reconstruction proceeds through the following steps [117]:

- hadronic jets are reconstructed starting from their energy deposits in the calorimeter cells, using the anti- k_t algorithm already described in Section 4.3, with a distance parameter $R = 0.4$ (small-R); additionally, tau candidates are required to have $p_T > 10$ GeV and $|\eta| < 2.5$; they constitute the jet seeds used in later steps;
- the primary tau production vertex (TV) is identified among the possible candidates by choosing the candidate track vertex with the largest fraction of momentum from tracks associated ($\Delta R < 0.2$) with the jet; the tracks must have $p_T > 1$ GeV and pass requirements on the number of hits, i.e. at least two hits in the pixel detector and seven in the total pixel and SCT layers;
- the last step of the reconstruction is achieved using a track association algorithm, imposing additional requirements on the shortest distance from the track to the tau vertex in the transverse plane, $|d_0| < 1$ mm, and the shortest distance in the longitudinal plane, $|\Delta z_0 \sin(\theta)| < 1.5$ mm, where θ is the polar angle of the track and z_0 is the point of closest approach along the longitudinal axis.

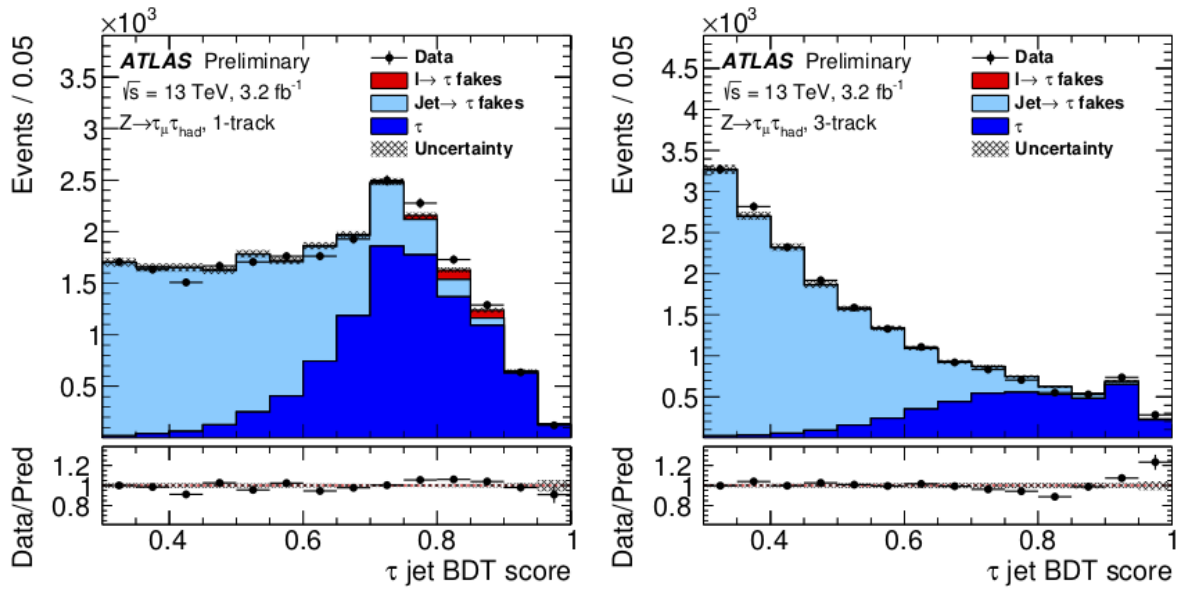


Figure 4.14: The jet discriminant BDT output distribution for one track (left) and three tracks (right) $\tau_{had-vis}$ candidates. The uncertainty band contains only the statistical uncertainty [117].

During the reconstruction process, no attempt is made in order to separate tau leptons from quark- and gluon-initiated jets. The tau identification algorithm is designed to address the rejection of these backgrounds through BDT-based methods [118, 119]. The BDT is separately trained for tau candidates with one or three associated tracks with simulated $Z/\gamma^* \rightarrow \tau^+\tau^-$ for signal and dijet events for background. In order to distinguish tau candidates from jets, a set of discriminating variables based on the shower in the calorimeter, the number of associated tracks and the displaced tau-lepton-decay vertex is used.

Figure 4.14 shows the jet BDT score distribution, for one and three tracks $\tau_{had-vis}$ candidates, i.e. neutral and charged hadrons stemming from the tau-lepton decay that make up the visible part of the tau lepton.

The performance of online and offline tau identification are measured using a tag-and-probe method applied to events enriched in the $Z \rightarrow \tau^+\tau^-$ process, with one tau lepton decaying to muon and neutrinos, τ_μ (tag), and the other decaying to hadrons and neutrino, τ_{had} (probe). Three working points are provided: Loose, Medium and Tight; they correspond to different tau identification efficiency values, with the efficiency designed to be independent of p_T .

4.6 Missing transverse momentum

Momentum conservation in the plane transverse to the beam axis ($x - y$) implies that the vector sum of the transverse momenta of all particles in the final state should be zero. An imbalance in the sum of the transverse momenta, known as missing transverse momentum E_T^{miss} , indicates the presence of undetectable particles like SM neutrinos but also new particles that do not interact with the detector materials such as particles included in BSM models.

The reconstruction of the E_T^{miss} [120] in ATLAS is a challenge involving all detector sub-systems; the E_T^{miss} is characterised by two contributions:

1. a *hard term*, i.e. a contribution from the hard-event signals comprising fully reconstructed and calibrated particles and jets (hard objects); the reconstructed particles are electrons, photons, τ -leptons, and muons;
2. a *soft term*, i.e. a contribution from the soft-event signals consisting of reconstructed charged-particle tracks (soft signals) associated with the hard-scatter vertex but not associated with all reconstructed hard objects; the soft component can be estimated through two main algorithms, the Calorimeter Soft Term (CST) algorithm, accounting for both neutral and charged particles, and the Track Soft Term (TST) algorithm, where the missing transverse momentum is reconstructed entirely from tracks avoiding pile-up contamination.

Considering dedicated variables corresponding to specific objects, the full E_T^{miss} is built as the negative vectorial sum in the transverse plane of missing transverse momentum terms $E_T^{miss,p}$, with $p \in \{e, \gamma, \tau_{had}, \mu, \text{jet}\}$ reconstructed from the $p_T = (p_x, p_y)$ of particles and jets, and the corresponding soft term, $E_T^{miss,soft}$, from the soft-event signals [120]:

$$\mathbf{E}_T^{miss} = - \underbrace{\sum \mathbf{p}_T^e}_{E_T^{miss,e}} - \underbrace{\sum \mathbf{p}_T^\gamma}_{E_T^{miss,\gamma}} - \underbrace{\sum \mathbf{p}_T^{\tau_{had}}}_{E_T^{miss,\tau_{had}}} - \underbrace{\sum \mathbf{p}_T^\mu}_{E_T^{miss,\mu}} - \underbrace{\sum \mathbf{p}_T^{track}}_{E_T^{miss,soft}}. \quad (4.6)$$

hard term soft term

The E_T^{miss} reconstruction performance is assessed by comparing a set of reconstructed E_T^{miss} -related observables in data and MC simulations for the same final-state selection, with the same object and event selections applied. Systematic uncertainties in the E_T^{miss}

response and resolution are derived from these comparisons and are used to quantify the level of understanding of the data from the physics models [120]. The performances of E_T^{miss} reconstruction may be quantified by the observed width of the E_T^{miss} distribution, an example of which is shown in Figure 4.15 for the soft term exploiting a TST algorithm for the complete Run 2 dataset, 2015-2018.

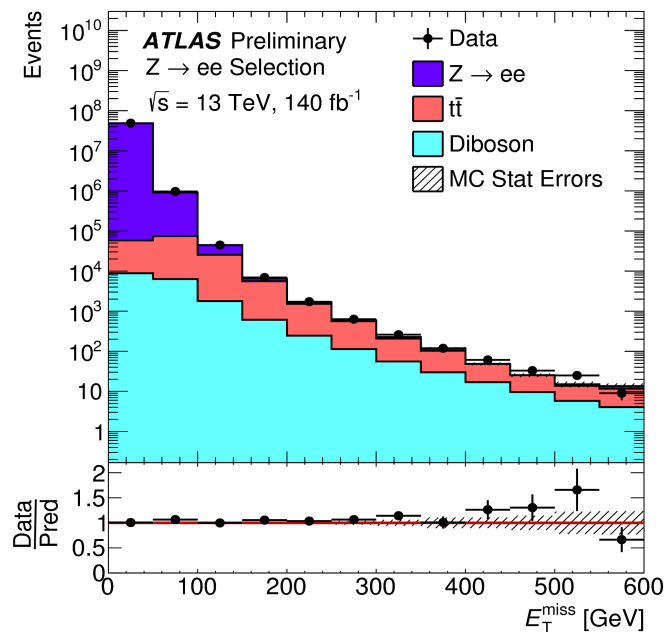


Figure 4.15: The TST E_T^{miss} distribution is shown for the complete dataset, 2015–2018, with an integrated luminosity of 140 fb^{-1} , and it is compared to Monte Carlo simulation. A $Z \rightarrow e^+e^-$ selection has been applied to the data. The tight E_T^{miss} working point is used: this requires that jets have transverse momentum (p_T) greater than 30 GeV and $|\eta| > 2.5$. The E_T^{miss} distribution is shown for data and compared to simulation which is broken up in the contribution from each physics process [121]

Chapter 5

Statistical Treatment

This chapter is dedicated to a brief description of the profile-likelihood technique (Section 5.1) together with all the statistical ingredients, like the definition of the sensitivity and of the p -value (Section 5.2), of the asymptotic limit and Asimov dataset (Section 5.3) and of the confidence intervals (Section 5.4), necessary to extract the results reported in Chapters 7, 8 and 9.

5.1 Profile-likelihood technique

The outcome of an experiment can be modelled as a set of random variables, $\mathbf{x} = x_1, \dots, x_n$, whose distribution takes into account the intrinsic physics randomness (theory) and the detector effects (like resolution, efficiency, etc.), also called statistical and systematic uncertainties. Theory and detector effects can be described according to some auxiliary parameters, $\boldsymbol{\theta} = \theta_1, \dots, \theta_m$, whose values are, in most of the cases, unknown and have to be fitted to data.

The overall Probability Density Function (PDF), evaluated for the parameters of interest (POI) and including the uncertainties which enter as nuisance parameters (NP), is called likelihood function; the global likelihood function is obtained as the product of the likelihoods of the input analyses. If a sample consisting of N independent measurements, typically each corresponding to a collision event, is considered, the likelihood function can be written as [122]:

$$L(\mathbf{x}, \boldsymbol{\theta}(x)) = \prod_{i=1}^N f(x_1^i, \dots, x_n^i; \boldsymbol{\theta}) \quad (5.1)$$

where the number of events N is treated as fixed.

Usually it is convenient to use $-\ln L$ or $-2 \ln L$ rather than L in numerical calculations and computations because of the properties of the logarithms.

In event-counting experiments, the actual number of observed events N is a quantity of interest and the probability of observing them depends on the $\boldsymbol{\theta}$ parameters. Thus, if N follows a Poisson distribution with mean m and all the \mathbf{x} values follow $f(\mathbf{x}; \boldsymbol{\theta})$ the likelihood function becomes an “extended” likelihood:

$$L(\mathbf{x}, \boldsymbol{\theta}) = \frac{m^N}{N!} e^{-m} \prod_{i=1}^N f(x_1^i, \dots, x_n^i; \boldsymbol{\theta}). \quad (5.2)$$

For a Poissonian process that is given by the sum of a signal plus a background process, summing over all the NPs (r) the extended likelihood function may be written as:

$$L(\mathbf{x}; s, b, \boldsymbol{\theta}) = \frac{e^{-(s+b)}}{N!} \prod_{i=1}^N (sP_s(x_i; \boldsymbol{\theta}) + bP_b(x_i; \boldsymbol{\theta})) \times \prod_{j=1}^r \rho_j(\theta_j) \quad (5.3)$$

where:

- s and b are the signal and background expected yields;
- P_s and P_b are the PDFs of the variable x for signal and background, respectively;
- $\rho_j(\theta_j)$ represents the functional distributions assumed for the nuisance parameters.

The NPs describe the systematic uncertainties that can affect the normalisation of the samples, the shape of the final discriminants or both normalisation and shape. Two different types of nuisance parameters are usually considered: unconstrained normalisation factors determined only from data and parameters associated to systematics that have external constraints and use information from auxiliary measurements, like experimental and modelling uncertainties. In the case of gaussian distributed systematics, like for experimental systematic uncertainties, $\rho(\theta) = e^{-(\vartheta-\theta)^2/2}/\sqrt{2\pi}$, where ϑ represents the central value of the measurement and θ the associated nuisance parameter for a given systematic uncertainty. For normalisation systematic uncertainties, where the θ parameter can only assume positive values and cannot be well described by a Gaussian distribution, a log-normal distribution is adopted, $\rho(\theta) = (1 + \epsilon)^\theta$, being ϵ the value of the uncertainty in question [123]. Finally, in order to describe systematic uncertainties associated to finite Montecarlo-sample size or to the number of observed events in a data control sample, a gamma distribution is adopted.

The correlation between nuisance parameters is implemented in the fit by associating the systematic uncertainties to the same nuisance parameter in the global likelihood.

Usually, the strengths of the signal process, $\boldsymbol{\mu}$, are introduced as the vector of parameters of interest of the model, while in the case of the analyses presented in this dissertation, being the signal strengths parameterised in terms of the rescaling of the Higgs self-coupling, κ_λ , or in terms of the coupling modifiers to the Higgs boson, identified by a generic κ , the substitution $\boldsymbol{\mu} \rightarrow \boldsymbol{\kappa}$ is made. When the likelihood function depends on many parameters, the achievable constraints on $\boldsymbol{\kappa}$ might be weak so that the true values of both the POIs and of the NPs can't be estimated; the main aim of the fit procedure is never determining the true values of $\boldsymbol{\theta}$, but rather obtaining tight intervals for $\boldsymbol{\kappa}$. To this end, the profile likelihood ratio is considered as test statistic:

$$q_\kappa = -2 \ln \lambda(\boldsymbol{\kappa}) = -2 \ln \left(\frac{L(\boldsymbol{\kappa}, \hat{\boldsymbol{\theta}})}{L(\hat{\boldsymbol{\kappa}}, \hat{\boldsymbol{\theta}})} \right) \quad (5.4)$$

where:

- $\hat{\boldsymbol{\theta}}$ denotes the value of $\boldsymbol{\theta}$ that maximises L for the specified $\boldsymbol{\kappa}$, i.e. it is the conditional Maximum-Likelihood (ML) estimator of $\boldsymbol{\theta}$;
- $\hat{\boldsymbol{\kappa}}$ and $\hat{\boldsymbol{\theta}}$ are the vectors of ML estimator of the unconditional likelihood.

The maximum-likelihood method takes as best-fit values of the unknown parameter the values that maximise the likelihood function. The choice of the POIs depends on the tested model under consideration, while the remaining parameters are “profiled”, i.e. they are set to the values that maximise the likelihood function.

The maximisation of the likelihood function can be performed analytically only in the simplest cases, while a numerical study of the likelihood in the θ parameter space is needed in most of the realistic case to localise the $\hat{\theta}$ point that minimises $-2\ln L$; this procedure is called a Maximum-Likelihood fit. MINUIT [124] is historically the most widely used minimisation software engine in High Energy Physics. It is conceived as a tool to find the minimum value of a multi-parameter function and analyse the shape of the function around the minimum. Minuit mainly works on χ^2 or log-likelihood functions, to compute the best-fit-parameter values and uncertainties, including correlations between the parameters. One of the most important Minuit program that has been widely exploited to provide the results reported in this thesis, is the Minuit processor MINOS that can calculate parameter errors taking into account both parameter correlations and non-linearities, thus leading, in general, to asymmetric error intervals, as shown in the example of Figure 5.1.

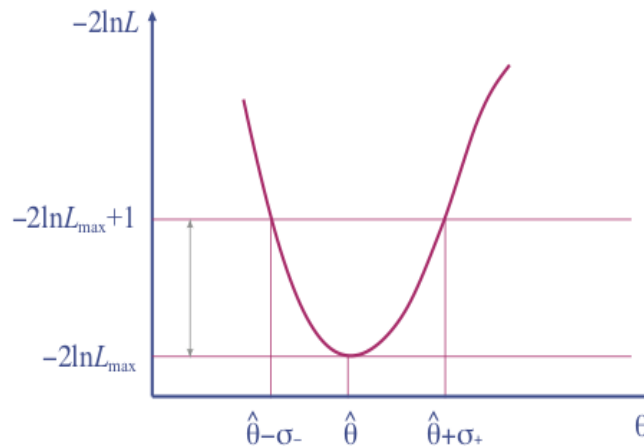


Figure 5.1: Scan of $-2\ln L$ in order to determine asymmetric 1σ errors [122].

5.2 Sensitivity and p – value

In order to discover a new process, the statistical significance of an observation can be quantified by evaluating the compatibility of the observed data with a given hypothesis H ; testing different hypotheses has the target of answering to the question whether some observed data sample is more compatible with one theory model or with an alternative one. The level of agreement of the observed data with a given hypothesis H is quantified by computing a p – value:

$$p_H = \int_{q_{obs}}^{\infty} f(q|H)dq \quad (5.5)$$

where q_{obs} is the observed value in data of the test statistic q and $f(q|H)$ represents the PDF of q under the assumption of the H hypothesis.

In particle physics usually two hypotheses are considered:

1. the null hypothesis, H_0 , describing only known processes, and designated as background ($\mu = 0$);
2. the alternative hypothesis H_1 , which includes both background and signal ($\mu = 1$).

Therefore, exploiting the definitions of these two hypotheses, the p – value is the probability, assuming H_0 to be true, of getting a value of the test statistic as result of the test at least as extreme as the observed test statistic; the significance level, denoted α , is the probability, assuming H_0 to be true, of rejecting H_0 ; an hypothesis can be rejected if its p – value is observed below a specific threshold, i.e. $p < \alpha$. Another quantity, related to the p – value, that is used to exclude/confirm a signal/background hypothesis, is the equivalent significance, Z . It is defined as the number of normal Gaussian standard deviations (σ) above which the mean of the Gaussian has an upper-tail probability equal to p [125]:

$$Z = \Phi^{-1}(1 - p) \quad (5.6)$$

where Φ^{-1} is the quantile (inverse of the cumulative distribution) of the standard Gaussian. As a convention, in the particle physics community, a threshold α of 0.05 for the p – value, which corresponds to $Z = 1.64$, is used to exclude a signal hypothesis, while the discovery threshold corresponds to $Z = 5$, i.e. p – value= 2.87×10^{-7} . Figure 5.2 shows how the significance is related to the p – value.

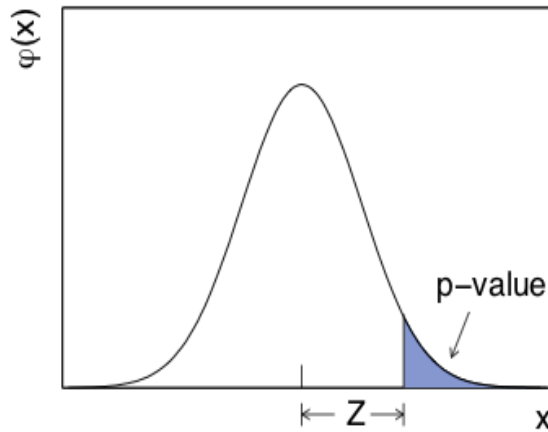


Figure 5.2: The standard normal distribution $\phi(x) = 1/\sqrt{2\pi}e^{-x^2/2}$ showing the relation between the significance Z and the p – value [125].

In the case where a little or no sensitivity occurs to some models, the CL_s technique [126] is used as the standard technique to set exclusion limits; the CL_s is defined as:

$$CL_s = \frac{p_\mu}{1 - p_b} \quad (5.7)$$

where p_b is the p – value for the background-only hypothesis and p_μ is the p – value for the signal plus background hypothesis. In the usual formulation of the method, these two quantities are computed using the same test statistic q_μ , and the definition of CL_s above assumes this statistic is continuous [127]. A point in a model’s parameter space is regarded as excluded if one finds $CL_s \leq \alpha$: for example, if the CL_s is below 5%, a hypothesis is excluded at 95% CL. Results can be presented providing confidence intervals, that are constructed so as to cover the true value of a parameter with a specified probability; how these intervals are constructed is reported in Section 5.4.

5.3 Asymptotic limit and Asimov Dataset

In the limit of large statistics, thanks to Wilks’ theorem [128] and Wald’s asymptotic approximation [129], the test statistic can be approximated as:

$$-2 \ln \lambda(\kappa) = \frac{(\kappa - \hat{\kappa})^2}{\sigma^2} + \mathcal{O}(1/\sqrt{N}) \quad (5.8)$$

where $\hat{\kappa}$ is distributed according to a Gaussian with average κ' and standard deviation σ and N represents the data sample size. The standard deviation is obtained from the covariance matrix of the estimators for all the parameters, $V_{ij} = \text{cov}[\hat{\theta}_i, \hat{\theta}_j]$, where here the θ_i represent both the parameter of interest, κ , as well as the nuisance parameters. In the asymptotic approximation, the covariance matrix is given by:

$$V_{ij}^{-1} = \left\langle \frac{\partial^2 \ln L}{\partial \theta_i \partial \theta_j} \right\rangle_{\kappa=\kappa'} \quad (5.9)$$

where κ' is assumed as the value of the κ parameter.

When several parameters of interest are considered and can be identified with a subset of the parameters $\boldsymbol{\theta}_n = (\theta_1, \dots, \theta_n)$, the test statistics can be generalised as [125]:

$$-2 \ln \lambda(\boldsymbol{\kappa}) = \sum_{i,j=1}^n (\theta_i - \theta'_i) \tilde{V}_{ij}^{-1} (\theta_j - \theta'_j) + \mathcal{O}(1/\sqrt{N}) \quad (5.10)$$

where \tilde{V}_{ij}^{-1} is the inverse of the submatrix obtained restricting to the parameters of interest the full covariance matrix defined in Equation 5.9. Thus $-2 \ln \Lambda(\boldsymbol{\kappa}, \boldsymbol{\theta})$ is approximately distributed as a χ^2 variable with n degrees of freedom, where n equals the number of parameters of interest in the model, i.e. the dimensionality of the vector $\boldsymbol{\kappa}$.

Asymptotic approximation can be written in terms of an Asimov dataset [125] that is a dataset obtained by replacing all observable (random) variables with their expected values.

5.4 Neyman’s confidence intervals

A procedure to determine frequentist confidence intervals, constructed to include the true value of the parameter/parameters of interest with a probability greater than or equal to a specified level, has been elaborated by Neyman [130] and it is described in the following lines [122]:

1. first of all a scan of the allowed range of the unknown parameter of interest κ has to be made;
2. given a value κ_0 of κ , the interval $[x_1(\kappa_0), x_2(\kappa_0)]$ that contains x with a probability $1-\alpha$ (confidence level, or CL) equal to 68.3% (or 90%, 95%) is computed; if x is discrete, the integral is replaced by the corresponding sum;
3. finally the confidence interval obtained for x has to be inverted in order to find the corresponding interval $[\kappa_1(x), \kappa_2(x)]$.

By construction, a fraction of the experiments equal to $1-\alpha$ will measure x such that the corresponding confidence interval $[\kappa_1(x), \kappa_2(x)]$ contains the true value of κ , i.e.:

$$1 - \alpha = P(x_1(\kappa) < x < x_2(\kappa)) = P(\kappa_2(x) < \kappa < \kappa_1(x)). \quad (5.11)$$

If a Gaussian distribution with known parameter $\sigma=1$ is considered, the inversion gives a central value $\hat{\kappa} = x$ and a confidence interval $[\kappa_1, \kappa_2] = [x - \sigma, x + \sigma]$. The result can be quoted as $\kappa = x \pm \sigma$.

An equivalent method of constructing confidence intervals consists in considering a test statistics, like the profile likelihood ratio q_κ . All values of κ , where the hypothesis would be rejected at a significance level less than α , are excluded; thus, the confidence interval is given by the interval $[\kappa_1, \kappa_2]$ for which all κ satisfy $q_\kappa < \lambda_\alpha$, where α denotes the confidence level and λ_α is computed from a χ^2 distribution with one degree of freedom. The values of λ_α for different confidence levels are reported in Reference [127]. As an example, for a confidence interval at 95% CL, considering one degree of freedom, λ_α is $\lambda_{0.95} = 1.92$. The 95% CL intervals, used to extract the results of this dissertation, are identified requiring $-2 \ln L < 3.84$, when one parameter of interest is considered.

The likelihood function can be easily written in terms of a vector of parameters of interest, thus the concept of confidence interval can be extended to the one of confidence regions, built through a scan of the phase space defined by the n parameters of interest and assuming a χ^2 distribution with n degrees of freedom.

The results presented in Chapters 7, 8 and 9, are based on the statistical tools described in this chapter, particularly on the profile-likelihood evaluation; 68% as well as 95% CL intervals are given in the asymptotic approximation [125].

Chapter 6

Probing the Higgs self-coupling

This chapter describes the theoretical models on the basis of which the results of the following chapters have been produced. Section 6.1 summarises how the trilinear Higgs self-coupling enters in double-Higgs processes and how the dependence on the Higgs self-coupling and top Yukawa coupling can be implemented in double-Higgs observables. Section 6.2 reports projections of κ_λ constraints coming from double-Higgs measurements and considering a luminosity of 3000 fb^{-1} . Section 6.3 describes a complementary approach in order to extract limits on the Higgs self-coupling exploiting Next-to-Leading-Order (NLO) EW corrections to single-Higgs production and decay processes; the parameterisations used to produce the results of this thesis are reported. Finally, Section 6.4 reports projections of κ_λ constraints coming from single-Higgs measurements and considering a luminosity of 300 and 3000 fb^{-1} .

6.1 Higgs self-coupling through direct Higgs-boson pair searches

Double-Higgs processes are directly sensitive to the trilinear Higgs self-coupling at the lowest order in electroweak expansion, like it is shown in the diagram (c) of Figure 6.1; in the SM, the ggF double-Higgs production process, that is mediated by top quark loops with a negligible contribution from bottom quark loops and is the only double-Higgs production process studied in this thesis, accounts for more than 90% of the total production cross section, while the second-largest production mechanism is vector-boson fusion $qq \rightarrow HHqq$. Due to the fact that the VBF double-Higgs cross section is an order of magnitude smaller than the ggF one and has a less sensitive topology, the VBF contribution to the estimation of the self-coupling is negligible [30].

The gluon-fusion mechanism proceeds via two amplitudes, \mathcal{A}_1 , proportional to the square of the Higgs coupling to the top quark, y_t , and represented by the diagrams (a) and (b) of Figure 6.1, and \mathcal{A}_2 , proportional to the product of the Higgs coupling to the top quark and the Higgs self-coupling, and represented by the diagram (c) of Figure 6.1.

In the SM, the interference between these two amplitudes is destructive and yields an overall cross-section value which is $\sim 10^3$ times smaller than the corresponding ggF single-Higgs production, i.e. 31.05 fb , according to recent calculations [31]. This cross section can be enhanced in the case of BSM physics modifying the relative sign of the amplitudes \mathcal{A}_1

and \mathcal{A}_2 , and increasing their contributions through modifications of the aforementioned couplings.

For BSM scenarios affecting y_t and λ_{HHH} , defining the coupling modifier to the top quark as $\kappa_t = y_t^{BSM}/y_t^{SM}$ and to the Higgs self-coupling as $\kappa_\lambda = \lambda_{HHH}^{BSM}/\lambda_{HHH}^{SM}$, the total amplitude can be written as:

$$\mathcal{A}(\kappa_t, \kappa_\lambda) = \kappa_t^2 \mathcal{A}_1 + \kappa_t \kappa_\lambda \mathcal{A}_2. \quad (6.1)$$

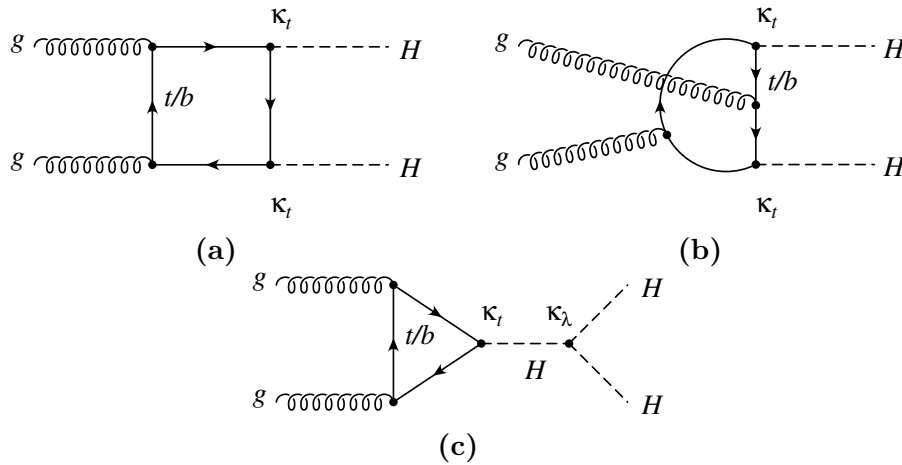


Figure 6.1: Examples of leading-order Feynman diagrams for double-Higgs ggF production.

Higher order QCD corrections do not add further $t\bar{t}H$ or HHH vertices to the diagrams shown in Figure 6.1, implying that Equation 6.1 is applicable to any order in QCD (i.e. also when the amplitudes \mathcal{A}_1 and \mathcal{A}_2 are modified to include their higher order QCD corrections) [132].

From Equation 6.1, after integrating over the final-state phase space and over the PDFs, the ggF double-Higgs cross section $\sigma_{ggF}(pp \rightarrow HH)$ can be written in terms of κ_λ and κ_t as:

$$\sigma_{ggF}(pp \rightarrow HH) \propto \int \kappa_t^4 \left[|\mathcal{A}_1|^2 + 2 \left(\frac{\kappa_\lambda}{\kappa_t} \right) \Re(\mathcal{A}_1^* \mathcal{A}_2) + \left(\frac{\kappa_\lambda}{\kappa_t} \right)^2 |\mathcal{A}_2|^2 \right]. \quad (6.2)$$

Expression 6.2 makes clear that the kinematic distributions and, consequently, the signal acceptance, depend only on κ_λ/κ_t , while the κ_t^4 factor affects only the total cross section. The effects of κ_b are negligible.

Assuming that new physics affects only the Higgs-boson self-coupling, the differential and inclusive ggF $pp \rightarrow HH$ cross section can be expressed as a second degree polynomial in κ_λ , i.e. [34]:

$$\frac{d\sigma}{d\Phi} = A + B\kappa_\lambda + C\kappa_\lambda^2 \quad (6.3)$$

being $d\Phi$ the infinitesimal phase-space volume. In a first approach, this feature can be used to simulate MC samples for any values of κ_λ combining three samples generated for three different values of κ_λ ; the procedure consists in solving the system of three equations depending on the value of κ_λ , computing the dependence of the coefficients A , B , C from the differential cross section in a given phase space volume, and inverting the matrix

above to obtain the coefficients reported in Reference [34]. As a natural choice $\kappa_\lambda = 0, 1$ are chosen, corresponding to the box-only and the SM cases, while the third value can be chosen close to the expected exclusion region, in order to optimise the signal generation. For the analyses reported in this dissertation, this corresponds to $\kappa_\lambda = 20$.

Furthermore, the three samples need to be properly normalised to the best cross-section computations, as the ones shown in Figure 6.2 [34]: leading order (LO); next-to-next-to-leading order (NNLO)+ next-to-next-to-leading-logarithmic (NNLL) SM cross section obtained in the limit of heavy top quarks rescaled with the NNLO+NNLL SM cross section obtained including finite top quark mass NLO contribution and NNLO corrections in the limit of heavy top quarks; finite top quark mass NLO for all κ_λ values rescaled with the NNLO SM cross section obtained with the FTApprox method (partial finite top quark mass).

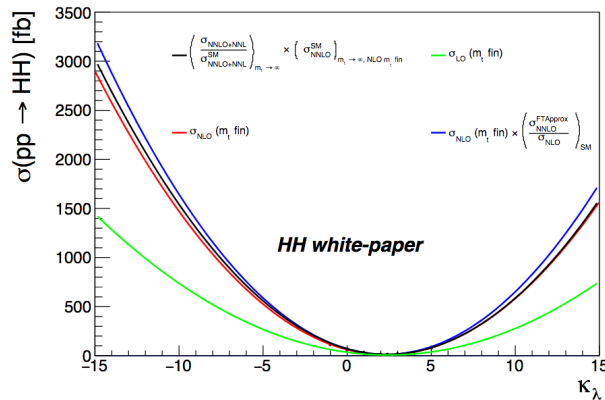


Figure 6.2: Double-Higgs ggF production cross section as a function of κ_λ including different cross-section computations [34].

Figure 6.3 shows the dependence of the ggF $pp \rightarrow HH$ cross section on κ_λ setting $\kappa_t = 1$ (a) and on κ_t setting $\kappa_\lambda = 1$ (b), given by a second order and a fourth order polynomial, respectively; the cross section as a minimum at $\kappa_\lambda/\kappa_t = 2.4$, i.e. where the maximal destructive interference between the two diagrams occurs.

6.2 HL-LHC projections for double-Higgs processes

The High Luminosity (HL)-LHC has the target of studying rare processes like double-Higgs production and achieving precision measurements of observables like the trilinear Higgs self-coupling, further pushing the LHC machine beyond its limits mainly through detector upgrades; the final goal would be to achieve a total integrated luminosity of 3000/4000 fb^{-1} at a centre-of-mass energy of 14 TeV. Prospects for the measurement of the trilinear Higgs self-coupling have been studied and reported in Reference [131].

The HL-LHC is expected to be a Higgs-boson factory, producing more than 10^5 double-Higgs pairs per experiment (ATLAS and CMS).

Thus, a significant improvement of current limits on κ_λ is expected together with an expected precision at the level of 50% on κ_λ at 68% CL. A combination between ATLAS and CMS projections has been made exploiting an Asimov dataset generated under the

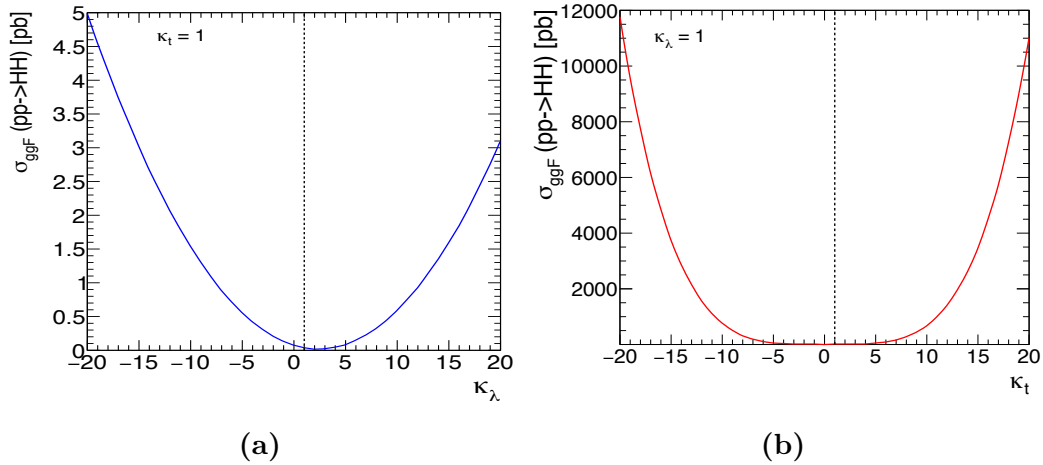


Figure 6.3: Double-Higgs ggF $pp \rightarrow HH$ cross section as a function of κ_λ setting $\kappa_t = 1$ (a) and as a function of κ_t setting $\kappa_\lambda = 1$; the vertical dashed lines represent the SM case, i.e. $\kappa_\lambda = 1$ (a) and $\kappa_t = 1$ (b).

SM hypothesis for a luminosity of 3000 fb^{-1} at $\sqrt{s} = 14 \text{ TeV}$, and using the following channels:

- CMS: $b\bar{b}b\bar{b}$, $b\bar{b}W^+W^-$, $b\bar{b}\tau^+\tau^-$, $b\bar{b}\gamma\gamma$ and $b\bar{b}ZZ$;
- ATLAS: $b\bar{b}b\bar{b}$, $b\bar{b}\tau^+\tau^-$ and $b\bar{b}\gamma\gamma$.

The channels are treated as uncorrelated, in particular because the systematic uncertainties, such as the theory uncertainties and the luminosity uncertainty, have little impact on the individual results. The combined minimum negative-log-likelihoods are shown in Figure 6.4.

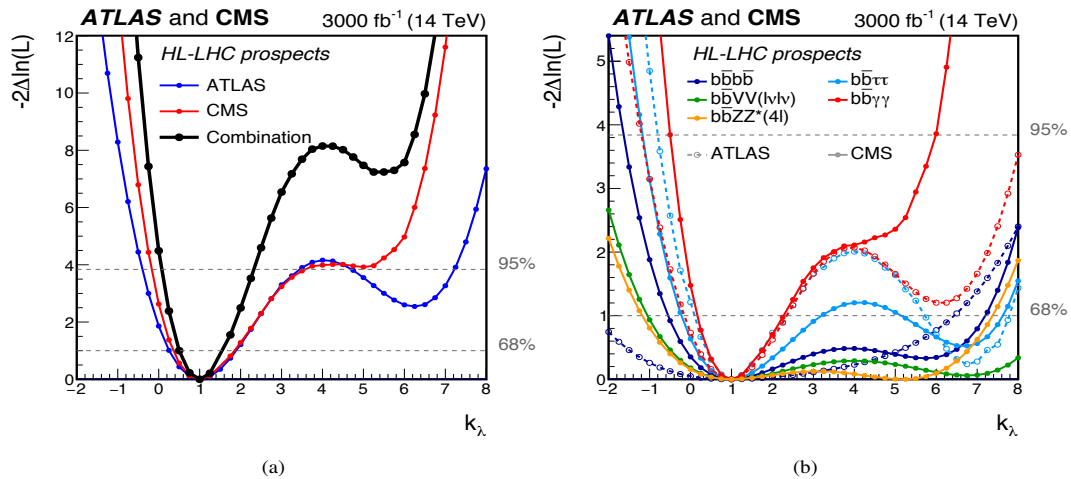


Figure 6.4: Value of $-2\ln\Lambda(\kappa_\lambda)$ as a function of κ_λ for an Asimov dataset generated under the SM hypothesis for a luminosity of 3000 fb^{-1} at $\sqrt{s} = 14 \text{ TeV}$; (a) black solid line: combined ATLAS and CMS results; blue and red solid lines: ATLAS and CMS standalone results, respectively; (b) the different colours correspond to the different channels, the solid lines correspond to the CMS results while the dashed lines correspond to the ATLAS results [131].

The 68% CL intervals for κ_λ are $0.52 \leq \kappa_\lambda \leq 1.5$ and $0.57 \leq \kappa_\lambda \leq 1.5$ with and without systematic uncertainties respectively. The second minimum of the likelihood is excluded at 99.4% CL [131].

6.3 Higgs self-coupling through loop corrections of single-Higgs production and decay modes

An alternative and complementary approach to constrain the Higgs-boson self-coupling has been proposed in References [55, 133], exploiting the fact that single-Higgs processes are sensitive to λ_{HHH} at NLO in electroweak interactions via weak loops, while they depend on the couplings of the Higgs boson to the other particles of the SM at leading order; thus, it is possible to constrain κ_λ through precise measurements of single-Higgs observables. The effect of new physics at the weak scale are parameterised via a single parameter κ_λ , i.e. the rescaling of the SM trilinear coupling, λ_{HHH}^{SM} . Thereby, the H^3 interaction in the potential, where H is the physical Higgs field, is given by [55]:

$$V_{H^3} = \lambda_{HHH} \nu H^3 = \kappa_\lambda \lambda_{HHH}^{SM} \nu H^3 \quad , \quad \lambda_{HHH}^{SM} = \frac{G_\mu}{\sqrt{2}} m_H^2 .$$

All the calculations reported in this chapter are based on the assumption that new physics affects only the Higgs self-coupling or modifies in a negligible way the other Higgs couplings. The NLO κ_λ -dependent corrections can be divided in two different contributions:

- a universal part, the C_2 coefficient, i.e. common to all processes, quadratically dependent on λ_{HHH} , which originates from the diagram in the wave function renormalisation constant of the external Higgs field, whose Feynman diagram is shown in Figure 6.5;
- a process- and kinematic-dependent part, the C_1 coefficients, linearly proportional to λ_{HHH} , which is different for each process and kinematics; for each observable, the corresponding C_1 coefficient is identified as the contribution linearly proportional to λ_{HHH}^{SM} in the NLO EW corrections and normalised to the LO result as evaluated in the SM. Figures 6.6 and 6.7 show examples of λ_{HHH} -dependent diagrams for the Higgs-boson production as well as for decay modes.

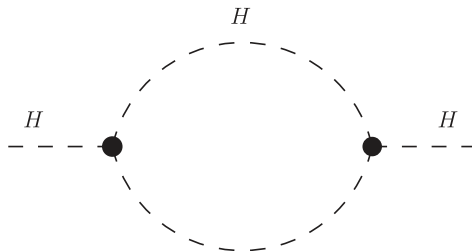


Figure 6.5: One-loop λ_{HHH} -dependent diagram in the Higgs self-energy [55].

The range of validity of these perturbative calculations is taken as $|\kappa_\lambda| < 20$, assumed in order to neglect $\mathcal{O}(\kappa_\lambda^3 \alpha^2)$ terms [55].

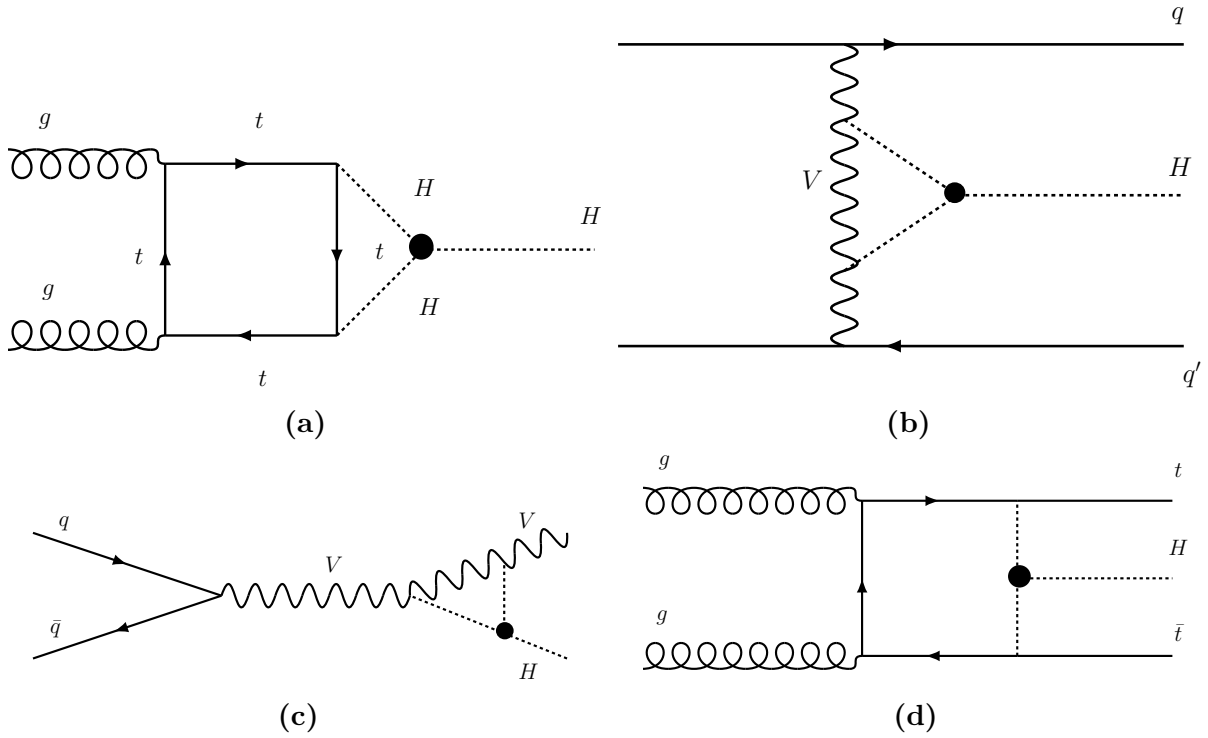


Figure 6.6: Diagrams contributing to the C_1 coefficients in the different Higgs-boson production modes, ggF (a), VBF (b), VH (c) and $t\bar{t}H$ (d) [55].

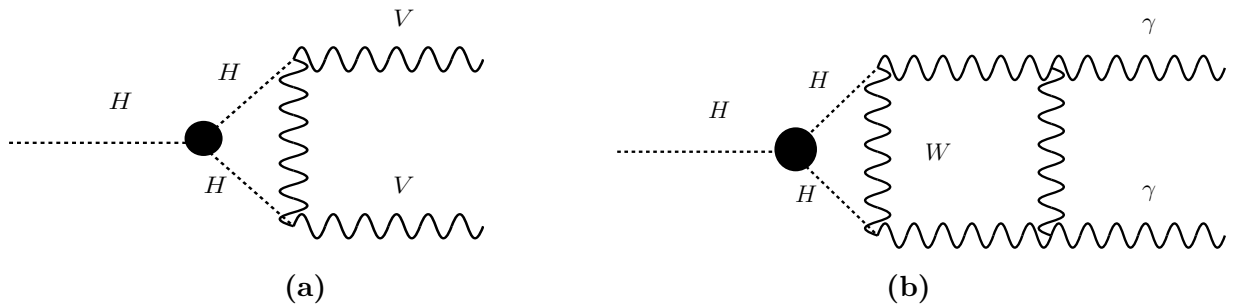


Figure 6.7: Examples of diagrams contributing to the C_1 coefficients in decay modes: $H \rightarrow VV$ (a), and $H \rightarrow \gamma\gamma$ (b) [55].

In addition to the κ_λ -dependent corrections to single-Higgs processes, NLO EW corrections in the SM hypothesis (i.e. $\kappa_\lambda = 1$), have to be taken into account; they are introduced through the coefficients $K_{\text{EW}} = \sigma_{\text{NLO}}^{\text{SM}} / \sigma_{\text{LO}}^{\text{SM}}$. The C_1 and K_{EW} coefficients are decoupled because of the approach that has been followed in References [55, 133]: the assumption that QCD corrections factorise λ_{HHH} effects is reasonable while it is not true, in general, for NLO EW corrections.

Assuming on-shell single Higgs production, the signal strength, defined in Chapter 1, for the process $i \rightarrow H \rightarrow f$, where i and f are the initial and final states, respectively, can be expressed as:

$$\mu_i = 1 + \delta\sigma_{\lambda_{H^3}}(i), \quad \mu_f = 1 + \delta BR_{\lambda_{H^3}}(f) \quad (6.4)$$

where $\delta\sigma_{\lambda_{H^3}}(i)$ and $\delta BR_{\lambda_{H^3}}(f)$ are the deviations induced by an anomalous interaction, including the case of the trilinear Higgs self-coupling, to the production cross sections and branching fractions, respectively.

Specifically, the signal strengths for the initial state i , i.e. the production cross sections normalised to their SM expectations, can be written as:

$$\mu_i(\kappa_\lambda, \kappa_i) = \frac{\sigma^{\text{BSM}}}{\sigma^{\text{SM}}} = Z_H^{\text{BSM}}(\kappa_\lambda) \left[\kappa_i^2 + \frac{(\kappa_\lambda - 1)C_1^i}{K_{\text{EW}}^i} \right], \quad (6.5)$$

where $Z_H^{\text{BSM}}(\kappa_\lambda)$ is defined as:

$$Z_H^{\text{BSM}}(\kappa_\lambda) = \frac{1}{1 - (\kappa_\lambda^2 - 1)\delta Z_H} \quad \text{with} \quad \delta Z_H = -1.536 \times 10^{-3}, \quad (6.6)$$

K_{EW}^i accounts for the complete NLO EW corrections of the production cross section for the process i in the SM hypothesis, C_1^i is the coefficient that provides the sensitivity of the measurement to κ_λ for the i process and $\kappa_i^2 = \sigma_{\text{LO},i}^{\text{BSM}} / \sigma_{\text{LO},i}^{\text{SM}}(\kappa_\lambda = 1)$ represents multiplicative modifiers to other Higgs boson couplings, parameterised as in the LO κ -framework [42], taking into account additional BSM effects entering at LO; κ_i can be taken equal to one when variations of the Higgs self-coupling only are considered.

Indicating with f a Higgs-boson final state, the decay branching fractions, normalised to their SM expectations, are modified as:

$$\mu_f(\kappa_\lambda, \kappa_f) = \frac{\text{BR}_f^{\text{BSM}}}{\text{BR}_f^{\text{SM}}} = \frac{\kappa_f^2 + (\kappa_\lambda - 1)C_1^f}{\sum_j \text{BR}_j^{\text{SM}} \left[\kappa_j^2 + (\kappa_\lambda - 1)C_1^j \right]} \quad (6.7)$$

where \sum_j runs over all the Higgs boson decay channels, BR_j^{SM} is the Higgs-boson SM decay rate to the j final state, C_1^f is the coefficient that provides the sensitivity of the measurement to κ_λ for the f final state, κ_f is the branching fraction modifier for the f final state while κ_j is the branching fraction modifier for all the Higgs-boson j final states ($\kappa_j^2 = \text{BR}_{\text{LO},j}^{\text{BSM}} / \text{BR}_{\text{LO},j}^{\text{SM}}$), parameterised as in the LO κ -framework. The model under discussion, as shown in Equation 6.5 and Equation 6.7, does not allow for any new physics beyond that encoded in the aforementioned κ parameters.

The process-independent factor C_2 can range from $C_2 = -1.536 \cdot 10^{-3}$ for $\kappa_\lambda = 1$ up to $C_2 = -9.514 \cdot 10^{-4}$ for $\kappa_\lambda = \pm 20$.

The C_1 coefficients computed for different production and decay modes are reported in Tables 6.1 and 6.2; it has been verified that, in the case of $H \rightarrow b\bar{b}$, $C_1^f = 2.5 \times 10^{-5}$, so these coefficients have been set to zero for any $H \rightarrow f\bar{f}$ decay [55, 133].

Production mode	ggF	VBF	ZH	WH	$t\bar{t}H$
$C_1^i \times 100$	0.66	0.63	1.19	1.03	3.52
K_{EW}^i	1.049	0.932	0.947	0.93	1.014

Table 6.1: Values of C_1^i and K_{EW}^i coefficients for Higgs-boson production processes [55, 133].

decay mode	$H \rightarrow \gamma\gamma$	$H \rightarrow WW^*$	$H \rightarrow ZZ^*$	$H \rightarrow f\bar{f}$	$H \rightarrow gg$
$C_1^f \times 100$	0.49	0.73	0.82	0	0.66

Table 6.2: Values of C_1^f coefficients for different Higgs-boson decay modes [55, 133].

The κ_λ -dependent variations of the production cross sections and of the decay branching fractions are shown in Figure 6.8.

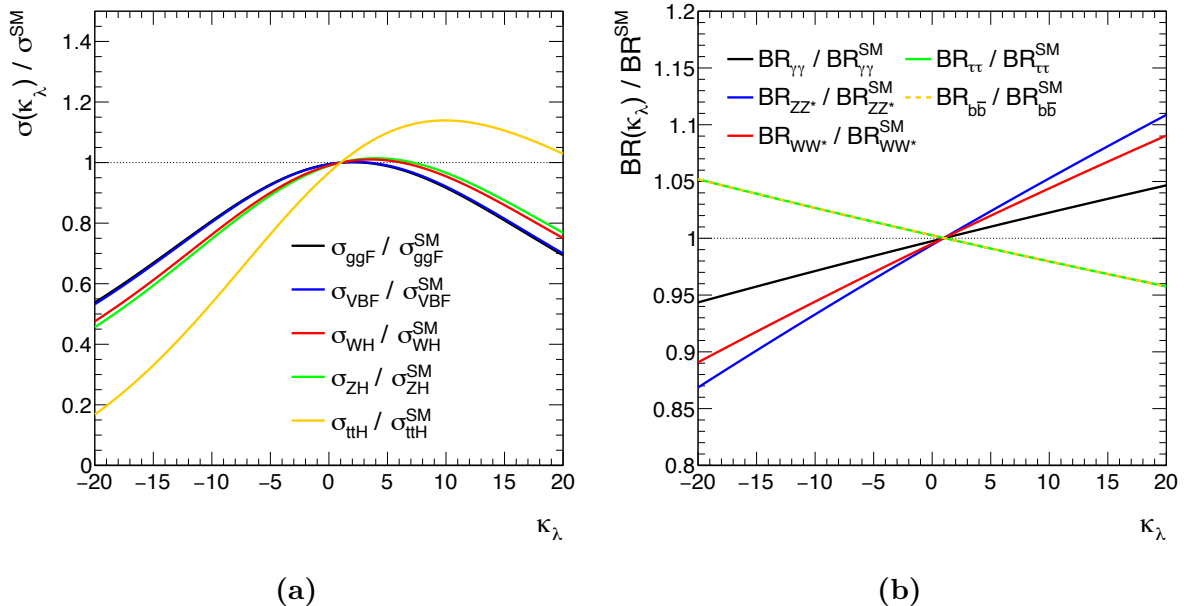


Figure 6.8: Variation of the cross sections (a) and branching fractions (b) as a function of the trilinear coupling modifier κ_λ [55, 133]; given the fact that the C_1^f coefficients are zero for all $H \rightarrow f\bar{f}$ decays, the $H \rightarrow \tau^+\tau^-$ (green solid line) and the $H \rightarrow b\bar{b}$ (yellow dashed line) lines are superimposed.

The $t\bar{t}H$ production mode represents the process receiving much larger corrections ($\sim 10\%$ at $\kappa_\lambda = 10$) with respect to the others, due to the fact that, being able to interact with another final-state particle, like WH and ZH production processes, it receives

a Sommerfeld enhancement in the non-relativistic regime [55]. The corrections to the branching fractions, shown in Figure 6.8 (b), reach a maximum value of $\sim 10\%$ in the ZZ^* decay channel and seem to be much smaller than the corrections to production modes considering the whole κ_λ validity interval; this effect comes from the linear dependence on κ_λ entering in these corrections and from the fact that there is a partial cancellation in the ratio, given the same sign of the C_1 coefficients. However, in the range close to the SM predictions where corrections are within 5% in absolute value for the production cross sections as it is shown in Figure 6.9, the decay modes are more sensitive to κ_λ than the production processes, apart from $t\bar{t}H$ production mode.

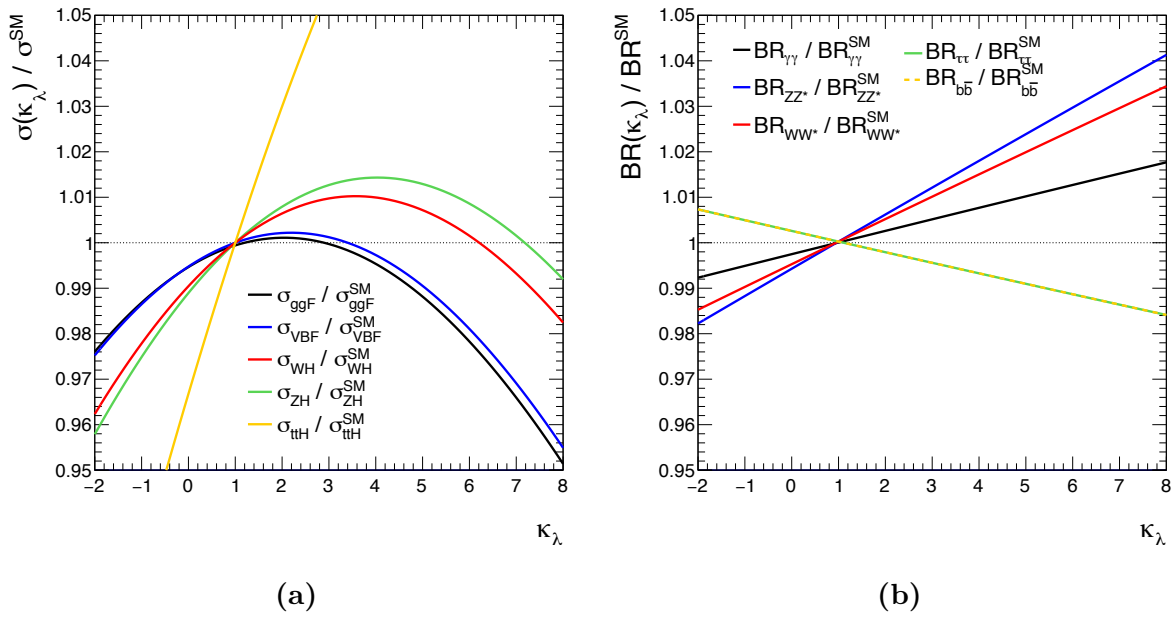


Figure 6.9: Variation of the cross sections (a) and branching fractions (b) as a function of the trilinear coupling modifier κ_λ zoomed in the range $-2 < \kappa_\lambda < 8$ [55, 133]; given the fact that the C_1 coefficients are zero for all fermion decays, the $H \rightarrow \tau^+\tau^-$ (green solid line) and the $H \rightarrow b\bar{b}$ (yellow dashed line) lines are superimposed.

Variations of the Higgs self-coupling affect not only the inclusive production modes and decay channels, but, being the C_1 coefficients kinematic-dependent, they modify also the kinematics of the event. The largest modifications in kinematic distributions are expected in the ZH , WH and $t\bar{t}H$ production modes, due to the interaction of the final-state vectors or the top quark with the Higgs boson.

Figure 6.10 shows the differential C_1 for WH (a) and ZH (b) production modes, considering the p_T^H distribution, i.e. the distribution of the transverse momentum of the Higgs boson. The shapes of the LO distributions are compared to the shapes of the contributions induced by C_1 [133]. C_1 coefficients at differential and inclusive level are also shown. The C_1 coefficients are enhanced for high- p_T^H regions where, however, the cross section is rather small.

No significant modifications are expected for what concerns the Higgs-boson decay kinematics; in fact, the angular distribution of the decay products, coming from the two bodies decay of the Higgs boson, is fully determined by momentum conservation laws and by the rotational symmetry of the decay, having the Higgs boson a null spin, and

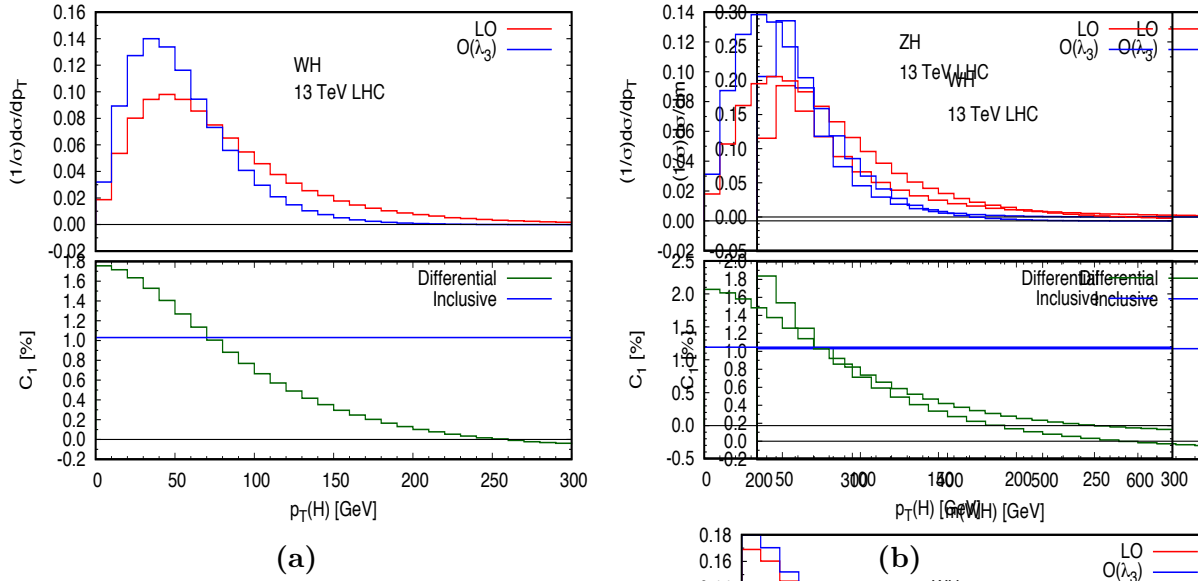


Figure 6.10: Effect of $\mathcal{O}(\lambda_{HHH})$ corrections to differential distributions (p_T^H) considering WH (a) and ZH (b) production modes at 13 TeV LHC. Upper panel: normalised distributions at LO (red) and at $\mathcal{O}(\lambda_{HHH})$ (blue). Lower panel: C_1 at the differential (green) and inclusive (blue) level [133].

cannot be affected by BSM effects. The only exception is represented by the decay to four fermions that is anyway characterised by an extremely small coupling of the Higgs boson to electrons and muons, thus leading to negligible differential κ_λ contributions, as shown in Figure 6.11 for leading (a) and subleading (b) opposite-sign same-flavour lepton pair invariant mass distributions in the $H \rightarrow e^+e^-\mu^+\mu^-$ decay channel.

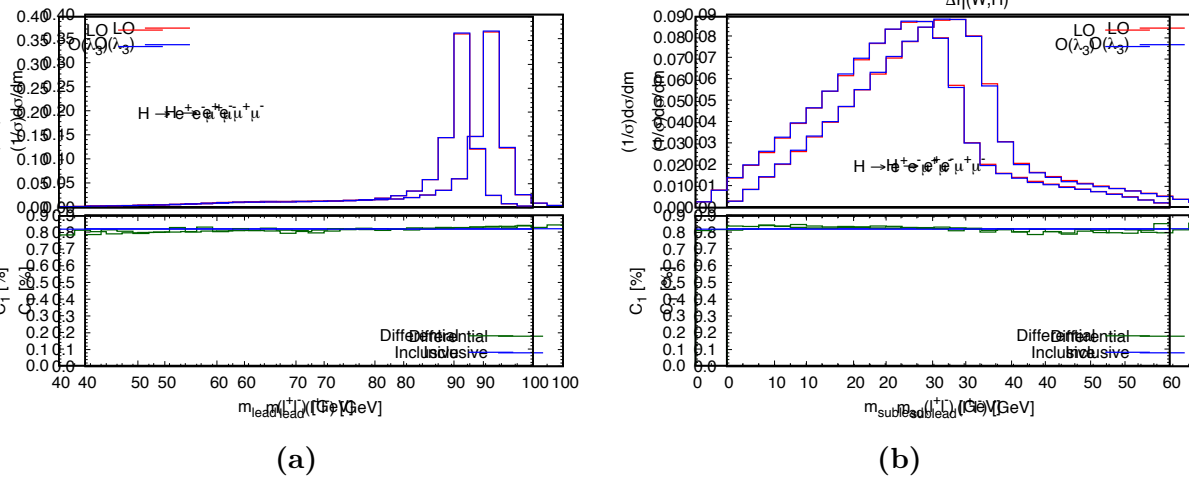


Figure 6.11: Leading (a) and subleading (b) opposite-sign same-flavour lepton pair invariant mass distributions in $H \rightarrow e^+e^-\mu^+\mu^-$. Upper panel: normalised LO (red) and $\mathcal{O}(\lambda_{HHH})$ (blue) distributions. Lower panel: C_1 for differential (green) and total decay width (blue) [133].

6.4 HL-LHC projections for single-Higgs processes

Projections for the measurement of the trilinear Higgs self-coupling at HL-LHC have been made considering NLO-EW corrections depending on κ_λ to single-Higgs processes; both the theoretical papers on the top of which the results of this thesis have been produced have performed these estimations, reported in detail in References [55, 133].

An estimation of the improvement in constraining κ_λ has been presented in Reference [55] exploiting projections of the CMS experiment at 300 fb^{-1} and 3000 fb^{-1} , using the uncertainties reported in Table 1 of Reference [134]; theoretical uncertainties are identical in the 3000 fb^{-1} and in the 300 fb^{-1} case, while experimental uncertainties are scaled with the square root of the ratio between the luminosities. The 1σ and 2σ intervals are identified assuming a χ^2 distribution. Figure 6.12 reports the χ^2 and p -value distributions as a function of κ_λ assuming that the central value of the measurements in every channel coincides with the predictions of the SM for “CMS-II” (300 fb^{-1}) and “CMS-HL-II” (3000 fb^{-1}); experimental and theoretical uncertainties are included. The constraints that can be obtained using 3000 fb^{-1} are [55]:

$$\kappa_\lambda^{1\sigma} = [-0.7, 4.2] \quad \text{and} \quad \kappa_\lambda^{2\sigma} = [-2.0, 6.8]$$

where $\kappa_\lambda^{1\sigma}$ and $\kappa_\lambda^{2\sigma}$ are the 1σ and 2σ intervals, respectively.

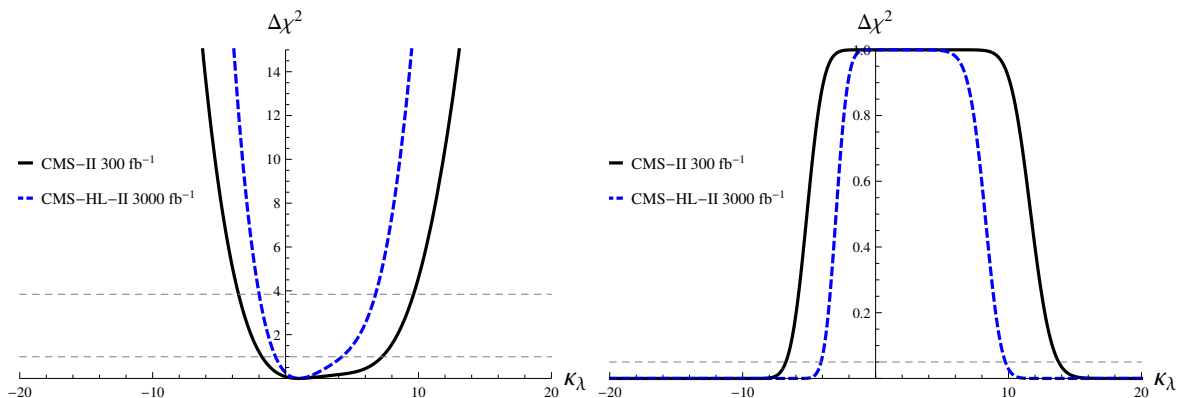


Figure 6.12: Left: $\chi^2(\kappa_\lambda)$ distribution as a function of κ_λ ; right: p -value distribution as a function of κ_λ for “CMS-II” (solid black line) and “CMS-HL-II” (blue dashed line) [55] where “CMS-II” (300 fb^{-1}) and “CMS-HL-II” (3000 fb^{-1}), are the scenarios presented in Table 1 of Reference [134].

A global fit to the likelihood function in order to extract κ_λ , based on the future projections of ATLAS-HL for single-Higgs production and decay at 14 TeV [135, 136], has been performed in Reference [133], assuming that the central value of the measurements in every channel coincides with the predictions of the SM. Two different scenarios concerning the uncertainties have been considered: in the first scenario (“Stat-only”), only the statistical uncertainty is included, describing an unrealistic scenario where theory and experimental systematic uncertainties are negligible; the second scenario (“Run 2 sys”), takes into account both theory and experimental systematic uncertainties. Differential information is included in the VH and $t\bar{t}H$ production modes, for both the C_1 and the

K_{EW} coefficients. The same future scenario at 14 TeV (ATLAS-HL) considered in Reference [137] is exploited. Figure 6.13 shows the likelihood distribution after combining all the production channels for Scenarios “Stat-only” (a) and “Run 2 sys” (b), under different assumptions: i) only κ_λ is anomalous, ii) κ_λ and κ_t or κ_λ and κ_V are anomalous, iii) all three parameters κ_λ , κ_t and κ_V are anomalous. Including additional degrees of freedom relaxes the limits in the region $\kappa_\lambda < 1$, even if they do not completely vanish, while the sensitivity to κ_λ in the region $\kappa_\lambda > 1$ is almost unaltered. On the contrary, the role of differential information may be relevant, critically depending on the assumptions on the future experimental and theoretical uncertainties [133].

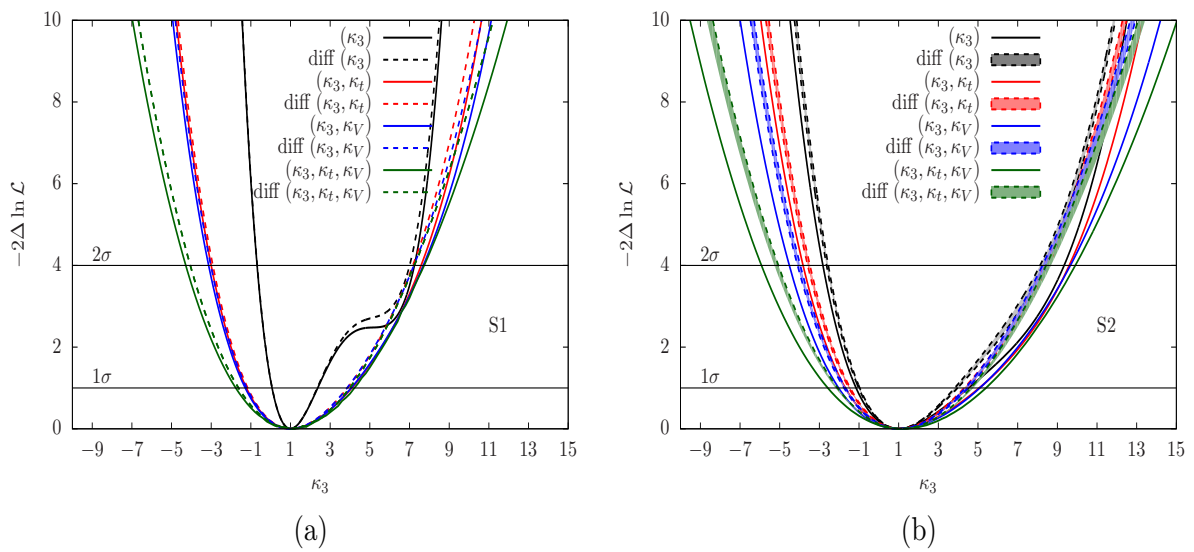


Figure 6.13: Value of $-2 \ln \Lambda(\kappa_\lambda)$ as a function of κ_λ for an Asimov dataset generated under the SM hypothesis considering a luminosity of 3000 fb^{-1} at $\sqrt{s} = 14 \text{ TeV}$. Two different scenarios are considered: only statistical uncertainty are considered (Stat-only=S1) (a), experimental systematic uncertainty and theory uncertainty included (Run 2 sys=S2) (b). Different fit configurations have been tested: κ_λ -only model (black line), κ_λ - κ_t model (red line), κ_λ - κ_V model (blu line) and κ_λ - κ_t - κ_V , (green line). All the coupling modifiers that are not included in the fit are set to their SM predictions. The dotted horizontal lines show the $-2 \ln \Lambda(\kappa_\lambda) = 1$ level that is used to define the $\pm 1\sigma$ uncertainty on κ_λ as well as the $-2 \ln \Lambda(\kappa_\lambda) = 4$ level used to define the $\pm 2\sigma$ uncertainty [133].

Finally, in order to give an indication of the power in constraining κ_λ coming from differential $t\bar{t}H$ measurements, a global likelihood fit considering $t\bar{t}H$ and tH production modes together with VH , $H \rightarrow \gamma\gamma$, is reported, performed by the CMS collaboration [131]. The C_1 coefficients have been computed for each bin of p_T^H in the fiducial region. Figure 6.14 shows the value of $-2 \ln \Lambda(\kappa_\lambda)$ as a function of κ_λ for an Asimov dataset generated under the SM hypothesis considering a luminosity of 3000 fb^{-1} at $\sqrt{s} = 14 \text{ TeV}$ and assuming all other couplings set to their SM values. For the purposes of constraining κ_λ , theoretical uncertainties in the differential $t\bar{t}H + tH$ cross section are included in the signal model. The results when only including the hadronic or leptonic categories are

shown in addition to the results obtained from their combination. From the differential cross-section measurement of a single Higgs-boson decay channel produced in association with top quarks, κ_λ is constrained at 95% CL in the interval $-4.1 < \kappa_\lambda < 14.1$ [131].

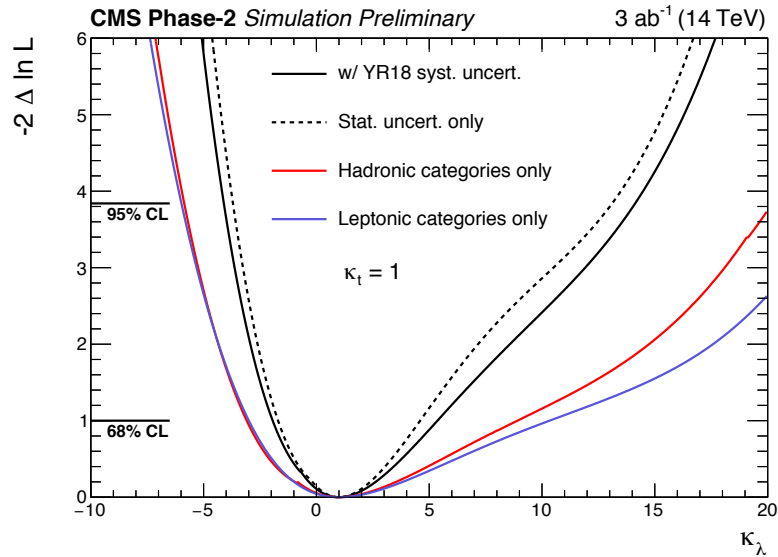


Figure 6.14: Value of $-2 \ln \Lambda(\kappa_\lambda)$ as a function of κ_λ for an Asimov dataset generated under the SM hypothesis considering a luminosity of 3000 fb^{-1} at $\sqrt{s} = 14 \text{ TeV}$. The individual contributions of the statistical and systematic uncertainties are separated performing a likelihood scan with all systematics removed. Additionally, the contributions from the hadronic and leptonic channels have been separated, and are shown as red and purple solid lines, respectively [131].

Chapter 7

Constraints on the Higgs-boson self-coupling from double-Higgs production and decay measurements

This chapter presents the results of the extraction of constraints on κ_λ from Higgs-boson pair production in the $b\bar{b}b\bar{b}$, $b\bar{b}\tau^+\tau^-$ and $b\bar{b}\gamma\gamma$ channels. Data and input measurements as well as main features of the different channels are briefly described in Section 7.1; the procedure exploited in order to simulate the signal samples used to extract κ_λ results together with the implementation of the theoretical framework described in Chapter 6 are reported in Sections 7.2 and 7.3, respectively.

Section 7.4 reports details on the statistical model, on the construction of the likelihood function and on the different uncertainties that are included in the likelihood as nuisance parameters. Section 7.5 describes a validation of the inputs of this combination aiming at reproducing the latest results from the ATLAS experiment reported in Reference [35]. Finally, Sections 7.6 and 7.7 present the constraints on κ_λ , starting from the double-Higgs single-channel constraints and then proceeding with the combination of the three double-Higgs decay channels.

7.1 Data and input measurements

The combination of searches for non-resonant Higgs-boson pair production exploits data collected by the ATLAS experiment in 2015 and 2016 from 13 TeV pp collisions corresponding to an integrated luminosity of up to 36.1 fb^{-1} . The double-Higgs analyses include the $b\bar{b}b\bar{b}$ [138], the $b\bar{b}\tau^+\tau^-$ [139] and the $b\bar{b}\gamma\gamma$ [140] decay channels. The integrated luminosity of the datasets used in each double-Higgs analysis included in this combination is reported in Table 7.1. Each analysis separates the selected events into orthogonal kinematic and topological regions, called categories. The $b\bar{b}b\bar{b}$ categories are orthogonal to both the $b\bar{b}\tau^+\tau^-$ and $b\bar{b}\gamma\gamma$ categories by definition, while a negligible overlap is present between the $b\bar{b}\tau^+\tau^-$ and $b\bar{b}\gamma\gamma$ analyses [35].

The double-Higgs event selections are targeting double-Higgs production, but select also single-Higgs events that need to be included in the double-Higgs signal regions if their contribution is not negligible. Details on single-Higgs backgrounds included in the different channels are reported in Section 7.2.

Analysis	Integrated luminosity (fb ⁻¹)	Reference
$HH \rightarrow b\bar{b}b\bar{b}$	27.5	[138]
$HH \rightarrow b\bar{b}\tau^+\tau^-$	36.1	[139]
$HH \rightarrow b\bar{b}\gamma\gamma$	36.1	[140]

Table 7.1: Integrated luminosity of the datasets used for each input analysis to the double-Higgs combination. The last column provides references to publications describing each measurement included in detail.

The double-Higgs analyses are categorised as in the following:

- the $b\bar{b}b\bar{b}$ analysis looks for final states with at least four small- R b -tagged jets reconstructed using the anti- k_t algorithm, as described in Chapter 4. The strategy exploited for the non-resonant search is to select two Higgs-boson candidates, each composed of two b -tagged jets, with invariant masses close to m_H . The invariant mass of the two-Higgs-boson-candidate system, m_{Aj} , is used as the final discriminant between Higgs-boson pair production and the backgrounds, which are principally QCD multijets and $t\bar{t}$ [138]. The dataset is split according to the years 2015 and 2016, and then statistically combined taking into account the different trigger algorithms used in 2015 and 2016. In part of the 2016 data period, inefficiencies in the online vertex reconstruction affected b -jet triggers that were used in the analysis, reducing the total available integrated luminosity to 27.5 fb⁻¹. The shape of the m_{HH} distribution has a strong dependence on κ_λ as shown in Figure 7.1 for various κ_λ values;

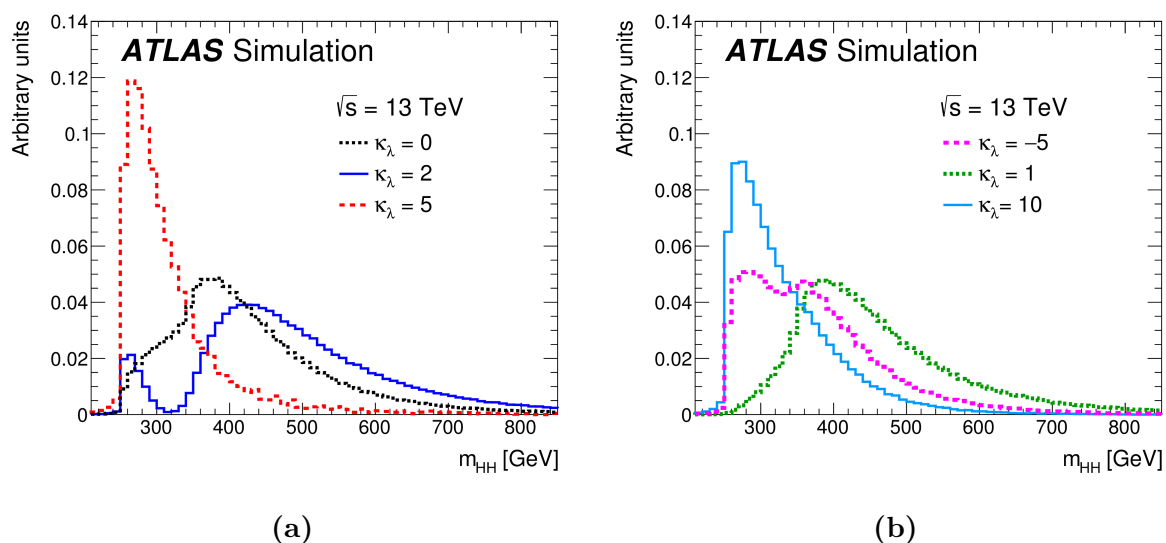


Figure 7.1: Generator-level m_{HH} distributions computed for various values of κ_λ by linearly combining three LO samples produced with MADGRAPH5_AMC@NLO. The m_{HH} shape is affected by the interference pattern between the box diagrams and the triangle diagram [35].

so does the signal acceptance that varies by a factor 2.5 over the probed range of κ_λ -values as presented in Figure 7.2.

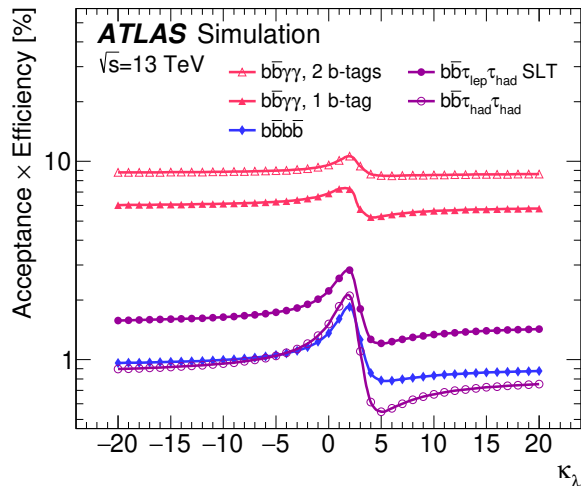


Figure 7.2: Signal acceptance times efficiency as a function of κ_λ for the $b\bar{b}\tau^+\tau^-$, $b\bar{b}b\bar{b}$ and $b\bar{b}\gamma\gamma$ channels [35].

- The $b\bar{b}\tau^+\tau^-$ analysis looks for final states with two $R = 0.4$ b -tagged jets reconstructed using the anti- k_t algorithm and two τ -leptons. Events are required to have at least one collision vertex reconstructed from at least two charged-particle tracks with transverse momentum $p_T > 0.4$ GeV. The analysis is split into two categories: the $\tau_{\text{lep}}\tau_{\text{had}}$ channel, in which events are required to contain an electron or a muon from one of the two τ -leptons decaying leptonically and a hadronically decaying τ -lepton of opposite charge, and the $\tau_{\text{had}}\tau_{\text{had}}$ channel, in which events are required to contain two hadronically decaying τ -leptons of opposite charge. BDTs, defined in Chapter 4, are used in the analysis to improve the separation of signal from background and, in order to compute the final results, the BDT score distributions, which have a dependence on κ_λ through the shape variations of some variables, in particular m_{HH} as shown in Figure 7.1, are used. In addition, the sensitivity of this analysis is affected by the variation of the signal acceptance by a factor 3 over the probed range of κ_λ , as shown in Figure 7.2.
- The $b\bar{b}\gamma\gamma$ analysis looks for final states with two photons and one or two $R = 0.4$ b -tagged jets. Particularly, two high- p_T isolated photons, accompanied by two jets with dijet invariant mass, m_{jj} , compatible with the mass of the Higgs boson, i.e. $80 < m_{jj} < 140$ GeV, are required to have $E_T/m_{\gamma\gamma} > 0.35$ and 0.25 respectively; the events are then analysed requiring a jet with $p_T > 40$ GeV and a second jet with $p_T > 25$ GeV. The signal consists of a narrow peak in the $m_{\gamma\gamma}$ distribution superimposed on a smoothly falling background. Events are subdivided into two categories according to the number of b -tagged jets. The $m_{\gamma\gamma}$ distribution dependence on κ_λ has been examined by comparing the generated $m_{\gamma\gamma}$ spectrum in simulation using different κ_λ values, and the one with $\kappa_\lambda = 1$ and finding an agreement within statistical uncertainties. Furthermore, being the shape of the diphoton mass distribution

described by the double-sided CrystalBall function [141], consisting of a Gaussian core with power-law tails on either side, the dependence on κ_λ of the key shape parameters of this function has been tested, resulting in an almost flat behaviour against κ_λ variations, however less influencing than the calibration uncertainties associated to these parameters. Thus the signal $m_{\gamma\gamma}$ distribution is implemented as a continuous function in the fit. The analysis acceptance, instead, varies by about 30% over the probed range of κ_λ -values, as shown in Figure 7.2.

7.2 Simulation of signal samples

Exploiting Equation 6.2, is possible to parameterise the signal distributions as a function of κ_λ/κ_t . In the $b\bar{b}b\bar{b}$ and $b\bar{b}\tau^+\tau^-$ case, three samples with different set of parameters κ_λ/κ_t have been simulated and used to reproduce the signal distributions for any value of κ_λ/κ_t through a linear combination method. Therefore signal samples have been generated choosing $\kappa_t = 1$ for all samples and $\kappa_\lambda/\kappa_t = 0$, called sample S(1,0), $\kappa_\lambda/\kappa_t = 1$, called S(1,1), and $\kappa_\lambda/\kappa_t = 20$, called S(1,20). Thus the cross section, using Equation 6.2, can be written in terms of these κ_λ/κ_t values as:

$$\begin{aligned}\sigma(\kappa_t = 1, \kappa_\lambda/\kappa_t = 0) &\sim |\mathcal{A}_1|^2 \\ \sigma(\kappa_t = 1, \kappa_\lambda/\kappa_t = 1) &\sim |\mathcal{A}_1|^2 + 2\Re(\mathcal{A}_1^*\mathcal{A}_2) + |\mathcal{A}_2|^2 \\ \sigma(\kappa_t = 1, \kappa_\lambda/\kappa_t = 20) &\sim |\mathcal{A}_1|^2 + 2 \cdot 20\Re(\mathcal{A}_1^*\mathcal{A}_2) + 20^2|\mathcal{A}_2|^2.\end{aligned}$$

The solution of this system of equations provides the expression of $|\mathcal{A}_1|^2$, $\Re(\mathcal{A}_1^*\mathcal{A}_2)$ and $|\mathcal{A}_2|^2$ as a function of the three arbitrary samples, leading to the following expression for the cross section, and the signal distributions:

$$\begin{aligned}\sigma(\kappa_\lambda, \kappa_t) \sim \kappa_t^2 &\left(\left(\kappa_t^2 + \frac{\kappa_\lambda^2}{20} - \frac{399}{380}\kappa_\lambda\kappa_t \right) |S(1,0)|^2 + \left(\frac{40}{38}\kappa_\lambda\kappa_t - \frac{2}{38}\kappa_\lambda^2 \right) |S(1,1)|^2 \right) + \\ &+ \left(\left(\frac{\kappa_\lambda^2 - \kappa_\lambda\kappa_t}{380} \right) |S(1,20)|^2 \right).\end{aligned}\tag{7.1}$$

The procedure followed in order to simulate the three signal samples with different κ_λ/κ_t values that are included in the fit for the $b\bar{b}b\bar{b}$ and $b\bar{b}\tau^+\tau^-$ decay channels is described in Reference [34].

7.3 Implementation of the theoretical model

The theoretical framework described in Chapter 6 is implemented in the double-Higgs channels taking into account that:

- double-Higgs kinematic distributions depend only on the ratio κ_λ/κ_t , and, consequently, the signal acceptance also depends only on κ_λ/κ_t ,
- the κ_t^4 factor affects only the total cross section;

- the self-coupling modifier κ_λ can affect the Higgs-boson branching fractions and cross sections due to NLO-EW corrections; thus these corrections have to be included in the parameterisations of single-Higgs background production cross sections and $b\bar{b}$, $\gamma\gamma$ and $\tau^+\tau^-$ decay branching fractions.

Furthermore, the expression of $|\mathcal{A}_1|^2$, $\Re(\mathcal{A}_1^*\mathcal{A}_2)$ and $|\mathcal{A}_2|^2$ reported in the previous section, are used in order to parameterise the three signal samples for the $b\bar{b}b\bar{b}$ and $b\bar{b}\tau^+\tau^-$ channels, included in the fit through the signal strength associated to each of them (μ_0, μ_1, μ_{20}), defined in Chapter 1, that are parameterised as in the following:

$$\begin{aligned}\mu_0 &= (\mu_f(H \rightarrow b\bar{b}))^2 \times \left(\kappa_t^4 + \frac{\kappa_t^2 \kappa_\lambda^2}{20} - \frac{399}{380} \kappa_t^3 \kappa_\lambda \right), \\ \mu_1 &= (\mu_f(H \rightarrow b\bar{b}))^2 \times \left(\frac{40}{38} \kappa_t^3 \kappa_\lambda - \frac{2}{38} \kappa_t^2 \kappa_\lambda^2 \right), \\ \mu_{20} &= (\mu_f(H \rightarrow b\bar{b}))^2 \times \left(\frac{\kappa_\lambda^2 \kappa_t^2 - \kappa_t^3 \kappa_\lambda}{380} \right)\end{aligned}$$

where μ_f describes the multiplicative corrections of each decay channel branching fraction ($BR_{SM,f}$) as a function of the anomalous values of the trilinear Higgs self-coupling and of the couplings of the Higgs boson to the other particles of the SM. In the case of the $b\bar{b}\gamma\gamma$ channel, no signal sample has been used in the fitting procedure, but the signal $m_{\gamma\gamma}$ distribution is implemented as a continuous function in the fit because its shape shows a negligible dependence on κ_λ . The analysis acceptance, instead, depends on κ_λ/κ_t and the dependence has been implemented as:

$$\text{Acceptance} = \frac{\text{Yield}(\kappa_\lambda/\kappa_t)}{\sigma(\kappa_\lambda/\kappa_t) \times BR(\kappa) \times \text{Luminosity} \times \text{Efficiency}} \quad (7.2)$$

where κ is a generic coupling modifier including both Higgs self-coupling and single-Higgs couplings, and $\sigma(\kappa_\lambda/\kappa_t) \times BR(\kappa)$ can be written as:

$$\sigma \times BR = \mu_{HH} = \mu_f(H \rightarrow b\bar{b}) \times \mu_f(H \rightarrow \gamma\gamma) \times \kappa_t^4 \times \sigma_{HH}(\kappa_\lambda/\kappa_t) \times 2 \times BR_{bb}^{SM} \times BR_{\gamma\gamma}^{SM}$$

where σ_{HH} is the SM double-Higgs cross section expressed as a function of κ_λ/κ_t and BR^{SM} are the branching fractions for a SM Higgs boson with $M_H = 125.09$ GeV, whose values are reported in Chapter 1.

The value of the SM double-Higgs production cross section used in this combination is: $\sigma_{ggF}^{SM}(pp \rightarrow HH) = 33.5_{-2.8}^{+2.4}$ fb at $\sqrt{s} = 13$ TeV [27], calculated at NLO in QCD with the measured value of the top-quark mass and corrected at NNLO in QCD matched to NNLL resummation using the heavy top-quark limit [27, 142–148], consistently with the cross section used for 2015-2016 analyses [35]. In addition to signal samples, the dominant single-Higgs background processes have to be included in the double-Higgs channels if their contribution is not negligible. Thus they have been considered in the $b\bar{b}\gamma\gamma$ and $b\bar{b}\tau^+\tau^-$ channels and they are parameterised as:

$$\begin{aligned}b\bar{b}\tau^+\tau^- : VH &= \mu_{ZH}^i \times \mu_f(H \rightarrow \tau\tau) \quad t\bar{t}H = \mu_{t\bar{t}H}^i \times \mu_f(H \rightarrow \tau\tau); \\ b\bar{b}\gamma\gamma : \mu_{XS\,ggF} &= \mu_{t\bar{t}H}^i \quad \mu_{XS\,VBF} = \mu_{ZH}^i\end{aligned}$$

where μ_i describes the multiplicative corrections of the expected SM Higgs production cross-sections ($\sigma_{\text{SM},i}$) as a function of the anomalous values of the trilinear Higgs self-coupling and of the couplings of the Higgs boson to the other SM particles, and the dominant production modes have been selected looking at the expected number of events in the single channels.

C_1 inclusive coefficients, representing linear κ_λ -dependent corrections to single-Higgs production modes and decay channels, are shown in Table 7.2 for ZH and $t\bar{t}H$ inclusive production modes together with the κ modifiers at LO for the initial state i ; the results of this thesis are presented exploiting the coupling modifiers κ_t , κ_b , κ_ℓ , κ_W , κ_Z , describing the modifications of the SM Higgs-boson coupling to up-type quarks, to down-type quarks, to leptons and to W and Z vector bosons, respectively, in addition to the Higgs self-coupling. The values of C_1^i and K_{EW}^i are averaged over the full phase space of these processes.

Production mode	ZH	$t\bar{t}H$
$C_1^i \times 100$	1.19	3.52
K_{EW}^i	0.947	1.014
κ_i^2	κ_Z^2	κ_t^2

Table 7.2: Values of the C_1^i coefficients, representing linear κ_λ -dependent corrections to single-Higgs production modes (second row); values of the K_{EW}^i coefficients [55, 133], taking into account NLO EW corrections in the SM hypothesis (third row); expressions of the initial state κ modifiers at LO [41], κ_i^2 , for the Higgs boson production process included as background in double-Higgs analyses (fourth row).

The coefficients for the decay channels, C_1^f , and the expressions of the κ modifiers at LO for the final state f are reported in Table 7.3 for all the analysed decay modes.

Decay mode	$H \rightarrow \gamma\gamma$	$H \rightarrow b\bar{b}$	$H \rightarrow \tau\tau$
$C_1^f \times 100$	0.49	0	0
κ_f^2	$1.59\kappa_W^2 + 0.07\kappa_t^2 - 0.67\kappa_W\kappa_t$	κ_b^2	κ_ℓ^2

Table 7.3: Values of C_1^f [55, 133] coefficients, representing linear κ_λ -dependent corrections to single-Higgs decay channels (second row); expressions of the final state κ modifiers at LO [41], κ_f^2 , for each considered double-Higgs decay mode (third row).

7.4 Statistical model

The target of this chapter is to set constraints on the Higgs self-coupling and, possibly, on other single-Higgs couplings, looking first of all at the double-Higgs channels separately, and then proceeding with their combination in order to get a more stringent limit on the self-coupling. This target is pursued through the statistical tools described in Chapter 5

that are adapted to the double-Higgs analyses and categories described in the previous sections, exploiting the aforementioned parameterisations of the different observables to introduce the dependence on the parameters of interest, which are extracted using the profile-likelihood technique.

The parameters of interest of the model, $\vec{\alpha}$, and the set of nuisance parameters, $\vec{\theta}$, including the systematic uncertainty contributions and background parameters that are constrained by side bands or control regions in data, are included in the global likelihood function, $L(\vec{\alpha}, \vec{\theta})$, defined in Chapter 5. For a combination of several channels and categories, the global likelihood function, $L(\vec{\alpha}, \vec{\theta})$ is obtained as the product of the likelihoods of the input analyses, that are, in turn, products of likelihoods computed in the mutually orthogonal categories optimised in each analysis. The number of signal events in each analysis category j is defined as:

$$n_j^{\text{signal}}(\boldsymbol{\kappa}, \vec{\theta}) = \mathcal{L}_j(\vec{\theta}) \sum_i \sum_f \mu_i(\boldsymbol{\kappa}) \times \mu_f(\boldsymbol{\kappa}) (\sigma_{\text{SM},i}(\vec{\theta}) \times \text{BR}_{\text{SM},f}(\vec{\theta})) (\epsilon \times A)_{if,j}(\vec{\theta}) \quad (7.3)$$

where the number of events is a function of the parameters of interest of the model, indicated by a generic $\boldsymbol{\kappa}$ standing for both the Higgs self-coupling and the single-Higgs couplings to other SM particles, and of the set of nuisance parameters $\vec{\theta}$, accounting for theoretical and experimental systematic uncertainties whose general features have been described in Chapter 5, characterised in detail in the next section. The index i runs over the double-Higgs production regions and the index f includes all the considered decay channels, i.e. $f = b\bar{b}b\bar{b}, b\bar{b}\tau^+\tau^-, b\bar{b}\gamma\gamma$. \mathcal{L}_j is the integrated luminosity of the dataset used in the j category, and $(\epsilon \times A)_{if,j}$ represents the acceptance and efficiency estimation for the category j , the production process i and the decay channel f . Finally, the term $\mu_i(\boldsymbol{\kappa}) \times \mu_f(\boldsymbol{\kappa})$, where μ_i is defined in Equation 6.5 and μ_f in Equation 6.7, describes the dependence of the signal strengths for the initial and final state on the Higgs-boson self-coupling modifier κ_λ , and on the single-Higgs boson coupling modifiers; these modifiers represent potential deviations from the SM expectation of the self-coupling and of the other Higgs couplings, respectively. Confidence intervals for the parameters of interests are determined using, as test statistics, the profile-likelihood ratio, described in Chapter 5:

$$q(\vec{\alpha}) = -2 \ln \Lambda(\vec{\alpha}) = -2 \ln \frac{L(\vec{\alpha}, \hat{\vec{\theta}}(\vec{\alpha}))}{L(\hat{\vec{\alpha}}, \hat{\vec{\theta}})} \quad (7.4)$$

where:

- in the numerator the nuisance parameters are set to their *profiled* values $\hat{\vec{\theta}}(\vec{\alpha})$, that maximise the likelihood for a given set of values of $\vec{\alpha}$;
- in the denominator both the parameters of interest and the nuisance parameters are respectively set to the values $\hat{\vec{\alpha}}$ and $\hat{\vec{\theta}}$, that simultaneously maximise the likelihood $L(\vec{\alpha}, \vec{\theta})$.

In the asymptotic limit, $-2 \log \Lambda(\vec{\alpha}, \vec{\theta})$ is approximately distributed as a χ^2 statistic with n degrees of freedom, where n equals the number of parameters of interests in the model. The results presented in this thesis are based on the profile-likelihood evaluation, and 68% as well as 95% CL intervals are given in the asymptotic approximation [125].

7.4.1 Systematic uncertainties

The systematic uncertainties included in the different analyses can be divided in two main categories: experimental uncertainties, related to object reconstruction and identifications algorithms or techniques, to data-taking conditions as well as detector response, to limited statistics in Montecarlo samples and data-driven background, and theoretical uncertainties, related to the cross-section computations and to the modelling of signal and background processes.

The ranking of the different uncertainties can be quantified looking at their impact on the final results. Considering as parameter of interest κ_λ and setting all other single-Higgs couplings to their SM values, the uncertainties having the greatest impact can be identified. The impact of each source of uncertainty is estimated by computing the maximum likelihood estimator of the parameter of interest, κ_λ , when the given uncertainty is fixed to its best-fit value $\pm 1\sigma$. Thus the pre-fit impact represents the impact of the nuisance parameters on the parameter of interest as they enter in the global likelihood while the post-fit impact represents the impact of the nuisance parameters on the parameter of interest after they have been adjusted to better describe data.

Experimental uncertainties

Electron, photon, muon and tau uncertainties

Uncertainties related to electrons, muons and taus are considered in the $b\bar{b}\tau^+\tau^-$ channel, being this channel the only channel using τ objects; they include uncertainties on electron and muon trigger, identification and reconstruction efficiencies. Tau uncertainties are included to take into account the corrections in the Montecarlo samples to the energy scale, the tau-reconstruction and identification efficiency, as well as the corrections due to the tau-electron overlap removal, or trigger and isolation requirements. Furthermore, uncertainties related to electron and photon energy calibration and momentum scale are included. The uncertainties having the greatest impact on the results are reported in Table 7.4.

NP name	Description
EG_RESOLUTION_ALL	Electron and photon energy resolution uncertainty
TAU_EFF_ID_TOTAL	Tau identification efficiency uncertainty
EG_SCALE_ALLCORR	Electron and photon energy scale uncertainty
TAU_EFF_RECO_TOTAL	Tau reconstruction efficiency uncertainty

Table 7.4: Electron, photon and tau uncertainties having the greatest impact on the results.

Missing energy uncertainties

Uncertainties on the E_T^{miss} are included only in the $b\bar{b}\tau^+\tau^-$ channel, using in the selections variables related to the E_T^{miss} . Uncertainties on the energy scale and resolution of the objects used to calculate the E_T^{miss} , such as electrons, muons, jets and taus are propagated to

the calculation of the E_T^{miss} . Additional uncertainties on the scale, resolution, and reconstruction efficiency of tracks not associated to the reconstructed objects, are also included.

Jets and flavour tagging uncertainties

As it was explained in Chapter 4, jets, after being reconstructed, have to be calibrated to take into account several effects, like energy-scale corrections, energy-resolution differences between simulation and data, pile-up effects. These corrections are included as uncertainties in the three decay channels, being all characterised by the presence of jets. The jet uncertainties having the greatest impact on the results, reported in Table 7.5, are those related to the energy resolution and energy scale. Furthermore, flavour-tagging uncertainties are included in all channels, coming from correction factors that take into account flavour-tagging-efficiency differences between simulation and data; these factors are measured separately for b , c and light-flavour jets and are decomposed into uncorrelated components, resulting in four uncertainties for b -jets, three uncertainties for c -jets and five uncertainties for light-flavour jets for all channels except for the $b\bar{b}\gamma\gamma$ channel, that has merged the flavour tagging NPs into one NP per flavour.

The flavour-tagging uncertainties having the greatest impact on the results, reported in Table 7.5, are those related to the flavour-tagging efficiency for b and c -flavour jets coming from the $b\bar{b}\gamma\gamma$ channel.

NP name	Description
JET_GroupedNP_3	Jet energy scale uncertainty split in different components
JES_EtaInter_NonClosure	Non closure uncertainty of the η -intercalibration method
JES_bbyy	Merged jet energy scale uncertainty - $b\bar{b}\gamma\gamma$
JET_Grouped NP_2	Jet energy scale uncertainty split in different components
JET_Grouped NP_1	Jet energy scale uncertainty split in different components
FT_EFF_Eigen_C_WP70_bbyy	Jet c -tagging uncertainty - 70% working point - $b\bar{b}\gamma\gamma$
JER_SINGLE_NP	Jet energy resolution uncertainty
FT_EFF_Eigen_B_WP70_bbyy	Jet b -tagging uncertainty - 70% working point - $b\bar{b}\gamma\gamma$

Table 7.5: Jets and flavour uncertainties having the greatest impact on the results.

Luminosity and pile-up uncertainties

The uncertainty on the integrated luminosity that has been recorded by the ATLAS experiment in 2015–2016 is 2.1%, derived using a methodology reported in Reference [64], thus through a calibration of the luminosity scale using $x - y$ beam-separation scans.

The nuisance parameters associated to the luminosity uncertainty are breakdown separately for the $b\bar{b}b\bar{b}$ channel considering 2015 and 2016 runs, given an inefficiency in the vertex reconstruction, and thereby b -tagging, at the trigger level during the 2016 data-taking, that led to an integrated luminosity not corresponding to the usual full dataset. Furthermore, an uncertainty related to the pile-up reweighting procedure, used in order to correctly reproduce the distribution of the number of pp collisions per bunch crossing in data, is included.

Experimental uncertainties coming from data-driven backgrounds

Background estimation is carried out using data-driven methods in double-Higgs channels, with the dominant background represented by multijet events and $t\bar{t}$ events. Uncertainties arising from the fitting procedure, from the data samples used, from the correction factors applied, have to be included. These uncertainties represent the dominant contribution to the total experimental and theoretical uncertainties; the background uncertainties having the greatest impact on the results are reported in Table 7.6 and are those related to the $b\bar{b}b\bar{b}$ and $b\bar{b}\gamma\gamma$ channels.

NP name	Description
bias_2tag_bbyy	Uncertainty due to the background modelling (spurious signal) for each $b\bar{b}\gamma\gamma$ category
r16_LowHtCR_bbbb	Background shape variation determined by the non-closure between Sideband and Control region derived models (2016) - $b\bar{b}b\bar{b}$
r16_HighHtCR_bbbb	Background shape variation determined by the non-closure between Sideband and Control region derived models (2016) - $b\bar{b}b\bar{b}$
r16_norm_NP2_bbbb	Background fit uncertainty corresponding to the uncertainty on the non all-hadronic $t\bar{t}$ normalisations (2016) - $b\bar{b}b\bar{b}$
bias_1tag_bbyy	Uncertainty due to the background modelling (spurious signal) for each $b\bar{b}\gamma\gamma$ category
r15_HighHtCR_bbbb	Background shape variation determined by the non-closure between Sideband and Control region derived models (2015) - $b\bar{b}b\bar{b}$
r15_LowHtCR_bbbb	Background shape variation determined by the non-closure between Sideband and Control region derived models (2015) - $b\bar{b}b\bar{b}$
r15_norm_NP2_bbbb	Background fit uncertainty corresponding to the uncertainty on the non all-hadronic $t\bar{t}$ normalisations (2015) - $b\bar{b}b\bar{b}$
Sys1tag2tagTF_bbtatau	Multi-jet uncertainty from data-driven estimation - $b\bar{b}\tau\tau$

Table 7.6: Experimental uncertainties coming from data-driven backgrounds having the greatest impact on the results.

Theoretical uncertainties

The theoretical uncertainties come from the modelling of signal and background processes; they include uncertainties on the QCD scales, i.e. renormalisation and factorisation scales, on the parton density function (PDF) used, on the modelling of the underlying events (UE) and parton shower (PS), on the running of the QCD coupling constant α_S ,

on the single-Higgs processes and on the theoretical-cross-section prediction. The theoretical uncertainties having the greatest impact on the results are reported in Table 7.7, and are the uncertainties coming from the modelling of the dominant background both in the shape and the acceptance normalisation for the $b\bar{b}\tau^+\tau^-$ channel, the ones coming from the QCD scale for all channels, from parton shower in the $b\bar{b}b\bar{b}$ channel and from ggF cross-section predictions.

NP name	Description
BkgTheory_SysZtataumBB_bbtatau	Z+heavy flavour shape modelling uncertainty - $b\bar{b}\tau\tau$
BkgTheory_SysTTbarMBB_bbtatau	$t\bar{t}$ shape modelling uncertainty - $b\bar{b}\tau\tau$
BkgTheory_SysRatioHHSRZhAcc2Tag_bbtatau	Z+heavy flavour relative acceptance normalisation between control region and signal region - $b\bar{b}\tau\tau$
BkgTheory_SysRatioHHSRTtbarAcc2Tag_bbtatau	$t\bar{t}$ relative acceptance normalisation between control region and signal region - $b\bar{b}\tau\tau$
BkgTheory_SysRatioLHSRZhAcc2Tag_bbtatau	Z+heavy flavour relative acceptance normalisation between control region and signal region - $b\bar{b}\tau\tau$
TheorySig_SIG_PS_bbbb	Uncertainty due to modelling of the parton shower - $b\bar{b}b\bar{b}$
TheorySig_QCDscale_hh	QCD scale uncertainty - diHiggs
TheorySig_QCDscale_ttH	QCD scale uncertainty - $t\bar{t}H$
TheorySig_HF_Higgs_ggF	Uncertainty associated to the heavy flavour content in ggF computation

Table 7.7: Theoretical uncertainties having the greatest impact on the results.

Correlation between systematic uncertainties

The correlation scheme adopted in the double-Higgs combination aiming at the extraction of κ_λ follows these guidelines:

- detector systematics uncertainties, like those related to jet reconstruction, b -jet tagging, muon and photon reconstruction and identification, are correlated between the different decay channels;

- uncertainties on the integrated luminosity are correlated among the different decay channels, even if, for the $b\bar{b}b\bar{b}$ decay channel, the nuisance parameters are not correlated with the luminosity NPs in the other channels, having this channel separate NPs for 2015 and 2016;
- uncertainties on the signal acceptance are correlated among the different decay channels;
- theoretical and modelling systematic uncertainties of the backgrounds are kept uncorrelated because of a negligible overlap between decay channels.

For the $HH \rightarrow b\bar{b}b\bar{b}$ channel, two different correlation schemes regarding flavour tagging (FT), jets (JET), parton shower (PS) and trigger uncertainties, have been considered and are described in details in Appendix A, Table A.1:

- all NPs related to the signal samples S(1,0), S(1,1) and S(1,20) uncorrelated, i.e. FT, JET, PS, trigger NPs kept split in the three signal samples (scheme 1);
- all NPs related to the signal samples S(1,0), S(1,1) and S(1,20), i.e. FT, JET, PS, trigger NPs, correlated to be consistent with the double-Higgs combination in Reference [35] (scheme 2); the list of the correlated NPs is reported in Appendix A.

The list of the nuisance parameters ranked by their post-fit impact on the parameter of interest from the greatest (top) to the least (bottom) dominant systematic uncertainty is shown in the so called “ranking plot”; the same plot shows also the nuisance parameter pulls, i.e. the difference between the best-fit values of the nuisance parameters and the initial one (θ_0), normalised to their pre-fit uncertainties; $\theta_0 = 0$ by construction of the likelihood function, so the compatibility of the pull with zero is a check of the robustness of the fit procedure.

Figure 7.3 shows the ranking plots for the double-Higgs combination considering the top 30 uncertainties for data (a) and for the Asimov dataset (b) generated in the SM hypothesis ($\kappa_\lambda=1$). The difference between the maximum likelihood estimator with or without varying the nuisance parameter is the $\Delta\hat{\kappa}_\lambda$ of the fit, that is normalised to the total error, $\Delta\hat{\kappa}_{\lambda_{tot}}$. Pre-fit and post-fit impacts of the different nuisance parameters on the central value κ_λ are reported as white empty and cyan (green) filled bars corresponding to downward (upwards) systematic uncertainty variations, respectively. The points indicate how the parameter had to be pulled up or down to adjust data/MC agreement in the fit, and associated error bars show the best-fit values of the nuisance parameters and their post-fit uncertainties. Most of the systematic uncertainties are within 1σ from the nominal (indicated by the dashed vertical lines) value, except for an experimental nuisance parameter, “ATLAS_r16_LowHtCR_bbbb” related to the data-driven background modelling (mainly multijets) of $HH \rightarrow b\bar{b}b\bar{b}$, that is also one of the nuisance parameter having the largest impact on κ_λ , together with other nuisance parameters all being related to the data-driven background modelling (mainly multijets) of $HH \rightarrow b\bar{b}b\bar{b}$ and $HH \rightarrow b\bar{b}\gamma\gamma$ analyses.

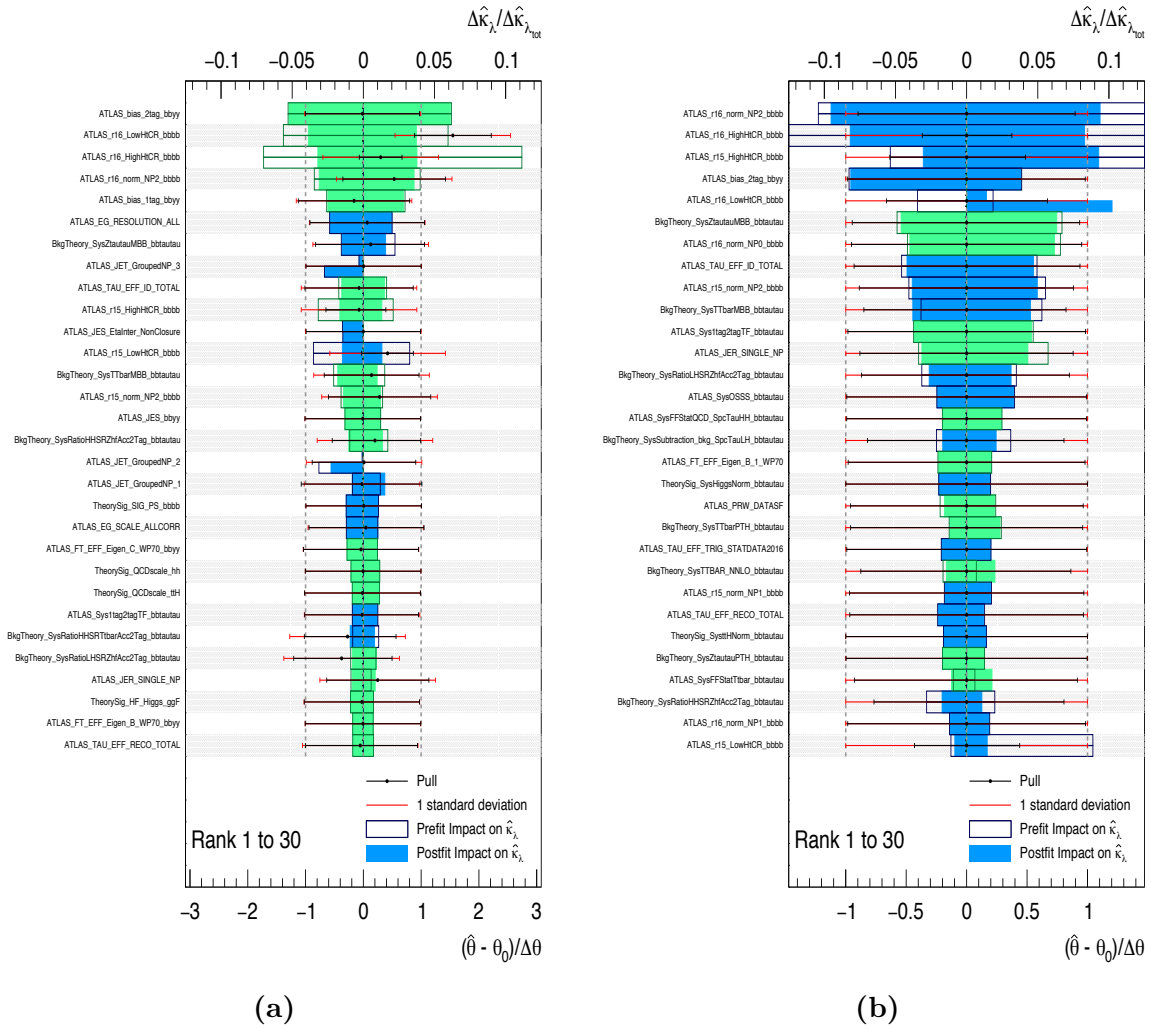


Figure 7.3: Ranking of the top 30 systematic uncertainties in the double-Higgs combination for data (a) and for the Asimov dataset (b) generated under the SM hypothesis.

7.5 Validation of double-Higgs results

The most recent constraints on the Higgs self-coupling from the ATLAS experiment, not considering the results of this thesis, come from the combination of the double-Higgs most sensitive final states that have been described in the previous sections, and are reported in Figure 7.4. In each analysis, the 95% CL upper limits on the $\sigma_{ggF}(pp \rightarrow HH)$ cross-section were computed for different κ_λ values; the intersection of the theoretical $\sigma_{ggF}(pp \rightarrow HH)$ as a function of κ_λ with the measured cross section was used to indirectly extract the confidence intervals at 95% for κ_λ . Uncertainties on the theoretical $\sigma_{ggF}(pp \rightarrow HH)$ cross section as well as the dependence of the Higgs-boson branching fractions and of the single-Higgs background on κ_λ , affecting both the double-Higgs signal and the single-Higgs-boson background, were neglected. This method will be referred to as “ κ_λ -scan method”.

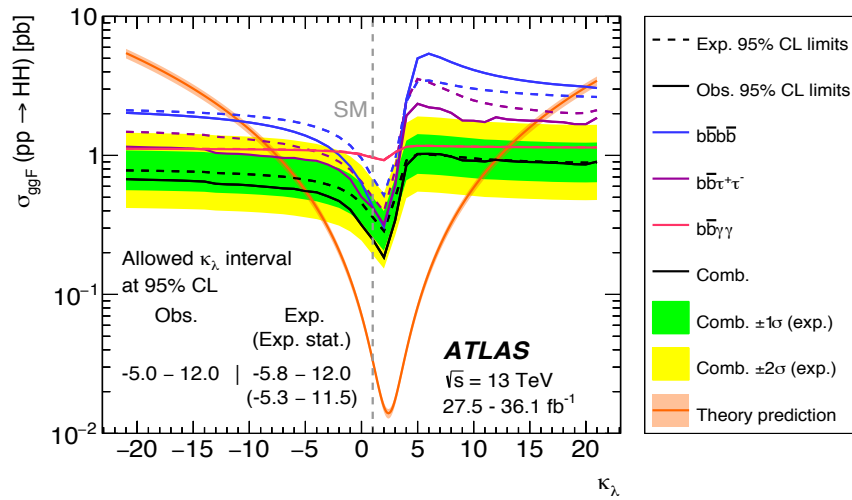


Figure 7.4: Upper limits at 95% CL on the cross section of the ggF non-resonant SM HH production as a function of κ_λ . The observed (expected) limits are shown as solid (dashed) lines. The $\pm 1\sigma$ and $\pm 2\sigma$ bands are only shown for the combined expected limit. The orange solid line represents the theoretical prediction of the double-Higgs ggF cross section as a function of κ_λ [35].

The main differences between the method used in this chapter and the κ_λ -scan method through which double-Higgs direct limits have been produced, are the profile-likelihood technique used, where the limits and best-fit values are extracted after building a likelihood function as described in Section 7.4, and the fact that the single-Higgs background and branching fractions are parameterised as a function of κ_λ . For the purpose of validating the approach followed in this combination, the published results have been reproduced exploiting the double-Higgs combined inputs used to produce the results of this chapter. In order to be consistent with the aforementioned results, all couplings except for κ_λ , have been set to their SM values and both branching fractions and single-Higgs background have not been parameterised as a function of κ_λ . Furthermore, theory uncertainties have not been injected. Thus the combined workspace has been used to measure the double-Higgs cross section as a function of κ_λ and the 95% CL of κ_λ has been estimated to be

$-5.1 < \kappa_\lambda < 11.9$ (observed) and $-5.9 < \kappa_\lambda < 12.0$ (expected). These results are comparable to the results reported in Reference [35], i.e. $-5.0 < \kappa_\lambda < 12.0$ (observed) and $-5.8 < \kappa_\lambda < 12.0$ (expected). Figure 7.5 shows the upper limits on the double-Higgs cross section as a function of κ_λ : the solid black curve is the observed limit, while the dashed curve is the expected one. The green and yellow bands show the 1σ and 2σ intervals of the expected limit, respectively. The theoretical $\sigma_{ggF}(pp \rightarrow HH)$, used to find the limits on κ_λ , is represented by the orange curve. Small differences with respect to the results reported in Reference [35] mainly come from the $b\bar{b}\tau^+\tau^-$ channel, that uses a varying binning of the BDT distribution optimised for different κ_λ values; the validation study, instead, uses a fixed binning (from $\kappa_\lambda = 1$) differently from the original inputs.

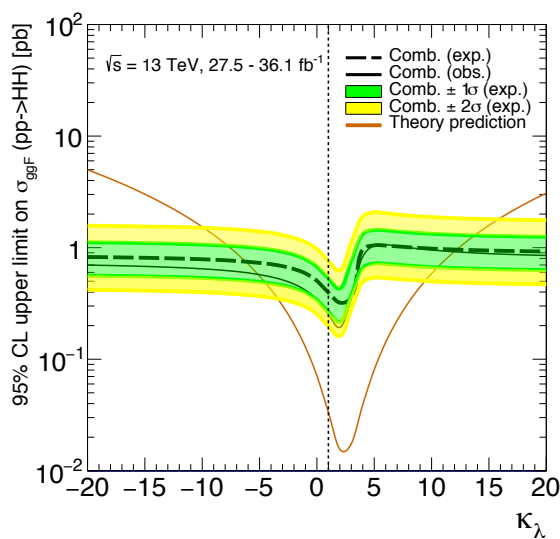


Figure 7.5: Upper limits at 95% CL on the cross-section of the ggF non-resonant SM HH production as a function of κ_λ obtained in order to validate the input of the double-Higgs analyses presented in this chapter. The observed (expected) limits are shown as solid (dashed) lines. The $\pm 1\sigma$ (green) and $\pm 2\sigma$ (yellow) bands are only shown for the combined expected limit. The orange solid line represents the theoretical prediction of the HH ggF cross section as a function of κ_λ used in order to extract κ_λ limits.

7.6 Results of fits to κ_λ from individual channels

In this section, the main results of the double-Higgs analyses are presented, where a global likelihood function is built as described in Section 7.4 as the product of the likelihoods of each double-Higgs category, implementing, as the parameter of interest, the Higgs self-coupling, and as nuisance parameters the theoretical and experimental uncertainties described in Section 7.4.1. The profile-likelihood technique is used to constrain the value of the Higgs-boson self-coupling κ_λ while leaving untouched other Higgs-boson couplings, taking as best-fit values of the unknown parameter of interest the values that maximise the likelihood function.

In order to check the impact of the Higgs-boson branching fractions and cross sections

on κ_λ , results are presented either including or not including the single-Higgs-background and branching-fraction parameterisations as a function of κ_λ . The standard configuration includes these parameterisations.

Specifically, the $b\bar{b}b\bar{b}$ decay channel is only affected by branching-fraction variations, while the $b\bar{b}\tau^+\tau^-$ and the $b\bar{b}\gamma\gamma$ decay channels are affected by both branching-fraction and cross-section variations for dominant single-Higgs background (ZH and $t\bar{t}H$).

Results are always presented for data and for the Asimov dataset, a dataset in which all observed quantities are set equal to their expected values, that is practically generated from the likelihood distribution Λ with nuisance parameters fixed to the best-fit values obtained on data and the parameter of interest fixed to the expected value, corresponding to the SM hypothesis (i.e. $\kappa_\lambda = 1$).

The κ_λ self-coupling modifier is probed in the range $-20 < \kappa_\lambda < 20$, because outside this range the calculation in References [55, 133] loses its validity.

Constraints from individual double-Higgs channels are reported in the following.

Starting from the $b\bar{b}\gamma\gamma$ channels, the value of $-2\ln\Lambda(\kappa_\lambda)$ as a function of κ_λ is shown in Figure 7.6 for data and for the Asimov dataset, either including or not including the branching-fraction and single-Higgs parameterisations.

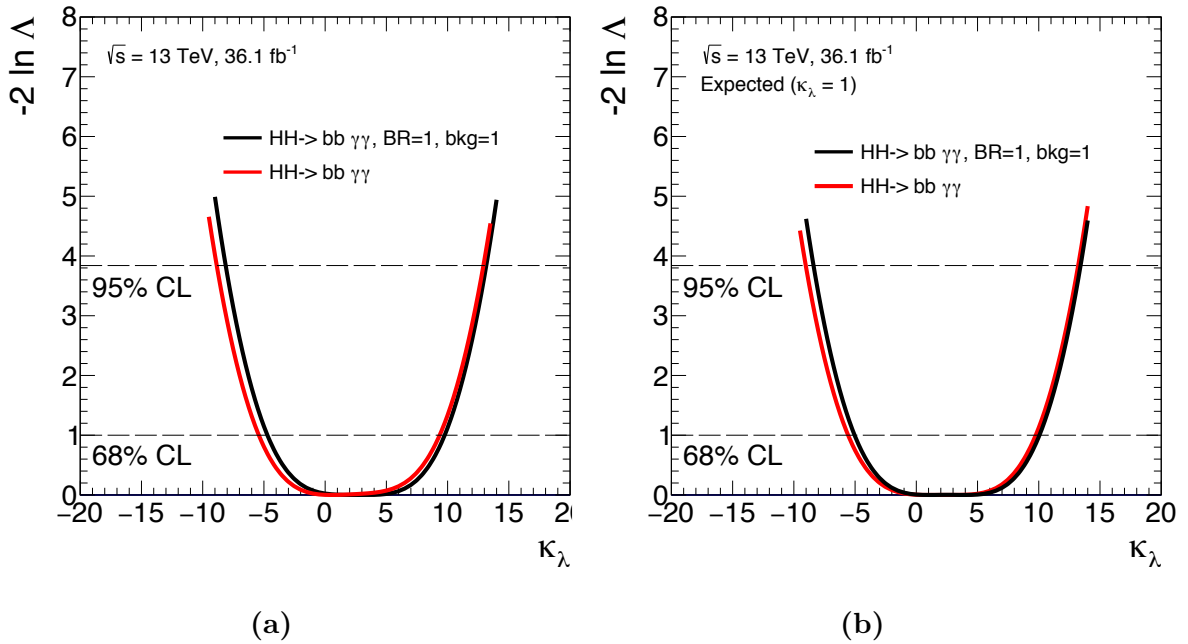


Figure 7.6: Value of $-2\ln\Lambda(\kappa_\lambda)$ as a function of κ_λ for the $HH \rightarrow b\bar{b}\gamma\gamma$ channel considering two configurations. Black solid line: neither branching fractions nor single-Higgs background parameterised as a function of κ_λ ; red solid line: branching fractions and single-Higgs background parameterised as a function of κ_λ . Likelihood distributions are reported for data (a) and for the Asimov dataset generated in the SM hypothesis (b). The dotted horizontal lines show the $-2\ln\Lambda(\kappa_\lambda) = 1$ level that is used to define the $\pm 1\sigma$ uncertainty on κ_λ as well as the $-2\ln\Lambda(\kappa_\lambda) = 3.84$ level used to define the 95% CL.

The κ_λ 95% CL intervals from the $HH \rightarrow b\bar{b}\gamma\gamma$ channel are $-8.9 < \kappa_\lambda < 12.9$ (observed) and $-9.0 < \kappa_\lambda < 13.2$ (expected). The impact of the Higgs-boson branching fractions and cross sections on the allowed κ_λ lower limit is $\sim 9\%$ while it is $\sim 2\%$ on the

upper limit; as it is shown in the following lines, this channel is affected by the largest κ_λ -dependent corrections, given the fact that the single-Higgs contribution in the $bb\gamma\gamma$ channel is largest with respect to the contribution to other channels, and that the C_1 coefficients are different from 0 for the $\gamma\gamma$ channel.

Even if a small deficit in data is present, as shown in Figure 1.14 reporting the upper limits at 95% CL on the double-Higgs ggF cross section, that would lead to more stringent observed limits with respect to the expected ones, the weaker dependence of the $bb\gamma\gamma$ acceptance on κ_λ with respect to the other channels, shown in Figure 7.2, leads to the fact that the observed and expected 95% CL intervals are comparable.

The best-final state for the non-resonant double-Higgs production is the $bb\tau^+\tau^-$ channel. The value of $-2\ln\Lambda(\kappa_\lambda)$ as a function of κ_λ is shown in Figure 7.7 for data and for the Asimov dataset, generated in the SM hypothesis (i.e. $\kappa_\lambda = 1$), either including or not including the branching-fraction and single-Higgs parameterisations.

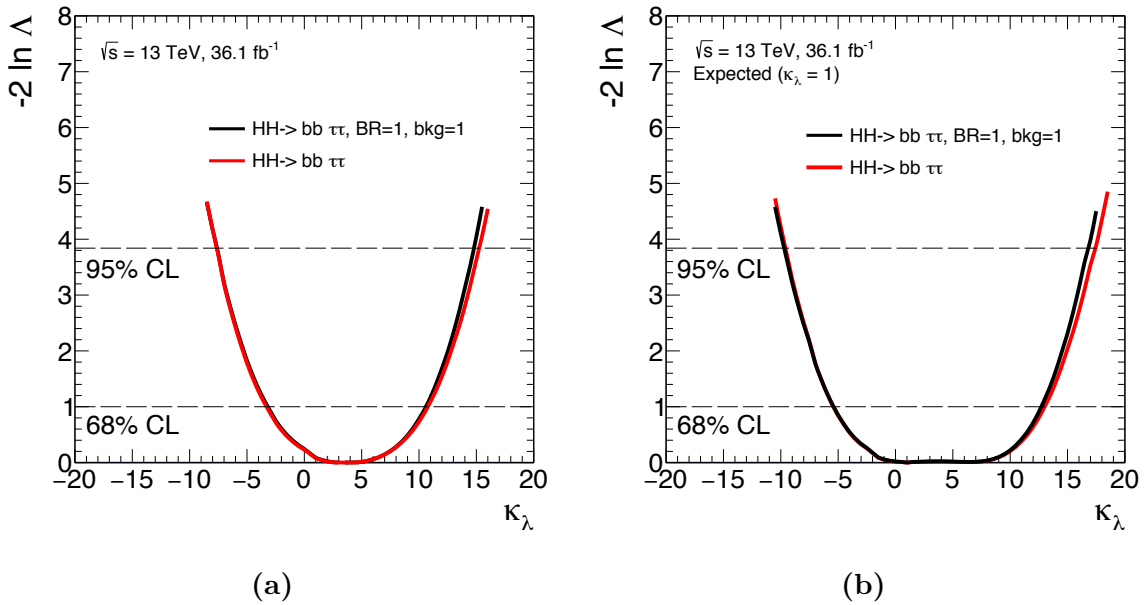


Figure 7.7: Value of $-2\ln\Lambda(\kappa_\lambda)$ as a function of κ_λ for the $HH \rightarrow bb\tau^+\tau^-$ channel considering two configurations. Black solid line: neither branching fractions nor single-Higgs background parameterised as a function of κ_λ ; red solid line: branching fractions and single-Higgs background parameterised as a function of κ_λ . Likelihood distributions are reported for data (a) and for the Asimov dataset generated in the SM hypothesis (b). The dotted horizontal lines show the $-2\ln\Lambda(\kappa_\lambda) = 1$ level that is used to define the $\pm 1\sigma$ uncertainty on κ_λ as well as the $-2\ln\Lambda(\kappa_\lambda) = 3.84$ level used to define the 95% CL.

The κ_λ 95% CL intervals are $-7.7 < \kappa_\lambda < 15.3$ (observed) and $-9.7 < \kappa_\lambda < 17.5$ (expected). The impact of the Higgs-boson branching fractions and cross sections on the allowed κ_λ lower limit is $< 1\%$ while it is $\sim 3\%$ on the upper limit; the dominant contribution affecting the upper limit of the interval comes from the parameterisations as a function on κ_λ of the branching fractions. The observed limits are more stringent than the expected ones, as it is shown in Figure 1.14, over the whole range of κ_λ , due to a deficit of data relative to the background predictions at high values of the BDT score [35], as illustrated in Figure 7.8 reporting BDT distributions used as final discriminants both

for the $\tau_{\text{lep}}\tau_{\text{had}}$ (a) and the $\tau_{\text{had}}\tau_{\text{had}}$ (b) channels.

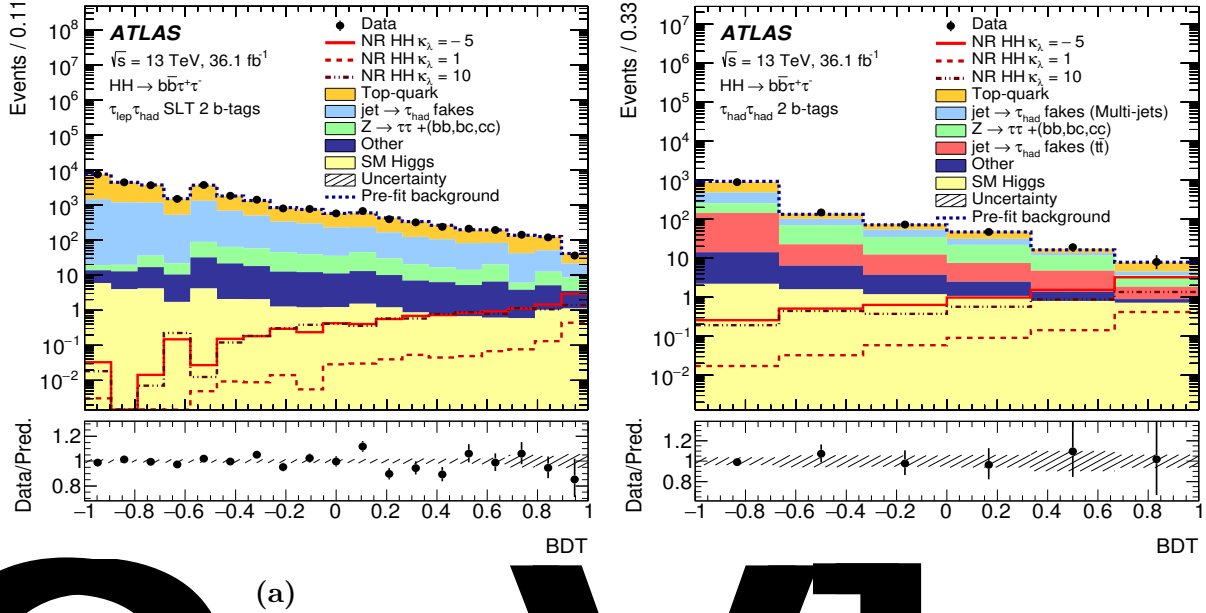


Figure 7.8: BDT distributions used as final discriminants in the κ_λ -scan analysis for $b\bar{b}\tau^+\tau^-$ final state; (a): $\tau_{\text{lep}}\tau_{\text{had}}$ and (b) $\tau_{\text{had}}\tau_{\text{had}}$ channels [35].

Finally, the fit has been performed exploiting the $b\bar{b}b\bar{b}$ channel and considering both correlation schemes introduced in Section 7.4, i.e. NPs related to signal samples correlated (scheme 1) or uncorrelated (scheme 2). The value of $-2\ln\Lambda(\kappa_\lambda)$ as a function of κ_λ is shown in Figure 7.9 for data and for the Asimov dataset, generated in the SM hypothesis (i.e. $\kappa_\lambda = 1$); the two schemes, labelled as “corr” and “uncorr”, respectively, are considered. Furthermore, the likelihood distribution as a function of κ_λ is shown for data and for the Asimov dataset not including the branching fraction parameterisations and considering NPs related to signal samples correlated among themselves. The single-Higgs background is not even included in the $b\bar{b}b\bar{b}$ analysis. The impact of these NLO-EW corrections on the allowed κ_λ lower limit is $\sim 4\%$ while it is $\sim 3\%$ on the upper limit.

The κ_λ 95% CL intervals for the $b\bar{b}b\bar{b}$ channel are $-9.3 < \kappa_\lambda < 20.9$ (observed) and $-11.4 < \kappa_\lambda < 19.6$ (expected). The observed limits are more stringent than the expected ones at low values of κ_λ ; in fact, for these κ_λ values, the signal m_{HH} distributions have significant populations in the region above 400 GeV, where a deficit of data is observed, see Figure 7.10. An excess in the data below 300 GeV leads to the observed limits being less stringent than expected for high κ_λ values. This non-significant excess tends to increase the $\kappa_\lambda = 10$ contribution and causes the displacement of the minimum of the $b\bar{b}b\bar{b}$ likelihood function towards higher values of κ_λ as shown in Figure 7.6. As expected, the constraint on κ_λ is smaller when the NPs related to the signal samples are not correlated, reflecting a looser constraint on the NPs themselves. This effect is enhanced in the fit to data, where NP post-fit values significantly differ from their nominal values.

The scheme that has been chosen for the results reported in this thesis is “scheme 1”, i.e. the one where the nuisance parameters related to signal samples are correlated, in order to be consistent with the results reported in Reference [35].

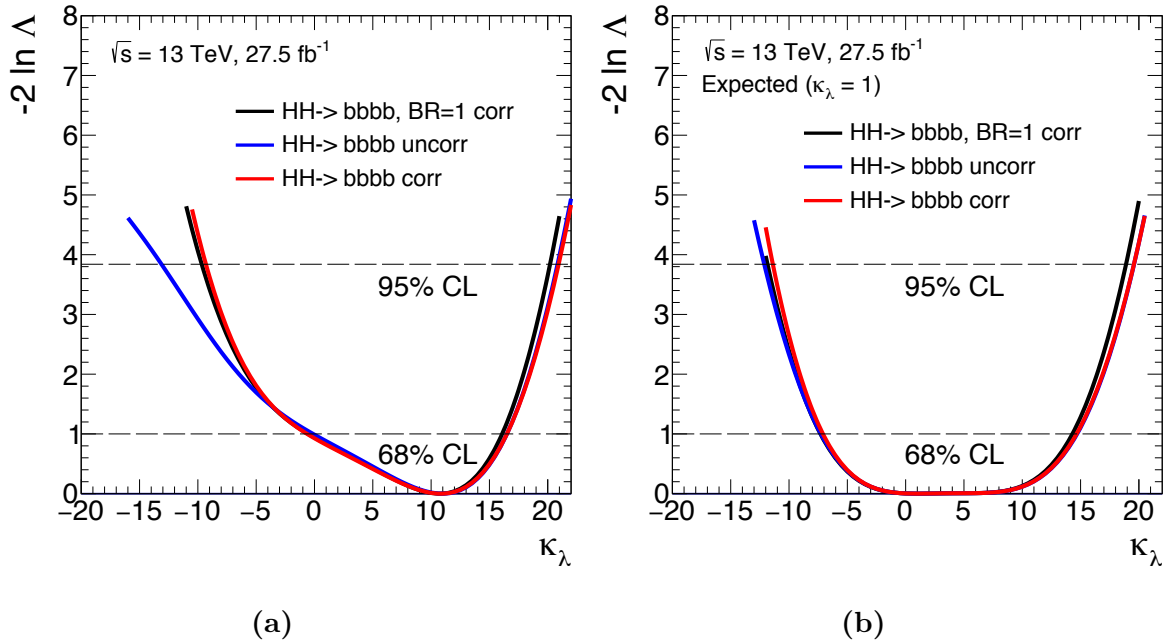


Figure 7.9: Value of $-2 \ln \Lambda(\kappa_\lambda)$ as a function of κ_λ for the $HH \rightarrow b\bar{b}b\bar{b}$ channel considering three configurations. Black solid line: branching fractions not parameterised as a function of κ_λ , NPs related to signal samples correlated; blue solid line: branching fractions and single-Higgs background parameterised as a function of κ_λ , NPs related to signal samples uncorrelated; red solid line: branching fractions and single-Higgs background parameterised as a function of κ_λ , NPs related to signal samples correlated. Likelihood distributions are reported for data (a) and for the Asimov dataset generated in the SM hypothesis (b). The dotted horizontal lines show the $-2 \ln \Lambda(\kappa_\lambda) = 1$ level that is used to define the $\pm 1\sigma$ uncertainty on κ_λ as well as the $-2 \ln \Lambda(\kappa_\lambda) = 3.84$ level used to define the 95% CL.

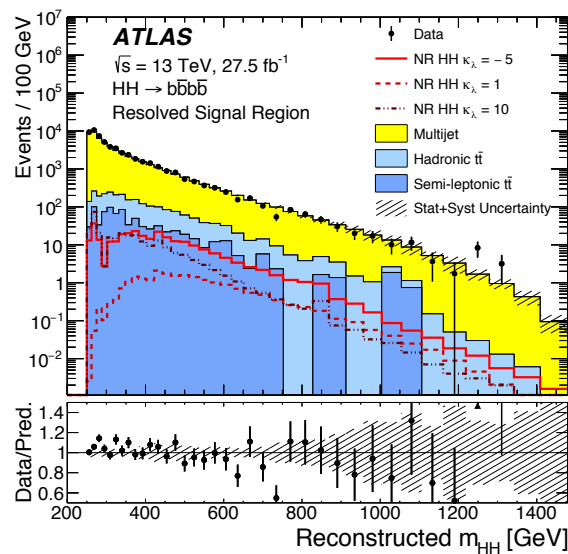


Figure 7.10: The reconstructed m_{HH} distribution used as final discriminant in the κ_λ -scan analysis for the $b\bar{b}b\bar{b}$ channel [35].

7.7 Results of fits to κ_λ from the combination of double-Higgs channels

This section reports the results of the combined fit to κ_λ exploiting the three most sensitive decay channels described in previous sections, whose individual results are presented in Section 7.6.

The combined fit has been performed following the global correlation scheme described in Section 7.4 and adopting two different correlation schemes for the $b\bar{b}b\bar{b}$ channel, namely the scheme 1, labelled as “corr” on the plots, and the scheme 2, labelled as “uncorr”.

Figure 7.11 shows the value of $-2\ln\Lambda(\kappa_\lambda)$ as a function of κ_λ for the three individual channels and their combination for data and for the Asimov dataset, generated under the SM hypothesis (i.e. $\kappa_\lambda = 1$). Negligible deviations are present adopting the different correlation schemes in the combination with all other channels.

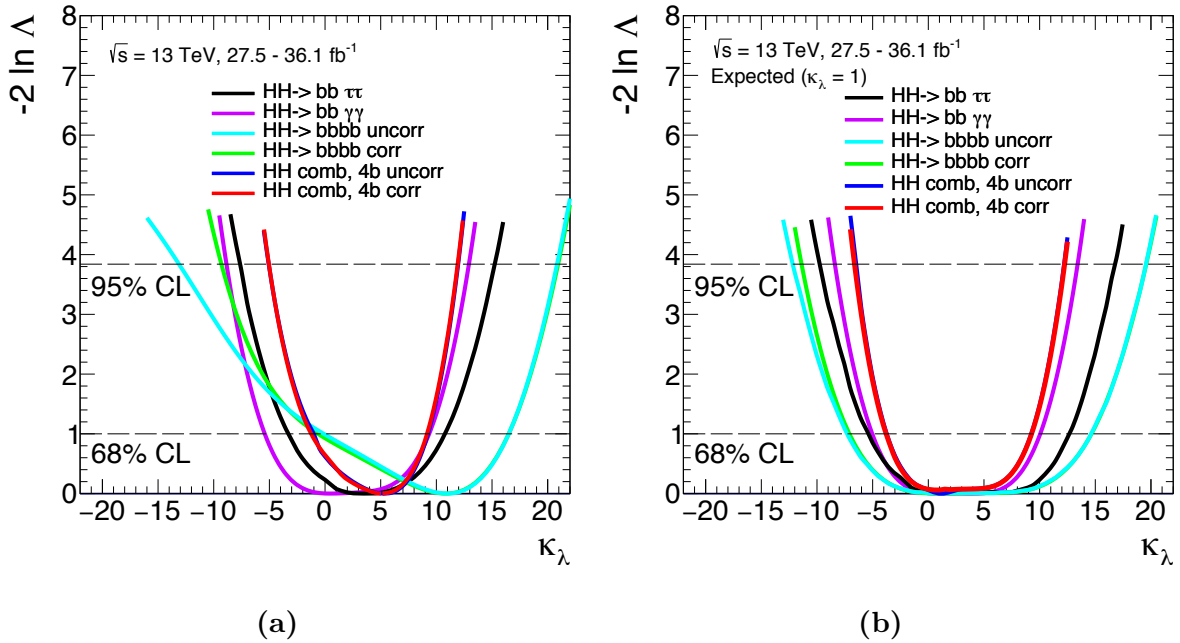


Figure 7.11: Value of $-2\ln\Lambda(\kappa_\lambda)$ as a function of κ_λ for the three individual channels and for their combination; the $HH \rightarrow b\bar{b}b\bar{b}$ likelihood distribution has been reported both with NPs related to signal samples correlated and uncorrelated. Therefore, the HH combination too has been considered in the two cases. Negligible deviations are present in the combination with all other channels. Likelihood distributions are reported for data (a) and for the Asimov dataset generated in the SM hypothesis (b). The dotted horizontal lines show the $-2\ln\Lambda(\kappa_\lambda) = 1$ level that is used to define the $\pm 1\sigma$ uncertainty on κ_λ as well as the $-2\ln\Lambda(\kappa_\lambda) = 3.84$ level used to define the 95% CL.

As shown in Figure 7.12 the likelihood has a peculiar shape, characterised by two local minima, that is related to the dependence of the total cross section and double-Higgs kinematic properties on κ_λ , while the relative height of the two minima depends on the capability of the different analyses to access differential m_{HH} information.

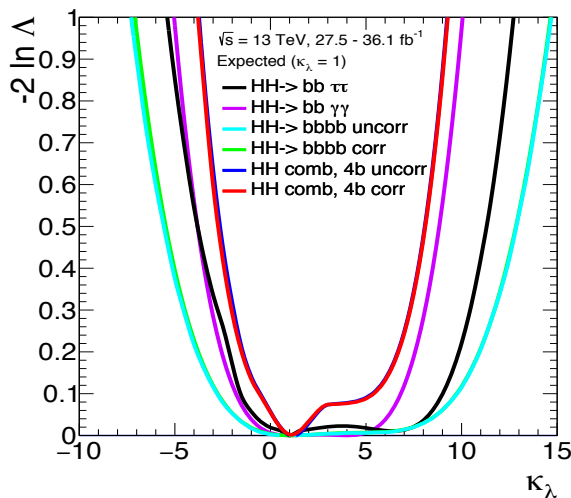


Figure 7.12: Value of $-2 \ln \Lambda(\kappa_\lambda)$ as a function of κ_λ for the three individual channels and their combination; the likelihood distribution is zoomed between $-2 \ln \Lambda(\kappa_\lambda) = 0$ and $-2 \ln \Lambda(\kappa_\lambda) = 1$ in order to show the peculiar likelihood function characterised by two local minima related to the total cross section and kinematic properties dependence on κ_λ .

The impacts of neglecting NLO-EW corrections depending on κ_λ , on the κ_λ intervals extracted from the double-Higgs combination, have also been checked.

The κ_λ 95% CL intervals for the three different channels, $b\bar{b}\tau^+\tau^-$, $b\bar{b}\gamma\gamma$ and $b\bar{b}b\bar{b}$ and for their combination are summarised in Table 7.8, where different configurations have been considered:

- branching fractions (BRs) and single-Higgs (SH) background parameterised as a function of κ_λ ;
- neither branching fractions nor single-Higgs background parameterised as a function of κ_λ .

The overall impact of the Higgs-boson branching fractions and cross sections on the allowed κ_λ intervals has been estimated to be less than 10%. These effects are taken into account in the present combination.

The best-fit value and $\pm 1\sigma$ uncertainties are determined to be $\kappa_\lambda = 5.2^{+4.0}_{-6.4}$ (observed) and $\kappa_\lambda = 1.0^{+8.3}_{-4.7}$ (expected). As expected, the best-fit value is guided by the most sensitive channel, i.e. the $b\bar{b}\tau^+\tau^-$ channel.

The 95% CL intervals for κ_λ are $-5.0 < \kappa_\lambda < 11.9$ (observed) and $-6.6 < \kappa_\lambda < 12.2$ (expected) leading to a significant improvement of single channel performances as a result of the comparable sensitivity.

Table 7.9 reports a summary of κ_λ fit values with $\pm 1\sigma$ uncertainties and 95% CL intervals for each decay channel entering the combination and for the combinations themselves.

A further element that has been introduced, with respect to the results in Reference [35], is the injection of branching-fraction uncertainties and uncertainties on the double-Higgs cross section. As reported in Table 7.9, the overall impact of these modifications is really small.

Channel	κ_λ interval at 95% CL	κ_λ interval, BR=1, bkg=1	NLO-EW corrections
$b\bar{b}\tau^+\tau^-$ (obs)	[-7.7 - 15.3]	[-7.7 - 14.8]	[< 1%, 3%]
$b\bar{b}\tau^+\tau^-$ (exp)	[-9.7 - 17.5]	[-9.7 - 16.8]	[< 1%, 4%]
$b\bar{b}b\bar{b}$ (obs)	[-9.3 - 20.9]	[-9.7 - 20.2]	[4%, 3%]
$b\bar{b}b\bar{b}$ (exp)	[-11.4 - 19.6]	[-11.8 - 18.9]	[3%, 4%]
$b\bar{b}\gamma\gamma$ (obs)	[-8.9 - 12.9]	[-8.1 - 13.2]	[9%, 2%]
$b\bar{b}\gamma\gamma$ (exp)	[-9.0 - 13.2]	[-8.4 - 13.4]	[8%, 1%]
Comb (obs)	[-5.0 - 11.9]	[-4.7 - 12.0]	[7%, < 1%]
Comb (exp)	[-6.6 - 12.2]	[-6.4 - 12.3]	[3%, < 1%]

Table 7.8: Allowed κ_λ intervals at 95% CL with different configurations and impact of the Higgs-boson branching-fraction and cross-section corrections on κ_λ limits for single channels and for the combination of the three channels.

Channels	$\kappa_\lambda^{+1\sigma}_{-1\sigma}$	κ_λ [95% CL]
$HH \rightarrow b\bar{b}\tau^+\tau^-$	$3.6^{+7.2}_{-7.0}$	[-7.7, 15.3]
	$1.0^{+12.1}_{-6.5}$	[-9.7, 17.5]
$HH \rightarrow b\bar{b}b\bar{b}$	$10.9^{+5.7}_{-11.5}$	[-9.3, 20.9]
	$1.0^{+13.7}_{-8.3}$	[-11.4, 19.6]
$HH \rightarrow b\bar{b}\gamma\gamma$	$0.5^{+8.9}_{-5.9}$	[-8.9, 12.9]
	$1.0^{+8.8}_{-6.6}$	[-9.0, 13.2]
Combination	$5.2^{+4.0}_{-6.4}$	[-5.0, 11.9]
	$1.0^{+8.3}_{-4.7}$	[-6.6, 12.2]
Combination injecting uncertainties	$5.2^{+4.0}_{-6.5}$	[-5.1, 12.0]
	$1.0^{+8.4}_{-4.9}$	[-6.8, 12.4]

Table 7.9: Best-fit κ_λ values with $\pm 1\sigma$ uncertainties. The first column shows each double-Higgs decay channel considered in the combination. The 95% CL interval for κ_λ are also reported. For each fit result the upper row corresponds to the observed results, and the lower row to the expected results obtained using Asimov datasets generated under the SM hypothesis.

A comparison of κ_λ likelihood scans including or not branching fractions and single-Higgs background parameterisation as a function of κ_λ , and including or not double-Higgs cross section theory uncertainties and branching-fraction uncertainties, is shown in Figure 7.13, in addition to the detailed results per channel reported in Table 7.8. The black solid line represents the likelihood distribution when neither branching fractions nor single-Higgs background are parameterised as a function of κ_λ ; the blue solid line when the branching fractions and single-Higgs background are parameterised as a function of κ_λ , while the red solid line represents the case in which branching fractions and single-Higgs background are parameterised as a function of κ_λ and theoretical uncertainties are injected.

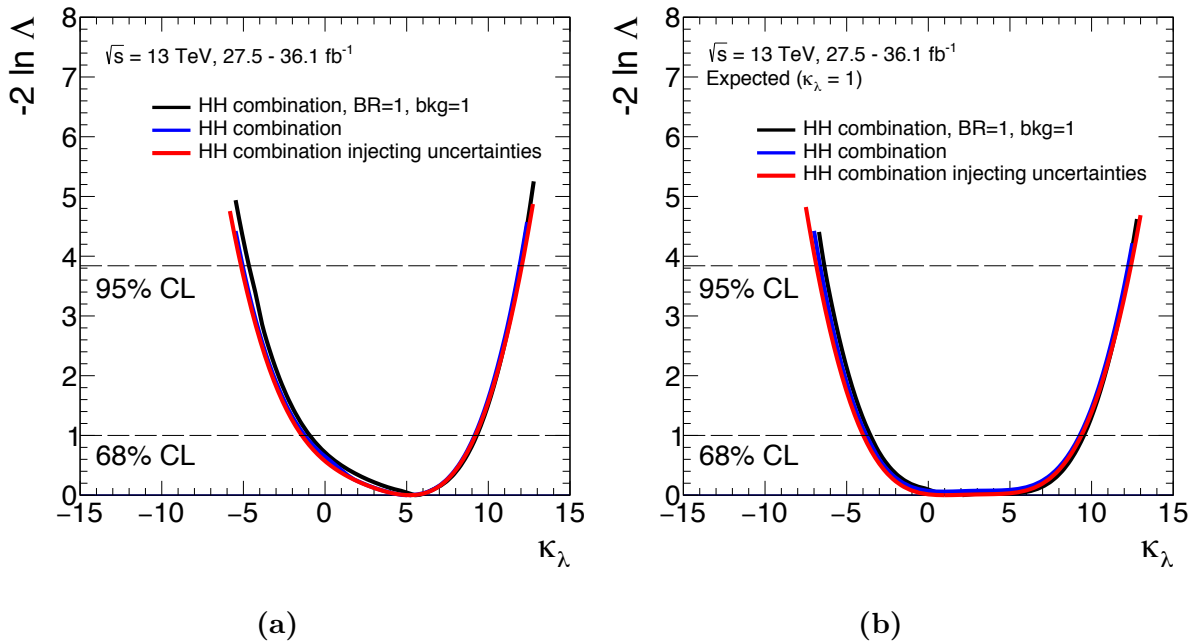


Figure 7.13: Value of $-2 \ln \Lambda(\kappa_\lambda)$ as a function of κ_λ considering different configurations. Black solid line: neither branching fractions nor single-Higgs background parameterised as a function of κ_λ ; blue solid line: branching fractions and single-Higgs background parameterised as a function of κ_λ ; red solid line: branching fractions and single-Higgs background parameterised as a function of κ_λ , theoretical uncertainties injected. Likelihood distributions are reported for data (a) and for the Asimov dataset generated in the SM hypothesis (b). The dotted horizontal lines show the $-2 \ln \Lambda(\kappa_\lambda) = 1$ level that is used to define the $\pm 1\sigma$ uncertainty on κ_λ as well as the $-2 \ln \Lambda(\kappa_\lambda) = 3.84$ level used to define the 95% CL.

Furthermore, differences between the CLs method and a likelihood-based approach have been studied. Table 7.10 summarises the different configurations that have been tested reporting the observed 95% CL intervals in the aforementioned cases. The difference between the CLs method and the profile likelihood one is at the level of a few percents. Recent computations of the double-Higgs production cross section have been performed, where QCD corrections are known up to next-to-leading order (NLO) and at next-to-next-to-leading order (NNLO) in the limit of heavy top quarks including partial finite top quark mass effects, leading to a small reduction of the SM cross section from 33.5 to 31.05 fb and a stronger dependence on κ_λ [34, 149, 150]. Figure 7.14 shows the comparison between

Method	κ_λ interval at 95% CL (obs)
CLs	[-5.1, 11.9]
Likelihood scan (BR=1, SH=1, no theory uncertainties)	[-4.7, 12.0]
Likelihood scan (BR and SH parameterised)	[-5.0, 11.9]
Likelihood scan (BR and SH parameterised, theory uncertainties)	[-5.1, 12.0]

Table 7.10: 95% CL comparisons for different approaches. The CLs approach is exploited in order to cross check double-Higgs publication results. In the likelihood approaches, the three different configurations listed in the first column have been tested.

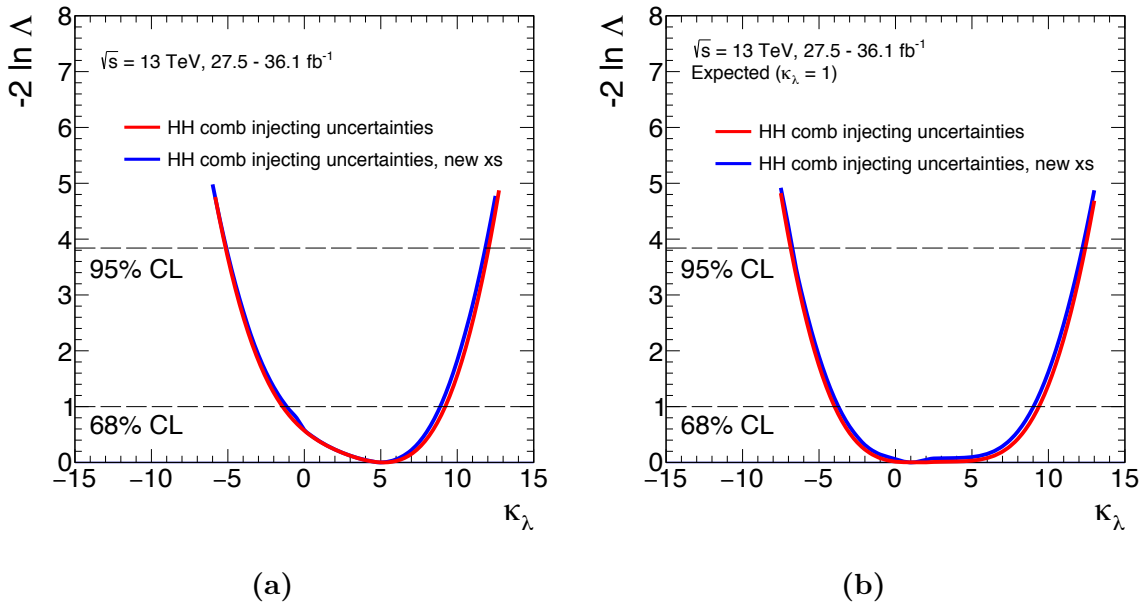


Figure 7.14: Value of $-2 \ln \Lambda(\kappa_\lambda)$ as a function of κ_λ for data (a) and for the Asimov dataset (b). Solid red line: HH combined likelihood distribution when BRs and SH background are parameterised as a function of κ_λ and theory uncertainties are injected; blue solid line: likelihood distribution including recent computation of the HH SM cross section. The dotted horizontal lines show the $-2 \ln \Lambda(\kappa_\lambda) = 1$ level that is used to define the $\pm 1\sigma$ uncertainty on κ_λ as well as the $-2 \ln \Lambda(\kappa_\lambda) = 3.84$ level used to define the 95% CL.

the likelihood distribution obtained exploiting the old recommendation and the likelihood distribution obtained including recent computation of the double-Higgs SM cross section for data and for the Asimov dataset. In order to be consistent with the double-Higgs results reported in Reference [35], these recent calculations have not been used, but their impact on the Higgs-boson self-coupling 95% CL interval has been evaluated to be less than 2%.

The strong dependence of the double-Higgs cross section $\sigma_{ggF}(pp \rightarrow HH)$ on κ_t can be exploited through a likelihood fit performed to constrain at the same time κ_λ and κ_t , setting all the other coupling modifiers to their SM values. Figure 7.15 shows negative log-likelihood contours on the $(\kappa_\lambda, \kappa_t)$ grid, where the coloured areas are not part of the allowed region because the acceptance of the $HH \rightarrow b\bar{b}\gamma\gamma$ analysis is not reliable for $|\kappa_\lambda/\kappa_t| \geq 20$. It is clear that there is no chance of measuring κ_λ and κ_t at the same time without assumptions on one of the two coupling modifiers, as it is also shown in the theoretical contours of Figure 7.16 where the reference values of 6.9 and 10 correspond to the ATLAS observed and expected upper limits on the $\sigma_{ggF}(pp \rightarrow HH)$ cross section times the predicted SM cross section [35]; furthermore κ_t is superiorly limited and can be measured better than κ_λ , given the cross-section dependences on κ_t^4 and on κ_λ/κ_t .

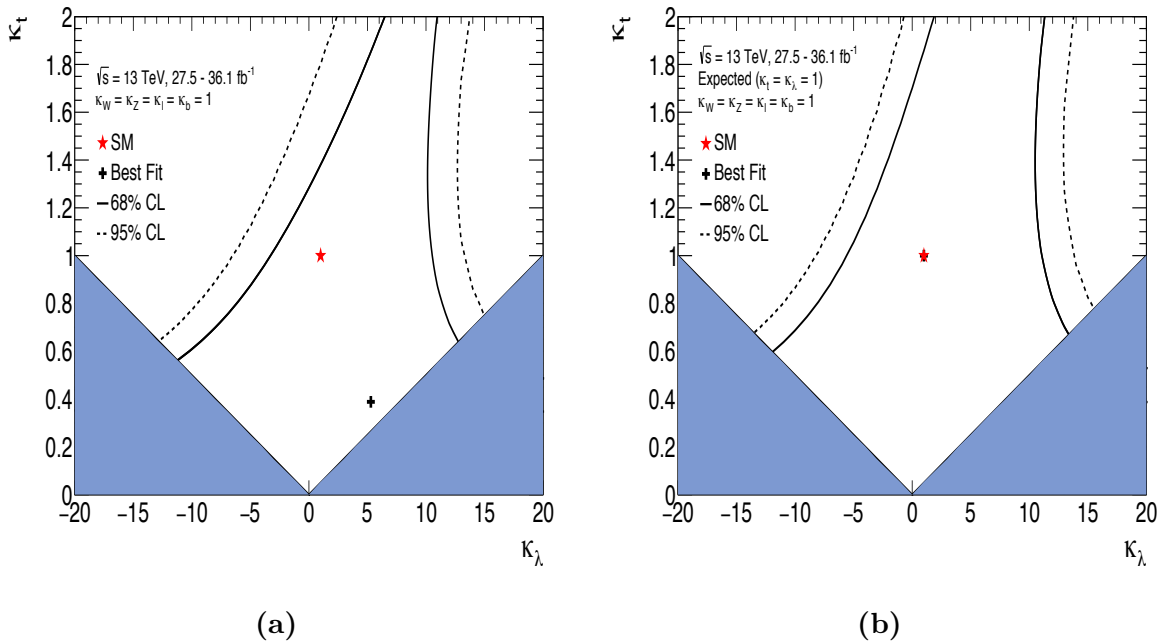


Figure 7.15: Negative log-likelihood contours at 68% and 95% CL in the $(\kappa_\lambda, \kappa_t)$ plane on data (a) and on the Asimov dataset generated under the SM hypothesis (b). The best-fit value is indicated by a cross while the SM hypothesis is indicated by a star. The plot assumes that the approximations in References [55, 133] are valid inside the shown contours. The degeneracy of measuring at the same time κ_λ and κ_t is shown; the coloured area corresponds to $|\kappa_\lambda/\kappa_t| < 20$, a constrain coming from the $HH \rightarrow b\bar{b}\gamma\gamma$ analysis.

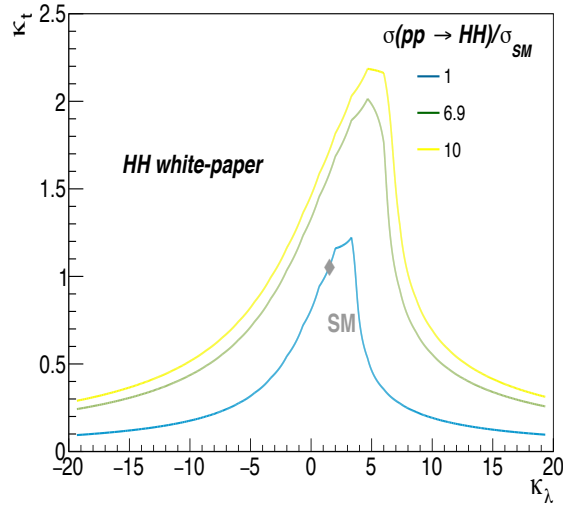


Figure 7.16: Contour level of $\sigma(pp \rightarrow HH)/\sigma_{SM}$ as a function of κ_t and κ_λ , under the assumption of no additional Higgs coupling vertices. The diamond indicates the SM predicted value. The reference values of 6.9 and 10 correspond to the best available observed and expected upper limits on the $\sigma_{ggF}(pp \rightarrow HH)/\sigma_{ggF}^{SM}(pp \rightarrow HH)$ as measured by the ATLAS experiment [34].

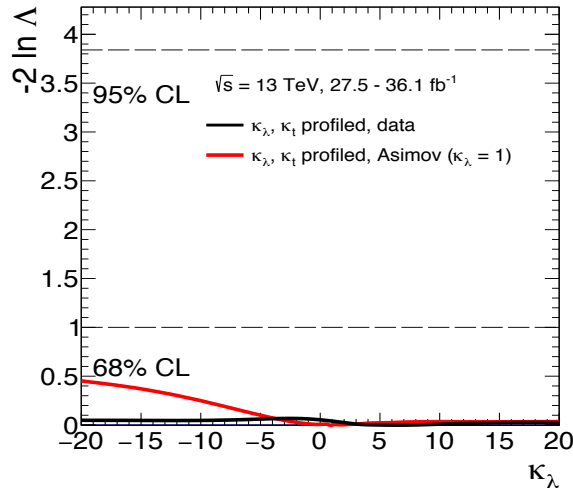


Figure 7.17: Value of $-2 \ln \Lambda(\kappa_\lambda)$ as a function of κ_λ ; the black solid line represents data while the red solid line represents the Asimov dataset generated in the SM hypothesis. The dotted horizontal lines show the $-2 \ln \Lambda(\kappa_\lambda) = 1$ level that is used to define the $\pm 1\sigma$ uncertainty on κ_λ as well as the $-2 \ln \Lambda(\kappa_\lambda) = 3.84$ level used to define the 95% CL.

This effect is clear also looking at the 1D scan, shown in Figure 7.17 both for data (black solid line) and for the Asimov dataset (red solid line). Due to the limited sensitivity of the double-Higgs analyses, even the 1σ interval cannot be reached in the κ_λ likelihood scan profiling κ_t and the curves are almost flat. The low constraining power, represented by a small raising of the likelihood distribution for negative κ_λ , comes from the parameterisation as a function of κ_λ and κ_t of the branching fractions and of the

single-Higgs production cross sections in double-Higgs background, otherwise the curves become completely flat.

From the 2D contours, it seems that, restricting κ_t lower bound away from the best-fit value, greater values of the likelihood compared to the minimum one can be found and thus the 1σ interval or even 95% CL can be reached. This effect is more evident looking at Figure 7.18 where the value of $-2 \ln \Lambda(\kappa_\lambda)$ as a function of κ_λ is shown varying κ_t ranges for the fit to data.

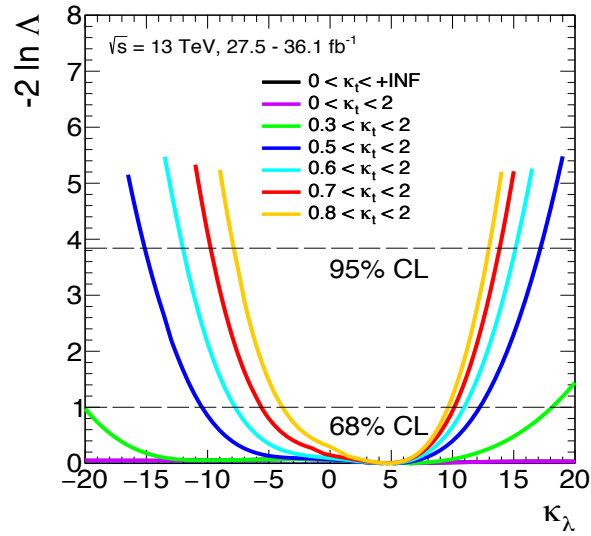


Figure 7.18: Value of $-2 \ln \Lambda(\kappa_\lambda)$ as a function of κ_λ varying κ_t ranges for data. The dotted horizontal lines show the $-2 \ln \Lambda(\kappa_\lambda) = 1$ level that is used to define the $\pm 1\sigma$ uncertainty on κ_λ as well as the $-2 \ln \Lambda(\kappa_\lambda) = 3.84$ level used to define the 95% CL.

It will be shown in Chapter 9 that the combination with the single-Higgs analyses allows to solve the degeneracy between κ_λ and κ_t and restores the ability of the double-Higgs analyses in constraining κ_λ .

Chapter 8

Constraints on the Higgs-boson self-coupling from single-Higgs production and decay measurements

This chapter presents the results of the extraction of κ_λ limits from single-Higgs production and decay modes exploiting the complementary approach to measure the Higgs self-coupling described in Chapter 6, applying next-to-leading order electroweak corrections depending on κ_λ at these processes. Section 8.1 introduces data and input measurements together with key elements of the analyses included in the combination. How the theoretical framework described in Chapter 6 is implemented in single-Higgs production and decay modes is briefly summarised in Section 8.2 while Section 8.3 expands the statistical description reported in Chapter 7 in order to introduce elements necessary to produce the results of this chapter. Constraints on κ_λ in different fit configurations are reported in Sections 8.4 and 8.5 while Section 8.6 reports projections of single-Higgs results considering a luminosity of 3000 fb^{-1} .

8.1 Data and input measurements

The results presented in this chapter are obtained using data collected by the ATLAS experiment in 2015, 2016 and 2017 from 13 TeV pp collision data corresponding to an integrated luminosity of up to 79.8 fb^{-1} . The integrated luminosity for each analysed decay channel is summarised in Table 8.1. The single-Higgs analyses exploited in order to make this combination include the ggF , VBF , WH , ZH and $t\bar{t}H$ production modes and the $\gamma\gamma$, WW^* , ZZ^* , $b\bar{b}$ and $\tau^+\tau^-$ decay channels. All single-Higgs regions are defined for a Higgs boson rapidity y_H satisfying $|y_H| < 2.5$. Jets are reconstructed from all stable particles with a lifetime greater than 10 ps, excluding the Higgs decay products, using the anti- k_t algorithm with a jet radius parameter $R = 0.4$, and must have a transverse momentum $p_{T,jet} > 30 \text{ GeV}$.

The simplified template cross-section (STXS) framework, when available, is used for single-Higgs production modes in order to minimise the dependence on theoretical uncertainties that are directly folded into the measurements and to maximise experimental sensitivity to different processes. Several stages with an increasing number of bins are defined within this framework; in particular, the categories included in this combination are

Analysis	Integrated luminosity (fb ⁻¹)	References
$H \rightarrow \gamma\gamma$ (including $t\bar{t}H$, $H \rightarrow \gamma\gamma$)	79.8	[151–153]
$H \rightarrow ZZ^* \rightarrow 4\ell$ (including $t\bar{t}H$, $H \rightarrow ZZ^* \rightarrow 4\ell$)	79.8	[154, 155]
$H \rightarrow WW^* \rightarrow e\nu\mu\nu$	36.1	[156]
$H \rightarrow \tau\tau$	36.1	[157]
VH , $H \rightarrow b\bar{b}$	79.8	[158, 159]
$t\bar{t}H$, $H \rightarrow b\bar{b}$ and $t\bar{t}H$ multilepton	36.1	[160, 161]

Table 8.1: Integrated luminosity of the datasets used for each input analysis to the single-Higgs combination. The last column provides references to publications describing each measurement included in detail.

based on the stage-1 of the STXS framework within which, depending on the Higgs-boson production mode, the phase space is subdivided as follows [27, 162]:

- the gluon-fusion production mode is subdivided in regions defined by jet multiplicity and transverse momentum of the Higgs boson, p_T^H . Additionally, two regions with VBF -like kinematics, defined by the presence of two high- η jets with large dijet mass, are considered. The $b\bar{b}H$ and $gg \rightarrow Z(\text{had})H$ production modes are considered as small additional contributions to the expected yields in each STXS bin;
- the phase space of quark-initiated production processes $qq \rightarrow Hqq$ is split using, as a variable, the transverse momentum of the highest- p_T jet, called p_T^{j1} ; in fact, the lower p_T^{j1} region is expected to be dominated by SM-like events, while the high- p_T^{j1} region is sensitive to potential BSM contributions. Other regions are then defined, i.e. two VBF -topology regions by using the presence of two jets with $m_{jj} \geq 400$ GeV and a pseudorapidity difference $|\Delta\eta_{jj}| \geq 2.8$, a region with two jets consistent with $V(\rightarrow qq)H$ production, and a region for the remaining events;
- VH production mode is split according to the vector boson, i.e. $W \rightarrow \ell\nu$ and $Z \rightarrow \ell\ell + \nu\bar{\nu}$ and a further split into bins of p_T^V is made, aligned with the quantity used in the $H \rightarrow b\bar{b}$ analysis, representing one of the dominant contribution in the VH bins. Bins depending on the number of jets, reflecting the different experimental sensitivity and with the target of avoiding the corresponding theory dependence, are also used;
- the $t\bar{t}H$ and tH production modes are considered inclusively in one single region.

The stage-1 of the STXS framework exploited in this combination are reported in Figure 8.1. The single-Higgs analysis categories are summarised in Tables 8.2 and 8.3 [41]:

- $t\bar{t}H$ production mode:
 - seven categories are defined to select $H \rightarrow \gamma\gamma$ decay channel, including both semileptonic and hadronic top-quark decay processes through various selections on the multiplicities and kinematics of leptons, jets, and jets tagged as containing b -hadrons;

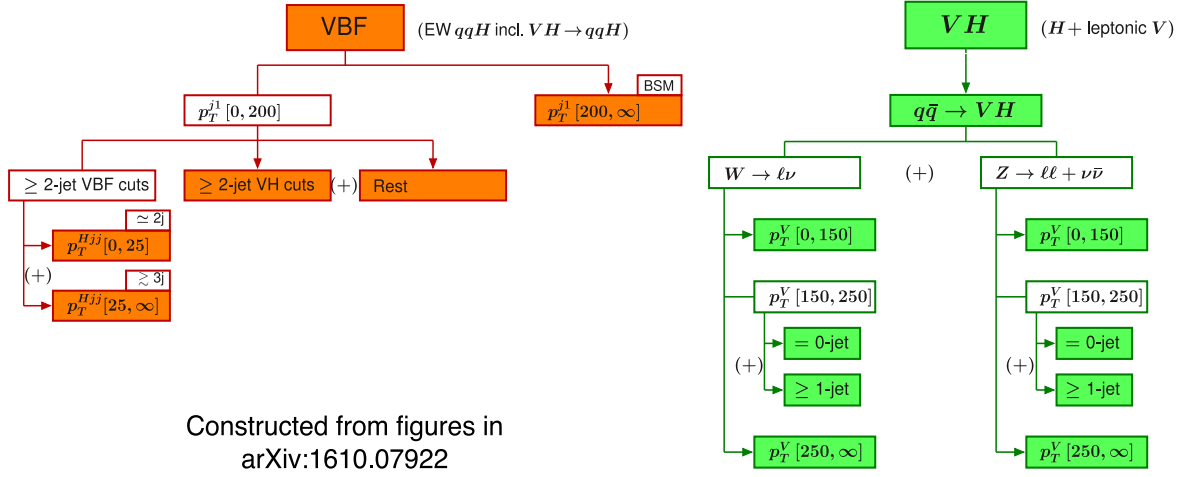


Figure 8.1: Schematic diagram of the $VBF + V(\text{had})H$ (left) and $V(\text{lep})H$ (right) STXS regions [163].

- two categories are defined to select $H \rightarrow ZZ^* \rightarrow 4\ell$ decay channel, with at least one b -tagged jet and three or more additional jets, or one additional lepton and at least two additional jets, with fully hadronic or semileptonic top-quark decays, respectively;
- seven categories are defined to select $H \rightarrow WW^*, ZZ^*$ (not 4ℓ), $\tau^+\tau^-$ decay channels; they are categorised by the number and the flavour of reconstructed charged-lepton candidates: one lepton with two τ_{had} candidates, two same-charge leptons with zero or one τ_{had} candidates, two opposite-charge leptons with one τ_{had} candidate, three leptons with zero or one τ_{had} candidates, and four leptons. Events in all channels are required to have at least two jets, at least one of which must be b -tagged;
- nineteen categories are defined to select $H \rightarrow b\bar{b}$ decay channel, events are classified into eleven (seven) orthogonal categories in the single-lepton (dilepton) channel, according to the jet multiplicity and to the values of the b -tagging discriminant for the jets. In the single-lepton channel, an additional category, referred to as “boosted”, is designed to select events with large transverse momenta for the Higgs candidate ($p_T^H > 200$ GeV) and one for the top-quark candidates ($p_T^t > 250$ GeV).
- VH production mode:
 - eight categories are defined to select $\gamma\gamma$ decay channel: five categories are defined to select WH and ZH production modes with leptonic decays of the W or of the Z bosons, based on the presence of leptons and missing transverse momentum E_T^{miss} , one category requires the presence of two jets, with the leading jet transverse momentum $p_T^{j1} > 200$ GeV and two categories select hadronic vector-boson decays by requiring two jets with an invariant mass compatible with the W or Z boson mass;

- three categories are defined to select $H \rightarrow ZZ^* \rightarrow 4\ell$ decay channel, one category with leptonic vector-boson decays, and the other two categories with 0-jet and $p_T^{A\ell} \geq 100$ GeV, and at least two jets with a hadronically decaying vector boson for $m_{jj} < 120$ GeV;
 - eight categories are defined to select $H \rightarrow b\bar{b}$ decay channel, where events are classified according to the charged-lepton multiplicity, the vector-boson transverse momentum, p_T^V , and the jet multiplicity. For final states with zero or one lepton, $p_T^V > 150$ GeV is required. In two-lepton final states, two regions are considered, $75 \text{ GeV} < p_T^V < 150 \text{ GeV}$ and $p_T^V > 150 \text{ GeV}$. Each of these regions is finally separated into a category with exactly two reconstructed jets and another with three or more.
- VBF production mode:
- four categories are defined for the $\gamma\gamma$ decay channel, in order to enrich VBF production by requiring forward jets in a VBF-like topology region;
 - two categories are defined to select $H \rightarrow ZZ^* \rightarrow 4\ell$ decay channel, in which the transverse momentum of the leading jet, p_T^{j1} , is required to be either above or below 200 GeV;
 - one category is defined to select $H \rightarrow WW^*$ decay channel, containing events with the number of jets ≥ 2 , naturally sensitive to this production mode;
 - three categories are defined to select $H \rightarrow \tau^+\tau^-$ decay channel, one category is defined by requiring the transverse momentum of the $\tau^+\tau^-$ system, $p_T^{\tau\tau}$, to be above 140 GeV, for $\tau_{had}\tau_{had}$ events only, while the other two categories are defined for lower and higher values of m_{jj} .
- ggF production mode:
- ten categories are defined for the $\gamma\gamma$ decay channel, separating events with 0, 1, and ≥ 2 jets and further classifying them according to the pseudorapidity of the two photons (for 0-jet events) or according to the transverse momentum of the diphoton system, $p_T^{\gamma\gamma}$, (for 1 and ≥ 2 -jet events);
 - four categories are defined to select $H \rightarrow ZZ^* \rightarrow 4\ell$ decay channel, one category containing 0-jet events and $p_T^{A\ell} < 100$ GeV and the other three categories containing 1-jet events with boundaries at $p_T^{A\ell} = 60$ GeV and $p_T^{A\ell} = 120$ GeV;
 - sixteen categories are defined to select $H \rightarrow WW^*$ decay channel, based on the flavour of the leading lepton (e or μ), based on two bins of the invariant mass of the dilepton system, $m_{\ell\ell}$, and on two bins of the transverse momentum of the subleading lepton, $p_T^{\ell_2}$;
 - two categories are defined to select $H \rightarrow \tau^+\tau^-$ decay channel, with selections on the angular separation between the τ -leptons and requiring $p_T^{\tau\tau} > 140$ GeV and $p_T^{\tau\tau} \leq 140$ GeV.

	$H \rightarrow \gamma\gamma$	$H \rightarrow ZZ^*$	$H \rightarrow WW^*$	$H \rightarrow \tau\tau$	$H \rightarrow b\bar{b}$
	$t\bar{t}H$ leptonic (3 categories) $t\bar{t}H$ hadronic (4 categories)	$t\bar{t}H$ multilepton $1 \ell + 2 \tau_{had}$ $t\bar{t}H$ multilepton 2 opposite-sign $\ell + 1 \tau_{had}$ $t\bar{t}H$ multilepton 2 same-sign ℓ (categories for 0 or 1 τ_{had}) $t\bar{t}H$ multilepton 3 ℓ (categories for 0 or 1 τ_{had}) $t\bar{t}H$ multilepton 4 ℓ (except $H \rightarrow ZZ^* \rightarrow 4\ell$) $t\bar{t}H$ leptonic, $H \rightarrow ZZ^* \rightarrow 4\ell$ $t\bar{t}H$ hadronic, $H \rightarrow ZZ^* \rightarrow 4\ell$			$t\bar{t}H$ 1 ℓ , boosted $t\bar{t}H$ 1 ℓ , resolved (11 categories) $t\bar{t}H$ 2 ℓ (7 categories)
$t\bar{t}H$					
	VH 2 ℓ VH 1 ℓ , $p_T^{\ell+E_T^{miss}} \geq 150$ GeV VH 1 ℓ , $p_T^{\ell+E_T^{miss}} < 150$ GeV VH E_T^{miss} , $E_T^{miss} \geq 150$ GeV VH E_T^{miss} , $E_T^{miss} < 150$ GeV $VH+VBF$ $p_T^{j1} \geq 200$ GeV VH hadronic (2 categories)	VH leptonic 0-jet, $p_T^{4\ell} \geq 100$ GeV 2-jet, $m_{jj} < 120$ GeV			2ℓ , $75 \leq p_T^V < 150$ GeV, $N_{jets} = 2$ 2ℓ , $75 \leq p_T^V < 150$ GeV, $N_{jets} \geq 3$ 2ℓ , $p_T^V \geq 150$ GeV, $N_{jets} = 2$ 2ℓ , $p_T^V \geq 150$ GeV, $N_{jets} \geq 3$ 1ℓ $p_T^V \geq 150$ GeV, $N_{jets} = 2$ 1ℓ $p_T^V \geq 150$ GeV, $N_{jets} = 3$ 0ℓ , $p_T^V \geq 150$ GeV, $N_{jets} = 2$ 0ℓ , $p_T^V \geq 150$ GeV, $N_{jets} = 3$
VH					

Table 8.2: Summary of the signal categories coming from the $t\bar{t}H$ and VH production modes entering the combined measurements. The following conventions are adopted: ℓ refers to e or μ , ℓ_2 to the lepton of lowest p_T , E_T^{miss} to the missing transverse energy, j to a light jet, $j1$ to the light jet of highest p_T ; $p_T^{\ell+E_T^{miss}}$ is the p_T of the ℓ, E_T^{miss} system, $p_T^{4\ell}$ the p_T of the four lepton system and similarly for $p_T^{\gamma\gamma}$, $p_T^{\tau\tau}$ and $p_T^{\gamma jj}$. p_T^V refers to the p_T of the vector boson (V) in the VH category, $m_{\ell\ell}$ is the invariant mass of the di-lepton system [163].

	$H \rightarrow \gamma\gamma$	$H \rightarrow ZZ^*$	$H \rightarrow WW^*$	$H \rightarrow \tau\tau$	$H \rightarrow b\bar{b}$
VBF	$VBF, p_T^{\gamma\gamma jj} \geq 25 \text{ GeV}$ (2 categories)	2-jet $VBF, p_T^{j1} \geq 200 \text{ GeV}$	2-jet VBF	$VBF, p_T^{\tau\tau} > 140 \text{ GeV}$ ($\tau_{had}\tau_{had}$ only)	
	$VBF, p_T^{\gamma\gamma} < 25 \text{ GeV}$ (2 categories)	2-jet $VBF, p_T^{j1} < 200 \text{ GeV}$		VBF high- m_{jj} VBF low- m_{jj}	
ggF	2-jet, $p_T^{\gamma\gamma} \geq 200 \text{ GeV}$	1-jet, $p_T^{4\ell} \geq 120 \text{ GeV}$	1-jet, $m_{\ell\ell} < 30 \text{ GeV}, p_T^{\ell_2} < 20 \text{ GeV}$	Boosted, $p_T^{\tau\tau} > 140 \text{ GeV}$	
	2-jet, $120 \text{ GeV} \leq p_T^{\gamma\gamma} < 200 \text{ GeV}$	1-jet, $60 \text{ GeV} \leq p_T^{4\ell} < 120 \text{ GeV}$	1-jet, $m_{\ell\ell} < 30 \text{ GeV}, p_T^{\ell_2} \geq 20 \text{ GeV}$	Boosted, $p_T^{\tau\tau} \leq 140 \text{ GeV}$	
	2-jet, $60 \text{ GeV} \leq p_T^{\gamma\gamma} < 120 \text{ GeV}$	1-jet, $p_T^{4\ell} < 60 \text{ GeV}$	1-jet, $m_{\ell\ell} \geq 30 \text{ GeV}, p_T^{\ell_2} < 20 \text{ GeV}$		
	2-jet, $p_T^{\gamma\gamma} < 60 \text{ GeV}$	0-jet, $p_T^{4\ell} < 100 \text{ GeV}$	1-jet, $m_{\ell\ell} \geq 30 \text{ GeV}, p_T^{\ell_2} \geq 20 \text{ GeV}$		
	1-jet, $p_T^{\gamma\gamma} \geq 200 \text{ GeV}$		0-jet, $m_{\ell\ell} < 30 \text{ GeV}, p_T^{\ell_2} < 20 \text{ GeV}$		
	1-jet, $120 \text{ GeV} \leq p_T^{\gamma\gamma} < 200 \text{ GeV}$		0-jet, $m_{\ell\ell} < 30 \text{ GeV}, p_T^{\ell_2} \geq 20 \text{ GeV}$		
	1-jet, $60 \text{ GeV} \leq p_T^{\gamma\gamma} < 120 \text{ GeV}$		0-jet, $m_{\ell\ell} \geq 30 \text{ GeV}, p_T^{\ell_2} < 20 \text{ GeV}$		
	1-jet, $p_T^{\gamma\gamma} < 60 \text{ GeV}$		0-jet, $m_{\ell\ell} \geq 30 \text{ GeV}, p_T^{\ell_2} \geq 20 \text{ GeV}$		
	0-jet (2 categories)		0-jet, $m_{\ell\ell} \geq 30 \text{ GeV}, p_T^{\ell_2} \geq 20 \text{ GeV}$		

Table 8.3: Summary of the signal categories coming from the VBF and ggF production modes entering the combined measurements. The following conventions are adopted: ℓ refers to e or μ , ℓ_2 to the lepton of lowest p_T , E_T^{miss} to the missing transverse energy, j to a light jet, $j1$ to the light jet of highest p_T ; $p_T^{\ell+E_T^{\text{miss}}}$ is the p_T of the ℓ, E_T^{miss} system, $p_T^{4\ell}$ the p_T of the four lepton system and similarly for $p_T^{\gamma\gamma}, p_T^{\tau\tau}$ and $p_T^{\gamma\gamma jj}$. p_T^V refers to the p_T of the vector boson (V) in the VH category, $m_{\ell\ell}$ is the invariant mass of the di-lepton system [163].

8.2 Implementation of the theoretical model

The theoretical framework described in Chapter 6 is implemented in the single-Higgs channels, i.e. in the parameterisations of the signal strengths, defined in Chapter 1, for the single-Higgs initial states, i , as:

$$\mu_i(\kappa_\lambda, \kappa_i) = \frac{\sigma^{\text{BSM}}}{\sigma^{\text{SM}}} = Z_H^{\text{BSM}}(\kappa_\lambda) \left[\kappa_i^2 + \frac{(\kappa_\lambda - 1)C_1^i}{K_{\text{EW}}^i} \right], \quad (8.1)$$

while the Higgs-boson decay final states, f , are modified as:

$$\mu_f(\kappa_\lambda, \kappa_f) = \frac{\text{BR}_f^{\text{BSM}}}{\text{BR}_f^{\text{SM}}} = \frac{\kappa_f^2 + (\kappa_\lambda - 1)C_1^f}{\sum_j \text{BR}_j^{\text{SM}} \left[\kappa_j^2 + (\kappa_\lambda - 1)C_1^j \right]} \quad (8.2)$$

being κ_i and κ_f the LO modifiers of the Higgs couplings to SM particles.

Concerning the inclusive production modes, the values of the C_1 and K_{EW} coefficients as well as the κ modifiers at LO for the initial state i , κ_i^2 , for the ggF , VBF , ZH , WH and $t\bar{t}H$ production modes are reported in Table 8.4 and are taken from References [41, 55, 133]; they are averaged over the full phase space accessible through these processes. In this chapter, only the coupling modifiers $\kappa_F = \kappa_t = \kappa_b = \kappa_\ell$ and $\kappa_V = \kappa_W = \kappa_Z$ are considered, describing the modifications of the SM Higgs boson couplings to fermions and vector bosons, respectively. For small deviations of the coupling modifiers from one, the dependence of NLO-EW corrections on these coupling modifiers can be neglected.

Production mode	ggF	VBF	ZH	WH	$t\bar{t}H$
$C_1^i \times 100$	0.66	0.63	1.19	1.03	3.52
K_{EW}^i	1.049	0.932	0.947	0.93	1.014
κ_i^2	$1.04 \kappa_t^2 + 0.002 \kappa_b^2 - 0.04 \kappa_t \kappa_b$	$0.73 \kappa_W^2 + 0.27 \kappa_Z^2$	κ_Z^2	κ_W^2	κ_t^2

Table 8.4: Values of the C_1^i coefficients, representing linear κ_λ -dependent corrections to single-Higgs production modes (second row); values of the K_{EW}^i coefficients [55, 133], taking into account NLO EW corrections in the SM hypothesis (third row); expressions of the initial state κ modifiers at LO, κ_i^2 , [41] for Higgs-boson production processes (fourth row).

The C_1^f coefficients and the expressions of the κ modifiers at LO for the final state f , κ_f^2 , are reported in Table 8.5 for all the analysed decay modes. The interactions between the Higgs boson and the gluons and photons are resolved in terms of the coupling modifiers of the SM particles that enter in the loop-level diagrams, i.e. in terms of the coupling modifiers $\kappa_b = \kappa_F$ and $\kappa_t = \kappa_F$, $\kappa_W = \kappa_V$ and $\kappa_t = \kappa_F$, respectively.

The simulation of the single-Higgs signal samples is performed using Montecarlo simulations generated under the SM hypothesis. This is possible because at the lowest order in the electroweak expansion only one diagram participates in the single-Higgs boson production, therefore the κ -modifiers (κ_t , κ_b , κ_{lep} , κ_W and κ_Z) factorise completely the total cross section; this holds also for all decays. The NLO-EW corrections depending on κ_λ , presenting quadratically and linearly dependent contributions, affect not only the inclusive rates of Higgs-boson production and decay processes, but also their kinematics,

Decay mode	$H \rightarrow \gamma\gamma$	$H \rightarrow WW^*$	$H \rightarrow ZZ^*$	$H \rightarrow b\bar{b}$	$H \rightarrow \tau\tau$
$C_1^f \times 100$	0.49	0.73	0.82	0	0
κ_f^2	$1.59\kappa_W^2 + 0.07\kappa_t^2 - 0.67\kappa_W\kappa_t$	κ_W^2	κ_Z^2	κ_b^2	κ_ℓ^2

Table 8.5: Values of C_1^f [55, 133] coefficients, representing linear κ_λ -dependent corrections to single-Higgs decay channels (second row); expressions of the final state κ modifiers at LO, κ_f^2 , [41] for Higgs-boson decay modes (third row).

varying as a function of variables like p_T^H . In particular, the largest deviations in kinematic distributions with respect to the SM are expected in the ZH , WH , and $t\bar{t}H$ production modes, while in Higgs-boson decay kinematics, no significant modifications are expected, as shown in Chapter 6.

This dependence has been partially taken into account by exploiting cross-section measurements in the regions defined by the STXS stage-1 framework defined in the previous section. Not all the differential information available for different production modes is used; in fact, the gluon fusion production mode is subdivided in regions defined by jet multiplicity and transverse momentum of the Higgs boson, but differential corrections are not yet available, involving higher order calculations including two loop corrections; therefore the corresponding STXS bins share the same parameterisation and coefficients used for the inclusive ggF production. The situation is reversed looking at $t\bar{t}H$ production mode that is considered inclusively in one single bin but because of the fact that, for this production mode, the STXS binned analyses are still under development. Furthermore, the $gg \rightarrow ZH$ cross section is not parameterised as a function of κ_λ due to the missing theoretical computations and contributing mostly in high- p_T^H regions where the sensitivity to κ_λ is small, as shown in Figure 6.10 (b).

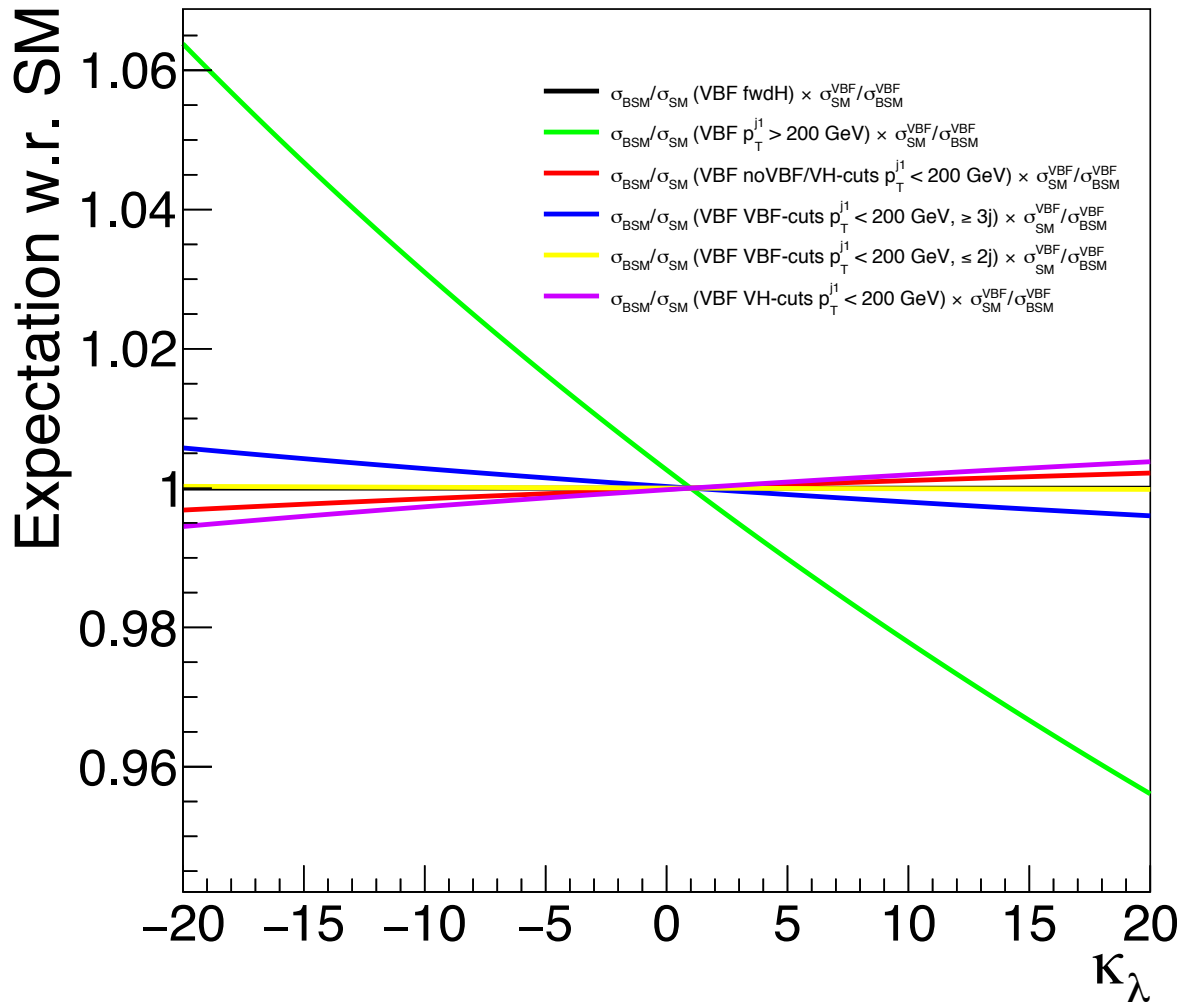
The parameterisation as a function of κ_λ of the signal strengths for the production modes, shown in Equation 8.1, can be adapted to describe the cross section in each STXS bin. This can be achieved re-deriving the value of the kinematic-dependent coefficients C_1^i in each region defined in the measurement [163]: the C_1^i coefficients have thus been computed using samples of events generated at LO EW using MADGRAPH5_AMC@NLO 2.5.5 [164], and reweighted on an event-by-event basis with the tool provided in Reference [165]. The C_1^i values for each STXS bin are reported in Table 8.6.

Modifications of the acceptances of the different production modes of the STXS framework have been tested, considering ZH , WH , and $t\bar{t}H$ production modes being characterised by a stronger kinematic-dependence on the Higgs self-coupling corrections with respect to the other modes. The largest variation is observed for $\kappa_\lambda < -10$ for the $t\bar{t}H \rightarrow \gamma\gamma$ channel, otherwise the acceptance is almost constant.

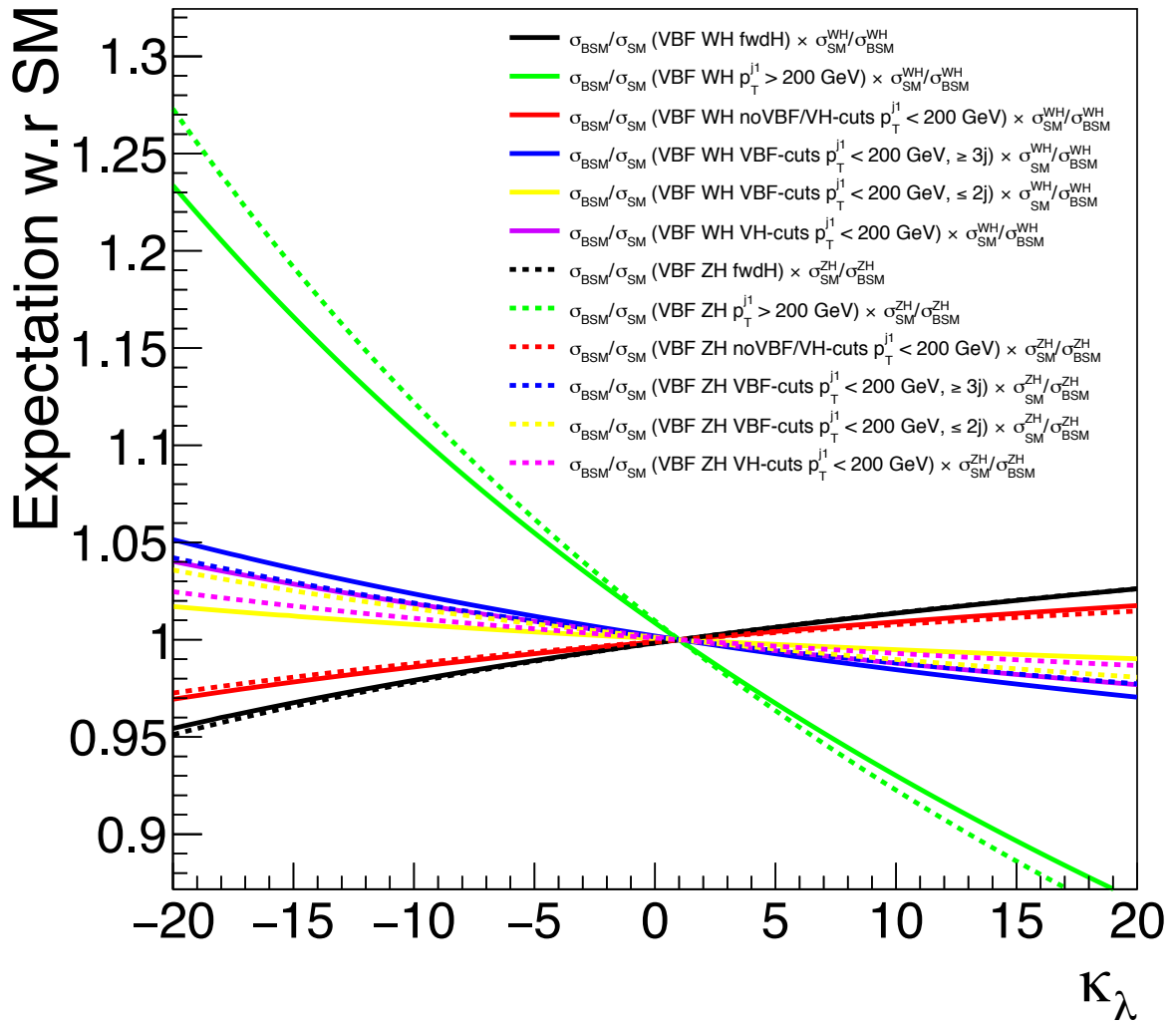
Figure 8.2 shows the ratio σ_{BSM}/σ_{SM} for each VBF , WH and ZH STXS bin normalised to the same ratio computed for the inclusive cross section of the corresponding production process. The STXS bins with the highest p_T are the ones with the strongest dependence on κ_λ , otherwise there is a negligible dependence; the WH and ZH are the production modes showing the largest kinematic dependence (excluding the $t\bar{t}H$ that does not have STXS bins).

STXS region		<i>VBF</i>	<i>WH</i>	<i>ZH</i>
		$C_1^i \times 100$		
<i>VBF</i> + V(had) <i>H</i>	<i>VBF</i> -cuts + $p_T^{j1} < 200$ GeV, $\leq 2j$	0.63	0.91	1.07
	<i>VBF</i> -cuts + $p_T^{j1} < 200$ GeV, $\geq 3j$	0.61	0.85	1.04
	<i>VH</i> -cuts + $p_T^{j1} < 200$ GeV	0.64	0.89	1.10
	no <i>VBF/VH</i> -cuts, $p_T^{j1} < 200$ GeV	0.65	1.13	1.28
	$p_T^{j1} > 200$ GeV	0.39	0.23	0.28
$qq \rightarrow H\ell\nu$	$p_T^V < 150$ GeV		1.15	
	$150 < p_T^V < 250$ GeV, $0j$		0.18	
	$150 < p_T^V < 250$ GeV, $\geq 1j$		0.33	
	$p_T^V > 250$ GeV		0	
$qq \rightarrow H\ell\ell$	$p_T^V < 150$ GeV			1.33
	$150 < p_T^V < 250$ GeV, $0j$			0.20
$qq \rightarrow H\nu\nu$	$150 < p_T^V < 250$ GeV, $\geq 1j$			0.39
	$p_T^V > 250$ GeV			0

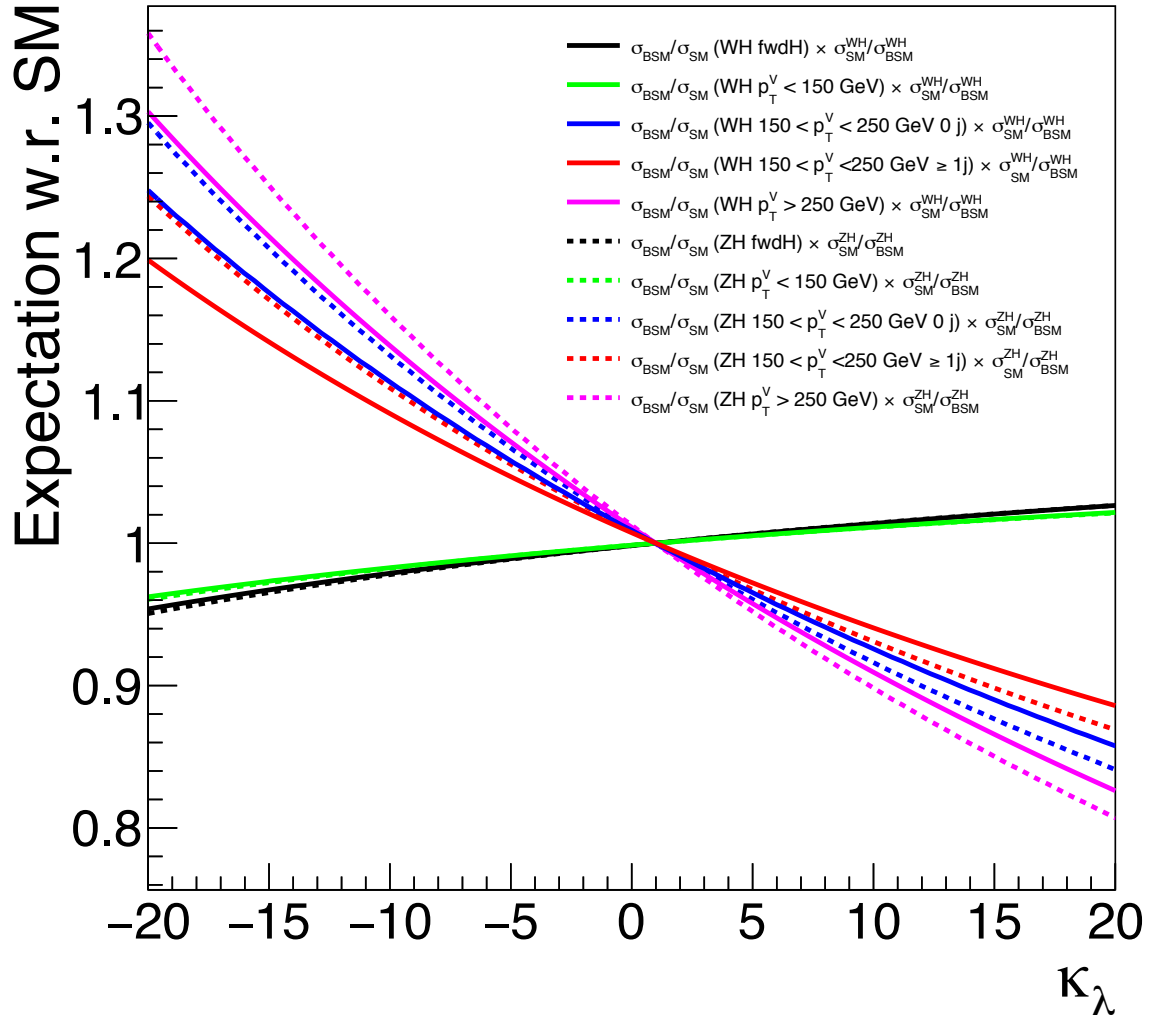
Table 8.6: C_1^i coefficients for each region of the STXS scheme for the *VBF*, *WH* and *ZH* production modes. The same definition for STXS regions and production modes as in Tables 8.2 and 8.3 is used. In the *VBF* categories, “*VBF*-cuts” [27] indicates selections applied to target the *VBF* dijet topology, with requirements on the dijet invariant mass (m_{jj}) and the difference in pseudorapidity between the two jets; the additional $\leq 2j$ and $\geq 3j$ region separation is performed indirectly by requesting $p_T^{Hjj} \leq 25$ GeV. “*VH*-cuts” select the $W, Z \rightarrow jj$ decays, requiring an m_{jj} value close to the vector boson mass [27]. The C_1^i coefficients of the $p_T^V > 250$ GeV regions are negligible, $\mathcal{O}(10^{-6})$, and are set to 0 [163].



(a) Variation of the fiducial cross section of the STXS categories normalised to the inclusive cross section of the corresponding production process: *VBF* categories.



(b) Variation of the fiducial cross section of the STXS categories normalised to the inclusive cross section of the corresponding production process: WH/ZH hadronic contributions in the VBF categories.



(c)

Figure 8.2: Variation of the fiducial cross section of the STXS categories normalised to the inclusive cross section of the corresponding production process: (a) *VBF* categories, (b) *WH/ZH* hadronic contributions in the *VBF* categories, (c) *WH/ZH* categories.

Even if electroweak corrections non-depending on κ_λ can vary as a function of the kinematics of the process, inclusive K_{EW} values, describing the ratio of NLO over LO cross-section in the SM case ($\kappa_\lambda = 1$), have been used in the different phase-space regions. This approach has been followed after testing different K_{EW} values for each STXS bin used in the analysis and ensuring that these corrections become more relevant for high value of the transverse momentum of the vector bosons, where the self-coupling correction is instead expected to be less significant; furthermore, the results from fits to the Asimov dataset and on data with the new K_{EW} configuration differ by less than percent level with respect to the nominal results.

8.3 Statistical model

The results presented in this chapter are obtained from a global likelihood function $L(\vec{\alpha}, \vec{\theta})$, defined in Chapter 5, where $\vec{\alpha}$ represents the vector of the parameters of interest of the model, i.e. the coupling modifiers and the Higgs self-coupling, and $\vec{\theta}$ is the set of nuisance parameters. The global likelihood function is built as the product of the likelihood of the single-Higgs analyses that are themselves products of the likelihood of the different categories included in the analyses. Thus, the number of signal events in each analysis category j is defined as:

$$n_j^{\text{signal}}(\kappa_\lambda, \kappa_F, \kappa_V, \vec{\theta}) = \mathcal{L}_j(\vec{\theta}) \sum_i \sum_f \mu_i(\kappa_\lambda, \kappa_F, \kappa_V) \times \mu_f(\kappa_\lambda, \kappa_F, \kappa_V) \times (\sigma_{\text{SM},i}(\vec{\theta}) \times \text{BR}_{\text{SM},f}(\vec{\theta})) (\epsilon \times A)_{if,j}(\vec{\theta}) \quad (8.3)$$

where, in this case, the index i runs over all the production-process regions defined by the STXS stage-1 framework and the index f over all the decay channels included in the combination, i.e. $f = b\bar{b}, \gamma\gamma, \tau^+\tau^-, WW^*$ and ZZ^* . The term $\mu_i(\kappa_\lambda, \kappa_F, \kappa_V) \times \mu_f(\kappa_\lambda, \kappa_F, \kappa_V)$, where μ_i is defined in Equation 6.5 and μ_f in Equation 6.7, describes the yield dependence on the Higgs-boson self-coupling modifier κ_λ , and on the single-Higgs boson coupling modifiers κ_F and κ_V , representing potential deviations from the SM expectation of the self-coupling and of the couplings to vector bosons and to fermions, respectively. A full description of other terms included in Equation 8.3 together with the test statistics used in order to determine confidence intervals for the parameters of interest are reported in Chapters 5 and 7.

When presenting the results of the fit to κ_λ , its uncertainty is presented as decomposed in separate components that are:

- theoretical uncertainties affecting the background processes, i.e. “bkg. th.”;
- theoretical uncertainties affecting the Higgs-boson signal, i.e. “sig. th.”;
- experimental uncertainties, i.e. “exp.”;
- statistical uncertainties, i.e. “stat”.

The different components contributing to the total uncertainty are derived iteratively by fixing a given set of nuisance parameters to their best-fit values in the numerator and the denominator of the profile likelihood ratio repeating this procedure for each

source of uncertainty following the order listed above. The value of each component is then evaluated as the quadratic difference between the resulting uncertainty at each step and the uncertainty obtained in the previous step, where for the initial step the total uncertainty is considered. The statistical uncertainty is evaluated as the last step, fixing to their best-fit values all the nuisance parameters except for the ones that are only constrained by data, such as the data-driven background normalisations.

8.3.1 Systematic uncertainties

The systematic uncertainties included in the single-Higgs combination and the correlation scheme adopted are reported in the following [41]:

- the main theoretical uncertainties come from the limited precision reached by theoretical predictions for the signal and background processes (like QCD scale uncertainties) as well as the degree of knowledge of the parton distribution functions (PDF uncertainties) and the models used to simulate soft physics (like parton-shower uncertainties). Given the fact that different channels entering the combination have harmonised the evaluation of uncertainties, like the ones related to signal processes, they are modelled by a common set of nuisance parameter, namely they are correlated, in most of the channels.

Looking at the uncertainties associated to the modelling of signal processes, the ones having the greatest impact on the results are the uncertainties related to the QCD scale for most of the production modes, to the PDFs and to underlying events and parton shower (UE/PS) on the signal acceptance, while for the background, they are the uncertainties coming from the modelling of the dominant background both in the normalisation and in the shape, as well as from the generators used. They are reported in Tables 8.7 and 8.8.

- The branching fraction uncertainty is correlated between the input channels.
- Experimental uncertainties are usually grouped into subsets of uncertainties related to the procedure followed in order to identify and calibrate all the objects of the analyses defined in Chapter 4, like electron and photon calibration, jet energy scale and resolution, flavour tagging, etc... The main issue concerning experimental uncertainties is related to the different releases of the ATLAS software, i.e. Release 20.7 exploited by 2015-2016 analyses and Release 21 exploited by the analyses that include also the 2017 dataset. The experimental uncertainties that are correlated among different releases are the luminosity, the jet energy scale, the electron and photon resolution and energy scale, and the electron reconstruction and identification efficiency.

The experimental uncertainties having the greatest impact on the results are the uncertainties coming from photon isolation efficiency, from jet energy scale and resolution, from tau identification efficiency and from data-driven background estimations; they are reported in Table 8.9.

NP name	Description
TheorySig_QCDscale_ttH	QCD scale uncertainty - $t\bar{t}H$
TheorySig_UEPS_ttH	Uncertainty on the choice of parton-shower and underlying event (PS / UE) model - $t\bar{t}H$
TheorySig_QCDscale_ggF_mu	QCD scale ggF uncertainty related to the total cross section
TheorySig_QCDscale_ggF_pTH120	QCD scale ggF variations related the Higgs p_T -shape uncertainties
TheorySig_SysTheoryDelta1_ggZH_VHbb	QCD scale uncertainty on STXS bins for ggZH production - $VH \rightarrow b\bar{b}$
TheorySig_QCDscale_ggF_res	QCD scale ggF uncertainty related to the total cross section
TheorySig_PDF_ttH	Uncertainty on parton distribution function - $t\bar{t}H$
TheorySig_QCDScaleDelta75_ggZH	QCD scale uncertainty on STXS bins for ggZH production
TheorySig_QCDScaleDeltaY_ggZH	QCD overall scale uncertainty for ggZH production

Table 8.7: Theoretical, signal related, uncertainties having the greatest impact on the results.

NP name	Description
BkgTheory_ttbb_Gen_ttHbb	Uncertainty on the choice of MC generator - $t\bar{t}H \rightarrow b\bar{b}$
BkgTheory_SysWPtV_VHbb	W+jet modelling uncertainty - $VH \rightarrow b\bar{b}$
BkgTheory_ttZ_XS_QCDscale	Uncertainty on the cross section and QCD scale - $t\bar{t}Z$ modelling
BkgTheory_ttW_XS_QCDscale	Uncertainty on the cross section and QCD scale - $t\bar{t}W$ modelling
BkgTheory_tttt_XS	Uncertainty on the cross section - $t\bar{t}t\bar{t}$ modelling
BkgTheory_ttbb_4F5Fshape_ttHbb	Uncertainty associated with the choice of NLO generator - $t\bar{t}H \rightarrow b\bar{b}$
BkgTheory_rareTop_XS_ttHML	Uncertainty on the cross section due to rare background contributions - $t\bar{t}H$ multilepton
BkgTheory_ttbb_PS_ttHbb	Uncertainty due to the choice of parton shower model - $t\bar{t}H \rightarrow b\bar{b}$
BkgTheory_ttW_Gen	Uncertainty on the matrix-element MC generator - $t\bar{t}W$ modelling
BkgTheory_SysVVMbbME_VHbb	Diboson modelling uncertainty - $VH \rightarrow b\bar{b}$
BkgTheory_ttbb_Rad_ttHbb	Uncertainty on the modelling of initial and final state radiation - $t\bar{t}H \rightarrow b\bar{b}$
BkgTheory_SysZMbb_VHbb	Z+jet modelling uncertainty - $VH \rightarrow b\bar{b}$

Table 8.8: Theoretical, background related, uncertainties having the greatest impact on the results.

NP name	Description
TAU_EFF_ID_TOTAL_ttHML	Tau identification efficiency - $t\bar{t}H$ multilepton
JES_Flavor_Comp_l20tau_Other_ttHML	Jet energy scale uncertainty related to flavour composition - $t\bar{t}H$ multilepton
JER_NP_0_Htautau	Jet energy resolution - $H \rightarrow \tau\tau$
JES_PU_Rho	Jet energy scale uncertainty related to the pileup (density ρ)
FT_EFF_Eigen_B_0_Rel21_WP70	Jet b -tagging uncertainty - 70% working point
Hgg_Bias_ggH_0J_FWD_HGam	Uncertainty due to the background modelling (spurious signal) for each $t\bar{t}H \rightarrow \gamma\gamma$ category
Fakes_l20tau_MM_Closure_em_ttHML	Data-driven non-prompt/fake leptons and charge misassignment uncertainty - $t\bar{t}H$ multilepton
Fakes_CR_Stat_l30tau_ttH_bin3_ttHML	Data-driven non-prompt/fake leptons and charge misassignment uncertainty - $t\bar{t}H$ multilepton
Fakes_l30tau_MM_Closure_ttHML	Data-driven non-prompt/fake leptons and charge misassignment uncertainty - $t\bar{t}H$ multilepton

Table 8.9: Experimental uncertainties having the greatest impact on the results.

Figure 8.3 shows the ranking plots, defined in Chapter 7, of the top 30 systematic uncertainties for the single-Higgs combination considering data (a) and the Asimov dataset (b). The impact is estimated by varying each nuisance parameter and computing the maximum likelihood estimator of the parameter of interest, κ_λ . The difference between the maximum likelihood estimator with or without varying the nuisance parameter is the $\Delta\hat{\kappa}_\lambda$ of the fit, that is normalised to the total error, $\Delta\hat{\kappa}_{\lambda_{tot}}$. Pre-fit and post-fit impacts of the different nuisance parameter on the central value κ_λ are reported as white empty and cyan (green) filled bars corresponding to downward (upwards) systematic uncertainty variations, respectively. The points indicate how the parameter had to be pulled up or down during the fit, and associated error bars show the best-fit values of the nuisance parameters and their post-fit uncertainties. Most of the systematic uncertainties are within 1σ from the nominal (indicated by the dashed vertical lines) value, except for the “BkgTheory_SysZMbb_VHbb”, a nuisance parameter related to the background modelling of the $VH \rightarrow b\bar{b}$ analysis that is pulled consistently with what is found in the combination analysis. The dominant uncertainties arise from the theory modelling of the signal and background processes in simulation.

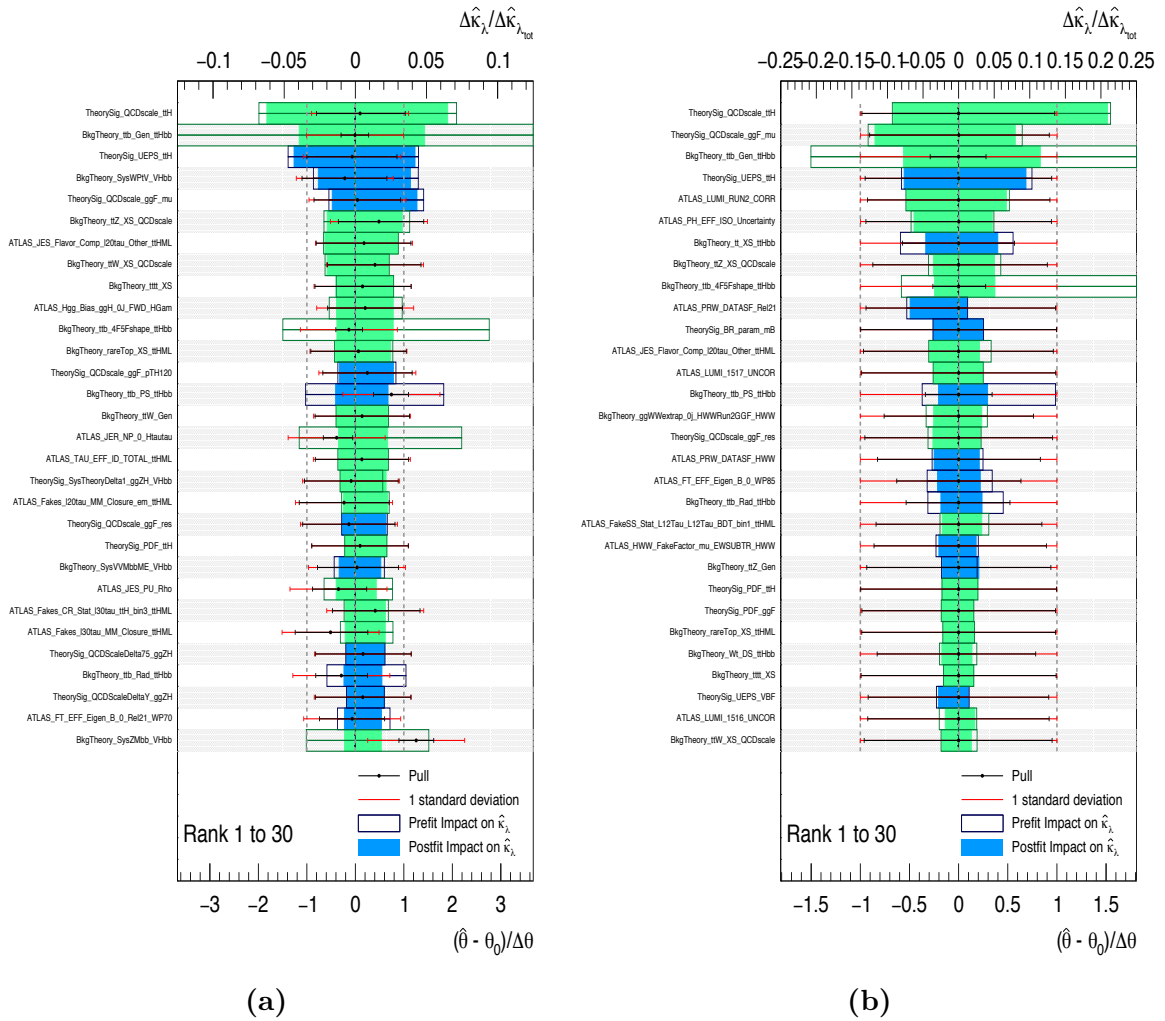


Figure 8.3: Ranking of the top 30 systematic uncertainties in the single-Higgs combination for data (a) and for the Asimov dataset generated under the SM hypothesis.

8.4 Results of fit to κ_λ

This section presents the main results of the analysis exploiting the combination of the aforementioned single-Higgs channels as well as the differential information. A likelihood fit is performed in the theoretically allowed range $-20 < \kappa_\lambda < 20$ to constrain the value of the Higgs-boson self-coupling κ_λ , setting all other Higgs-boson couplings to their SM values ($\kappa_F = \kappa_V = 1$). This fit configuration targets scenarios and BSM models where new physics is expected to appear only as a modification of the Higgs-boson self-coupling, as for example the next-to-minimal supersymmetric extension of the Standard Model (NMSSM) in the alignment limit, where one of the neutral Higgs fields lies approximately in the same direction in field space as the doublet Higgs vacuum expectation value, and the observed Higgs boson is predicted to have Standard-Model-like properties [166]. Figure 8.4 shows the value of $-2 \ln \Lambda(\kappa_\lambda)$ as a function of κ_λ for data and for the Asimov dataset, generated from the likelihood distribution Λ with nuisance parameters fixed at the best-fit value obtained on data and the parameter of interest fixed to SM hypothesis (i.e. $\kappa_\lambda = 1$). Likelihood distributions including either all or a selected part of the uncertainties are shown.

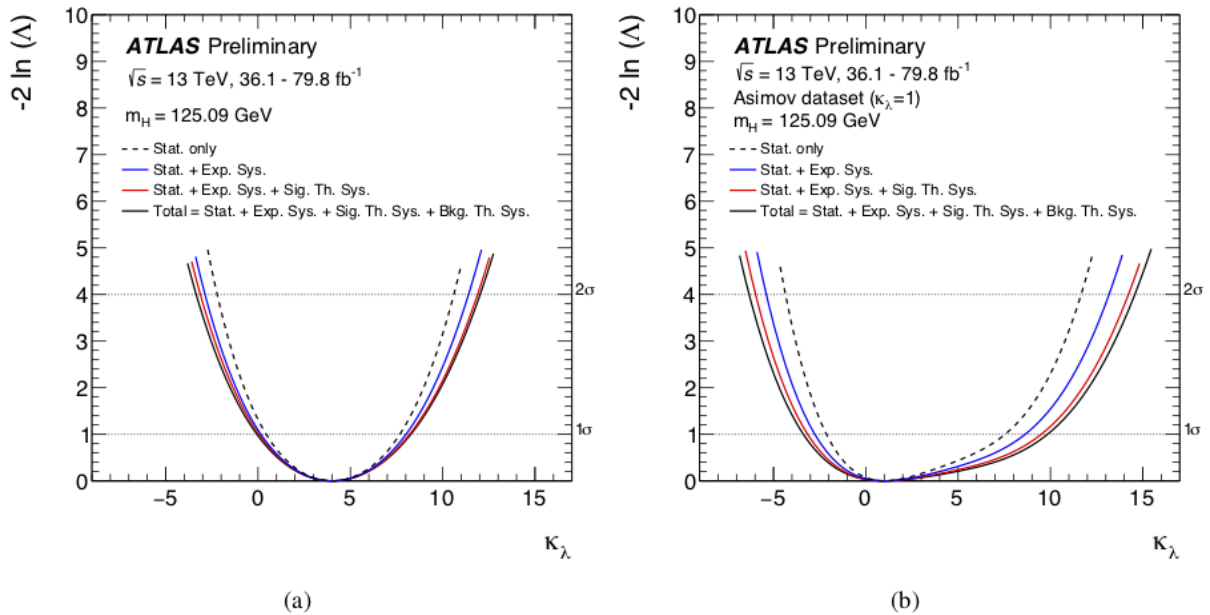


Figure 8.4: Value of $-2 \ln \Lambda(\kappa_\lambda)$ as a function of κ_λ for data (a) and for the Asimov dataset generated under the SM hypothesis (b). The solid black line shows the profile likelihood distributions obtained including all systematic uncertainties (“Total”). Results from a statistic only fit “Stat. only” (black dashed line), including the experimental systematics “Stat. + Exp. Sys.” (blue solid line), adding theory systematics related to the signal “Stat.+ Exp. Sys.+ Sig. Th. Sys.” (red solid line) are also shown. The dotted horizontal lines show the $-2 \ln \Lambda(\kappa_\lambda) = 1$ level that is used to define the $\pm 1\sigma$ uncertainty on κ_λ as well as the $-2 \ln \Lambda(\kappa_\lambda) = 4$ level used to define the $\pm 2\sigma$ uncertainty [163].

Differences in the shapes of the likelihood curves reported in Figures 8.4 between data and Asimov dataset are due to the non-linearity of the cross-section dependence on κ_λ ,

and the difference of the best-fit values of κ_λ in the two cases. This effect has been thoroughly studied generating different Asimov datasets fixing κ_λ to increasing values from 2 to 5. Figure 8.5 presents the likelihood distributions for each Asimov dataset and for the Asimov dataset generated under the SM hypothesis showing that the shapes of the likelihood distribution, and thus the 1σ error and confidence interval around the best-fit value, are strictly dependent on the fitted value itself; the Asimov dataset generated at $\kappa_\lambda \simeq 4$ reproduces the symmetric shape as observed in data.

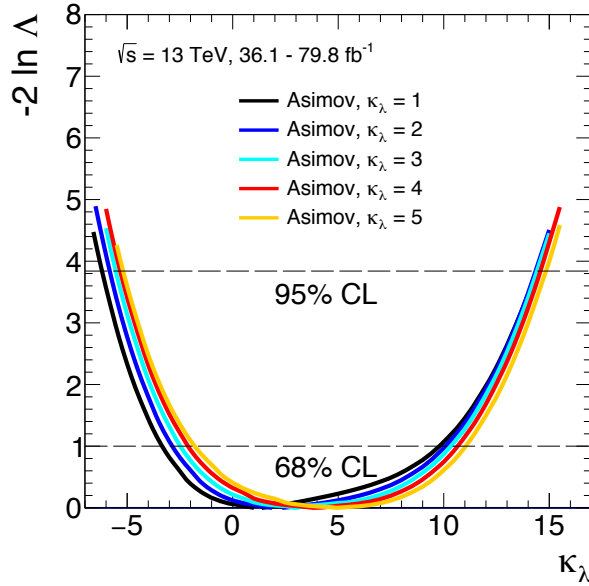


Figure 8.5: Value of $-2 \ln \Lambda(\kappa_\lambda)$ as a function of κ_λ for Asimov datasets generated with $\kappa_\lambda = 1$ (black line), $\kappa_\lambda = 2$ (blue line), $\kappa_\lambda = 3$ (light blue line), $\kappa_\lambda = 4$ (red line) and $\kappa_\lambda = 5$ (orange line). The dotted horizontal lines show the $-2 \ln \Lambda(\kappa_\lambda) = 1$ level that is used to define the $\pm 1\sigma$ uncertainty on κ_λ as well as the $-2 \ln \Lambda(\kappa_\lambda) = 3.84$ level used to define the 95% CL.

The central value and uncertainty of the κ_λ modifier of the trilinear Higgs boson self-coupling are determined to be:

$$\kappa_\lambda = 4.0_{-4.1}^{+4.3} = 4.0_{-3.6}^{+3.7} (\text{stat.}) +_{-1.5}^{+1.6} (\text{exp.}) +_{-0.9}^{+1.3} (\text{sig. th.}) +_{-0.9}^{+0.8} (\text{bkg. th.}) (\text{observed})$$

$$\kappa_\lambda = 1.0_{-4.4}^{+8.8} = 1.0_{-3.1}^{+6.5} (\text{stat.}) +_{-2.0}^{+3.9} (\text{exp.}) +_{-1.7}^{+3.7} (\text{sig. th.}) +_{-1.6}^{+2.4} (\text{bkg. th.}) (\text{expected})$$

where the total uncertainty is decomposed into components for statistical uncertainties, experimental systematic uncertainties, and theory uncertainties on signal and background modelling, following the procedure described in Section 8.3. The total uncertainty is dominated by the statistical component.

Table 8.10 reports the detailed breakdown of the uncertainties affecting the κ_λ measurement; the procedure used to produce the numbers of the table is the following: in each case the corresponding nuisance parameters are fixed to their best-fit values, while other nuisance parameters are left free, and the resulting uncertainty is subtracted in quadrature from the total uncertainty.

Uncertainty source	$\Delta\kappa_\lambda/\kappa_\lambda$ %
Statistical uncertainty	90
Systematic uncertainties	45
Theory uncertainties	30
Signal	25
Background	21
Experimental uncertainties (excl. MC stat.)	23
MC statistical uncertainty	11
Total uncertainty	106

Table 8.10: Summary of the relative uncertainties $\Delta\kappa_\lambda/\kappa_\lambda$ affecting the measurement of the combined κ_λ . The sum in quadrature of systematic uncertainties from individual sources differs from the uncertainty evaluated for the corresponding group in general, due to the presence of small correlations among nuisance parameters describing the different sources.

The observed 95% CL interval of κ_λ is $-3.2 < \kappa_\lambda < 11.9$ while the expected interval is $-6.2 < \kappa_\lambda < 14.4$, competitive with the intervals coming from double-Higgs measurements reported in Chapter 7. Inclusive corrections and cross-section measurements have been used in order to check the difference and the expected gain using the differential cross-section information contained in the STXS bins. Thus, the VBF , ZH and WH production modes have been considered as inclusive regions. The differential information slightly improves the results as it is summarised in Table 8.11, as well it is shown in Figure 8.6 reporting the value of $-2\ln\Lambda(\kappa_\lambda)$ as a function of κ_λ for the two different granularities.

POIs	Granularity	$\kappa_\lambda^{+1\sigma}_{-1\sigma}$	κ_λ [95% CL]
κ_λ	STXS	$4.0^{+4.3}_{-4.1}$	$[-3.2, 11.9]$
		$1.0^{+8.8}_{-4.4}$	$[-6.2, 14.4]$
κ_λ	inclusive	$4.6^{+4.3}_{-4.2}$	$[-2.9, 12.5]$
		$1.0^{+9.5}_{-4.3}$	$[-6.1, 15.0]$

Table 8.11: Best-fit values for κ_λ with $\pm 1\sigma$ uncertainties and 95% CL interval are reported for the inclusive and differential configurations. For each fit result the upper row corresponds to the observed results, and the lower row to the expected results obtained using Asimov datasets generated under the SM hypothesis.

The global likelihood shape depends on how the contributions from different production and decay modes are combined: while for $\kappa_\lambda < 1$ both the κ_λ and κ_λ^2 terms induce negative contributions in the production signal strengths, for $\kappa_\lambda > 1$, the interplay between positive κ_λ and κ_λ^2 terms leads to cancellations that suppress the effect of κ_λ . Likelihood distributions for each production and decay modes are presented in Figure 8.7;

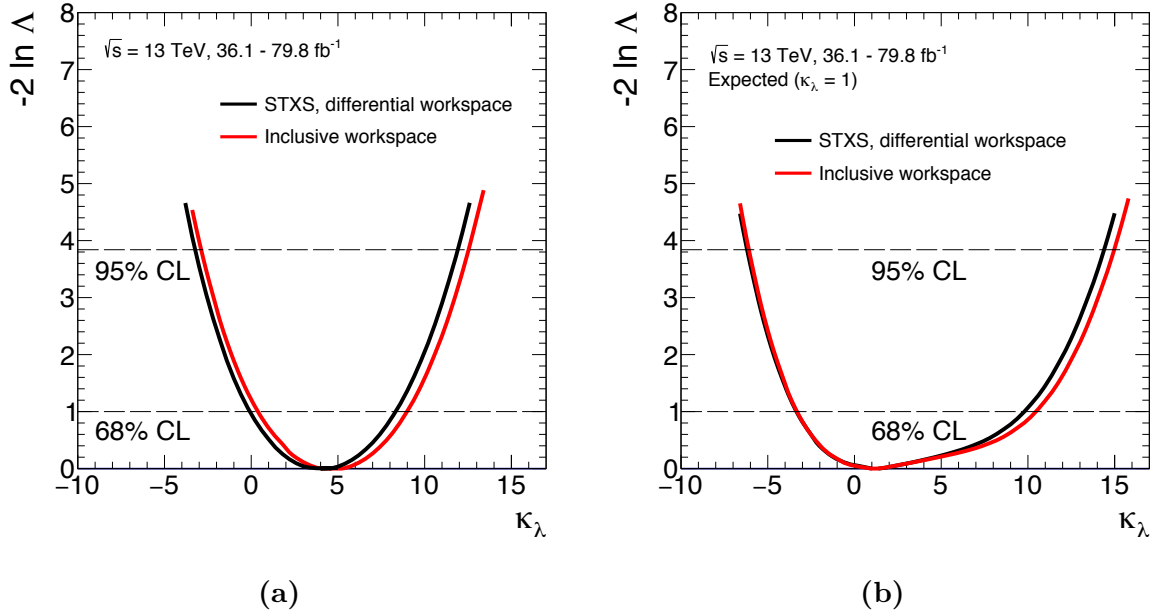


Figure 8.6: Value of $-2 \ln \Lambda(\kappa_\lambda)$ as a function of κ_λ for data (a) and for the Asimov dataset generated under the SM hypothesis (b). The solid black line shows the likelihood distribution using the C_1 coefficients computed for each STXS bin while the solid red line presents the likelihood distribution using inclusive C_1 coefficients for the VBF , ZH and WH production modes. The dotted horizontal lines show the $-2 \ln \Lambda(\kappa_\lambda) = 1$ level that is used to define the $\pm 1\sigma$ uncertainty on κ_λ as well as the $-2 \ln \Lambda(\kappa_\lambda) = 3.84$ level used to define the 95% CL.

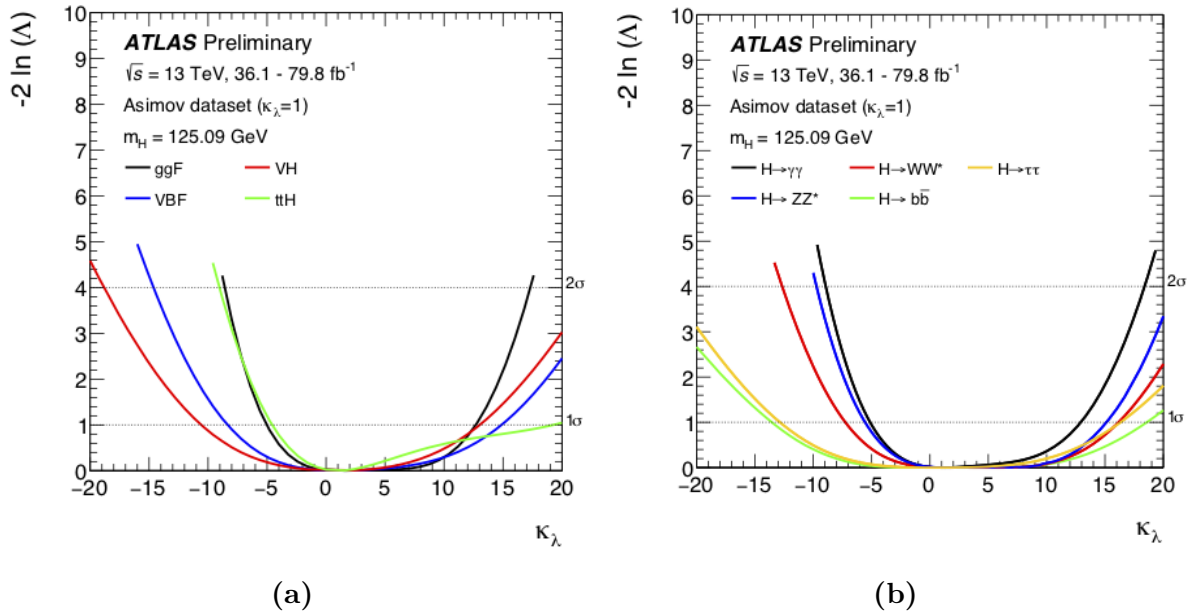


Figure 8.7: Expected value of $-2 \ln \Lambda(\kappa_\lambda)$ as a function of κ_λ for Asimov datasets generated under the SM hypothesis for Higgs-boson production modes (a) and decay channels (b). The $t\bar{t}H$ multi-lepton categories are excluded from the $H \rightarrow ZZ^*$, $H \rightarrow WW^*$, and $H \rightarrow \tau\tau$ fits [163].

concerning production modes, each curve is obtained fitting κ_λ for one production mode, keeping the other production modes fixed to the SM; from the decay side, instead, the dataset is directly split in the different decay channels which are fitted one at a time independently.

The dominant contributions to the κ_λ sensitivity derive from the di-boson decay channels $\gamma\gamma$, ZZ^* , WW^* and from the ggF and $t\bar{t}H$ production modes. Differential information would improve even more the constraints on κ_λ particularly including the most sensitive production modes, i.e. $t\bar{t}H$ and ggF . Given the fact that the dominant contribution to constrain κ_λ , comes from the ggF production, in order to check that no significant bias on the final results is introduced by considering the ggF production mode as inclusive regions of the phase space, i.e. using a kinematic independent parameterisation as a function of κ_λ , a fit has been performed excluding the STXS bins where a great impact is expected, i.e. the bins with Higgs-boson transverse momentum above 120 GeV. This study has been realised by introducing signal strength parameters for these STXS bins and profiling them independently in the fit. The result is a minimal change of the central value ($\sim 5\%$) and uncertainty on κ_λ .

In order to investigate the constraining power of each single-Higgs channel included in this combination, a test has been performed removing different categories, corresponding to the different single-Higgs decay channels, from the combined fit and checking the κ_λ 95% CL interval obtained using the remaining channels. In order to avoid statistics fluctuations, Asimov datasets are used. Results are reported in Table 8.12 showing the ranking of the different channels in constraining κ_λ : each row shows the 1σ interval and the 95% CL κ_λ interval obtained by removing the specific channel listed in the first column.

Channels	$\kappa_\lambda^{+1\sigma}_{-1\sigma}$	κ_λ [95% CL]
$H \rightarrow \gamma\gamma$	$1.00^{+10.0}_{-5.0}$	[-7.2, 15.9]
$t\bar{t}H$ multilepton	$1.00^{+9.3}_{-7.3}$	[-6.6, 14.5]
$H \rightarrow ZZ^*$	$1.00^{+8.9}_{-6.8}$	[-6.8, 14.8]
$VH \rightarrow b\bar{b}$	$1.00^{+9.6}_{-6.3}$	[-6.2, 15.2]
$H \rightarrow WW^*$	$1.00^{+8.9}_{-6.4}$	[-6.5, 14.7]
$H \rightarrow \tau^+\tau^-$	$1.00^{+9.1}_{-6.1}$	[-6.2, 14.8]
$t\bar{t}H \rightarrow b\bar{b}$	$1.00^{+8.8}_{-6.4}$	[-6.3, 14.3]
Nominal expected result	$1.00^{+8.8}_{-4.4}$	[-6.2, 14.4]

Table 8.12: Ranking of single-Higgs channels in constraining κ_λ using the Asimov dataset. Each row shows the 1σ interval and 95% CL of κ_λ obtained by removing one specific channel.

The more important a channel is in constraining κ_λ , the larger would be the expected CL interval obtained removing this channel with respect to the nominal results reported in the last row of Table 8.12. Keeping in mind that the analyses use different integrated luminosities, similar results are obtained.

8.5 Results of fit to κ_λ and either κ_F or κ_V

The constraints on κ_λ , comparable to the double-Higgs limits in the case of an exclusive κ_λ fit, become weaker including additional degrees of freedom to the fit, i.e. when BSM modifications of the single-Higgs couplings are taken into account. Additional fit configurations are tested, i.e. a simultaneous fit is performed to $(\kappa_\lambda, \kappa_F)$ and $(\kappa_\lambda, \kappa_V)$. These fits target BSM physics scenarios where new physics could affect only the Yukawa type terms ($\kappa_V=1$) of the SM or only the couplings to vector bosons ($\kappa_F=1$), in addition to the Higgs-boson self-coupling (κ_λ) [167]. Figures 8.8 (a) and (b) show observed negative log-likelihood contours on the $(\kappa_\lambda, \kappa_F)$ and $(\kappa_\lambda, \kappa_V)$ grids obtained from fits performed for the $\kappa_V=1$ or $\kappa_F=1$ hypothesis, respectively. The sensitivity is not much degraded when simultaneously fitting κ_λ and κ_F while it is degraded by 50% in the κ_V case (expected lower limit of 95% CL interval).

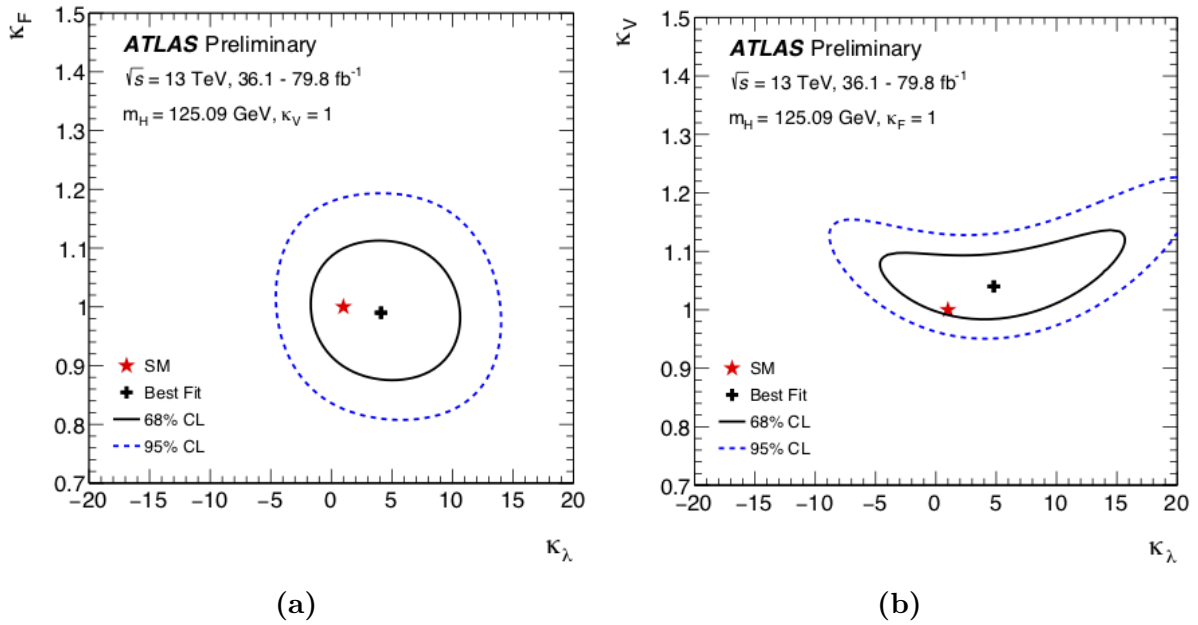


Figure 8.8: Negative log-likelihood contours at 68% and 95% CL in the $(\kappa_\lambda, \kappa_F)$ plane under the assumption of $\kappa_V=1$ (a) and in the $(\kappa_\lambda, \kappa_V)$ plane under the assumption of $\kappa_F=1$ (b). The best-fit value is indicated by a cross while the SM hypothesis is indicated by a star. The plot assumes that the approximations in References [55, 133] are valid inside the shown contours.

An even less constrained fit, performed by simultaneously fitting κ_λ and κ , where κ stands for a common Higgs-boson coupling modifier ($\kappa = \kappa_F = \kappa_V$), results in nearly no sensitivity to κ_λ within the theoretically allowed range of $|\kappa_\lambda| < 20$ as it is shown in Table 8.13 and in Figure 8.9, summarising all the fit configurations tested.

POIs	Granularity	$\kappa_F^{+1\sigma}$ $\kappa_F^{-1\sigma}$	$\kappa_V^{+1\sigma}$ $\kappa_V^{-1\sigma}$	$\kappa_\lambda^{+1\sigma}$ $\kappa_\lambda^{-1\sigma}$	κ_λ [95% CL]
κ_λ, κ_V	STXS	1	$1.04^{+0.05}_{-0.04}$	$4.8^{+7.4}_{-6.7}$	$[-6.7, 18.4]$
			$1.00^{+0.05}_{-0.04}$	$1.0^{+9.9}_{-6.1}$	$[-9.4, 18.9]$
κ_λ, κ_F	STXS	$0.99^{+0.08}_{-0.08}$	1	$4.1^{+4.3}_{-4.1}$	$[-3.2, 11.9]$
		$1.00^{+0.08}_{-0.08}$		$1.0^{+8.8}_{-4.4}$	$[-6.3, 14.4]$
$\kappa_\lambda - \kappa = \kappa_F = \kappa_V$	STXS	$1.05^{+0.58}_{-0.05}$	$1.05^{+0.58}_{-0.05}$	$5.3^{>14.7}_{-9.7}$	$[< -20, > 20]$
		$1.00^{+0.10}_{-0.04}$	$1.00^{+0.10}_{-0.04}$	$1.0^{+10.7}_{-9.3}$	$[< -20, > 20]$

Table 8.13: Best-fit values for κ modifiers with $\pm 1\sigma$ uncertainties. The first column shows the parameter(s) of interest in each fit configuration, where the other coupling modifiers are kept fixed to the SM prediction. The 95% CL interval for κ_λ is also reported. For each fit result the upper row corresponds to the observed results, and the lower row to the expected results obtained using Asimov datasets generated under the SM hypothesis.

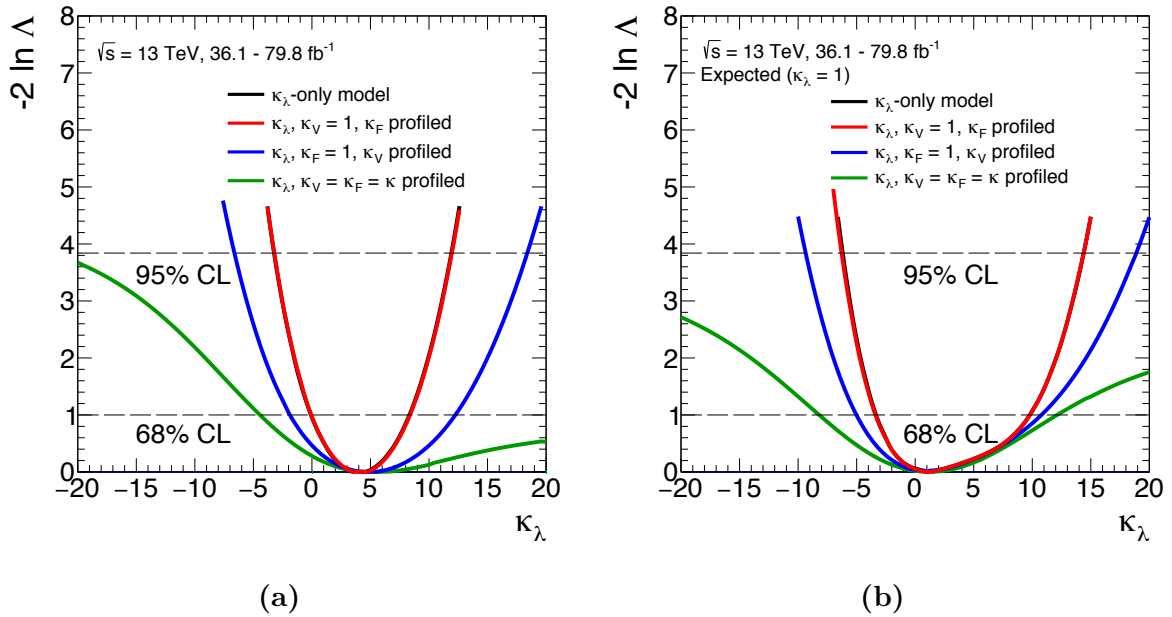


Figure 8.9: Value of $-2 \ln \Lambda(\kappa_\lambda)$ as a function of κ_λ for data (a) and for the Asimov dataset generated under the SM hypothesis (b). Different fit configurations have been tested: κ_λ -only model (black line), $\kappa_\lambda - \kappa_F$ model (red line), $\kappa_\lambda - \kappa_V$ model (blue line) and $\kappa_\lambda - \kappa$, where κ stands for a common single Higgs-boson coupling modifier, $\kappa = \kappa_V = \kappa_F$, (green line). All the coupling modifiers that are not included in the fit are set to their SM predictions. The dotted horizontal lines show the $-2 \ln \Lambda(\kappa_\lambda) = 1$ level that is used to define the $\pm 1\sigma$ uncertainty on κ_λ as well as the $-2 \ln \Lambda(\kappa_\lambda) = 3.84$ level used to define the 95% CL.

The correlations among the parameters of interest, i.e. κ_λ , κ_F and κ_V , are shown in Figure 8.10 for data (a) and for the Asimov dataset (b). A strong correlation is present between κ_F and κ_V .

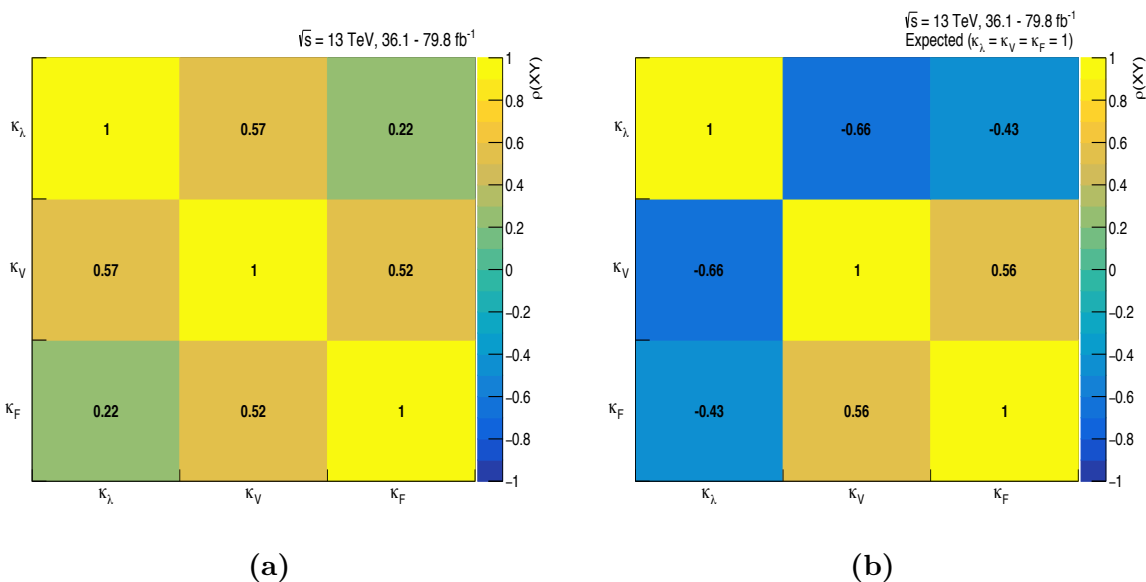


Figure 8.10: Correlations between the parameters of interest, i.e. κ_λ , κ_F and κ_V , for data (a) and for the Asimov dataset generated under the SM hypothesis (b).

8.5.1 Cross-check on the validity of the theoretical approximations

In order to ascertain the robustness of the nominal approach and of the approximations of the theoretical framework described in Chapter 6, against higher-order terms regarding modifications of the LO coupling modifiers κ_i or κ_f included in Equations 8.1 and 8.2, a test has been made exploiting a different approach with respect to Reference [133].

Indeed, the aforementioned paper used an “additive approach” to include κ_i or κ_f coupling modifications with respect to κ_λ (except for the multiplicative term $Z_H^{BSM} \kappa_i^2$); a pure “multiplicative approach” was not possible without guesses on higher orders, that can be only treated with a full Effective-Field-Theory (EFT) approach.

Thus, as a check, the authors of Reference [133] suggested to add additional higher-order κ_i and κ_f terms, like κ_i^3 or κ_f^3 terms, coming from the interference between tree-level and one-loop diagrams like the ones shown in Figure 8.11. The study including additional κ_i^3 terms to Equations 6.5 is here reported, where κ_i modifies also the loops together with κ_λ , like it is shown in Equation 8.4:

$$\mu_i(\kappa_\lambda, \kappa_i) = \frac{\sigma^{BSM}}{\sigma^{SM}} = Z_H^{BSM}(\kappa_\lambda) \left[\kappa_i^2 + \frac{(\kappa_\lambda - 1)\kappa_i^3 C_1^i}{K_{EW}^i} \right]. \quad (8.4)$$

Results of the fit to κ_λ and either κ_F or κ_V with the remaining Higgs-boson modifier set to its SM value, are summarised in Table 8.14, reporting best-fit observed values and 95% CL κ_λ intervals considering both the nominal configuration and the configuration

testing higher order corrections. Small discrepancies with respect to the nominal results have been found; this effect is clear looking at Figure 8.12, reporting a comparison of the observed $-2 \ln \Lambda(\kappa_\lambda)$ as a function of κ_λ profiling κ_F ($\kappa_V = 1$) (a) and κ_V ($\kappa_F = 1$) (b), and Figure 8.13 showing negative log-likelihood contours at 68% and 95% CL on the $(\kappa_\lambda, \kappa_F)$ (a) and $(\kappa_\lambda, \kappa_V)$ (b) planes; the black solid lines both for the scans and for the contours represent the nominal configuration, while the red solid lines show the modified configuration.

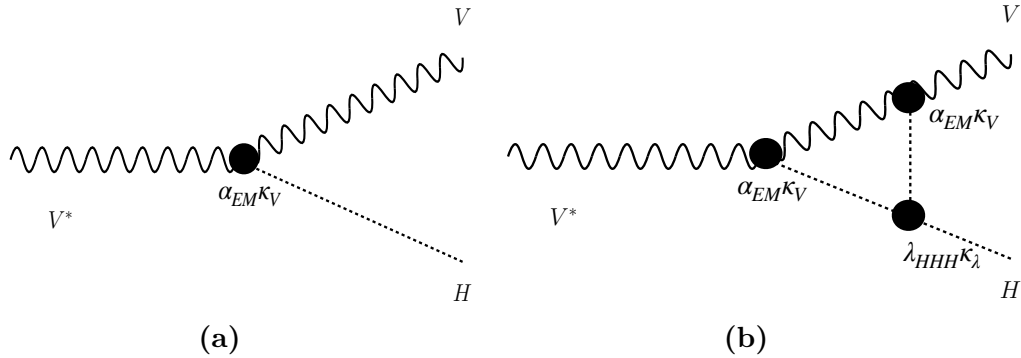


Figure 8.11: VH tree-level and one-loop diagrams.

POIs	$\kappa_F^{+1\sigma}_{-1\sigma}$	$\kappa_V^{+1\sigma}_{-1\sigma}$	$\kappa_\lambda^{+1\sigma}_{-1\sigma}$	κ_λ [95% CL]
Nominal				
κ_λ, κ_V	1	$1.04^{+0.05}_{-0.04}$	$4.8^{+7.4}_{-6.7}$	$[-6.7, 18.4]$
κ_λ, κ_F	$0.99^{+0.08}_{-0.08}$	1	$4.1^{+4.3}_{-4.1}$	$[-3.2, 11.9]$
Modified with κ_i^3 terms				
κ_λ, κ_V	1	$1.04^{+0.05}_{-0.04}$	$4.8^{+7.4}_{-6.7}$	$[-6.7, 18.3]$
κ_λ, κ_F	$0.99^{+0.08}_{-0.07}$	1	$4.0^{+4.3}_{-4.1}$	$[-3.3, 11.9]$

Table 8.14: Best-fit observed values for κ modifiers with $\pm 1\sigma$ uncertainties. The 95% CL interval for κ_λ is also reported. The first column shows the parameters of interest included in each fit configuration, where the other coupling modifiers are kept fixed to the SM prediction. The set of rows on the top of the table shows fit results obtained under the nominal assumption while the set on the bottom shows the results obtained introducing the κ_i^3 corrections.

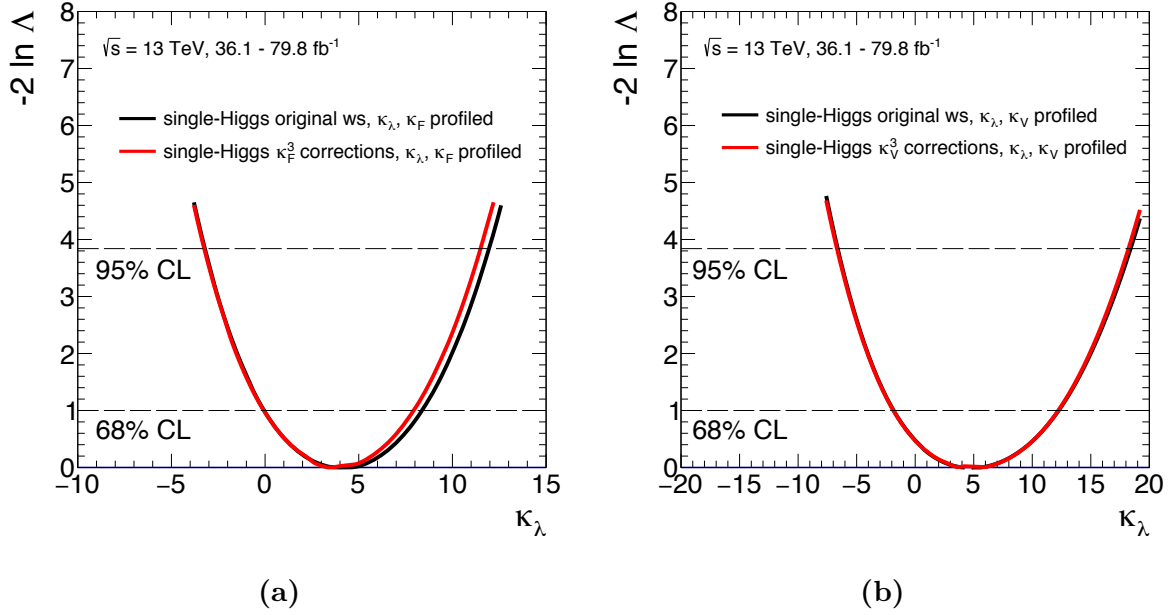


Figure 8.12: Value of the observed $-2 \ln \Lambda(\kappa_\lambda)$ as a function of κ_λ with κ_F profiled under the assumption of $\kappa_V = 1$ (a) and with κ_V profiled under the assumption of $\kappa_F = 1$ (b). The solid black lines show the nominal approximation in the two fit configurations while the solid red lines show the likelihood distribution including higher order corrections. The dotted horizontal lines show the $-2 \ln \Lambda(\kappa_\lambda) = 1$ level that is used to define the $\pm 1\sigma$ uncertainty on κ_λ as well as the $-2 \ln \Lambda(\kappa_\lambda) = 3.84$ level used to define the 95% CL.

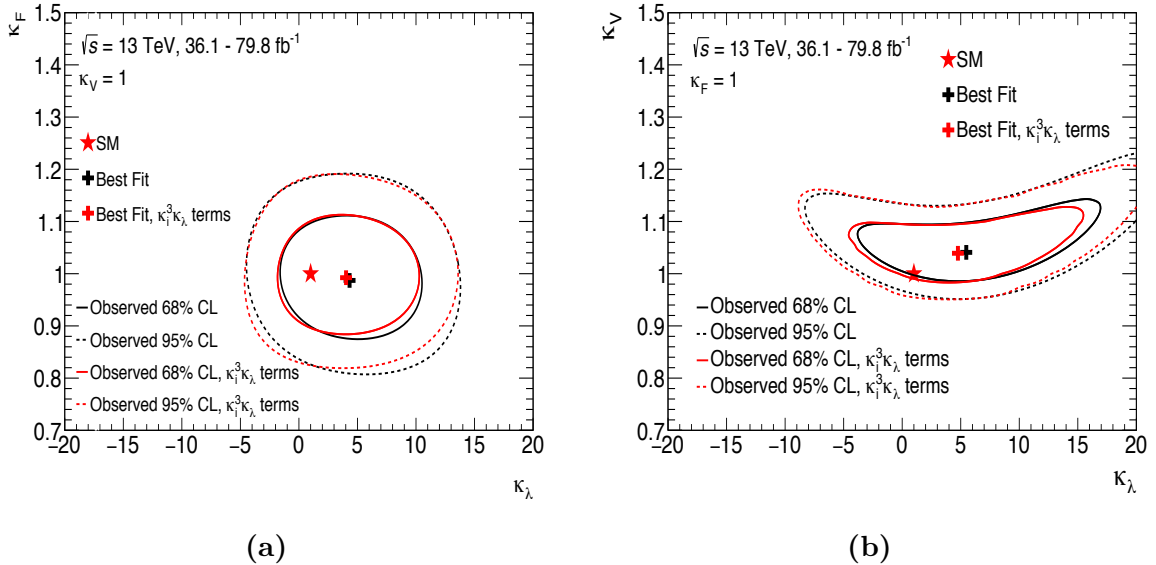


Figure 8.13: Negative log-likelihood contours at 68% and 95% CL in the $(\kappa_\lambda, \kappa_F)$ plane under the assumption of $\kappa_V = 1$ (a), and in the $(\kappa_\lambda, \kappa_V)$ plane under the assumption of $\kappa_F = 1$ (b). The best-fit value is indicated by a cross while the SM hypothesis is indicated by a star. The red contour is produced using the nominal input corrected with κ_i^3 terms, where $\kappa_i = \kappa_F$ in (a) and $\kappa_i = \kappa_V$ in (b), while the black contour represents the nominal results. Negligible discrepancies are present adding these correction terms.

8.6 HL-LHC projections

Projections for the measurement of the trilinear Higgs self-coupling at HL-LHC have been made considering NLO-EW corrections depending on κ_λ to single-Higgs processes. The parameterisations described at the beginning of this chapter and in Chapter 6 have been exploited in order to give an estimation of ATLAS HL-LHC projections in constraining κ_λ ; the differential information has not been used because of the fact that only inclusive inputs are available for these HL-LHC studies; these inputs have been obtained starting from the inclusive inputs tested in Section 8.4 and studying different systematic scenarios. An Asimov dataset generated under the SM hypothesis considering a luminosity of 3000 fb^{-1} at $\sqrt{s} = 14 \text{ TeV}$ has been used. Concerning systematic uncertainties, two different scenarios have been considered: a “Run 2 sys” scenario, where the uncertainties are assumed to be equal to the Run 2 ones and a “Reduced sys” scenario, considering reduced systematics uncertainties obtained thanks to the much larger amount of data collected, i.e. the theory uncertainties are halved with respect to the Run 2 uncertainties and the other systematic uncertainties are scaled as the statistical errors. Table 8.15 summarises all the configurations tested in the two systematic scenarios.

POIs	Systematic scenarios	$\kappa_F^{+1\sigma}_{-1\sigma}$	$\kappa_V^{+1\sigma}_{-1\sigma}$	$\kappa_\lambda^{+1\sigma}_{-1\sigma}$	κ_λ [95% CL]
κ_λ	Run 2 sys	1	1	$1.0^{+3.6}_{-2.3}$	$[-3.0, 9.0]$
	Reduced sys			$1.0^{+2.3}_{-1.7}$	$[-2.0, 6.5]$
κ_λ, κ_V	Run 2 sys	1	$1.00^{+0.02}_{-0.02}$	$1.0^{+4.2}_{-2.8}$	$[-3.9, 8.9]$
	Reduced sys		$1.00^{+0.01}_{-0.01}$	$1.0^{+2.6}_{-2.1}$	$[-2.7, 6.5]$
κ_λ, κ_F	Run 2 sys	$1.00^{+0.02}_{-0.02}$	1	$1.0^{+3.8}_{-2.3}$	$[-3.0, 9.3]$
	Reduced sys	$1.00^{+0.02}_{-0.02}$		$1.0^{+2.3}_{-1.7}$	$[-2.0, 6.6]$
$\kappa_\lambda - \kappa_F - \kappa_V$	Run 2 sys	$1.00^{+0.03}_{-0.03}$	$1.00^{+0.03}_{-0.02}$	$1.0^{+4.1}_{-3.5}$	$[-6.0, 10.4]$
	Reduced sys	$1.00^{+0.02}_{-0.02}$	$1.00^{+0.02}_{-0.02}$	$1.0^{+2.6}_{-2.4}$	$[-3.8, 6.6]$

Table 8.15: Best-fit values for κ modifiers with $\pm 1\sigma$ uncertainties using an Asimov dataset generated under the SM hypothesis considering a luminosity of 3000 fb^{-1} at $\sqrt{s} = 14 \text{ TeV}$. The first column shows the parameter(s) of interest in each fit configuration, where the other coupling modifiers are kept fixed to the SM prediction. The 95% CL interval for κ_λ is also reported.

The value of $-2 \ln \Lambda(\kappa_\lambda)$ as a function of κ_λ for an Asimov dataset generated under the SM hypothesis is shown in Figures 8.14 and 8.15 for the different fit configurations listed in Table 8.15 and for the different systematic scenarios. Solid and dotted lines represent the “Run 2 sys” and the “Reduced sys” scenarios in the different fit configurations, respectively. The expected 95% CL intervals of κ_λ , considering just modifications of the self-coupling, are $-2.0 < \kappa_\lambda < 6.5$ and $-3.0 < \kappa_\lambda < 9.0$ for the Reduced Scenario and for the Run 2 systematic scenario, respectively. The “Run 2 sys” interval, considering just modifications of the Higgs self-coupling (κ_λ -only), is comparable to the interval obtained in Reference [133], “Run 2 sys” scenario, shown in Figure 6.13, and the likelihood shapes of the additional fit configurations are also compatible. The “Reduced sys” κ_λ -only interval is, instead, comparable to the one obtained in Reference [55], shown in Figure 6.12, considering the same uncertainty scenario.

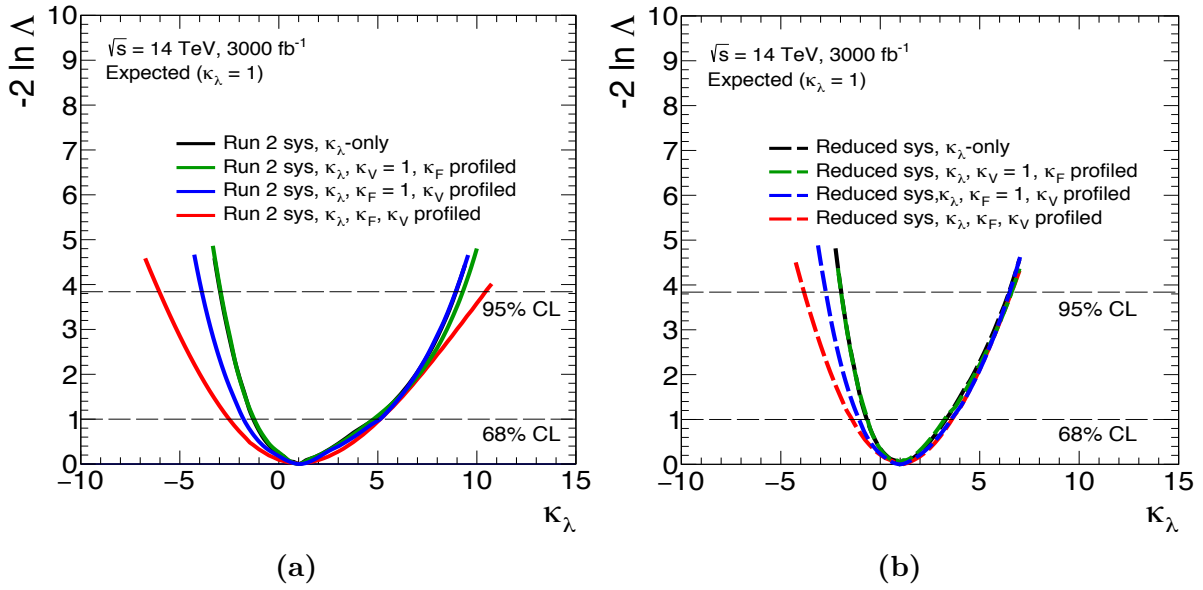


Figure 8.14: Value of $-2 \ln \Lambda(\kappa_\lambda)$ as a function of κ_λ for an Asimov dataset generated under the SM hypothesis considering a luminosity of 3000 fb^{-1} at $\sqrt{s} = 14 \text{ TeV}$. Two different scenarios are considered: “Run 2 sys” (a) and “Reduced sys” (b). Different fit configurations have been tested: κ_λ -only model (black line), κ_λ - κ_F model (green line), κ_λ - κ_V model (blue line) and κ_λ - κ_F - κ_V model, (red line). All the coupling modifiers that are not included in the fit are set to their SM predictions. The dotted horizontal lines show the $-2 \ln \Lambda(\kappa_\lambda) = 1$ level that is used to define the $\pm 1\sigma$ uncertainty on κ_λ as well as the $-2 \ln \Lambda(\kappa_\lambda) = 3.84$ level used to define the 95% CL.

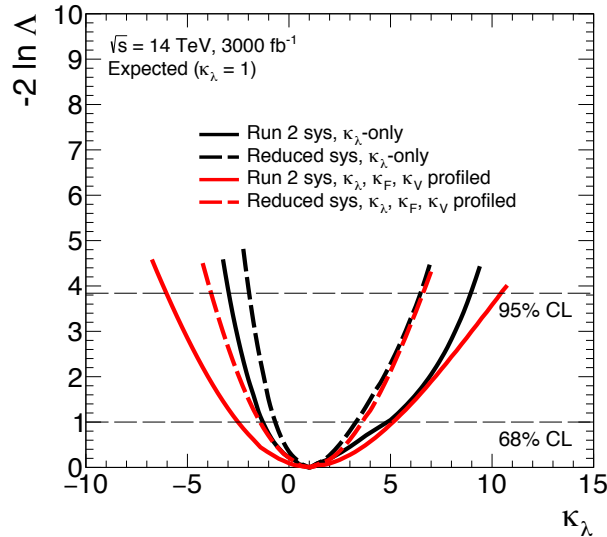


Figure 8.15: Value of $-2 \ln \Lambda(\kappa_\lambda)$ as a function of κ_λ for an Asimov dataset generated under the SM hypothesis considering a luminosity of 3000 fb^{-1} at $\sqrt{s} = 14 \text{ TeV}$. Two different scenarios are considered: “Run 2 sys” (solid lines) and “Reduced sys” (dashed lines). Two different fit configurations are reported: κ_λ -only model (black line) and κ_λ - κ_F - κ_V model, (red line). All the coupling modifiers that are not included in the fit are set to their SM predictions. The dotted horizontal lines show the $-2 \ln \Lambda(\kappa_\lambda) = 1$ level that is used to define the $\pm 1\sigma$ uncertainty on κ_λ as well as the $-2 \ln \Lambda(\kappa_\lambda) = 3.84$ level used to define the 95% CL.

Chapter 9

Constraining the Higgs-boson self-coupling combining single- and double-Higgs production and decay measurements

This chapter presents the final results of this dissertation, providing the most stringent constraint on κ_λ from experimental measurements through the combination of the double- and single-Higgs analyses whose details have been described in Chapters 7 and 8. The chapter is organised as follows: Section 9.1 presents a brief summary of the analyses exploited in this combination; Sections 9.2 and 9.3 revise the theoretical framework that has been implemented and the statistical model including nuisance parameter correlations between single- and double-Higgs analyses, respectively. Overlap studies aiming to understand and take into account overlaps between categories of the different analyses are shown in Section 9.4, while a validation of the inputs of the combination performed separately for single- and double-Higgs analyses is presented in Section 9.5. Finally, Sections 9.6, 9.7 and 9.8 summarise the results of this combination exploiting different fit configurations ranging from a κ_λ -only model to a generic model.

9.1 Data and input measurements

The results presented in this chapter are obtained using data collected by the ATLAS experiment in 2015, 2016 and 2017 from 13 TeV pp collision data corresponding to a luminosity of up to 79.8 fb^{-1} . The integrated luminosity for each analysed decay channel is summarised in Table 9.1. The combination takes as inputs the double-Higgs analyses described in Chapter 7, i.e. $b\bar{b}\tau^+\tau^-$, $b\bar{b}\gamma\gamma$ and $b\bar{b}b\bar{b}$ final states, as well as the single-Higgs analyses described in Chapter 8, including the ggF , VBF , WH , ZH and $t\bar{t}H$ production modes and the $\gamma\gamma$, WW^* , ZZ^* , $b\bar{b}$ and $\tau^+\tau^-$ decay channels. Details on the individual channels are already reported in the aforementioned chapters.

The single-Higgs and double-Higgs categories are not all orthogonal to each other. The overlap between these categories has been studied and is described in Section 9.4; only categories with negligible overlap have been included in this combination: thus the $t\bar{t}H \rightarrow \gamma\gamma$ categories included in the results of Chapter 8 have been removed from this combination

as they show large overlap with the $HH \rightarrow b\bar{b}\gamma\gamma$ categories and have an impact which is significantly smaller than the impact coming from $HH \rightarrow b\bar{b}\gamma\gamma$ categories.

Analysis	Integrated luminosity (fb ⁻¹)	Reference
$HH \rightarrow b\bar{b}b\bar{b}$	27.5	[138]
$HH \rightarrow b\bar{b}\tau^+\tau^-$	36.1	[139]
$HH \rightarrow b\bar{b}\gamma\gamma$	36.1	[140]
$H \rightarrow \gamma\gamma$ (excluding $t\bar{t}H$, $H \rightarrow \gamma\gamma$)	79.8	[151–153]
$H \rightarrow ZZ^* \rightarrow 4\ell$ (including $t\bar{t}H$, $H \rightarrow ZZ^* \rightarrow 4\ell$)	79.8	[154, 155]
$H \rightarrow WW^* \rightarrow e\nu\mu\nu$	36.1	[156]
$H \rightarrow \tau\tau$	36.1	[157]
VH , $H \rightarrow b\bar{b}$	79.8	[158, 159]
$t\bar{t}H$, $H \rightarrow b\bar{b}$ and $t\bar{t}H$ multilepton	36.1	[160, 161]

Table 9.1: Integrated luminosity of the datasets used for each input analysis to the $H + HH$ combination. The last column provides references to publications describing each measurement included in detail.

9.2 Theoretical model

The theoretical models described in Chapter 6 are exploited in order to implement the dependence on κ_λ and on the other coupling modifiers in double- and single-Higgs analyses. Details on how this dependence has been implemented are reported in the chapters describing the corresponding analyses, Chapters 7 and 8. The values of the C_1 coefficients for both the initial, i , and the final, f , states and the K_{EW} coefficients are reported in Chapter 6, while the κ modifiers at LO for the initial and final states are reported in Chapters 7 and 8. For single-Higgs analyses, the differential information is exploited in the regions defined by the STXS stage-1 framework, particularly in the VBF , ZH and WH production modes.

The results of this chapter are presented exploiting the coupling modifiers κ_t , κ_b , κ_ℓ , κ_W , κ_Z . They describe the modifications of the SM Higgs boson couplings to up-type quarks, to down-type quarks, to leptons and to W and Z vector bosons, respectively; alternatively, the coupling modifiers $\kappa_F = \kappa_t = \kappa_b = \kappa_\ell$ and $\kappa_V = \kappa_W = \kappa_Z$ are used, describing modifications of SM Higgs boson couplings to fermions and vector bosons, respectively.

9.3 Statistical model

The main principles used in order to extract the final results have been reported in both Chapters 7 and 8. In this section elements that have been added in order to produce the results of the combination are reported, together with the basic principles of the

correlation scheme used to combine single- and double-Higgs analyses. The results of the $H + HH$ combination are obtained from a likelihood function $L(\vec{\alpha}, \vec{\theta})$, where $\vec{\alpha}$ represents the vector of POIs of the model and $\vec{\theta}$ is the set of nuisance parameters, including the systematic uncertainty contributions and background parameters that are constrained by side bands or control regions in data. The number of signal events in each analysis category j is defined as:

$$n_j^{\text{signal}}(\kappa_\lambda, \kappa_t, \kappa_b, \kappa_\ell, \kappa_W, \kappa_Z, \vec{\theta}) = \mathcal{L}_j(\vec{\theta}) \sum_i \sum_f \mu_i(\kappa) \times \mu_f(\kappa) (\sigma_{\text{SM},i}(\vec{\theta}) \times \text{BR}_{\text{SM},f}(\vec{\theta})) (\epsilon \times A)_{if,j}(\vec{\theta}) \quad (9.1)$$

where the index i runs over all the production regions defined by the STXS stage-1 framework and all the double-Higgs regions and the index f includes all the considered decay channels, i.e. $f = \gamma\gamma, ZZ^*, WW^*, \tau^+\tau^-, b\bar{b}$ for the single-Higgs part while $f = b\bar{b}b\bar{b}, b\bar{b}\tau^+\tau^-, b\bar{b}\gamma\gamma$ for the double-Higgs part. \mathcal{L}_j is the integrated luminosity of the dataset used in the j category, and $(\epsilon \times A)_{if,j}$ represents the acceptance and efficiency estimation for the category j , the production process i and the decay channel f . All these terms depend also on a set of nuisance parameters $\vec{\theta}$, that account for theoretical and systematic uncertainties that can affect the luminosity, the cross-section and branching fraction prediction, the efficiency estimation, and the background estimation. Finally, $\mu_i(\kappa) \times \mu_f(\kappa) = \mu_i(\kappa_\lambda, \kappa_t, \kappa_b, \kappa_\ell, \kappa_W, \kappa_Z) \times \mu_f(\kappa_\lambda, \kappa_t, \kappa_b, \kappa_\ell, \kappa_W, \kappa_Z)$, describes the yield dependence on the Higgs boson self-coupling modifier κ_λ , and on the single Higgs boson coupling modifiers $\kappa_t, \kappa_b, \kappa_\ell, \kappa_W$ and κ_Z , representing potential deviations from the SM expectation.

Confidence intervals for the POIs are determined using the profile likelihood ratio, described in previous chapters, as the test statistic, using the 68% as well as the 95% CL intervals in the asymptotic limit [125].

The correlations between the systematic uncertainties within the single-Higgs and double-Higgs individual combinations are described in the chapters corresponding to the two analyses, i.e. Chapters 7 and 8. The correlation of the systematic uncertainties between single- and double-Higgs analyses has also been investigated and is taken into account in this combination, as described in the following section.

9.3.1 Correlation scheme between single- and double-Higgs analyses

The correlation scheme adopted in order to make the $H + HH$ combination is driven by the following guidelines [132]:

- experimental uncertainties have been correlated whenever relevant, like it was made in the case of the uncertainty on the integrated luminosity;
- experimental uncertainties that are related to the same physics object but determined with different methodologies or implemented with different parameterisations have been kept uncorrelated, like in the case of flavour tagging uncertainties;
- theory uncertainties related to signal processes have been kept uncorrelated;
- theory uncertainties on the decay branching fractions have been correlated;

- data-driven background uncertainties in double-Higgs analyses are not correlated with single-Higgs analyses.

Several studies have been made in order to study the impact of correlating different uncertainties, that are kept uncorrelated in the nominal configuration; the strategy that has been adopted has been not to correlate uncertainties whose correlation has a negligible or a null impact on the results:

- in the configuration scheme adopted for the combination:
 - the theoretical α_S uncertainties and pile-up reweighting (PRW) uncertainties are uncorrelated among single-Higgs and double-Higgs analyses and among $HH \rightarrow b\bar{b}\gamma\gamma$ and other channels, respectively; the impact on κ_λ results of correlating these uncertainties is negligible as reported in Table 9.2 where a comparison with the nominal correlation scheme adopted in this combination is made;

Correlation scheme	1 σ	95% CL
Nominal	$4.6^{+3.2}_{-3.8}$	[-2.3, 10.3]
	$1.0^{+7.3}_{-3.8}$	[-5.1, 11.2]
Correlating α_S , PRW	$4.6^{+3.2}_{-3.8}$	[-2.3, 10.3]
	$1.0^{+7.3}_{-3.8}$	[-5.1, 11.2]

Table 9.2: Comparison of the κ_λ measurement nominal results with the results obtained correlating α_S and PRW uncertainties. Both κ_λ 1σ uncertainty and 95% CL interval are reported. The first row shows the observed results while the second row shows the expected results.

- the experimental uncertainties related to the identification and energy scale of τ leptons, i.e. “TAU_EFF_ID_HIGHPT”, “TAU_EFF_ID_TOTAL TAU_TES_DET” and “TAU_TES_INSITU, TAU_TES_MODEL”, are uncorrelated among $t\bar{t}H \rightarrow$ multilepton and the double-Higgs channels; the impact on κ_λ of correlating these uncertainties is negligible as reported in Table 9.3 where a comparison with the nominal correlation scheme adopted in this combination is made;
- flavour tagging uncertainties, i.e. “FT_EFF_Eigen_X_N (X = B, C, Light, N = 0, 1, 2, 3, 4)”, “FT_EFF_extrapolation”, “FT_EFF_extrapolation_from_charm”, are uncorrelated since single-Higgs analyses use the 85% efficiency b -tagging working point, for 2015-2016 analyses using Release 20.7, while double-Higgs analyses use the 70% efficiency working point for the same release. No significant changes with respect to the nominal results are found correlating these uncertainties, as shown in Table 9.4;
- due to the fact that, in single-Higgs and double-Higgs analyses, ggF QCD scale and PDF uncertainties use different schemes and number of nuisance parameters, they are not correlated.

Correlation scheme	1σ	95% CL
Nominal	$4.6^{+3.2}_{-3.8}$	[-2.3, 10.3]
	$1.0^{+7.3}_{-3.8}$	[-5.1, 11.2]
Correlating TAU	$4.6^{+3.2}_{-3.8}$	[-2.3, 10.3]
	$1.0^{+7.3}_{-3.8}$	[-5.1, 11.2]

Table 9.3: Comparison of the κ_λ measurement nominal results with the results obtained correlating the TAU-related experimental uncertainties. Both κ_λ 1σ uncertainty and 95% CL interval are reported. The first row shows the observed results while the second row shows the expected results.

Correlation scheme	1σ	95% CL
Nominal	$4.6^{+3.2}_{-3.8}$	[-2.3, 10.3]
	$1.0^{+7.3}_{-3.8}$	[-5.1, 11.2]
Correlating FT	$4.6^{+3.2}_{-3.8}$	[-2.3, 10.3]
	$1.0^{+7.3}_{-3.8}$	[-5.1, 11.2]

Table 9.4: κ_λ measurement results by correlating FT uncertainties with different WPs. Both κ_λ 1σ uncertainty and 95% CL interval are reported. The first row shows the observed results while the second row shows the expected results.

The list of the NPs included in single-Higgs analyses, in double-Higgs analyses and in the combination of the two of them is reported in Appendix B.

Figure 9.1 shows the ranking plots, defined in Chapter 7, of the top 30 systematic uncertainties for the $H + HH$ combination considering data (a) and considering the Asimov dataset (b). The nuisance parameters having the largest impact on κ_λ are the ones related to the theory modelling of signal and background processes in simulation coming from the single-Higgs analyses, to the data-driven background modelling (mainly multi-jets) of $HH \rightarrow b\bar{b}b\bar{b}$ and $HH \rightarrow b\bar{b}\gamma\gamma$ analyses and the experimental nuisance parameters related to photons and jets, consistently with what has been found in double- and single-Higgs combinations. The different nuisance parameters ranked in Figure 9.1 have been described in Chapters 7 and 8. Being the measurement statically dominated, this impact is small compared to the statistical uncertainties as it is shown in the result section.

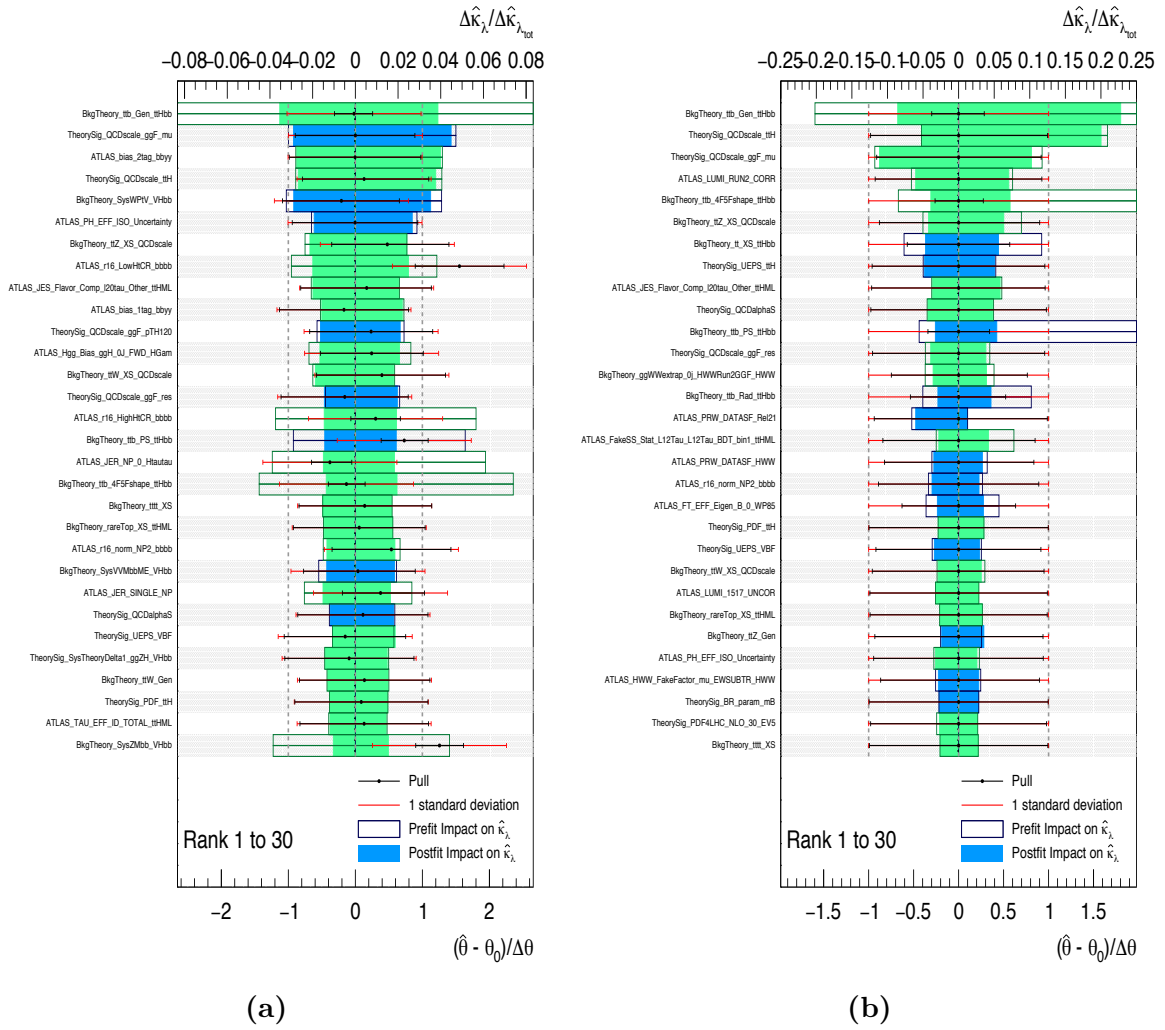


Figure 9.1: Ranking of the top 30 systematic uncertainties in the $H + HH$ combination for data (a) and for the Asimov dataset (b) generated under the SM hypothesis.

9.4 Overlap studies

The event selection of the double-Higgs categories is not orthogonal by construction to the event selection of all the single-Higgs categories included in the combined fit. Thus some events might pass both selections and might be double counted. Overlap checks have been performed in order to quantify the expected fraction of shared events among overlapping categories normalised to the total number of events that pass the single-Higgs or the double-Higgs selections. In cases where a non-negligible overlap was found between the double-Higgs and single-Higgs signal regions, a fit has been performed to constrain κ_λ , with all other single-Higgs couplings set to their SM values, and to constrain κ_λ and κ_t , setting all other couplings to their SM values except for κ_t , in order to exploit the dependence on κ_λ and κ_t of the double-Higgs analyses. The impact of the overlap on the combined κ_λ -only and $\kappa_\lambda - \kappa_t$ results has thus been checked removing the overlapping single-Higgs categories from the combined fit.

9.4.1 $HH \rightarrow b\bar{b}\gamma\gamma$ and $H \rightarrow \gamma\gamma$ overlap

The single-Higgs $H \rightarrow \gamma\gamma$ analysis applies the following event selection:

- two isolated (FixedCutLoose isolation criterion, defined in Chapter 4) and identified (Tight identification criterion, defined in Chapter 4) photons;
- $p_T^\gamma/m_{\gamma\gamma} > 0.35$ and 0.25 for leading and subleading photons, respectively;
- $105 \text{ GeV} < m_{\gamma\gamma} < 160 \text{ GeV}$.

The double-Higgs $HH \rightarrow b\bar{b}\gamma\gamma$ event selection adds to the listed requirements, the following:

- 1-tag:
 - single-Higgs selection;
 - two jets $|\eta| < 2.5$;
 - one b -tagged jet (at the 60% b -tagging efficiency working point);
 - the highest- p_T jet is required to have $p_T^{j,1} > 40 \text{ GeV}$ and the next-highest- p_T jet must satisfy $p_T^{j,2} > 25 \text{ GeV}$;
 - $80 < m_{jj} < 140 \text{ GeV}$.
- 2-tag:
 - single-Higgs selection;
 - two jets $|\eta| < 2.5$;
 - exactly two b -tagged jets (at the 70% b -tagging efficiency working point, as defined in Chapter 4);
 - $p_T^{j,1} > 40 \text{ GeV}$ and $p_T^{j,2} > 25 \text{ GeV}$;
 - $80 < m_{jj} < 140 \text{ GeV}$.

The overlap between $b\bar{b}\gamma\gamma$ and $H \rightarrow \gamma\gamma$ analyses, defined as the number of $b\bar{b}\gamma\gamma$ signal events in $H \rightarrow \gamma\gamma$ categories normalised to the number of $b\bar{b}\gamma\gamma$ signal events, is 100%, being the $HH \rightarrow b\bar{b}\gamma\gamma$ analysis a subsample of the $H \rightarrow \gamma\gamma$ analysis. A comparison between the data events passing the $HH \rightarrow b\bar{b}\gamma\gamma$ event selection and the data events passing the event selection of each $H \rightarrow \gamma\gamma$ category has been made in order to identify the most overlapping regions and quantify the size of this overlap; thus the run number, assigned uniquely to each data taking run that starts after the declaration of stable beams, and the event number that, combined with the run number, uniquely identifies an event, of these double-Higgs and single-Higgs events have been compared. The fraction of overlapping events is negligible for all the processes, at the level of a few percent, except for the $t\bar{t}H \rightarrow \gamma\gamma$ production mode, considering both hadronic and leptonic categories, given the absence of any lepton veto at the selection level of this double-Higgs analysis: indeed, in $t\bar{t}H$ production mode, there are categories where up to 50% of the selected $t\bar{t}H \rightarrow \gamma\gamma$ events are also selected by the $HH \rightarrow b\bar{b}\gamma\gamma$ analysis.

The impact of the overlap on the results has been checked performing the combined fit removing the single-Higgs most overlapping categories. Tables 9.5 and 9.6 report the expected and observed fit results either excluding or including all $t\bar{t}H \rightarrow \gamma\gamma$ categories or all $HH \rightarrow b\bar{b}\gamma\gamma$ categories as well as excluding overlapped events in the $H + HH$ combination; considering the κ_λ -only fit, where all the other Higgs couplings are set to their SM values, the impact on the results removing different categories/events is summarised as follows:

- removing all $t\bar{t}H$ categories: 2.5% (2%) impact on the 95% CL interval considering data (asimov);
- removing overlapped events: 1% (2%) impact on the 95% CL interval considering data (asimov);
- removing all $b\bar{b}\gamma\gamma$ categories: 10% (14%) impact on the 95% CL interval considering data (asimov).

All the $t\bar{t}H \rightarrow \gamma\gamma$ categories have been removed from this combination as they show large overlap with the $HH \rightarrow b\bar{b}\gamma\gamma$ categories; such a decision has been made after also checking that the impact on the expected and observed combined limits of removing these categories is smaller with respect to removing $HH \rightarrow b\bar{b}\gamma\gamma$ categories; in fact these categories, as it will be shown in Section 9.6, represent one of the dominant contributions in order to constrain κ_λ .

Analysis	Fit configuration	κ_λ interval at 95% CL (exp)	κ_t interval at 95% CL (exp)
single-Higgs v9 (no $t\bar{t}H \rightarrow \gamma\gamma$) + HH	κ_λ only	[-5.107 - 11.232]	–
	$\kappa_\lambda - \kappa_t$	[-5.534 - 11.280]	[0.872 - 1.139]
single-Higgs v9 (no overlapped events) + HH	κ_λ -only	[-4.830 - 10.933]	–
	$\kappa_\lambda - \kappa_t$	[-5.297 - 10.966]	[0.874 - 1.138]
single-Higgs v9 + HH (no $b\bar{b}\gamma\gamma$ categories)	κ_λ only	[-5.349 - 12.910]	–
	$\kappa_\lambda - \kappa_t$	[-6.241 - 13.139]	[0.872 - 1.147]
single-Higgs v9 + HH	κ_λ -only	[-4.893 - 11.122]	–
	$\kappa_\lambda - \kappa_t$	[-5.393 - 11.159]	[0.871 - 1.139]

Table 9.5: 95% CL expected intervals for κ_λ only and κ_λ, κ_t fit configurations exploiting $H + HH$ combination. The fit has been performed either excluding or including the categories listed in the first column.

Analysis	Fit configuration	κ_λ interval at 95% CL (obs)	κ_t interval at 95% CL (obs)
single-Higgs v9 (no $t\bar{t}H \rightarrow \gamma\gamma$) + HH	κ_λ -only	[-2.302 - 10.287]	–
	$\kappa_\lambda - \kappa_t$	[-2.882 - 10.642]	[0.912 - 1.169]
single-Higgs v9 (no overlapped events) + HH	κ_λ -only	[-2.677 - 9.744]	–
	$\kappa_\lambda - \kappa_t$	[-3.264 - 10.042]	[0.910 - 1.161]
single-Higgs v9 + HH (no $b\bar{b}\gamma\gamma$ categories)	κ_λ -only	[-2.236 - 11.261]	–
	$\kappa_\lambda - \kappa_t$	[-3.073 - 11.992]	[0.914 - 1.174]
single-Higgs v9 + HH	κ_λ -only	[-2.186 - 10.099]	–
	$\kappa_\lambda - \kappa_t$	[-2.833 - 10.433]	[0.913 - 1.166]

Table 9.6: 95% CL observed intervals for κ_λ only and κ_λ, κ_t fit configurations exploiting $H + HH$ combination. The fit has been performed either excluding or including the categories listed in the first column.

9.4.2 $HH \rightarrow b\bar{b}\tau^+\tau^-$ overlap with $H \rightarrow \tau^+\tau^-$, $t\bar{t}H \rightarrow b\bar{b}$, $t\bar{t}H$ multilepton, $VH \rightarrow b\bar{b}$

The $HH \rightarrow b\bar{b}\tau^+\tau^-$ analysis selects events using two categories, the $\tau_{\text{had}}\tau_{\text{had}}$ category and the $\tau_{\text{lep}}\tau_{\text{had}}$ category, described in detail in Chapter 7.

Thus, looking at single-Higgs similar final states and event selections, possible overlapping analyses have been identified as the $H \rightarrow \tau^+\tau^-$, $t\bar{t}H \rightarrow b\bar{b}$, $t\bar{t}H \rightarrow$ multilepton and $VH \rightarrow b\bar{b}$ single-Higgs analyses. In order to quantify the overlap between signal regions, the run and event number of the data events passing the $HH \rightarrow b\bar{b}\tau^+\tau^-$ event selection have been compared to the ones of the data events passing the event selection of the single-Higgs signal regions listed above. As the $HH \rightarrow b\bar{b}\tau^+\tau^-$ analysis uses a BDT distribution as the final discriminant of the analysis, being the last BDT bin the most sensitive, the check comparing run and event number of double- and single-Higgs analyses has been performed also looking exclusively at this bin. The fraction of data events that passes both the $HH \rightarrow b\bar{b}\tau^+\tau^-$ selections and the selections of a certain single-Higgs category, normalised to the number of double-Higgs events, gives an estimation of the overlap:

- $H \rightarrow \tau^+\tau^-$: the overlap is present only between $HH \rightarrow b\bar{b}\tau^+\tau^-$ ($\tau_{\text{had}}\tau_{\text{had}}$) category and $H \rightarrow \tau^+\tau^-$ HadHad boosted category; the fraction of overlapping events is quantified as 3.4×10^{-3} of full $HH \rightarrow b\bar{b}\tau^+\tau^-$ ($\tau_{\text{had}}\tau_{\text{had}}$) signal region and 1.4×10^{-1} in last BDT bin;
- $t\bar{t}H \rightarrow b\bar{b}$: the overlap is present between $HH \rightarrow b\bar{b}\tau^+\tau^-$ ($\tau_{\text{lep}}\tau_{\text{had}}$) category and $t\bar{t}H \rightarrow b\bar{b}$ single lepton (6j SR2, 6j SR3, 5j SR, boosted) categories; the fraction of overlapping events is quantified as 10^{-4} of full $HH \rightarrow b\bar{b}\tau^+\tau^-$ ($\tau_{\text{lep}}\tau_{\text{had}}$) signal region and 0 in last BDT bin;
- $t\bar{t}H \rightarrow$ multilepton; the categories are orthogonal, so no overlap is present;
- $VH \rightarrow b\bar{b}$: the overlap is present between $HH \rightarrow b\bar{b}\tau^+\tau^-$ and $VH \rightarrow b\bar{b}$ categories (1lep 2btags \geq 3jets) and (0lep 2btags \geq 3jets), while other categories are orthogonal: the fraction of overlapping events is quantified as:
 - 1lep 2btags \geq 3 jets: overlap of 1.7×10^{-2} of full $HH \rightarrow b\bar{b}\tau^+\tau^-$ ($\tau_{\text{lep}}\tau_{\text{had}}$) signal region and 5.3×10^{-2} in last BDT bin;
 - 0lep 2btags \geq 3 jets: overlap of 10^{-3} of full $HH \rightarrow b\bar{b}\tau^+\tau^-$ ($\tau_{\text{had}}\tau_{\text{had}}$) signal region and 0 in last BDT bin.

The impact of the overlap on the results has been checked performing the combined fit removing the single-Higgs categories showing an overlap with double-Higgs categories above 1%. Table 9.7 reports the expected fit results either excluding or including the $H \rightarrow \tau\tau$ (Had Had boosted category) in the $H + HH$ combination and either excluding or including the $VH \rightarrow b\bar{b}$ (2 btags 1 lep 3 jets) category in the $H + HH$ combination.

The choice of keeping these categories in the combination arises from the fact that the overlap is relatively small and their impact on the κ_λ extraction is smaller than 1% so the overlapping events are not biasing it; furthermore, the approach of not removing categories that, although not having a significant impact on κ_λ , can have an impact on the other Higgs couplings, has been followed.

Analysis	Fit configuration	κ_λ interval at 95% CL (exp)	κ_t interval at 95% CL (exp)
single-Higgs v8 (excluding $H \rightarrow \tau\tau$ categories) + HH	κ_λ only	[-4.78 - 11.00]	–
	$\kappa_\lambda - \kappa_t$	[-5.15 - 11.02]	[0.90 - 1.11]
single-Higgs v8 (excluding $VH \rightarrow bb$ category) + HH	κ_λ only	[-4.77 - 11.03]	–
	$\kappa_\lambda - \kappa_t$	[-5.14 - 11.03]	[0.88 - 1.12]
single-Higgs v8 + HH	κ_λ only	[-4.75 - 11.00]	–
	$\kappa_\lambda - \kappa_t$	[-5.17 - 11.00]	[0.88 - 1.12]

Table 9.7: 95% CL expected intervals for κ_λ only and κ_λ, κ_t fit configurations exploiting $H + HH$ combination. The fit has been performed either excluding or including $H \rightarrow \tau\tau$ (had had boosted) category or $VH \rightarrow bb$ (2 btags 1 lep 3 jets) category.

9.4.3 $HH \rightarrow b\bar{b}b\bar{b}$ and $t\bar{t}H \rightarrow b\bar{b}$ overlap

The $HH \rightarrow b\bar{b}b\bar{b}$ analysis selects events with two Higgs boson candidates, each composed of two b -tagged anti- k_t $R=0.4$ jets, with invariant masses near m_H , as described in Chapter 7. Possible overlaps can be found with $t\bar{t}H \rightarrow b\bar{b}$ signal regions. To check this overlap, the run and event number of the data events passing the $HH \rightarrow b\bar{b}b\bar{b}$ event selection have been compared to the ones of the data events passing the $t\bar{t}H \rightarrow b\bar{b}$ event selection. It is found that there is overlap with some of the $t\bar{t}H \rightarrow b\bar{b}$ categories with fractions of overlapping events between 1.2×10^{-4} and 1.5×10^{-3} . These categories are kept in this combination as the overlap is small and cannot affect the results.

9.4.4 Signal contamination in double-Higgs and single-Higgs channels

The double-Higgs event selections, in addition to targeting double-Higgs processes, also select a number of single-Higgs signal events that have to be taken into account in double-Higgs signal regions if their contribution is not negligible. Thus this contribution has been taken into account both for $HH \rightarrow b\bar{b}\tau^+\tau^-$ and $HH \rightarrow b\bar{b}\tau^+\tau^-$ channels, while it is negligible for the $HH \rightarrow b\bar{b}b\bar{b}$ channel. Events from ZH and $t\bar{t}H$ single-Higgs production modes passing the $HH \rightarrow b\bar{b}\gamma\gamma$ event selection are not negligible and are therefore included in the $HH \rightarrow b\bar{b}\gamma\gamma$ signal regions. Double-Higgs contribution into $H \rightarrow \gamma\gamma$ categories has been checked: for high negative κ_λ values, double-Higgs contribution becomes comparable to single-Higgs expectation, particularly looking at $t\bar{t}H \rightarrow \gamma\gamma$ hadronic categories where the double-Higgs contribution becomes even three times bigger than the one expected from single Higgs.

Events from ZH and $t\bar{t}H$ single-Higgs production modes passing the $HH \rightarrow b\bar{b}\tau^+\tau^-$ event selection are not negligible and are therefore included in the $HH \rightarrow b\bar{b}\tau^+\tau^-$ signal regions. The highest contamination, given in terms of acceptance times efficiency, is 10^{-2} coming from the contamination between double-Higgs $\tau_{\text{lep}}\tau_{\text{had}}$ and the $Z(\rightarrow \tau\tau)H(\rightarrow b\bar{b})$ signal regions.

9.5 Validation of single- and double-Higgs inputs

Both κ_λ measurement results reported in Chapter 8 and in Chapter 7 have been cross-checked before combining the different analyses.

9.5.1 Single-Higgs input validation

Some updates have been made with respect to the input used in the single-Higgs results reported in Chapter 8, that will be named as “Nominal input”, while the single-Higgs input entering this combination will be named as “Updated input”. The Updated input has the following modifications:

- the sign of the α_S in the $H \rightarrow ZZ$ channel has been flipped to be consistent with other channels.

- theoretical Underlying Events and Parton Shower (UE/PS) uncertainties on the signal acceptance, “UEPS_WH/ZH/ggZH” and “UEPS_VH”, have been merged in the $H \rightarrow \gamma\gamma$ channel.

These updates have been validated to have negligible impacts on the Higgs-coupling estimations of Reference [41]. Besides those, an additional modification having a negligible impact has been made:

- the branching fractions of $H \rightarrow s\bar{s}$ (0.04%) is included in the parameterisation of the Higgs total width in Equation 6.7.

The negligible differences including these updates are clear looking at Table 9.8 reporting κ_λ best-fit values, together with 1σ interval and 95% CL intervals for both data and for the Asimov dataset generated under the SM hypothesis.

Input workspaces	$\kappa_\lambda^{+1\sigma}_{-1\sigma}$	κ_λ interval at 95% CL
Nominal input	$4.0^{+4.3}_{-4.1}$	[-3.2, 11.9]
	$1.0^{+8.8}_{-4.4}$	[-6.2, 14.4]
Updated input	$4.0^{+4.3}_{-4.1}$	[-3.3, 11.9]
	$1.0^{+8.9}_{-4.4}$	[-6.3, 14.5]

Table 9.8: 1σ interval and 95% CL results of κ_λ considering different single-Higgs inputs. Observed results are reported in the first row, while expected results are reported in the second row.

After the studies reported in Section 9.4, it was decided to exclude $t\bar{t}H \rightarrow \gamma\gamma$ categories from this combination; the impacts on the κ_λ single-Higgs best-fit value and 95% CL interval on data are determined to be 8% and 4%, respectively; a 2% difference is found in the expected 95% CL interval with respect to the nominal configurations. The impacts on the global signal strength, μ , and on the signal strength for the $t\bar{t}H$ production mode, $\mu_{t\bar{t}H}$, fitting simultaneously the signal strengths of the other production modes, have been checked and the values of the signal strengths considering the different configurations are reported in Table 9.9. The changes on the global and “local” signal strengths are 1% and 8%, respectively.

Signal strength	Nominal input	Removing $t\bar{t}H \rightarrow \gamma\gamma$
μ	$1.11^{+0.09}_{-0.08}$	$1.10^{+0.09}_{-0.08}$
$\mu_{t\bar{t}H}$	$1.09^{+0.29}_{-0.25}$	$1.18^{+0.34}_{-0.30}$

Table 9.9: Global signal strengths coming from single-Higgs combined input either including or excluding $t\bar{t}H \rightarrow \gamma\gamma$ (second row); signal strengths associated to the $t\bar{t}H$ production mode either including or excluding $t\bar{t}H \rightarrow \gamma\gamma$ (third row).

Figure 9.2 reports the value of $-2 \ln \Lambda(\kappa_\lambda)$ as a function of κ_λ for single-Higgs analyses comparing the inputs either including or excluding $t\bar{t}H \rightarrow \gamma\gamma$ categories both for data (a) and for the Asimov dataset (b) generated under the SM hypothesis.

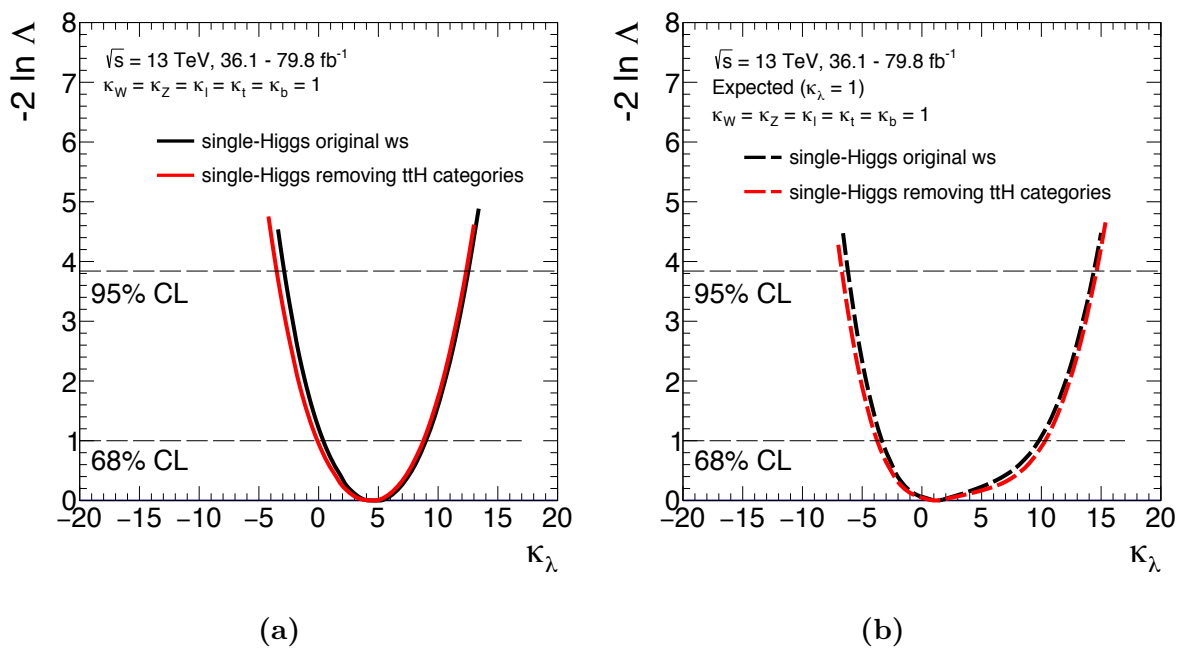


Figure 9.2: Value of $-2 \ln \Lambda(\kappa_\lambda)$ as a function of κ_λ for single-Higgs analysis comparing the inputs used to extract κ_λ results reported in Chapter 8 and removing $t\bar{t}H \rightarrow \gamma\gamma$ categories; the likelihood distribution for data is reported in (a) while (b) is for the Asimov dataset generated under the SM hypothesis. The dotted horizontal lines show the $-2 \ln \Lambda(\kappa_\lambda) = 1$ level that is used to define the $\pm 1\sigma$ uncertainty on κ_λ as well as the $-2 \ln \Lambda(\kappa_\lambda) = 3.84$ level used to define the 95% CL.

9.5.2 Double-Higgs input validation

In order to check that the $H + HH$ combination is behaving correctly, the results coming from the double-Higgs workspace extracted from the combined $H + HH$ workspace and the ones coming from the combination of double-Higgs channels, reported in Chapter 7, have been compared, exploiting a global normalisation floating for single-Higgs analysis which does not depend on κ_λ . Figure 9.3 shows the comparison between the two double-Higgs κ_λ measurements; they are not completely identical due to the correlations of systematic uncertainties.

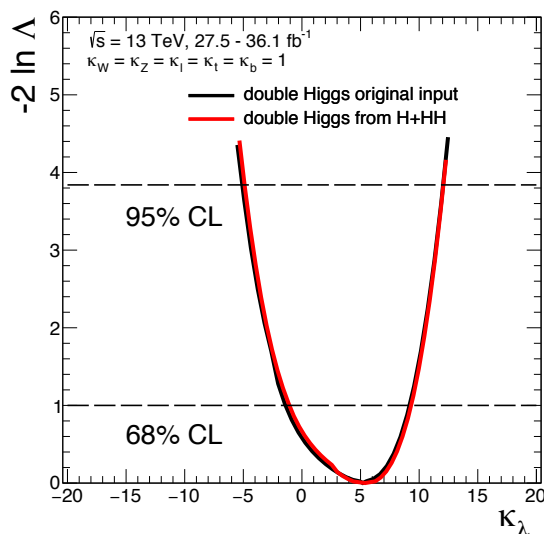


Figure 9.3: Value of $-2 \ln \Lambda(\kappa_\lambda)$ as a function of κ_λ for data considering double-Higgs analyses; the black solid line shows the original double-Higgs workspace used in order to produce the results of Chapter 7 while the red solid line represents the double-Higgs input extracted from the combined $H + HH$ analysis.

9.6 Results of fit to κ_λ

In this section the main result of the analysis is presented, where a likelihood fit is performed to constrain the value of the Higgs-boson self-coupling κ_λ , while setting all other Higgs boson couplings to their SM values ($\kappa_t = \kappa_b = \kappa_\ell = \kappa_W = \kappa_Z = 1$).

The constraints on κ_λ , derived exploiting the NLO EW κ_λ -dependent corrections to single-Higgs processes, can be directly compared to the constraints set by double-Higgs production analyses and the sensitivity gain from their combination can be evaluated.

The κ_λ self-coupling modifier is probed in the range $-20 < \kappa_\lambda < 20$. The central value and uncertainty of the κ_λ modifier of the trilinear Higgs-boson self-coupling for the combination of single- and double-Higgs analyses are determined to be:

$$\kappa_\lambda = 4.6_{-3.8}^{+3.2} = 4.6_{-3.5}^{+2.9} (\text{stat.})_{-1.2}^{+1.2} (\text{exp.})_{-0.5}^{+0.7} (\text{sig. th.})_{-1.0}^{+0.6} (\text{bkg. th.})(\text{observed})$$

$$\kappa_\lambda = 1.0_{-3.8}^{+7.3} = 1.0_{-3.0}^{+6.2} (\text{stat.})_{-1.7}^{+3.0} (\text{exp.})_{-1.2}^{+1.8} (\text{sig. th.})_{-1.1}^{+1.7} (\text{bkg. th.})(\text{expected})$$

where the total uncertainty is decomposed into components for statistical uncertainties, experimental systematic uncertainties, and theory uncertainties on signal and background modelling. The total uncertainty is dominated by the statistical component.

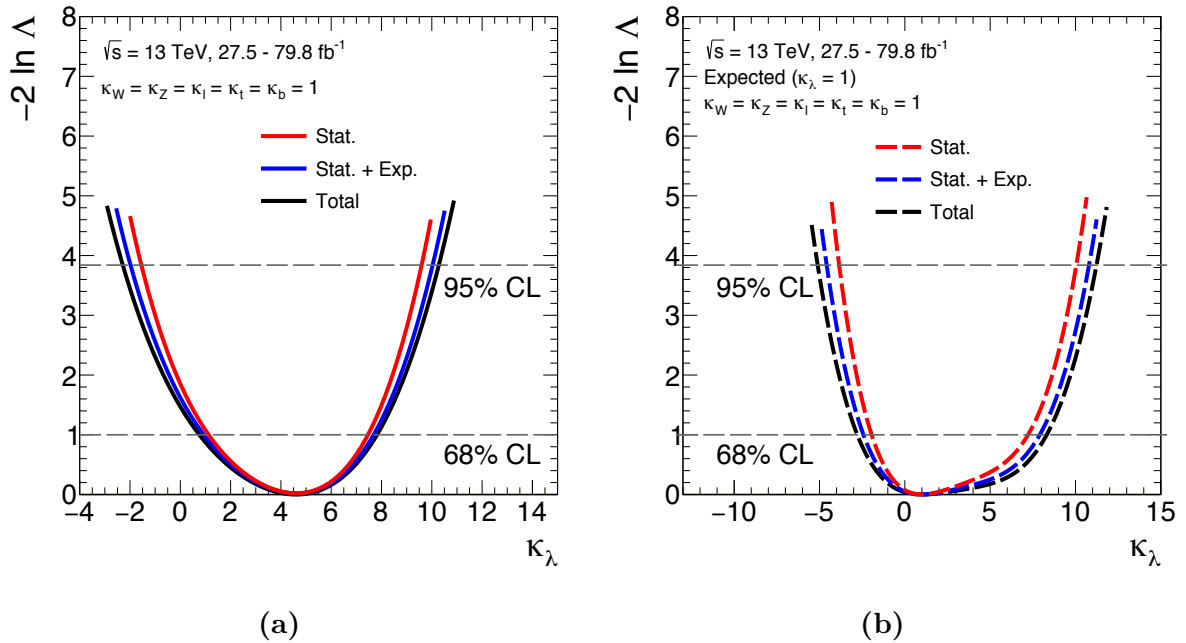


Figure 9.4: Value of $-2 \ln \Lambda(\kappa_\lambda)$ as a function of κ_λ for data (a), solid lines, and for the Asimov dataset generated in the SM hypothesis (b), dashed lines. The dotted horizontal lines show the $-2 \ln \Lambda(\kappa_\lambda) = 1$ level that is used to define the $\pm 1\sigma$ uncertainty on κ_λ as well as the $-2 \ln \Lambda(\kappa_\lambda) = 3.84$ level used to define the 95% CL. The black lines show the profile likelihood distributions obtained including all systematic uncertainties (“Total”). Results from a statistics only fit “Stat.” (red lines) and including the experimental systematics “Stat. + Exp.” (blue lines) are also shown.

The value of $-2 \ln \Lambda(\kappa_\lambda)$ as a function of κ_λ is shown in Figure 9.4 for data and for the Asimov dataset, generated from the likelihood distribution Λ with nuisance parameters

fixed at the best-fit value obtained on data and the parameter of interest fixed to SM hypothesis (i.e. $\kappa_\lambda = 1$). The profile likelihood distribution is obtained including statistical uncertainties, statistical and experimental systematic uncertainties, and including all statistical and systematic uncertainties.

The 95% CL intervals for κ_λ are $-2.3 < \kappa_\lambda < 10.3$ (observed) and $-5.1 < \kappa_\lambda < 11.2$ (expected).

Table 9.10 reports the detailed breakdown of the uncertainties affecting the measurement of the combined κ_λ ; the procedure used to produce the numbers of the table is the following: in each case the corresponding nuisance parameters are fixed to their best-fit values, while other nuisance parameters are left free, and the resulting uncertainty is subtracted in quadrature from the total uncertainty.

Uncertainty source	$\Delta\kappa_\lambda/\kappa_\lambda$ %
Statistical uncertainty	70
Systematic uncertainties	33
Theory uncertainties	20
Signal	12
Background	15
Experimental uncertainties (excl. MC stat.)	18
MC statistical uncertainty	8
Total uncertainty	77

Table 9.10: Summary of the relative uncertainties $\Delta\kappa_\lambda/\kappa_\lambda$ affecting the measurement of the combined κ_λ . The sum in quadrature of systematic uncertainties from individual sources differs from the uncertainty evaluated for the corresponding group in general, due to the presence of small correlations between nuisance parameters describing the different sources.

Table 9.11 presents the comparison of κ_λ intervals at 95% CL for single-Higgs analyses, double-Higgs analyses and for the $H + HH$ combination; a sensitivity gain of more than 20% is achieved in the combination with respect to single- and double-Higgs analyses alone.

Analysis	κ_λ interval at 95% CL(obs)	κ_λ interval at 95% CL(exp)
Single-Higgs	[-3.5 - 12.3]	[-6.7 - 14.6]
Double-Higgs	[-5.1 - 12.1]	[-6.9 - 12.4]
$H + HH$	[-2.3 - 10.3]	[-5.1 - 11.2]

Table 9.11: Comparison of κ_λ interval at 95% CL for single-Higgs analyses, double-Higgs analyses and for the combination of the two of them.

Figure 9.5 shows the value of $-2 \ln \Lambda(\kappa_\lambda)$ as a function of κ_λ for single- and double-Higgs analyses separately and for the combination of the two analyses. The double-Higgs

analyses are more sensitive than the single-Higgs measurement for $\kappa_\lambda \gg 1$ and show similar sensitivity for negative κ_λ .

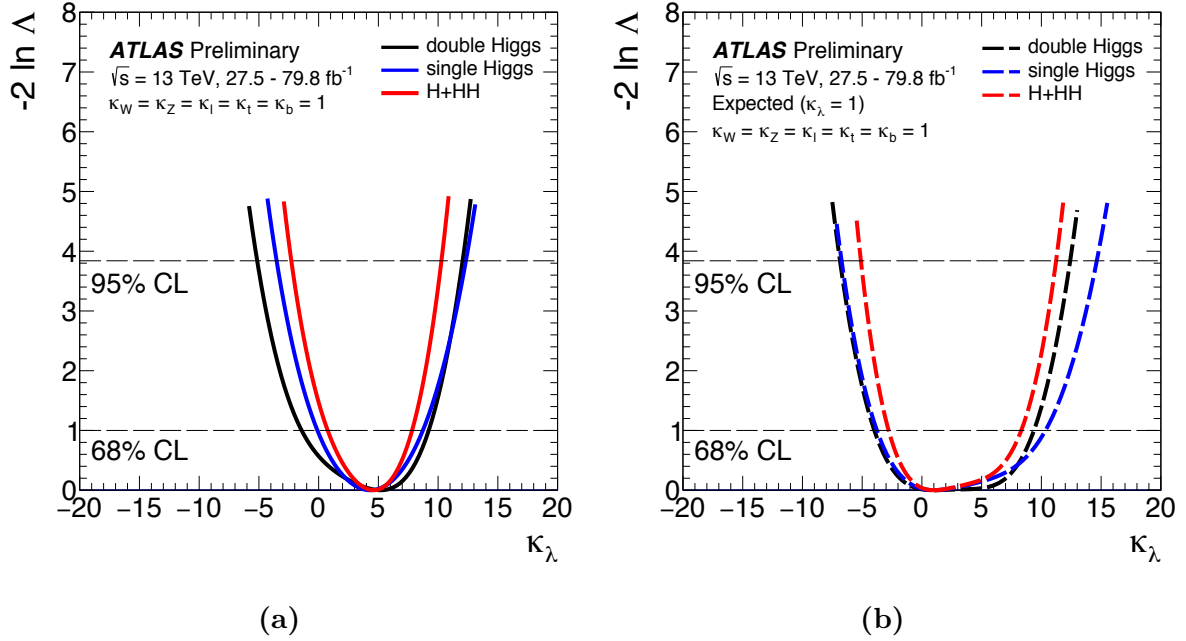


Figure 9.5: Value of $-2 \ln \Lambda(\kappa_\lambda)$ as a function of κ_λ for single and double-Higgs analyses separately and for the combination of the two analyses: (a) is for data and (b) is for the Asimov dataset. The dotted horizontal lines show the $-2 \ln \Lambda(\kappa_\lambda) = 1$ level that is used to define the $\pm 1\sigma$ uncertainty on κ_λ as well as the $-2 \ln \Lambda(\kappa_\lambda) = 3.84$ level used to define the 95% CL.

Differences in the shapes of the likelihood curves, reported in Figures 9.4 and 9.5, in the best-fit values of κ_λ between data and Asimov dataset are due to the non-linearity of the cross-section dependence from κ_λ , i.e. due to the interplay between κ_λ and κ_λ^2 terms in Equations 6.5 and 6.7, and due to the fact that the measured yields from single-Higgs and double-Higgs processes are slightly different than the expectation. This effect has been investigated generating two different Asimov datasets, the first one fixing κ_λ to the generic model best-fit value, $\kappa_\lambda = 5.5$, and all other couplings to their SM values, while the second one is generated fixing all κ to their observed values. While in the first Asimov dataset, data and Asimov likelihood shapes still have large differences due to a tension between data and the model assumption, after fixing the other couplings to the observed values, the likelihoods have similar shapes. Figure 9.6 shows the comparison between the likelihood curves for data (black solid line) and for the two Asimov datasets (blue and red shaded lines). Furthermore, the Asimov dataset generated fixing all the κ to their observed values, has been used in order to check the asymmetric uncertainty decomposition of the Asimov dataset generated under the SM hypothesis ($\kappa_\lambda = 1$), thus leading to a κ_λ central value and uncertainty:

$$\kappa_\lambda = 4.0^{+4.0}_{-4.7} = 4.0^{+3.5}_{-4.0} (\text{stat.})^{+1.6}_{-1.8} (\text{exp.})^{+0.9}_{-1.0} (\text{sig. th.})^{+0.6}_{-1.2} (\text{bkg. th.}) (\text{expected})$$

where the total uncertainty is decomposed into components for statistical uncertainties, experimental systematic uncertainties, and theory uncertainties on signal and background modelling. It is clear that the shapes of the likelihood distribution, the 1σ errors and

95% CL intervals around the best-fit value, are strictly dependent on the fitted value itself.

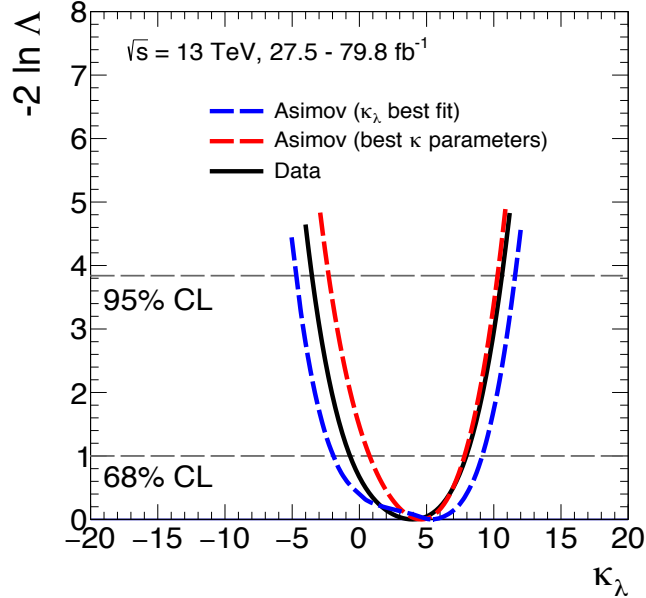


Figure 9.6: Value of $-2 \ln \Lambda(\kappa_\lambda)$ as a function of κ_λ comparing data (black solid line), and the two Asimov dataset generated with κ_λ fixed to the generic model best-fit value (blue solid line) and all κ parameters fixed to the best-fit values (red solid line). The dotted horizontal lines show the $-2 \ln \Lambda(\kappa_\lambda) = 1$ level that is used to define the $\pm 1\sigma$ uncertainty on κ_λ as well as the $-2 \ln \Lambda(\kappa_\lambda) = 3.84$ level used to define the 95% CL.

In order to investigate the constraining power of the several channels included in this combination, the test explained in Chapter 8 has been performed removing different categories, corresponding for example to the different double-Higgs decay channels, from the combined fit and checking the κ_λ 95% CL intervals obtained using the remaining channels. In order to avoid statistics fluctuations, Asimov datasets are used.

Table 9.12 shows the ranking of the different channels in constraining κ_λ : each row shows the 1σ interval and 95% CL of κ_λ obtained by removing one specific channel. The $b\bar{b}\gamma\gamma$ channel is the most sensitive one.

Figures 9.7 and 9.8 show the expected dependence of $-2 \ln \Lambda(\kappa_\lambda)$ on κ_λ for the κ_λ -only model (obtained in the $\kappa_\lambda = 1$ hypothesis) considering different production modes and decay channels; when showing a specific production or decay channels, all the κ_λ involved in the parameterisation of the corresponding signal yields (including those entering in the parameterisation of the branching ratios) are correlated in the $-2 \ln \Lambda(\kappa_\lambda)$ scan, while all the others are profiled. Looking at the single-Higgs, the di-boson decay channels $\gamma\gamma$, ZZ^* , WW^* and ggF and $t\bar{t}H$ production modes represent the dominant contributions. The $t\bar{t}H$ production mode is not sensitive for $\kappa_\lambda > 0$ because of the degeneracy in the cross-section.

Channels	$\kappa_\lambda^{+1\sigma}_{-1\sigma}$	κ_λ [95% CL]
$HH \rightarrow b\bar{b}\gamma\gamma$	$1.00^{+8.68}_{-4.05}$	[-5.60, 13.05]
$HH \rightarrow b\bar{b}\tau^+\tau^-$	$1.00^{+7.44}_{-4.10}$	[-5.55, 11.53]
$H \rightarrow \gamma\gamma$	$1.00^{+7.47}_{-3.88}$	[-5.28, 11.48]
$t\bar{t}H$ multilepton	$1.00^{+7.63}_{-3.98}$	[-5.33, 11.36]
$H \rightarrow ZZ^*$	$1.00^{+7.38}_{-3.97}$	[-5.38, 11.29]
$HH \rightarrow b\bar{b}b\bar{b}$	$1.00^{+7.41}_{-3.91}$	[-5.30, 11.39]
$VH \rightarrow b\bar{b}$	$1.00^{+7.57}_{-3.79}$	[-5.10, 11.49]
$H \rightarrow WW^*$	$1.00^{+7.37}_{-3.88}$	[-5.25, 11.32]
$H \rightarrow \tau^+\tau^-$	$1.00^{+7.46}_{-3.76}$	[-5.07, 11.34]
$t\bar{t}H \rightarrow b\bar{b}$	$1.00^{+7.39}_{-3.84}$	[-5.17, 11.25]
Nominal expected result	$1.00^{+7.31}_{-3.79}$	[-5.11, 11.23]

Table 9.12: Ranking of channels in constraining κ_λ . Each row shows the 1σ interval and 95% CL of κ_λ obtained by removing one specific channel. The $HH \rightarrow b\bar{b}\gamma\gamma$ channel is the most sensitive one.

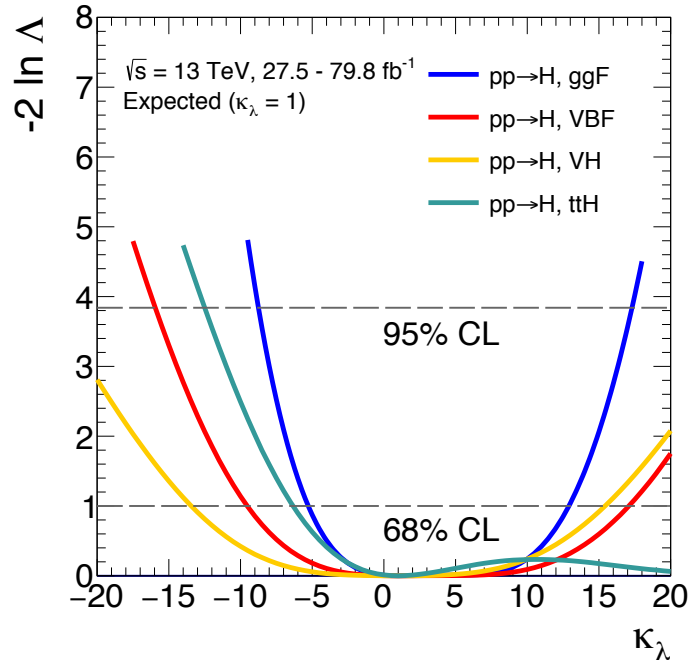


Figure 9.7: Expected value of $-2 \ln \Delta(\kappa_\lambda)$ as a function of κ_λ in the κ_λ -only model with all other couplings set to their SM values obtained in the $\kappa_\lambda=1$ hypothesis for each single-Higgs production mode.

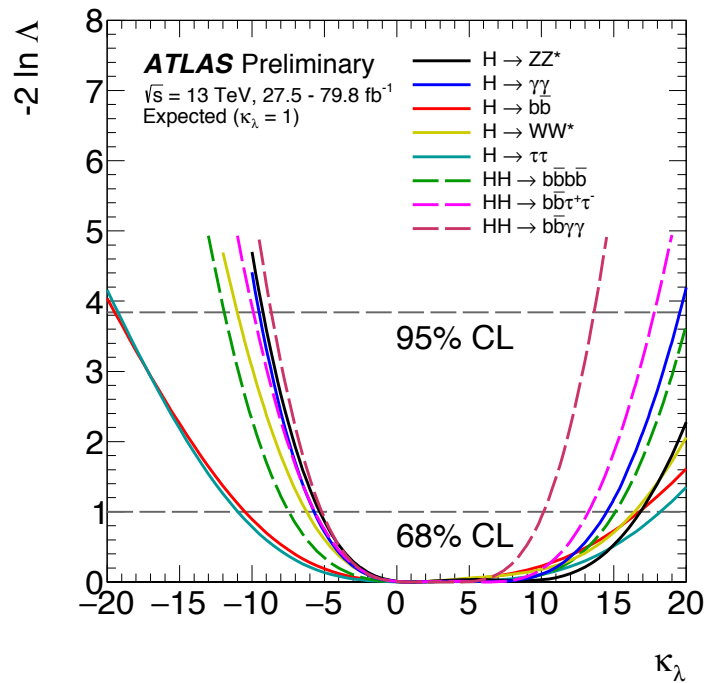


Figure 9.8: Expected value of $-2 \ln \Delta(\kappa_\lambda)$ as a function of κ_λ with all other couplings set to their SM values obtained in the $\kappa_\lambda=1$ hypothesis for the single-Higgs and double-Higgs decay modes [132].

Recent computations of the double-Higgs production cross section have been performed leading to a small reduction of the SM cross section from 33.5 to 31.05 fb and a stronger dependence on κ_λ , as it was described in Chapter 7. In order to be consistent with the double-Higgs results in Reference [35], these recent calculations have not been used, but their impact on the self-coupling combined interval at 95% CL has been evaluated to be less than 2%. Figure 9.9 shows the comparison between the likelihood distribution presented in Figure 9.4 and the likelihood distribution obtained including recent computation of the HH SM cross section that are not included in the results presented in this thesis and taking into account the uncertainties on this recent computation both for data and for the Asimov dataset.

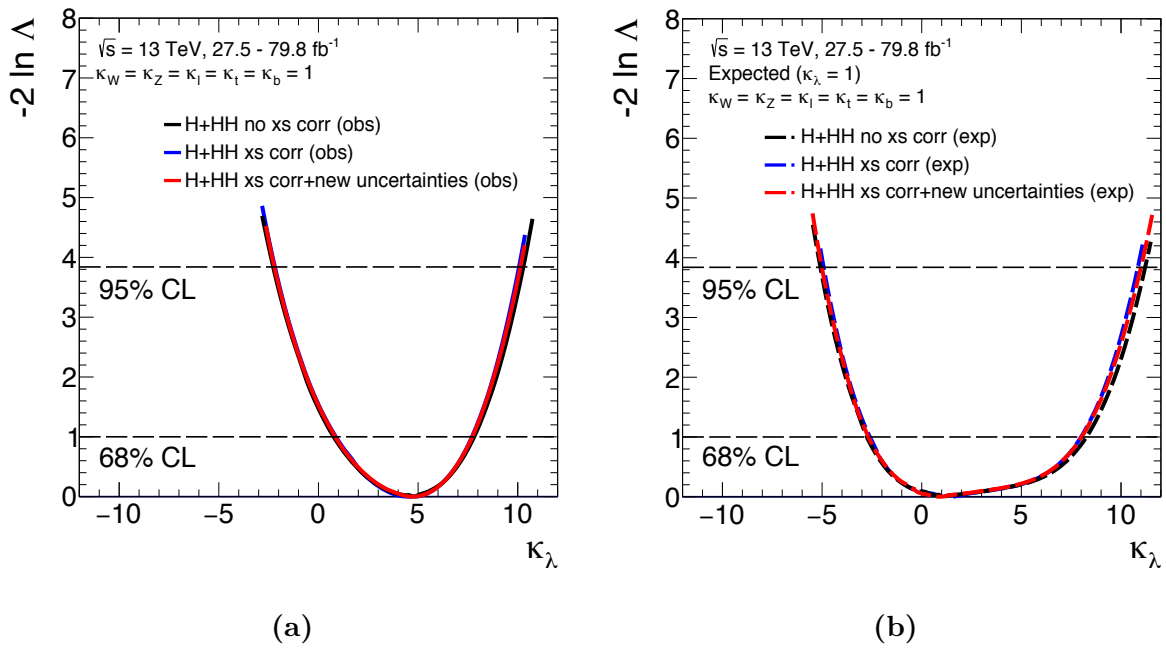


Figure 9.9: Value of $-2 \ln \Lambda(\kappa_\lambda)$ as a function of κ_λ for data (a) and for the Asimov dataset (b). The solid black line shows the combined likelihood distribution used to extract κ_λ public results; the blue solid line represents the same likelihood distribution including recent computations of the double-Higgs SM cross section that are not exploited for the results presented in this thesis, while the red solid line takes into account also the uncertainties on this recent computation. The dotted horizontal lines show the $-2 \ln \Lambda(\kappa_\lambda) = 1$ level that is used to define the $\pm 1\sigma$ uncertainty on κ_λ as well as the $-2 \ln \Lambda(\kappa_\lambda) = 3.84$ level used to define the 95% CL.

The single-Higgs and double-Higgs production cross sections are shown in Figure 9.10 for all the production modes included in the combination and for the gluon-gluon fusion $pp \rightarrow HH$ production mode as a function of κ_λ [27, 55, 133].

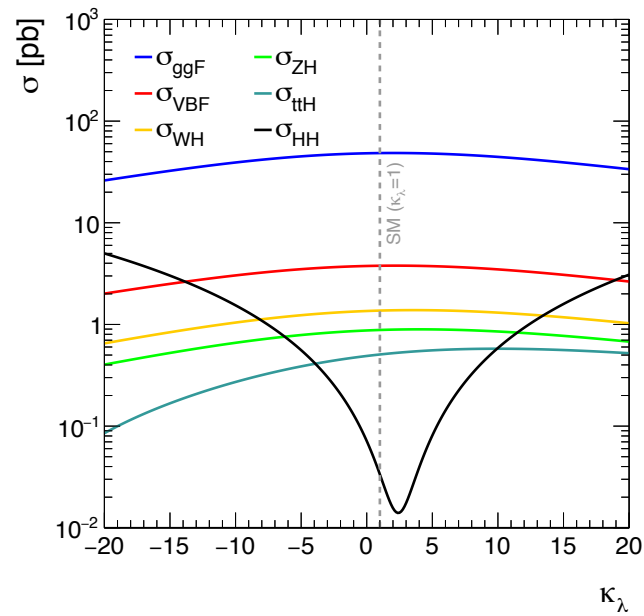


Figure 9.10: Single-Higgs and double-Higgs production cross section as a function of κ_λ [27,55, 133]. The dashed line intercepts the values corresponding to the SM hypothesis ($\kappa_\lambda = 1$) [132].

9.7 Results of fit to κ_λ and κ_t

In order to exploit the sensitivity of the double-Higgs production mechanism and the strong dependence of the double-Higgs cross section $\sigma(pp \rightarrow HH)$ on κ_t , a likelihood fit is performed to constrain at the same time κ_λ and κ_t , setting all the other coupling modifiers to their SM values.

The value of $-2 \ln \Lambda(\kappa_\lambda)$ as a function of κ_λ is shown in Figure 9.11 for data and for the Asimov dataset, generated under the SM hypothesis (*i.e.* $\kappa_\lambda = \kappa_t = 1$); single and double-Higgs analyses are shown both separately and combined in order to extract κ_λ best-fit values and 95% CL intervals. While in single-Higgs analyses a significant loss in sensitivity is present when fitting both κ_λ and κ_t , the constraining power of the combined $H + HH$ measurement is only slightly worse than in the κ_λ -only model ($\kappa_t = 1$). The small constraining power, represented by a small raising of the likelihood distribution for negative κ_λ in the double-Higgs analyses, comes from the parameterisation as a function of κ_λ and κ_t of the Higgs decay channels and single-Higgs productions in double-Higgs background, otherwise the curve becomes flat as it has been shown in Chapter 7. Due to the limited sensitivity of the double-Higgs analyses, the 1σ interval cannot be reached in the κ_λ scan profiling κ_t .

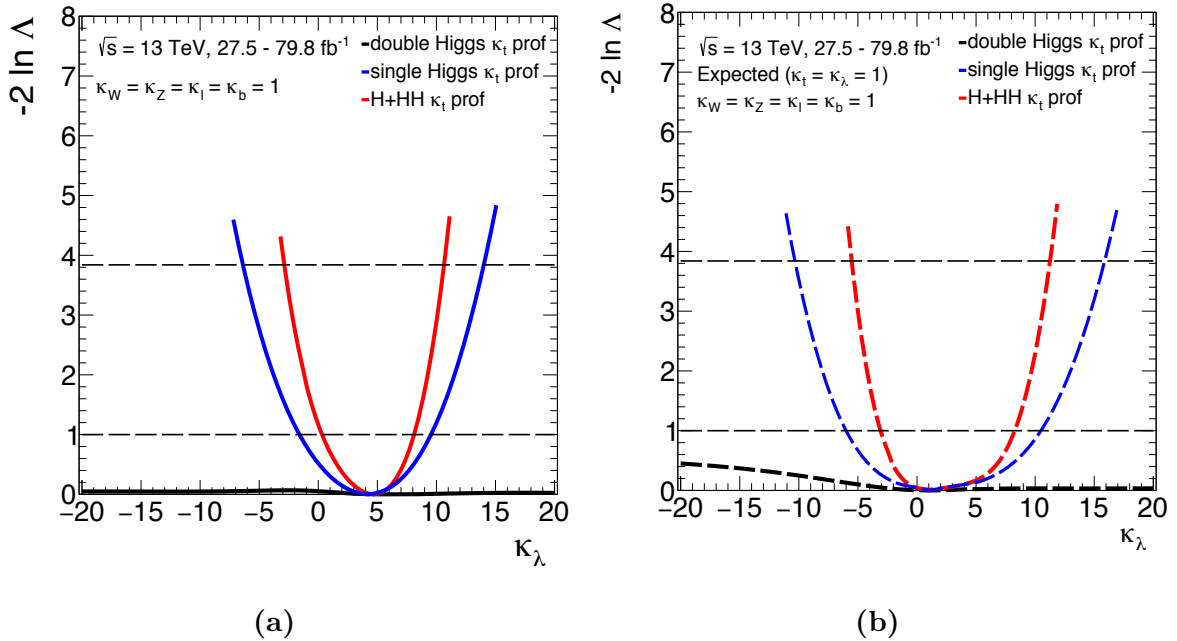


Figure 9.11: Value of $-2 \ln \Lambda(\kappa_\lambda)$ as a function of κ_λ (with κ_t profiled) for single and double-Higgs analyses separately and for the combination of the two analyses; for data (a) and for the Asimov dataset generated in the SM hypothesis (b). The dotted horizontal lines show the $-2 \ln \Lambda(\kappa_\lambda) = 1$ level that is used to define the $\pm 1\sigma$ uncertainty on κ_λ as well as the $-2 \ln \Lambda(\kappa_\lambda) = 3.84$ level used to define the 95% CL. The double-Higgs analyses have almost no sensitivity to κ_λ profiling κ_t .

Table 9.13 reports a summary of fit results in the κ_λ -only and the $\kappa_\lambda - \kappa_t$ fit configurations. The κ_t best-fit value is compatible with the SM prediction.

POIs	$\kappa_W^{+1\sigma}_{-1\sigma}$	$\kappa_Z^{+1\sigma}_{-1\sigma}$	$\kappa_t^{+1\sigma}_{-1\sigma}$	$\kappa_b^{+1\sigma}_{-1\sigma}$	$\kappa_\ell^{+1\sigma}_{-1\sigma}$	$\kappa_\lambda^{+1\sigma}_{-1\sigma}$	κ_λ [95% CL]
κ_λ	1	1	1	1	1	$4.6^{+3.2}_{-3.8}$	[-2.3, 10.3]
						$1.0^{+7.3}_{-3.8}$	[-5.1, 11.2]
$\kappa_\lambda\text{-}\kappa_t$	1	1	$1.03^{+0.07}_{-0.06}$	1	1	$4.7^{+3.4}_{-4.3}$	[-2.9, 10.6]
			$1.00^{+0.07}_{-0.07}$			$1.0^{+7.3}_{-4.1}$	[-5.5, 11.3]

Table 9.13: Best-fit values for κ modifiers with $\pm 1\sigma$ uncertainties. The 95% CL interval for κ_λ is also reported. For the fit result the upper row corresponds to the observed results, and the lower row to the expected results obtained using Asimov datasets generated under the SM hypothesis.

Figure 9.12 shows negative log-likelihood contours on the $(\kappa_\lambda, \kappa_t)$ grid obtained from fits performed in the $\kappa_b = \kappa_\ell = \kappa_W = \kappa_Z = 1$ hypothesis for single and double-Higgs analyses separately and for the combination of the two analyses. Considering the log-likelihood contour of the double-Higgs analyses, it is clear that κ_λ and κ_t cannot be constrained at the same time, as it has already been shown in Chapter 7, Figure 7.16. The combination with the single-Higgs measurements allows, even for κ_λ values deviating from the SM prediction, the determination of κ_t to a sufficient precision to restore most of the ability of the double-Higgs analyses to constrain κ_λ [132]. Furthermore, the combination allows to retain sensitivity to κ_λ and solve the degeneracy even when introducing additional degrees of freedom. In both single-Higgs and combined measurements, κ_t is roughly constrained away from its best-fit value coming from double-Higgs analyses, in a range where greater values of the double-Higgs likelihood compared to the minimum one can be found and thus the 1σ interval or even 95% CL can be reached: in this range the combination can get benefits from double-Higgs measurements.

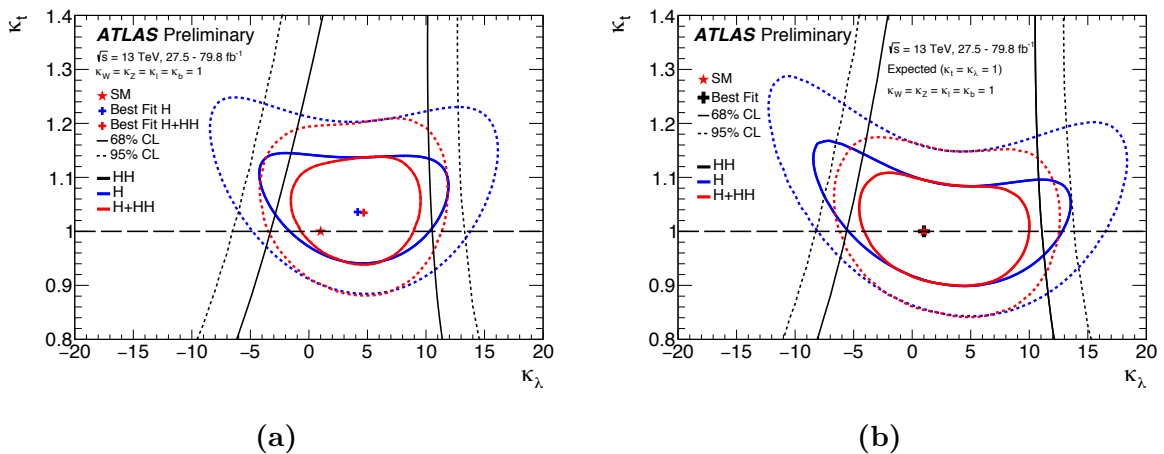


Figure 9.12: Negative log-likelihood contours at 68% and 95% CL in the $(\kappa_\lambda, \kappa_t)$ plane on data (a) and on the Asimov dataset generated under the SM hypothesis (b). The best-fit value is indicated by a cross while the SM hypothesis is indicated by a star. The dotted horizontal line at $\kappa_t=1$ shows the κ_λ -only fit result. The plot assumes that the approximations in References [55, 133] are valid inside the shown contours.

The same negative log-likelihood contours on the $(\kappa_\lambda, \kappa_t)$ grid are shown in Figure 9.13 in an extended range, where the degeneracy of the double-Higgs analyses when fitting simultaneously κ_λ and κ_t is more evident. The coloured areas are not part of the allowed region because the acceptance of the $HH \rightarrow b\bar{b}\gamma\gamma$ analysis is not reliable for $|\kappa_\lambda/\kappa_t| \geq 20$.

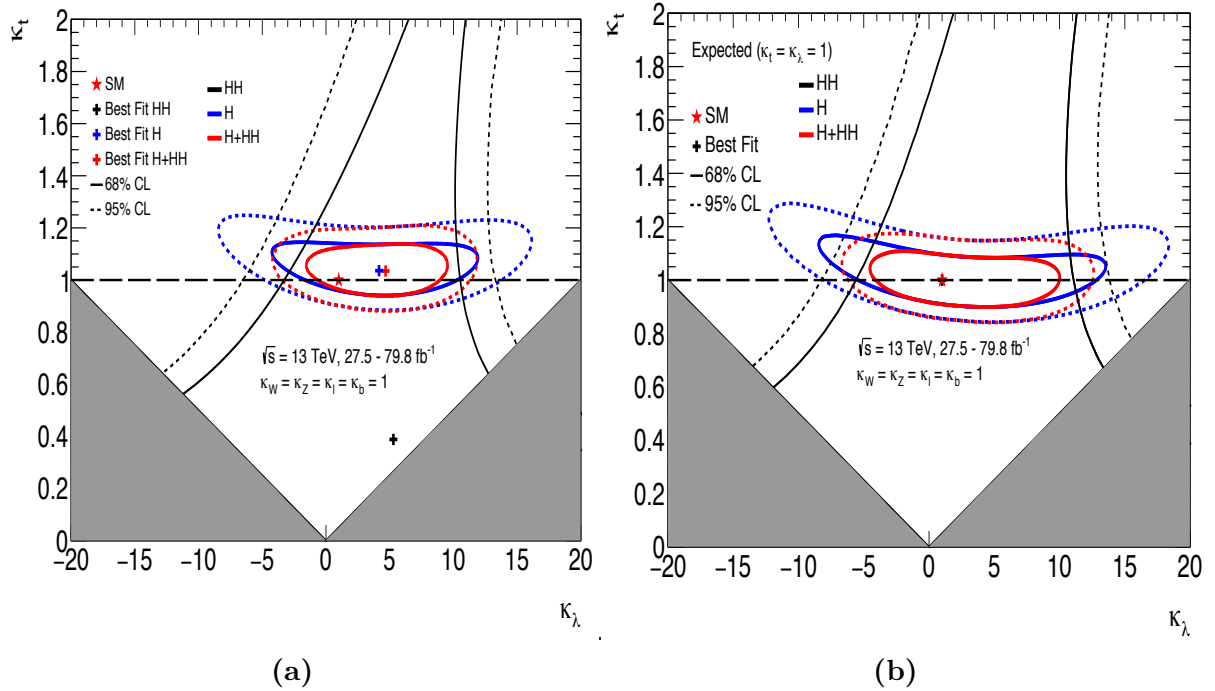


Figure 9.13: Negative log-likelihood contours at 68% and 95% CL in the $(\kappa_\lambda, \kappa_t)$ plane on data (a) and on the Asimov dataset generated under the SM hypothesis (b). The best-fit value is indicated by a cross while the SM hypothesis is indicated by a star. The dotted horizontal line at $\kappa_t=1$ shows the κ_λ -only fit result. The plot assumes that the approximations in References [55, 133] are valid inside the shown contours. The extended range of the contour makes the double-Higgs κ_λ best-fit value visible, showing also the degeneracy of measuring at the same time κ_λ and κ_t ; the shaded area corresponds to $|\kappa_\lambda/\kappa_t| < 20$, a constrain coming from the $HH \rightarrow b\bar{b}\gamma\gamma$ analysis.

9.8 Results of fit to more generic models

The combination with double-Higgs analyses allows to include further degrees of freedom without losing too much power in constraining κ_λ . Thus, additional fit configurations have been tested, in which a simultaneous fit is performed to constrain κ_λ , $\kappa_F = \kappa_t = \kappa_b = \kappa_\ell$ for fermions and $\kappa_V = \kappa_W = \kappa_Z$ for vector bosons ($\kappa_\lambda - \kappa_F - \kappa_V$ model) and κ_λ, κ_W for W boson, κ_Z for Z boson, κ_t for up type quarks, κ_b for down type quarks and κ_ℓ for charged leptons. The value of $-2 \ln \Lambda(\kappa_\lambda)$ as a function of κ_λ for the $\kappa_\lambda - \kappa_F - \kappa_V$ model is shown in Figure 9.14 for data and for the Asimov dataset, and it is compared to the curves obtained in the κ_λ -only model. The sensitivity is degraded at most by $\sim 20\%$ in the $\kappa_\lambda - \kappa_F - \kappa_V$ model. Figures 9.15 - 9.17 show negative log-likelihood contours in the $(\kappa_\lambda, \kappa_V)$, $(\kappa_\lambda, \kappa_F)$ and (κ_V, κ_F) planes obtained profiling the remaining coupling, κ_F , κ_V and κ_λ , respectively.

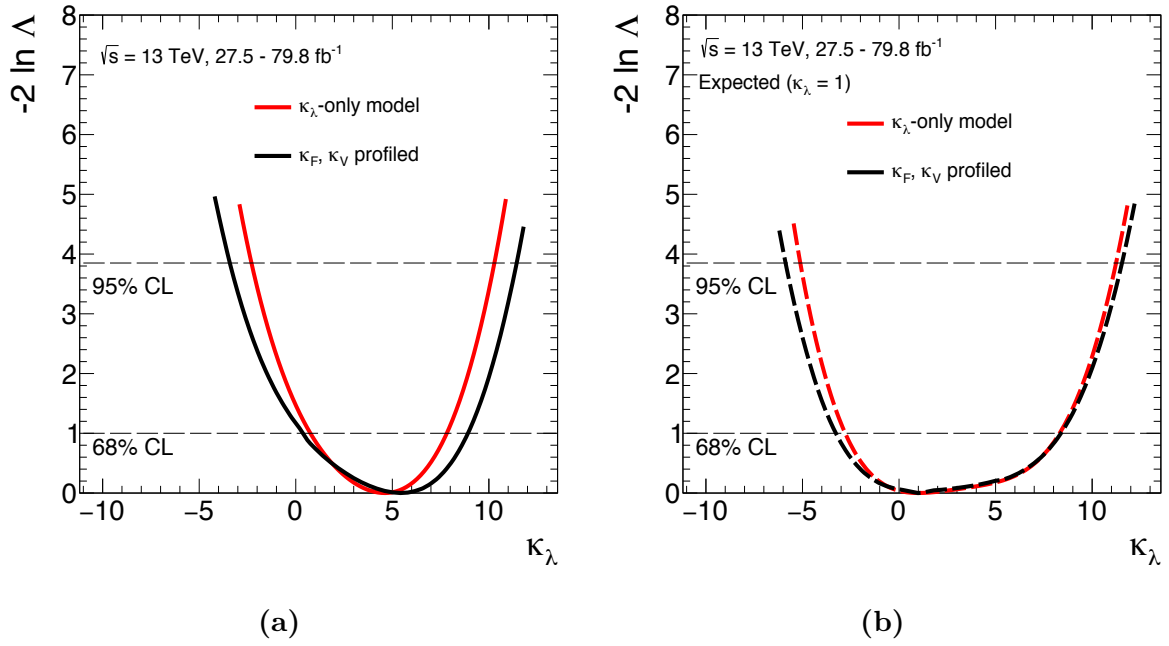


Figure 9.14: Value of $-2 \ln \Lambda(\kappa_\lambda)$ as a function of κ_λ (with κ_F and κ_V profiled); for data (a) and for the Asimov dataset generated in the SM hypothesis (b). The dotted horizontal lines show the $-2 \ln \Lambda(\kappa_\lambda) = 1$ level that is used to define the $\pm 1\sigma$ uncertainty on κ_λ as well as the $-2 \ln \Lambda(\kappa_\lambda) = 3.84$ level used to define the 95% CL. .

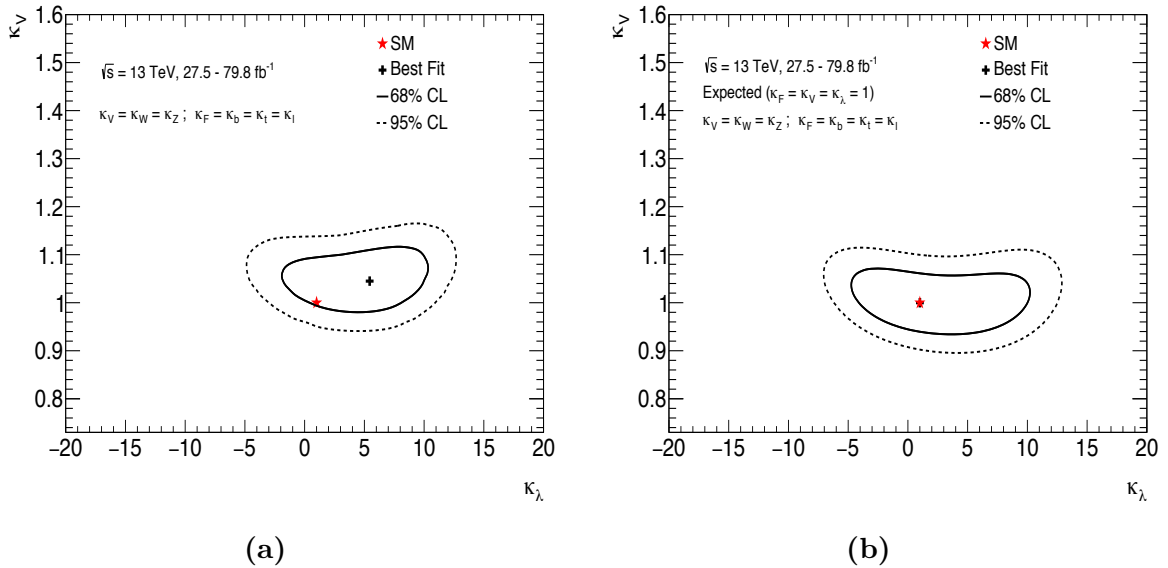


Figure 9.15: Negative log-likelihood contours at 68% and 95% CL in the $(\kappa_\lambda, \kappa_V)$ plane (κ_F profiled) on data (a) and on the Asimov dataset generated under the SM hypothesis (b). The best-fit value is indicated by a cross while the SM hypothesis is indicated by a star. The plot assumes that the approximations in References [55, 133] are valid inside the shown contours.

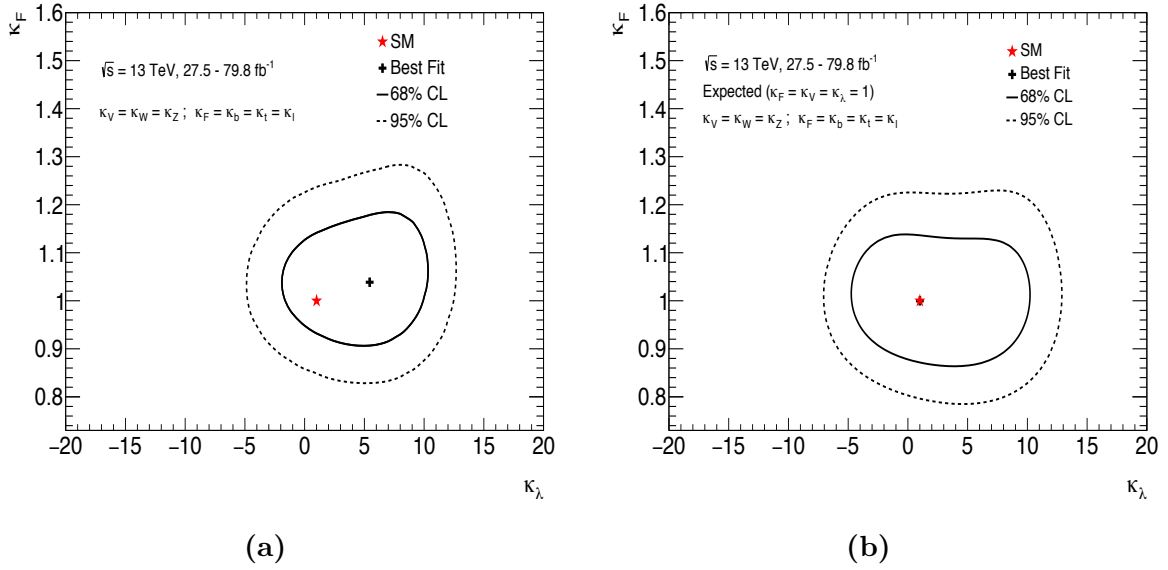


Figure 9.16: Negative log-likelihood contours at 68% and 95% CL in the $(\kappa_\lambda, \kappa_F)$ plane (κ_V profiled) on data (a) and on the Asimov dataset generated under the SM hypothesis (b). The best-fit value is indicated by a cross while the SM hypothesis is indicated by a star. The plot assumes that the approximations in References [55, 133] are valid inside the shown contours.

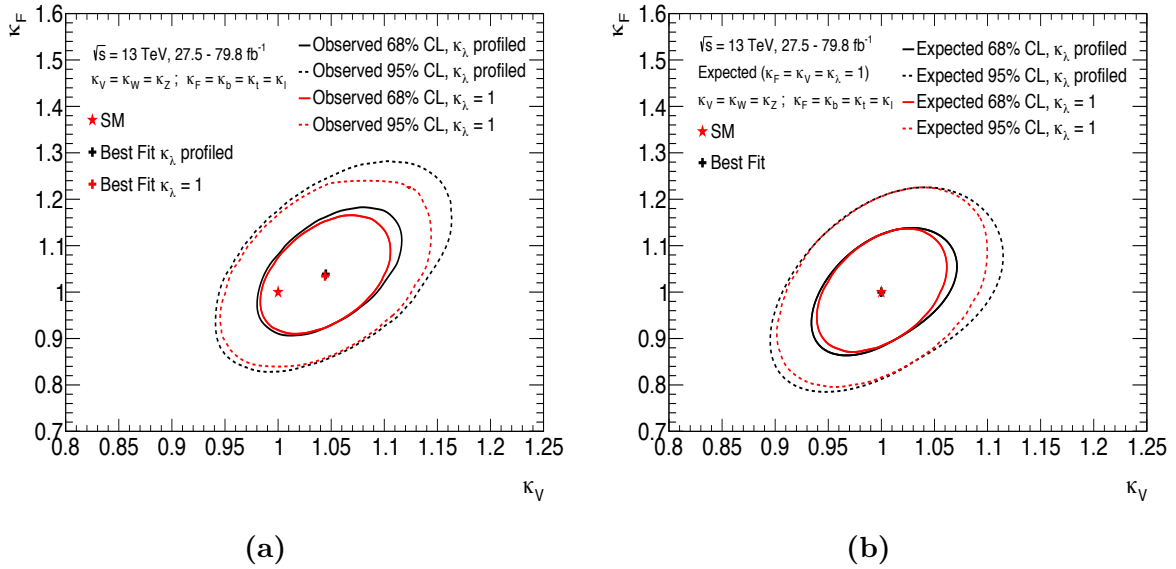


Figure 9.17: Negative log-likelihood contours at 68% and 95% CL in the (κ_V, κ_F) plane with κ_λ profiled (black line) and $\kappa_\lambda=1$ (red line) on data (a) and on the Asimov dataset generated under the SM hypothesis (b). The best-fit value is indicated by a cross while the SM hypothesis is indicated by a star. The plot assumes that the approximations in References [55, 133] are valid inside the shown contours.

The correlations among the parameters of interest, i.e. κ_λ , κ_F and κ_V are shown in Figure 9.18 for data (a) and for the Asimov dataset. A weaker correlation between κ_F and κ_V with respect to the single-Higgs combination is present given the introduction of further terms from the double-Higgs analyses.

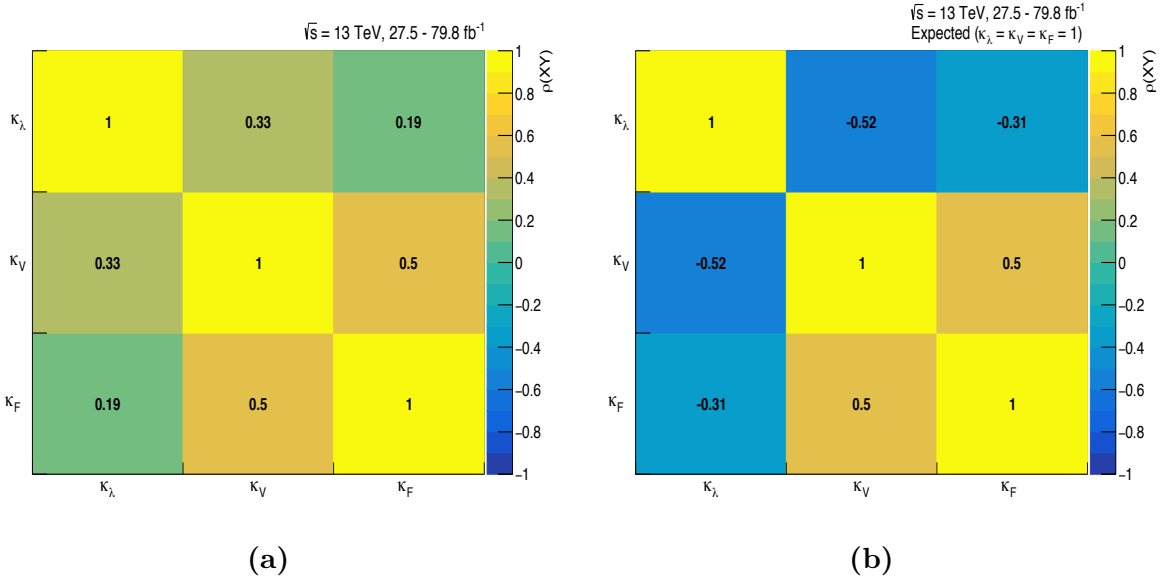


Figure 9.18: Correlations between the parameters of interest, i.e. κ_λ , κ_F and κ_V , for (a) data and for (b) Asimov dataset generated under the SM hypothesis.

A more generic model has been considered, performing a likelihood fit to constrain simultaneously κ_λ , κ_W , κ_Z , κ_t , κ_b and κ_ℓ ; this generic model represents an intermediate parameterisations with respect to a very general EFT parameterisation, like the one presented in Reference [137] thus targeting BSM models than can modify at the same time the Higgs boson self-coupling and other SM couplings.

Table 9.14 reports a summary of fit results in the different configurations. The best-fit values for all the couplings are compatible with the SM prediction.

POIs	$\kappa_W^{+1\sigma}_{-1\sigma}$	$\kappa_Z^{+1\sigma}_{-1\sigma}$	$\kappa_t^{+1\sigma}_{-1\sigma}$	$\kappa_b^{+1\sigma}_{-1\sigma}$	$\kappa_\ell^{+1\sigma}_{-1\sigma}$	$\kappa_\lambda^{+1\sigma}_{-1\sigma}$	κ_λ [95% CL]
κ_λ	1	1	1	1	1	$4.6^{+3.2}_{-3.8}$	[-2.3, 10.3]
						$1.0^{+7.3}_{-3.8}$	[-5.1, 11.2]
$\kappa_\lambda - \kappa_F - \kappa_V$	$1.04^{+0.05}_{-0.04}$	$1.04^{+0.05}_{-0.04}$	$1.04^{+0.09}_{-0.09}$	$1.04^{+0.09}_{-0.09}$	$1.04^{+0.09}_{-0.09}$	$5.4^{+3.5}_{-5.1}$	[-3.4, 11.4]
	$1.00^{+0.05}_{-0.04}$	$1.00^{+0.05}_{-0.04}$	$1.00^{+0.09}_{-0.09}$	$1.00^{+0.09}_{-0.09}$	$1.00^{+0.09}_{-0.09}$	$1.0^{+7.4}_{-4.3}$	[-5.9, 11.6]
κ_λ generic	$1.03^{+0.08}_{-0.08}$	$1.10^{+0.09}_{-0.09}$	$1.00^{+0.12}_{-0.11}$	$1.03^{+0.20}_{-0.18}$	$1.06^{+0.16}_{-0.16}$	$5.5^{+3.5}_{-5.2}$	[-3.7, 11.5]
	$1.00^{+0.08}_{-0.08}$	$1.00^{+0.08}_{-0.08}$	$1.00^{+0.12}_{-0.12}$	$1.00^{+0.21}_{-0.19}$	$1.00^{+0.16}_{-0.15}$	$1.0^{+7.6}_{-4.5}$	[-6.2, 11.6]

Table 9.14: Best-fit values for κ modifiers with $\pm 1\sigma$ uncertainties for the different fit configurations listed in the first column. The 95% CL interval for κ_λ is also reported. For the fit result the upper row corresponds to the observed results, and the lower row to the expected results obtained using Asimov datasets generated under the SM hypothesis.

The value of $-2 \ln \Lambda(\kappa_\lambda)$ as a function of κ_λ profiling all the other couplings is shown in Figure 9.19 for data and for the Asimov dataset and it is compared to the curves obtained in the κ_λ -only model and in the κ_λ - κ_t model. The sensitivity is degraded at most by $\sim 20\%$ going from the 95% CL interval for the κ_λ -only model to the 95% CL interval for the generic model. Concerning other couplings, their best-fit values are compatible with the SM prediction. The combination allows to put sizeable constraints also in this generic model, despite the number of degrees of freedom introduced.

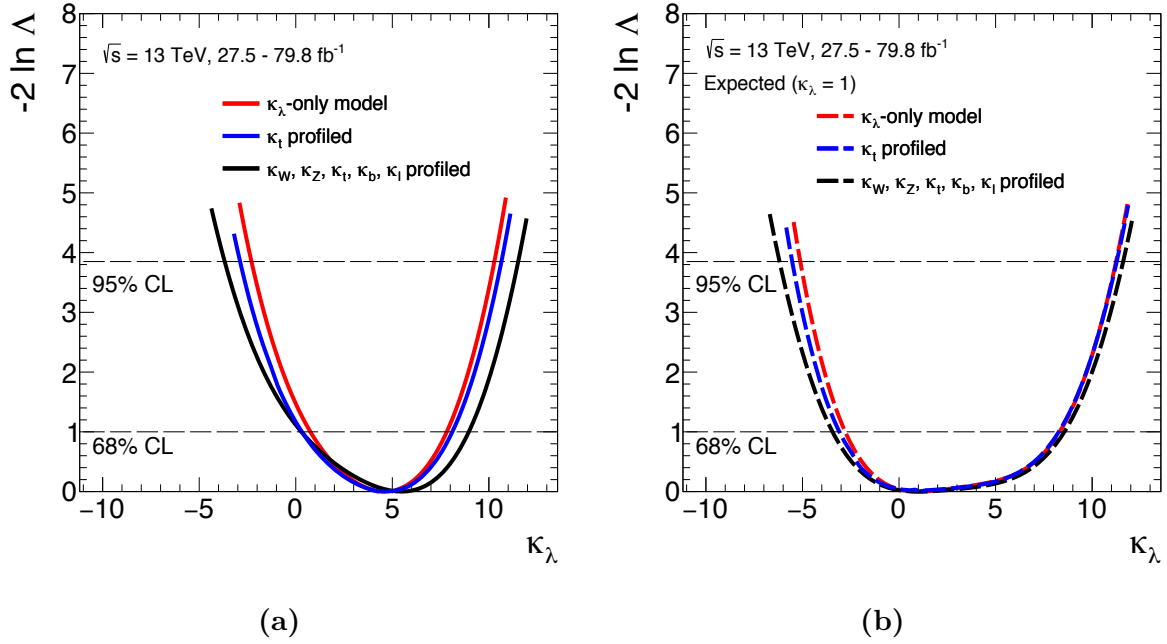


Figure 9.19: Value of $-2 \ln \Lambda(\kappa_\lambda)$ as a function of κ_λ with $\kappa_W, \kappa_Z, \kappa_t, \kappa_b, \kappa_{lep}$ profiled for data (a) and for the Asimov dataset (b), generated under the SM hypothesis. The generic model curves both for data and for the Asimov dataset are compared to the corresponding curves for the κ_λ -only model where all the couplings, except for κ_λ , are set to their SM values and κ_λ - κ_t model where all the other couplings are set to their SM values. The dotted horizontal lines show the $-2 \ln \Lambda(\kappa_\lambda) = 1$ level that is used to define the $\pm 1\sigma$ uncertainty on κ_λ as well as the $-2 \ln \Lambda(\kappa_\lambda) = 3.84$ level used to define the 95% CL.

The correlations between the parameters of interest, i.e. $\kappa_\lambda, \kappa_W, \kappa_Z, \kappa_t, \kappa_b$ and κ_l , are shown in Figure 9.20 for data (a) and for the Asimov dataset. A strong correlation is found between κ_W, κ_Z and κ_b being mostly constrained by the $VH \rightarrow b\bar{b}$ channel as well as κ_t and κ_b constrained by the $t\bar{t}H \rightarrow b\bar{b}$ channel.

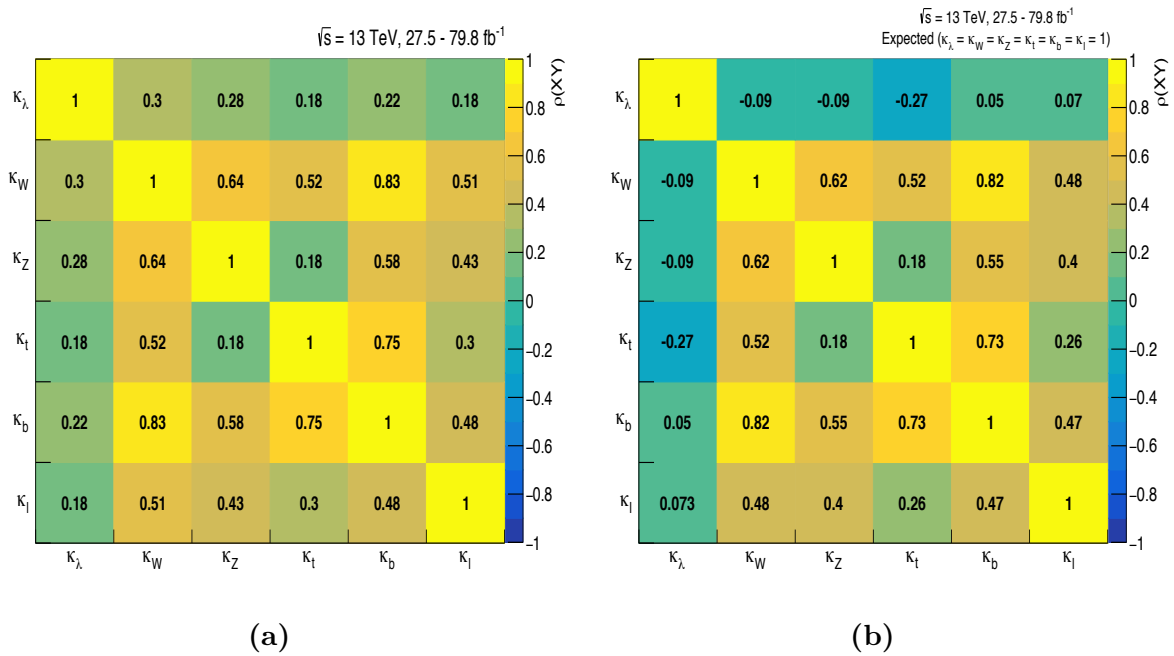


Figure 9.20: Correlations between the parameters of interest, i.e. κ_λ , κ_W , κ_Z , κ_t , κ_b and κ_l , for (a) data and for (b) Asimov dataset generated under the SM hypothesis.

Conclusion

The Higgs-boson self-coupling has been constrained through single-Higgs processes, exploiting the next-to-leading order dependence of these processes on κ_λ via weak loops; this approach has been applied to the combination of analyses targeting single-Higgs production and decay modes, i.e. ggF , VBF , ZH , WH and $t\bar{t}H$ production modes together with WW^* , ZZ^* , $\tau^+\tau^-$, $\gamma\gamma$ and $b\bar{b}$ decay channels, on data collected with the ATLAS experiment using up to 80 fb^{-1} of LHC proton-proton collisions.

In the simplified assumption that all deviations from the SM expectation have to be interpreted as modifications of the trilinear coupling of the Higgs boson, the Higgs-boson self-coupling modifier $\kappa_\lambda = \lambda_{HHH}/\lambda_{HHH}^{SM}$, extracted with a global fit procedure, is determined to be $\kappa_\lambda = 4.0_{-4.1}^{+4.3}$, excluding at the 95% CL values outside the interval $-3.2 < \kappa_\lambda < 11.9$. Additional results, including the simultaneous determination of the Higgs self-coupling and single-Higgs couplings to either fermions or bosons, have been derived. The constraints on κ_λ become weaker when further degrees of freedom are introduced, to the point where no sensitivity to κ_λ is found when considering modifications to the self-coupling and to a common single-Higgs coupling modifier.

Being the limits on κ_λ competitive with the ones coming from double-Higgs measurements, a combination between the most sensitive double-Higgs channels, $bb\tau^+\tau^-$, $b\bar{b}\gamma\gamma$ and $b\bar{b}b\bar{b}$ exploiting data collected with the ATLAS experiment using up to 36.1 fb^{-1} of LHC proton-proton collisions, and the aforementioned single-Higgs analyses has been performed. The dependence of the double-Higgs cross section on both the coupling of the Higgs boson to the top quark and the Higgs self-coupling has been taken into account. Under the assumption that new physics affects only the Higgs-boson self-coupling, the combined best-fit value of the coupling modifier is $\kappa_\lambda = 4.6_{-3.8}^{+3.2}$, excluding values outside the interval $-2.3 < \kappa_\lambda < 10.3$ at 95% CL. This result represents a significant improvement in constraining κ_λ with respect to single-Higgs and double-Higgs analyses alone. The single- and double-Higgs combination allows to decouple the self-coupling and top-Yukawa coupling as well as other couplings. Thus, sizeable constraints on κ_λ can be set also when less model dependent parameterisation are considered, including coupling modifiers for the Higgs-boson self-coupling, for the up- and down-type quarks, for leptons and for W and Z bosons. In this more generic configuration, the self-coupling modifier has been constrained at the 95% CL value to the interval $-3.7 < \kappa_\lambda < 11.5$. All other coupling modifiers are compatible with the SM predictions. Being the measurements statistically dominated, both from single-Higgs and double-Higgs side, a significant improvement in constraining κ_λ is expected at the High-Luminosity LHC.

Bibliography

- [1] S. L. Glashow: *Partial Symmetries of Weak Interactions*, [Nucl. Phys. 22 \(1961\) 579](#), 1961;
- [2] S. Weinberg: *A Model of Leptons*, [Phys. Rev. Lett. 19 \(1967\) 1264](#), 1967;
- [3] A. Salam: *Weak and Electromagnetic Interactions*, [Conf. Proc. C 680519 \(1968\) 367](#), 1968;
- [4] S. L. Glashow, J. Iliopoulos and L. Maiani: *Weak Interactions with Lepton-Hadron Symmetry*, [Phys. Rev. D2 \(1970\) 1285](#), 1970;
- [5] F. Englert and R. Brout: *Broken Symmetry and the Mass of Gauge Vector Mesons*, [Phys. Rev. Lett. 13 \(1964\) 321](#), 1964;
- [6] P. W. Higgs: *Broken Symmetries and the Masses of Gauge Bosons*, [Phys. Rev. Lett. 13 \(1964\) 508](#), 1964.
- [7] P. W. Higgs: *Spontaneous Symmetry Breakdown without Massless Bosons*, [Phys. Rev. 145 \(1966\) 1156](#), 1966;
- [8] M. Tanabashi et al.: *Particle Data Group: 2019 Review of Particle Physics*, [Phys. Rev. D98, 030001](#), 2018 and 2019 update;
- [9] *Planck 2018 results. VI. Cosmological parameters*, [arXiv:1807.06209](#), 2019;
- [10] E. Noether: *Invariante Variationsprobleme*, [Nachrichten von der Gesellschaft der Wissenschaften zu Göttingen, Mathematisch-Physikalische Klasse \(1918\) 235](#), 1918;
- [11] A. Pich: *The Standard Model of Electroweak Interactions*, [arXiv:1201.0537v1](#), 2012;
- [12] M. Tanabashi et al.: *Particle Data Group: Quantum Chromodynamics*, [Phys. Rev. D98, 030001 \(2018\)](#), 2017;
- [13] E. Fermi: *An attempt of a theory of beta radiation*, [Z. Phys. 88 \(1934\) 161](#), 1934;
- [14] E. C. G. Sudarshan and R. E. Marshak: *Chirality Invariance and the Universal Fermi Interaction*, [Phys. Rev. 109 \(1958\) 1860](#), 1958;
- [15] R. P. Feynman and M. Gell-Mann: *Theory of the Fermi Interaction*, [Phys. Rev. 109 \(1958\) 193](#), 1958;

- [16] M. Tanabashi et al: *Particle Data Group: CKM Quark-Mixing Matrix*, [Phys. Rev. D 98, 030001](#), 2018 and 2019 update;
- [17] A. Djouadi: *The Anatomy of Electro-Weak Symmetry Breaking. I: The Higgs boson in the Standard Model*, [arXiv:hep-ph/0503172](#), 2005;
- [18] J. Goldstone: *Field theories with “Superconductor” solutions*, [Nuov. Cim.19\(1961\) 154](#), 1961;
- [19] J. Goldstone, A. Salam, and S. Weinberg: *Broken Symmetries*, [Phys. Rev. 127, 965](#), 1962;
- [20] ALEPH Collaboration, DELPHI Collaboration, L3 Collaboration, OPAL Collaboration, the LEP Working Group for Higgs Boson Searches: *Search for the Standard Model Higgs Boson at LEP*, [Phys.Lett.B565:61-75,2003](#), [arXiv:hep-ex/0306033](#), 2003;
- [21] The TEVNPH Working Group: *Combined CDF and D0 Search for Standard Model Higgs Boson Production with up to 10.0 fb^{-1} of Data*, [arXiv:1203.3774](#), 2012;
- [22] Lyndon Evans and Philip Bryant: *LHC Machine*, [JINST 3 S08001](#), 2008;
- [23] ATLAS Collaboration: *The ATLAS Experiment at the CERN Large Hadron Collider*, [JINST3 S08003](#), 2008;
- [24] ATLAS Collaboration: *Observation of a new particle in the search for the Standard Model Higgs boson with the ATLAS detector at the LHC*, [Phys.Lett. B716 \(2012\) 1-29](#), [arXiv:1207.7214](#), 2012;
- [25] CMS Collaboration: *The CMS experiment at the CERN LHC*, [JINST3 S08004](#), 2008;
- [26] CMS Collaboration: *Observation of a new boson at a mass of 125 GeV with the CMS experiment at the LHC*, [Phys. Lett. B 716 \(2012\) 30](#), [arXiv:1207.7235](#), 2012;
- [27] D. de Florian et al.: *Handbook of LHC Higgs Cross Sections: 4. Deciphering the Nature of the Higgs Sector*, [arXiv:1610.07922](#), 2017;
- [28] ATLAS and CMS Collaborations: *Combined Measurement of the Higgs Boson Mass in pp Collisions at $\sqrt{s} = 7$ and 8 TeV with the ATLAS and CMS Experiments*, [Phys. Rev. Lett. 114, 191803 \(2015\)](#), [arXiv:1503.07589](#), 2015;
- [29] LHC Higgs Cross Section Working Group: *Higgs cross sections for HL-LHC and HE-LHC*, [website](#);
- [30] ATLAS Collaboration: *Search for the $HH \rightarrow b\bar{b}b\bar{b}$ process via vector boson fusion production using proton-proton collisions at $\sqrt{s} = 13$ TeV with the ATLAS detector*, [ATLAS-CONF-2019-03](#), 2019;
- [31] LHC Higgs Cross Section HH Sub-group, [website](#), 2019;
- [32] M. Grazzini, G. Heinrich, S. Jones, S. Kallweit, M. Kerner, J. M. Lindert, J. Mazzitelli: *Higgs boson pair production at NNLO with top quark mass effects*, [JHEP05\(2018\)059](#), [arXiv:1803.02463](#), 2018;

- [33] J. Baglio, A. Djouadib and J. Quevillon: *Prospects for Higgs physics at energies up to 100 TeV*, [arXiv:1511.07853](#), 2016;
- [34] B. Di Micco, M. Gouzevitch, J. Mazzitelli, C. Vernieri et al.: *Higgs boson pair production at colliders: status and perspectives*, [arXiv:1910.00012](#), 2019 and update;
- [35] ATLAS Collaboration: *Combination of searches for Higgs boson pairs in pp collisions at $\sqrt{s} = 13$ TeV with the ATLAS detector*, [arXiv:1906.02025](#), 2019;
- [36] CMS Collaboration: *A measurement of the Higgs boson mass in the diphoton decay channel*, [CMS-PAS-HIG-19-004](#), 2019;
- [37] ATLAS Collaboration: *Measurement of the Higgs boson mass in the $H \rightarrow ZZ^* \rightarrow 4\ell$ and $H \rightarrow \gamma\gamma$ channels with $\sqrt{s} = 13$ TeV pp collisions using the ATLAS detector*, [Physics Letters B 784 \(2018\) 345-366](#), 2018;
- [38] ATLAS Collaboration: *Constraints on off-shell Higgs boson production and the Higgs boson total width in $ZZ \rightarrow 4\ell$ and $ZZ \rightarrow 2\ell 2\nu$ final states with the ATLAS detector*, [Phys. Lett. B 786 \(2018\) 223](#), [arXiv:1808.01191](#), 2018;
- [39] CMS Collaboration: *Measurements of the Higgs boson width and anomalous HVV couplings from on-shell and off-shell production in the four-lepton final state*, [PRD 99 \(2019\) 112003](#), [arXiv:1901.00174](#), 2019;
- [40] ATLAS and CMS Collaborations: *Measurements of the Higgs boson production and decay rates and constraints on its couplings from a combined ATLAS and CMS analysis of the LHC pp collision data at $\sqrt{s} = 7$ and 8 TeV*, [JHEP08\(2016\)045](#), [arXiv:1606.02266](#), 2016;
- [41] ATLAS Collaboration: *Combined measurements of Higgs boson production and decay using up to 80 fb⁻¹ of proton-proton collision data at $\sqrt{s} = 13$ TeV collected with the ATLAS experiment*, [arXiv:1909.02845](#), 2019;
- [42] A. David, A. Denner, M. Duehrssen, M. Grazzini, C. Grojean, G. Passarino, M. Schumacher, M. Spira, G. Weiglein, M. Zanetti: *LHC HXSWG interim recommendations to explore the coupling structure of a Higgs-like particle*, [arXiv:1209.0040](#), 2012;
- [43] S. Kanemura et al.: *New Physics Effect on the Higgs Self-Coupling*, [Phys. Lett. B558, 157 \(2003\)](#), [arXiv:hep-ph/0211308](#), 2003;
- [44] E. Gildener and S. Weinberg: *Symmetry breaking and scalar bosons*, [Phys. Rev. D 13, 3333](#), 1976;
- [45] S. R. Coleman and E. J. Weinberg: *Radiative Corrections as the Origin of Spontaneous Symmetry Breaking*, [Phys. Rev. D 7, 1888](#), 1973;
- [46] K. Lane, E. Pilon: *Higgs Scalars' Self-Couplings in Gildener-Weinberg Models*, [arXiv:1909.02111](#), 2019;
- [47] D. B. Kaplan and H. Georgi: *SU(2) \times U(1) breaking by vacuum misalignment*, [Phys. Lett.136B, 183 \(1984\)](#), 1984;

- [48] C. Csaki et al.: *Variations of Little Higgs Models and their Electroweak Constraints*, *Phys. Rev. D* **68**, 035009 (2003), [arXiv:hep-ph/0303236](#), 2003;
- [49] T. Han, H. E. Logan, B. McElrath and L. T. Wang: *Phenomenology of the little Higgs model*, *Phys. Rev. D* **67**, 095004 (2003), [arXiv:hep-ph/0301040](#), 2003;
- [50] C. Dib, R. Rosenfeld and A. Zerwekh: *Higgs production and decay in the little Higgs model*, [arXiv:hep-ph/0302068](#), 2003;
- [51] T. Plehn and M. Rauch: *The quartic higgs coupling at hadron colliders*, *Phys. Rev. D* **72**(2005) 053008, [arXiv:hep-ph/050732](#), 2005;
- [52] CMS Collaboration: *Combination of searches for Higgs boson pair production in proton-proton collisions at $\sqrt{s}=13$ TeV*, [arXiv:1811.09689](#), 2018;
- [53] G. Degrassi, M. Fedele, P. P. Giardino: *Constraints on the trilinear Higgs self coupling from precision observables*, *JHEP* **1704**, 155 (2017), [arXiv:1702.01737](#), 2017;
- [54] *Electroweak oblique parameters as a probe of the trilinear Higgs boson self-interaction*, *Phys. Rev. D* **95**, 093004 (2017), [arXiv:1702.07678](#), 2017;
- [55] G. Degrassi, P. P. Giardino, F. Maltoni and D. Pagani: *Probing the Higgs self coupling via single Higgs production at the LHC*, *JHEP* **12** (2016) 080, [arXiv:1607.04251](#), 2016;
- [56] G.F. Giudice: *Naturally Speaking: The Naturalness Criterion and Physics at the LHC*, [arXiv:0801.2562](#), 2008;
- [57] L. Canetti, M. Drewes, M. Shaposhnikov: *Matter and Antimatter in the Universe*, *New J. Phys.* **14** (2012) 095012, [arXiv:1204.4186](#), 2012;
- [58] ALICE Collaboration: *The ALICE experiment at the CERN LHC*, [JINST3 S08002](#), 2008;
- [59] LHCb Collaboration: *The LHCb Detector at the LHC*, [JINST3 S08005](#), 2008;
- [60] Marcastel, Fabienne: *CERN's Accelerator Complex*, Oct 2013, OPEN-PHO-CHART-2013-001, [General Photo](#);
- [61] TOTEM Collaboration: *The TOTEM Experiment at the CERN Large Hadron Collider*, [JINST3 S08007](#), 2008;
- [62] LHCf Collaboration: *The LHCf detector at the CERN Large Hadron Collider*, [JINST3 S08006](#), 2008;
- [63] Oliver Sim Brüning et al.: *LHC Design Report*, CERN Yellow Reports: Monographs, [DOI: 10.5170/CERN-2004-003-V-1](#), Geneva: CERN, 2004;
- [64] ATLAS Collaboration: *Luminosity determination in pp collisions at $\sqrt{s}=13$ TeV using the ATLAS detector at the LHC*, [ATLAS-CONF-2019-021](#), 2019;

-
- [65] TOTEM Collaboration: *First measurement of elastic, inelastic and total cross-section at $\sqrt{s}=13$ TeV by TOTEM and overview of cross-section data at LHC energies*, *Eur. Phys. J. C* (2019) 79:103, 2019;
- [66] ATLAS Collaboration: *Luminosity Public Results Run 2*, [website](#);
- [67] *High Luminosity LHC Project*, [website](#), last update October 2019;
- [68] ATLAS Collaboration: *Luminosity Public Results Run 1*, [website](#);
- [69] ATLAS Collaboration: *ATLAS detector and physics performance: Technical Design Report 1*, ATLAS-TDR-14, [CERN-LHCC-99-014](#), 1999;
- [70] ATLAS Collaboration: *ATLAS detector and physics performance: Technical Design Report 2*, ATLAS-TDR-15, [CERN-LHCC-99-015](#), 1999;
- [71] ATLAS Collaboration: *ATLAS inner detector: Technical Design Report 1*, ATLAS-TDR-4, [CERN-LHCC-97-016](#), 1997;
- [72] ATLAS Collaboration: *ATLAS liquid-argon calorimeter: Technical Design Report*, ATLAS-TDR-2, [CERN-LHCC-96-041](#), 1996;
- [73] ATLAS Collaboration: *ATLAS tile calorimeter: Technical Design Report*, ATLAS-TDR-3, [CERN-LHCC-96-042](#), 1996;
- [74] ATLAS Collaboration: *ATLAS muon spectrometer: Technical Design Report*, ATLAS-TDR-10, [CERN-LHCC-97-022](#), 1997;
- [75] L. Fabbri on behalf of the ATLAS Collaboration: *Forward Detectors in ATLAS: LUCID, ZDC and ALFA*, [INSPIRE-1678149](#), 2009;
- [76] C. Kourkoumelis and S. Vourakis: *HYPATIA - an online tool for ATLAS event visualisation*, *Phys. Educ.* 49 21, 2014;
- [77] M. Schott and M. Dunford: *Review of single vector boson production in pp collisions at $\sqrt{s}=7$ TeV*, *Eur. Phys. J. C* 74 (2014) 2916, [arXiv:1405.1160](#), 2014;
- [78] ATLAS Collaboration: *ATLAS magnet system: Technical Design Report 1*, ATLAS-TDR-6, [CERN-LHCC-97-018](#), 1997;
- [79] ATLAS Collaboration: *ATLAS Insertable B-Layer Technical Design Report*, ATLAS-TDR-19, [CERN-LHCC-2010-013](#), 2010;
- [80] ATLAS Collaboration: *Commissioning of the ATLAS Muon Spectrometer with cosmic rays*, *Eur. Phys. J. C* (2010) 70: 875, 2010;
- [81] ATLAS Collaboration: *Approved Plots DAQ*, [website](#);
- [82] A. Ruiz Martinez on behalf of the ATLAS Collaboration: *The Run-2 ATLAS Trigger System*, *J. Phys.: Conf. Ser.* 762 012003, 2016;

- [83] ATLAS Collaboration: *ATLAS level-1 trigger: Technical Design Report*, ATLAS-TDR-12, [CERN-LHCC-98-014](#), 1998;
- [84] ATLAS Collaboration: *ATLAS high-level trigger, data-acquisition and controls: Technical Design Report*, ATLAS-TDR-16, [CERN-LHCC-2003-022](#), 2003;
- [85] ATLAS Collaboration: *Trigger Operation Public Result*, [website](#);
- [86] ATLAS Collaboration: *ATLAS Forward Detectors*, [ATLAS-PHOTO-2018-018](#), General Photo, 2018;
- [87] *Roman pots for the LHC*, [article](#), 1999;
- [88] ATLAS Collaboration: *ATLAS Event Displays: Higgs boson decaying to two b-quarks*, [ATLAS-PHOTO-2018-022-1](#), 2018;
- [89] ATLAS Collaboration: *Performance of the ATLAS track reconstruction algorithms in dense environments in LHC Run 2*, [Eur. Phys. J. C 77 \(2017\) 673](#), [arXiv:1704.07983](#), 2017;
- [90] R.Frühwirth: *Application of Kalman filtering to track and vertex fitting*, [Nucl.Instrum. Meth.A 262 \(1987\) 444](#), 1987;
- [91] ATLAS Collaboration: *A neural network clustering algorithm for the ATLAS silicon pixel detector*, [JINST 9 \(2014\) P09009](#), [arXiv:1406.7690](#), 2014;
- [92] G Piacquadio, K Prokofiev, A Wildauer: *Primary Vertex Reconstruction in the ATLAS Experiment at LHC*, [J. Phys.: Conf. Ser. 119 \(2008\) 032033](#), 2008;
- [93] ATLAS Collaboration: *Vertex performance in 2018 data*, [website](#), 2018;
- [94] F. Meloni on behalf of the ATLAS Collaboration: *Primary vertex reconstruction with the ATLAS detector*, [ATL-PHYS-PROC-2016-163](#), [JINST11 C12060](#), 2016;
- [95] ATLAS Collaboration: *Electron and photon performance measurements with the ATLAS detector using the 2015-2017 LHC proton-proton collision data*, [CERN-EP-2019-145](#), [arXiv:1908.00005](#), 2019;
- [96] ATLAS Collaboration: *Topological cell clustering in the ATLAS calorimeters and its performance in LHC Run 1*, [Eur. Phys. J. C 77 \(2017\) 490](#), [arXiv:1603.02934](#), 2017;
- [97] W. Lampl et al.: *Calorimeter Clustering Algorithms: Description and Performance*, [ATL-LARG- PUB-2008-002](#), 2008;
- [98] ATLAS Collaboration: *Electron reconstruction and identification in the ATLAS experiment using the 2015 and 2016 LHC proton-proton collision data at $\sqrt{s} = 13$ TeV*, [Eur. Phys. J. C 79 \(2019\) 639](#), [arXiv:1902.04655](#), 2019;
- [99] ATLAS Collaboration: *Improved electron reconstruction in ATLAS using the Gaussian Sum Filter-based model for bremsstrahlung*, [ATLAS-CONF-2012-047 \(2012\)](#), 2012;

- [100] T. Cornelissen et al.: *The global χ^2 track fitter in ATLAS*, *J. Phys. Conf. Ser.*119 (2008) 032013, 2008;
- [101] CDF Collaboration: *First measurement of inclusive W and Z cross sections from Run II of the Fermilab Tevatron Collider*, *Phys. Rev. Lett.*94 (2005) 091803, [arXiv:hep-ex/0406078](#), 2005;
- [102] D0 Collaboration: *Measurement of the shape of the boson rapidity distribution for $p\bar{p} \rightarrow Z/\gamma^* \rightarrow e^+e^- + X$ events produced at \sqrt{s} of 1.96 TeV*, *Phys. Rev.*D76 (2007) 012003, [arXiv:hep-ex/0702025](#), 2007;
- [103] ATLAS Collaboration: *Electron and Photon Performance*, [website](#), 2019;
- [104] Ryan Atkin: *Review of jet reconstruction algorithms*, *J. Phys.: Conf. Ser.*645 012008, 2015;
- [105] Steven Schramm on behalf of the ATLAS Collaboration: *ATLAS Jet Reconstruction, Calibration, and Tagging of Lorentz-boosted Objects*, [ATL-PHYS-PROC-2017-236](#), 2017;
- [106] M. Cacciari, G. P. Salam, and G. Soyez: *The anti- k_t jet clustering algorithm*, *JHEP*04(2008) 63, [arXiv:0802.1189](#), 2008;
- [107] Ariel Schwartzman: *Jet energy calibration at the LHC*, [arXiv:1509.05459](#), 2015;
- [108] ATLAS Collaboration: *Monte Carlo Calibration and Combination of In-situ Measurements of Jet Energy Scale, Jet Energy Resolution and Jet Mass in ATLAS*, [ATLAS-CONF-2015-037](#), 2015;
- [109] ATLAS Collaboration: *Optimisation of the ATLAS b-tagging performance for the 2016 LHC Run*, [ATL-PHYS-PUB-2016-012](#), 2016;
- [110] Sylvestre Pires: *Impact of the Insertable B-Layer on b-tagging performance for ATLAS Run- II*, *Acta Physica Polonica B*, Jagellonian University, Cracow, 2014, 45 (7), [pp.1567-1574](#), 2014;
- [111] ATLAS Collaboration: *Measurements of b-jet tagging efficiency with the ATLAS detector using $t\bar{t}$ events at $\sqrt{s}=13$ TeV*, *JHEP* 08 (2018) 089, 2018;
- [112] J. Illingworth and J. Kittler: *A survey of the Hough transform*, [DOI: 10.1016/S0734-189X\(88\)80033-1](#), 1988;
- [113] ATLAS Collaboration: *Muon reconstruction performance of the ATLAS detector in proton-proton collision data at $\sqrt{s}=13$ TeV*, *Eur. Phys. J.*C76:292 (2016), [arXiv:1603.05598](#), 2016;
- [114] ATLAS Collaboration: *Measurement of the muon reconstruction performance of the ATLAS detector using 2011 and 2012 LHC proton-proton collision data*, *Eur. Phys. J.*C74.11 (2014) 3130, [arXiv:1407.3935](#), 2014;
- [115] Nicolas Kohler on behalf of the ATLAS Collaboration: *ATLAS Muon Reconstruction Performance in LHC Run 2*, [Proceedings of the LHCP2015 Conference](#), 2015;

- [116] ATLAS Collaboration: *ATLAS Muon Combined Performance with the full 2016 dataset*, [website](#), 2017;
- [117] ATLAS Collaboration: *Measurement of the tau lepton reconstruction and identification performance in the ATLAS experiment using pp collisions at $\sqrt{s}=13$ TeV*, [ATLAS-CONF-2017-029](#), 2017;
- [118] L. Breiman, J. Friedman, R. Olshen and C. Stone: *Classification and Regression Trees*, [Chapman & Hall](#), 1984;
- [119] Y. Freund and R. E. Schapire: *A decision-theoretic generalization of on-line learning and an application to boosting*, [Journal of Computer and System Sciences](#) **55**, 119139, 1997;
- [120] ATLAS Collaboration: *Performance of missing transverse momentum reconstruction with the ATLAS detector using proton proton collisions at $\sqrt{s} = 13$ TeV*, [Eur. Phys. J. C](#) **78** (2018) 903, [arXiv:1802.08168](#), 2018;
- [121] ATLAS Collaboration: *Jet and Etmis Performance*, [website](#), 2019;
- [122] Luca Lista: *Practical Statistics for Particle Physicists*, [DOI:10.23730/CYRSP-2017-005.213](#), [arXiv:1609.04150](#), 2017;
- [123] ATLAS Collaboration: *Observation and measurement of Higgs boson decays to WW with the ATLAS detector*, [Phys. Rev. D](#) **92**, 012006 (2015), [arXiv:1412.2641](#), 2015;
- [124] F. James, M. Roos: *Minuit: A System for Function Minimization and Analysis of the Parameter Errors and Correlations*, [Comput. Phys. Commun.](#) **10**, 343-367, 1975;
- [125] Glen Cowan, Kyle Cranmer, Eilam Gross, Ofer Vitells: *Asymptotic formulae for likelihood-based tests of new physics*, [Eur.Phys.J.C](#)**71:1554,2011**, [arXiv:1007.1727](#), 2011;
- [126] A. L. Read: *Presentation of search results: The CL(s) technique*, [J. Phys. G: Nucl. Part. Phys.](#)**28** 2693, 2002;
- [127] M. Tanabashi et al.: *Particle Data Group- Statistics*, [Phys. Rev. D](#) **98**, 030001, 2018;
- [128] S.S. Wilks: *The Large-Sample Distribution of the Likelihood Ratio for Testing Composite Hypotheses*, [Ann. Math. Statist. Volume 9, Number 1 \(1938\)](#), 60-62. 1938;
- [129] Abraham Wald: *Tests of statistical hypotheses concerning several parameters when the number of observation is large*, [Trans. Amer. Math. Soc.](#) **54** (1943), 426-482, 1943;
- [130] J.Neyman: *Outline of a theory of statistical estimation based on the classical theory of probability*, [Philosophical Transactions of the Royal Society of London, Series A, Mathematical and Physical Sciences](#), vol. 236, pp. 333-380, 1937;
- [131] M. Cepeda, S. Gori, P. Ilten, M. Kado, F. Riva et al.: *Higgs Physics at the HL-LHC and HE-LHC*, [arXiv:1902.00134](#), 2019;

- [132] ATLAS Collaboration: *Constraints on the Higgs boson self-coupling from the combination of single-Higgs and double-Higgs production analyses performed with the ATLAS experiment*, [ATLAS-CONF-2019-049](#), 2019;
- [133] F. Maltoni, D. Pagani, A. Shivaji and X. Zhao: *Trilinear Higgs coupling determination via single-Higgs differential measurements at the LHC*, [Eur. Phys. J. C77 \(2017\) 887](#), [arXiv:1709.08649](#), 2017;
- [134] M. E. Peskin: *Estimation of LHC and ILC Capabilities for Precision Higgs Boson Coupling Measurements*, [arXiv:1312.4974](#), 2013;
- [135] ATLAS Collaboration: *Projections for measurements of Higgs boson cross sections, branching ratios and coupling parameters with the ATLAS detector at a HL-LHC*, [ATL-PHYS-PUB-2013-014](#), 2013;
- [136] ATLAS Collaboration: *HL-LHC projections for signal and background yield measurements of the $H \rightarrow \gamma\gamma$ when the Higgs boson is produced in association with t quarks, W or Z bosons*, [ATL-PHYS-PUB-2014-012](#), 2014;
- [137] S. Di Vita, C. Grojean, G. Panico, M. Riembau, T. Vantalón: *A global view on the Higgs self-coupling*, [JHEP 1709 \(2017\) 069](#), [arXiv:1704.01953](#), 2017.
- [138] ATLAS Collaboration: *Search for pair production of Higgs bosons in the $b\bar{b}b\bar{b}$ final state using proton-proton collisions at $\sqrt{s} = 13$ TeV with the ATLAS detector*, [JHEP 01 \(2019\) 030](#), [arXiv:1804.06174](#), 2019;
- [139] ATLAS Collaboration: *Search for Resonant and Nonresonant Higgs Boson Pair Production in the $b\bar{b}\tau^+\tau^-$ Decay Channel in pp Collisions at $\sqrt{s} = 13$ TeV with the ATLAS Detector*, [Phys. Rev. Lett. 121, 191801 \(2018\)](#), [arXiv:1808.00336](#), 2018;
- [140] ATLAS Collaboration: *Search for Higgs boson pair production in the $\gamma\gamma b\bar{b}$ final state with 13 TeV pp collision data collected by the ATLAS experiment*, [JHEP 11 \(2018\) 040](#), [arXiv:1807.04873](#), 2018;
- [141] ATLAS Collaboration: *Measurements of Higgs boson properties in the diphoton decay channel with 36 fb^{-1} of pp collision data at $\sqrt{s} = 13$ TeV with the ATLAS detector*, [Phys. Rev. D 98 \(2018\) 052005](#), [arXiv:1802.04146](#), 2018;
- [142] S. Dawson, S. Dittmaier, M. Spira: *Neutral Higgs boson pair production at hadron colliders: QCD corrections*, [Phys.Rev.D58:115012,1998](#), [arXiv:hep-ph/9805244](#), 1998;
- [143] S. Borowka, N. Greiner, G. Heinrich, S.P. Jones, M. Kerner, J. Schlenk, U. Schubert, T. Zirke: *Higgs boson pair production in gluon fusion at NLO with full top-quark mass dependence*, [Phys. Rev. Lett. 117, 012001 \(2016\)](#), [arXiv:1604.06447](#), 2016;
- [144] J. Baglio, F. Campanario, S. Glaus, M. Mühlleitner, M. Spira, J. Streicher: *Gluon fusion into Higgs pairs at NLO QCD and the top mass scheme*, [Eur. Phys. J. C 79 \(2019\) 459](#), [arXiv:1811.05692](#), 2019;

- [145] R. Bonciani, G. Degrassi, P. P. Giardino, R. Gröber: *An Analytical Method for the NLO QCD Corrections to Double-Higgs Production*, [Phys. Rev. Lett. 121, 162003 \(2018\)](#), [arXiv:1806.11564](#), 2018;
- [146] D. de Florian, J. Mazzitelli: *Higgs Boson Pair Production at Next-to-Next-to-Leading Order in QCD*, [Phys.Rev.Lett. 111 \(2013\) 201801](#), [arXiv:1309.6594](#), 2013;
- [147] Ding Yu Shao, Chong Sheng Li, Hai Tao Li, Jian Wang: *Threshold resummation effects in Higgs boson pair production at the LHC*, [JHEP07\(2013\)169](#), [arXiv:1301.1245](#), 2013;
- [148] D. de Florian, J. Mazzitelli: *Higgs pair production at next-to-next-to-leading logarithmic accuracy at the LHC*, [arXiv:1505.07122](#), 2015;
- [149] M. Grazzini et al.: *Higgs boson pair production at NNLO with top quark mass effects*, [JHEP 05 \(2018\) 059](#), [arXiv:1803.02463](#), 2018;
- [150] G. Heinrich, S. P. Jones, M. Kerner, G. Luisoni and L. Scyboz: *Probing the trilinear Higgs boson coupling in di-Higgs production at NLO QCD including parton shower effects*, [JHEP 06 \(2019\) 066](#), [arXiv:1903.08137](#), 2019;
- [151] ATLAS Collaboration: *Measurement of Higgs boson properties in the diphoton decay channel using 80 fb⁻¹ of pp collision data at $\sqrt{s} = 13$ TeV with the ATLAS detector*, [ATLAS-CONF-2018-028](#), 2018;
- [152] ATLAS Collaboration: *Measurements of Higgs boson properties in the diphoton decay channel with 36 fb⁻¹ of pp collision data at $\sqrt{s} = 13$ TeV with the ATLAS detector*, [Phys. Rev. D 98 \(2018\) 052005](#), [arXiv:1802.04146](#), 2018.
- [153] ATLAS Collaboration: *Observation of Higgs boson production in association with a top quark pair at the LHC with the ATLAS detector*, [Phys. Lett. B 784 \(2018\) 173](#), [arXiv:1806.00425](#), 2018;
- [154] ATLAS Collaboration: *Measurements of the Higgs boson production, fiducial and differential cross sections in the 4 ℓ decay channel at $\sqrt{s} = 13$ TeV with the ATLAS detector*, [ATLAS-CONF-2018-018](#), 2018;
- [155] ATLAS Collaboration: *Measurement of the Higgs boson coupling properties in the $H \rightarrow ZZ^* \rightarrow 4\ell$ decay channel at $\sqrt{s} = 13$ TeV with the ATLAS detector*, [JHEP 03 \(2018\) 095](#), [arXiv:1712.02304](#), 2018;
- [156] ATLAS Collaboration: *Measurements of gluon-gluon fusion and vector-boson fusion Higgs boson production cross-sections in the $H \rightarrow WW^* \rightarrow e\nu\mu\nu$ decay channel in pp collisions at $\sqrt{s} = 13$ TeV with the ATLAS detector*, [arXiv:1808.09054](#), 2018;
- [157] ATLAS Collaboration: *Cross-section measurements of the Higgs boson decaying into a pair of τ -leptons in proton-proton collisions at $\sqrt{s} = 13$ TeV with the ATLAS detector*, [Phys. Rev. D 99, 072001 \(2019\)](#), [arXiv:1811.08856](#), 2018;
- [158] ATLAS Collaboration: *Observation of $H \rightarrow b\bar{b}$ decays and VH production with the ATLAS detector*, [Phys. Lett. B 786 \(2018\) 59](#), [arXiv:1808.08238](#), 2018;

- [159] ATLAS Collaboration: *Measurements of VH , $H \rightarrow b\bar{b}$ production as a function of the vector boson transverse momentum in 13 TeV pp collisions with the ATLAS detector*, [ATLAS-CONF-2018-053](#), 2018;
- [160] ATLAS Collaboration: *Evidence for the associated production of the Higgs boson and a top quark pair with the ATLAS detector*, [Phys. Rev. D 97 \(2018\) 072003](#), [arXiv:1712.08891](#), 2018;
- [161] ATLAS Collaboration: *Search for the standard model Higgs boson produced in association with top quarks and decaying into a $b\bar{b}$ pair in pp collisions at $\sqrt{s} = 13$ TeV with the ATLAS detector*, [Phys. Rev. D 97 \(2018\) 072016](#), [arXiv:1712.08895](#), 2018;
- [162] S. Badger et al.: *Les Houches 2015: Physics at TeV Colliders Standard Model Working Group Report*, [arXiv:1605.04692](#), 2016;
- [163] ATLAS Collaboration: *Constraint of the Higgs boson self-coupling from Higgs boson differential production and decay measurements*, [ATL-PHYS-PUB-2019-009](#), 2019;
- [164] J. Alwall, R. Frederix, S. Frixione, V. Hirschi, F. Maltoni, O. Mattelaer, H.S. Shao, T. Stelzer, P. Torrielli, M. Zaro: *The automated computation of tree-level and next-to-leading order differential cross sections, and their matching to parton shower simulations*, [JHEP07\(2014\)079](#), [arXiv:1405.0301](#), 2014;
- [165] A. Shivaji and X. Zhao: *Higgs Trilinear self-coupling determination through one-loop effects*, [website](#), 2017;
- [166] M. Carena, H. E. Haber, I. Low, N. R. Shah, C. E. M. Wagner: *On the Alignment Limit of the NMSSM Higgs Sector*, [Phys. Rev. D 93, 035013 \(2016\)](#), [arXiv:1510.09137](#), 2015;
- [167] M. B. Einhorn, J. Wudka: *Higgs-Boson Couplings Beyond the Standard Model*, [arXiv:1308.2255](#), 2013.

Appendix A

Correlations between double-Higgs analyses

For the $HH \rightarrow b\bar{b}b\bar{b}$ channel, two different correlation schemes regarding flavour tagging, jet, parton shower and trigger uncertainties, have been considered and are described in Table A.1:

- all NPs related to the signal samples uncorrelated, i.e. keeping FT, JET, PS, trigger NPs split in the three signal samples (scheme 1);
- all NPs related to the signal samples correlated to be consistent with the published double-Higgs combination [35] (scheme 2).

Scheme 1	Scheme 2
alpha_FT_EFF_Eigen_B_0_lhh00 alpha_FT_EFF_Eigen_B_0_lhh01 alpha_FT_EFF_Eigen_B_0_lhh20	alpha_FT_EFF_Eigen_B_0
alpha_FT_EFF_Eigen_B_1_lhh00 alpha_FT_EFF_Eigen_B_1_lhh01 alpha_FT_EFF_Eigen_B_1_lhh20	alpha_FT_EFF_Eigen_B_1
alpha_FT_EFF_Eigen_B_2_lhh00 alpha_FT_EFF_Eigen_B_2_lhh01 alpha_FT_EFF_Eigen_B_2_lhh20	alpha_FT_EFF_Eigen_B_2
alpha_FT_EFF_Eigen_B_3_lhh00 alpha_FT_EFF_Eigen_B_3_lhh01 alpha_FT_EFF_Eigen_B_3_lhh20	alpha_FT_EFF_Eigen_B_3
alpha_FT_EFF_Eigen_B_4_lhh00 alpha_FT_EFF_Eigen_B_4_lhh01 alpha_FT_EFF_Eigen_B_4_lhh20	alpha_FT_EFF_Eigen_B_4
alpha_FT_EFF_extrapolation_lhh00 alpha_FT_EFF_extrapolation_lhh01 alpha_FT_EFF_extrapolation_lhh20	alpha_FT_EFF_extrapolation
alpha_JET_EtaIntercalib_Nonclos_lhh00 alpha_JET_EtaIntercalib_Nonclos_lhh01 alpha_JET_EtaIntercalib_Nonclos_lhh20	alpha_JET_EtaIntercalib_Nonclos

Scheme 1	Scheme 2
alpha_JET_GroupedNP_1_lhh00 alpha_JET_GroupedNP_1_lhh01 alpha_JET_GroupedNP_1_lhh20	alpha_JET_GroupedNP_1
alpha_JET_GroupedNP_2_lhh00 alpha_JET_GroupedNP_2_lhh01 alpha_JET_GroupedNP_2_lhh20	alpha_JET_GroupedNP_2
alpha_JET_GroupedNP_3_lhh00 alpha_JET_GroupedNP_3_lhh01 alpha_JET_GroupedNP_3_lhh20	alpha_JET_GroupedNP_3
alpha_JET_JER_lhh00 alpha_JET_JER_lhh01 alpha_JET_JER_lhh20	alpha_JET_JER
alpha_Theoretical_lhh00 alpha_Theoretical_lhh01 alpha_Theoretical_lhh20	alpha_Theoretical
alpha_trig_r15_lhh00 alpha_trig_r15_lhh01 alpha_trig_r15_lhh20	alpha_trig_r15
alpha_trig_r16_lhh00 alpha_trig_r16_lhh01 alpha_trig_r16_lhh20	alpha_trig_r16

Appendix B

Correlations between single- and double-Higgs analyses

The nuisance parameters correlation scheme adopted in the H+HH combination, in addition to the correlations between single-Higgs and double-Higgs individual combination described in Chapters 7 and 8, is reported in the following tables. Experimental uncertainties have been correlated whenever relevant, like in the case of the integrated luminosity and detector related uncertainties. Experimental uncertainties that are related to the same physics object but determined with different methodologies or implemented with different parameterisations, like the flavour tagging uncertainties, have been kept uncorrelated. Signal theory uncertainties have been kept uncorrelated while the systematic uncertainties on the decay branching ratios have been correlated. Theoretical uncertainties on the $pp \rightarrow HH$ ggF cross section have been included in the double-Higgs analyses. The correlation between the systematic uncertainties is implemented in the final fit procedure by associating different uncertainties to the same nuisance parameter in the combined likelihood function.

NP name	single Higgs	double Higgs
Experimental uncertainties		
Jet uncertainties		
ATLAS_BJES	○	
ATLAS_JER_CR2_3j_dl_ttHbb	○	
ATLAS_JER_CROSSCALIBFWD_Htautau	○	
ATLAS_JER_NOISEFWD_Htautau	○	
ATLAS_JER_NP_0_Htautau	○	
ATLAS_JER_NP_1_Htautau	○	
ATLAS_JER_NP_2_Htautau	○	
ATLAS_JER_NP_3_Htautau	○	
ATLAS_JER_NP_4_Htautau	○	
ATLAS_JER_NP_5_Htautau	○	
ATLAS_JER_NP_6_Htautau	○	
ATLAS_JER_NP_7_Htautau	○	
ATLAS_JER_NP_8_Htautau	○	
ATLAS_JER_SINGLE_NP	○	○
ATLAS_JER_SINGLE_NP_Rel21	○	

NP name	single Higgs	double Higgs
Experimental uncertainties		
Jet uncertainties		
ATLAS_JES_BJES_Response_Rel21	○	
ATLAS_JES_EffectiveNP_1	○	
ATLAS_JES_EffectiveNP_1_Rel21	○	
ATLAS_JES_EffectiveNP_2	○	
ATLAS_JES_EffectiveNP_3	○	
ATLAS_JES_EffectiveNP_3_Rel21	○	
ATLAS_JES_EffectiveNP_4	○	
ATLAS_JES_EffectiveNP_4_Rel21	○	
ATLAS_JES_EffectiveNP_5	○	
ATLAS_JES_EffectiveNP_5_Rel21	○	
ATLAS_JES_EffectiveNP_6	○	
ATLAS_JES_EffectiveNP_6_Rel21	○	
ATLAS_JES_EffectiveNP_7	○	
ATLAS_JES_EffectiveNP_7_Rel21	○	
ATLAS_JES_EffectiveNP_8restTerm	○	
ATLAS_JES_EffectiveNP_8restTerm_Rel21	○	
ATLAS_JES_EtaInter_Model	○	
ATLAS_JES_EtaInter_NonClosure	○	○
ATLAS_JES_EtaInter_Stat	○	
ATLAS_JES_EtaIntercalibration_Modelling_Rel21	○	
ATLAS_JES_EtaIntercalibration_NonClosure_highE_Rel21	○	
ATLAS_JES_EtaIntercalibration_NonClosure_negEta_Rel21	○	
ATLAS_JES_EtaIntercalibration_NonClosure_posEta_Rel21	○	
ATLAS_JES_EtaIntercalibration_TotalStat_Rel21	○	
ATLAS_JES_Flavor_Comp	○	
ATLAS_JES_Flavor_Comp_Rel21_HZZ	○	
ATLAS_JES_Flavor_Comp_Top	○	
ATLAS_JES_Flavor_Comp_Top_Rel21	○	
ATLAS_JES_Flavor_Comp_VBF_Rel21	○	
ATLAS_JES_Flavor_Comp_VH_Rel21	○	
ATLAS_JES_Flavor_Comp_VV_Rel21	○	
ATLAS_JES_Flavor_Comp_Vjets_Rel21	○	
ATLAS_JES_Flavor_Comp_WW	○	
ATLAS_JES_Flavor_Comp_bbH_Rel21	○	
ATLAS_JES_Flavor_Comp_ggF_Rel21	○	
ATLAS_JES_Flavor_Comp_ggZH_Rel21	○	
ATLAS_JES_Flavor_Comp_l20tau_Other_ttHML	○	
ATLAS_JES_Flavor_Comp_l20tau_VV_ttHML	○	
ATLAS_JES_Flavor_Comp_l20tau_ttZ_ttHML	○	
ATLAS_JES_Flavor_Comp_l30tau_Other_ttHML	○	
ATLAS_JES_Flavor_Comp_l30tau_ttW_ttHML	○	
ATLAS_JES_Flavor_Comp_l4_ttHML	○	
ATLAS_JES_Flavor_Comp_lephadzll_Htautau	○	
ATLAS_JES_Flavor_Comp_lelepzll_Htautau	○	
ATLAS_JES_Flavor_Comp_qqZZ_Rel21_HZZ	○	

NP name	single Higgs	double Higgs
Experimental uncertainties		
Jet uncertainties		
ATLAS_JES_Flavor_Comp_tHW_Rel21	○	
ATLAS_JES_Flavor_Comp_tHqb_Rel21	○	
ATLAS_JES_Flavor_Comp_ttH_Rel21	○	
ATLAS_JES_Flavor_Comp_ttbar_L2_Rel21	○	
ATLAS_JES_Flavor_Resp	○	
ATLAS_JES_Flavor_Resp_Rel21	○	
ATLAS_JES_Flavor_Resp_VBF_Rel21	○	
ATLAS_JES_Flavor_Resp_VH_Rel21	○	
ATLAS_JES_Flavor_Resp_bbH_Rel21	○	
ATLAS_JES_Flavor_Resp_ggF_Rel21	○	
ATLAS_JES_Flavor_Resp_ggZH_Rel21	○	
ATLAS_JES_Flavor_Resp_lephadzll_Htautau	○	
ATLAS_JES_Flavor_Resp_lelepzll_Htautau	○	
ATLAS_JES_Flavor_Resp_qqZZ_Rel21_HZZ	○	
ATLAS_JES_Flavor_Resp_tHW_Rel21	○	
ATLAS_JES_Flavor_Resp_tHqb_Rel21	○	
ATLAS_JES_Flavor_Resp_ttH_Rel21	○	
ATLAS_JES_PU_OffsetMu	○	
ATLAS_JES_PU_OffsetMu_Rel21	○	
ATLAS_JES_PU_OffsetNPV	○	
ATLAS_JES_PU_OffsetNPV_Rel21	○	
ATLAS_JES_PU_PtTerm	○	
ATLAS_JES_PU_PtTerm_Rel21	○	
ATLAS_JES_PU_Rho	○	
ATLAS_JES_PU_Rho_Rel21	○	
ATLAS_JES_PU_Rho_top_HWW	○	
ATLAS_JES_PunchThrough	○	
ATLAS_JES_PunchThrough_Rel21	○	
ATLAS_JES_SinglePart_ttHML	○	
ATLAS_JES_SingleParticle_HighPt_Rel21	○	
ATLAS_JES_bbyy		○
ATLAS_JET_GroupedNP_1		○
ATLAS_JET_GroupedNP_2		○
ATLAS_JET_GroupedNP_3		○
ATLAS_JVT	○	
ATLAS_JVT_Rel21	○	
ATLAS_fJVT	○	
ATLAS_Signal_trig_r15_bbbb		○
ATLAS_Signal_trig_r16_bbbb		○

NP name	single Higgs	double Higgs
Experimental uncertainties		
Flavour tagging uncertainties		
ATLAS_FTAG_B0	○	

NP name	single Higgs	double Higgs
Experimental uncertainties		
Flavour tagging uncertainties		
ATLAS_FTAG_B1	○	
ATLAS_FTAG_B10	○	
ATLAS_FTAG_B11	○	
ATLAS_FTAG_B12	○	
ATLAS_FTAG_B13	○	
ATLAS_FTAG_B14	○	
ATLAS_FTAG_B15	○	
ATLAS_FTAG_B16_ttHML	○	
ATLAS_FTAG_B17	○	
ATLAS_FTAG_B18	○	
ATLAS_FTAG_B19_ttHML	○	
ATLAS_FTAG_B2	○	
ATLAS_FTAG_B20	○	
ATLAS_FTAG_B21	○	
ATLAS_FTAG_B22	○	
ATLAS_FTAG_B23	○	
ATLAS_FTAG_B24_ttHML	○	
ATLAS_FTAG_B26	○	
ATLAS_FTAG_B27	○	
ATLAS_FTAG_B28_ttHbb	○	
ATLAS_FTAG_B29	○	
ATLAS_FTAG_B3	○	
ATLAS_FTAG_B4	○	
ATLAS_FTAG_B5	○	
ATLAS_FTAG_B6	○	
ATLAS_FTAG_B7	○	
ATLAS_FTAG_B8	○	
ATLAS_FTAG_B9	○	
ATLAS_FTAG_C0	○	
ATLAS_FTAG_C1	○	
ATLAS_FTAG_C10	○	
ATLAS_FTAG_C11	○	
ATLAS_FTAG_C12_ttHML	○	
ATLAS_FTAG_C13_ttHML	○	
ATLAS_FTAG_C14	○	
ATLAS_FTAG_C2	○	
ATLAS_FTAG_C3	○	
ATLAS_FTAG_C4	○	
ATLAS_FTAG_C5	○	
ATLAS_FTAG_C6	○	
ATLAS_FTAG_C7	○	
ATLAS_FTAG_C8	○	
ATLAS_FTAG_C9	○	
ATLAS_FTAG_L0	○	
ATLAS_FTAG_L1	○	

NP name	single Higgs	double Higgs
Experimental uncertainties		
Flavour tagging uncertainties		
ATLAS_FTAG_L10	○	
ATLAS_FTAG_L11	○	
ATLAS_FTAG_L12	○	
ATLAS_FTAG_L13	○	
ATLAS_FTAG_L14	○	
ATLAS_FTAG_L15	○	
ATLAS_FTAG_L16	○	
ATLAS_FTAG_L17	○	
ATLAS_FTAG_L18	○	
ATLAS_FTAG_L19	○	
ATLAS_FTAG_L2	○	
ATLAS_FTAG_L20	○	
ATLAS_FTAG_L21	○	
ATLAS_FTAG_L22_ttHML	○	
ATLAS_FTAG_L23_ttHML	○	
ATLAS_FTAG_L24	○	
ATLAS_FTAG_L25	○	
ATLAS_FTAG_L26	○	
ATLAS_FTAG_L27	○	
ATLAS_FTAG_L28	○	
ATLAS_FTAG_L3	○	
ATLAS_FTAG_L31	○	
ATLAS_FTAG_L32_ttHML	○	
ATLAS_FTAG_L33_ttHbb	○	
ATLAS_FTAG_L35	○	
ATLAS_FTAG_L36_ttHML	○	
ATLAS_FTAG_L37_ttHML	○	
ATLAS_FTAG_L38_ttHML	○	
ATLAS_FTAG_L4	○	
ATLAS_FTAG_L42_ttHML	○	
ATLAS_FTAG_L44_ttHML	○	
ATLAS_FTAG_L5	○	
ATLAS_FTAG_L50_ttHML	○	
ATLAS_FTAG_L6	○	
ATLAS_FTAG_L7	○	
ATLAS_FTAG_L8	○	
ATLAS_FTAG_L9	○	
ATLAS_FT_EFF_Eigen_B_0_Rel21_WP70	○	
ATLAS_FT_EFF_Eigen_B_0_Rel21_WP77	○	
ATLAS_FT_EFF_Eigen_B_0_WP70		○
ATLAS_FT_EFF_Eigen_B_0_WP85	○	
ATLAS_FT_EFF_Eigen_B_1_Rel21_WP70	○	
ATLAS_FT_EFF_Eigen_B_1_Rel21_WP77	○	
ATLAS_FT_EFF_Eigen_B_1_WP70		○
ATLAS_FT_EFF_Eigen_B_1_WP85	○	

NP name	single Higgs	double Higgs
Experimental uncertainties		
Flavour tagging uncertainties		
ATLAS_FT_EFF_Eigen_B_2_Rel21_WP70	○	
ATLAS_FT_EFF_Eigen_B_2_Rel21_WP77	○	
ATLAS_FT_EFF_Eigen_B_2_WP70		○
ATLAS_FT_EFF_Eigen_B_2_WP85	○	
ATLAS_FT_EFF_Eigen_B_3_WP70		○
ATLAS_FT_EFF_Eigen_B_4_WP70		○
ATLAS_FT_EFF_Eigen_B_WP70_bbyy		○
ATLAS_FT_EFF_Eigen_C_0_Rel21_WP70	○	
ATLAS_FT_EFF_Eigen_C_0_Rel21_WP77	○	
ATLAS_FT_EFF_Eigen_C_0_WP70		○
ATLAS_FT_EFF_Eigen_C_0_WP85	○	
ATLAS_FT_EFF_Eigen_C_1_Rel21_WP70	○	
ATLAS_FT_EFF_Eigen_C_1_Rel21_WP77	○	
ATLAS_FT_EFF_Eigen_C_1_WP70		○
ATLAS_FT_EFF_Eigen_C_1_WP85	○	
ATLAS_FT_EFF_Eigen_C_2_Rel21_WP70	○	
ATLAS_FT_EFF_Eigen_C_2_Rel21_WP77	○	
ATLAS_FT_EFF_Eigen_C_2_WP70		○
ATLAS_FT_EFF_Eigen_C_2_WP85	○	
ATLAS_FT_EFF_Eigen_C_3_WP85_HWW	○	
ATLAS_FT_EFF_Eigen_C_WP70_bbyy		○
ATLAS_FT_EFF_Eigen_Light_0_Rel21_WP70	○	
ATLAS_FT_EFF_Eigen_Light_0_Rel21_WP77	○	
ATLAS_FT_EFF_Eigen_Light_0_WP70		○
ATLAS_FT_EFF_Eigen_Light_0_WP85	○	
ATLAS_FT_EFF_Eigen_Light_1_Rel21_WP70	○	
ATLAS_FT_EFF_Eigen_Light_1_Rel21_WP77	○	
ATLAS_FT_EFF_Eigen_Light_1_WP70		○
ATLAS_FT_EFF_Eigen_Light_1_WP85	○	
ATLAS_FT_EFF_Eigen_Light_2_Rel21_WP70	○	
ATLAS_FT_EFF_Eigen_Light_2_Rel21_WP77	○	
ATLAS_FT_EFF_Eigen_Light_2_WP70		○
ATLAS_FT_EFF_Eigen_Light_2_WP85	○	
ATLAS_FT_EFF_Eigen_Light_3_Rel21_WP70	○	
ATLAS_FT_EFF_Eigen_Light_3_Rel21_WP77	○	
ATLAS_FT_EFF_Eigen_Light_3_WP70		○
ATLAS_FT_EFF_Eigen_Light_3_WP85	○	
ATLAS_FT_EFF_Eigen_Light_4_WP70		○
ATLAS_FT_EFF_Eigen_Light_4_WP85	○	
ATLAS_FT_EFF_Eigen_Light_WP70_bbyy		○
ATLAS_FT_EFF_extrapolation_Rel21_WP70	○	
ATLAS_FT_EFF_extrapolation_Rel21_WP77	○	
ATLAS_FT_EFF_extrapolation_WP70		○
ATLAS_FT_EFF_extrapolation_WP85	○	
ATLAS_FT_EFF_extrapolation_from_charm_Rel21_WP70	○	

NP name	single Higgs	double Higgs
Experimental uncertainties		
Flavour tagging uncertainties		
ATLAS_FT_EFF_extrapolation_from_charm_Rel21_WP77	○	
ATLAS_FT_EFF_extrapolation_from_charm_WP70		○
ATLAS_FT_EFF_extrapolation_from_charm_WP85	○	

NP name	single Higgs	double Higgs
Theoretical uncertainties		
Signal uncertainties		
TheorySig_BR_HiggsDecayWidthTHU_hVV	○	○
TheorySig_BR_HiggsDecayWidthTHU_hbb	○	○
TheorySig_BR_HiggsDecayWidthTHU_hgg	○	○
TheorySig_BR_HiggsDecayWidthTHU_htautau	○	○
TheorySig_BR_HiggsDecayWidthTHU_hyy	○	○
TheorySig_BR_Others_ttHML	○	
TheorySig_BR_Others_ttHbb	○	
TheorySig_BR_param_mB	○	○
TheorySig_BR_param_mC	○	○
TheorySig_GenComp_ggF_FxFxComp_HZZ	○	
TheorySig_GenComp_ggF_MinloComp_HZZ	○	
TheorySig_HF_Higgs_VBF	○	
TheorySig_HF_Higgs_VH	○	
TheorySig_HF_Higgs_ggF	○	○
TheorySig_ME_ggF_GGFsel_HWW	○	
TheorySig_ME_ggF_VBFsel_HWW	○	
TheorySig_NLO_EW_Higgs_total_Htautau	○	
TheorySig_PDF4LHC_NLO_30_EV1	○	
TheorySig_PDF4LHC_NLO_30_EV10	○	
TheorySig_PDF4LHC_NLO_30_EV11	○	
TheorySig_PDF4LHC_NLO_30_EV12	○	
TheorySig_PDF4LHC_NLO_30_EV13	○	
TheorySig_PDF4LHC_NLO_30_EV14	○	
TheorySig_PDF4LHC_NLO_30_EV15	○	
TheorySig_PDF4LHC_NLO_30_EV16	○	
TheorySig_PDF4LHC_NLO_30_EV17	○	
TheorySig_PDF4LHC_NLO_30_EV18	○	
TheorySig_PDF4LHC_NLO_30_EV19	○	
TheorySig_PDF4LHC_NLO_30_EV2	○	
TheorySig_PDF4LHC_NLO_30_EV20	○	
TheorySig_PDF4LHC_NLO_30_EV21	○	
TheorySig_PDF4LHC_NLO_30_EV22	○	
TheorySig_PDF4LHC_NLO_30_EV23	○	
TheorySig_PDF4LHC_NLO_30_EV24	○	
TheorySig_PDF4LHC_NLO_30_EV25	○	

NP name	single Higgs	double Higgs
Theoretical uncertainties		
Signal uncertainties		
TheorySig_PDF4LHC_NLO_30_EV26	○	
TheorySig_PDF4LHC_NLO_30_EV27	○	
TheorySig_PDF4LHC_NLO_30_EV28	○	
TheorySig_PDF4LHC_NLO_30_EV29	○	
TheorySig_PDF4LHC_NLO_30_EV3	○	
TheorySig_PDF4LHC_NLO_30_EV30	○	
TheorySig_PDF4LHC_NLO_30_EV4	○	
TheorySig_PDF4LHC_NLO_30_EV5	○	
TheorySig_PDF4LHC_NLO_30_EV6	○	
TheorySig_PDF4LHC_NLO_30_EV7	○	
TheorySig_PDF4LHC_NLO_30_EV8	○	
TheorySig_PDF4LHC_NLO_30_EV9	○	
TheorySig_PDF_VBF	○	
TheorySig_PDF_VBF_VBFsel_ACC_HWW	○	
TheorySig_PDF_bbH	○	○
TheorySig_PDF_ggF	○	○
TheorySig_PDF_ggF_GGFsel_ACC_HWW	○	
TheorySig_PDF_ggF_VBFsel_ACC_HWW	○	
TheorySig_PDF_hh		○
TheorySig_PDF_tHW	○	
TheorySig_PDF_tHqb	○	
TheorySig_PDF_ttH	○	
TheorySig_QCDScaleDelta150_ggZH	○	
TheorySig_QCDScaleDelta150_qqVH	○	
TheorySig_QCDScaleDelta250_ggZH	○	
TheorySig_QCDScaleDelta250_qqVH	○	
TheorySig_QCDScaleDelta75_ggZH	○	
TheorySig_QCDScaleDelta75_qqVH	○	
TheorySig_QCDScaleDeltaY_ggZH	○	
TheorySig_QCDScaleDeltaY_qqVH	○	
TheorySig_QCDalphaS	○	○
TheorySig_QCDalphaS_hh		○
TheorySig_QCDscale_VBF	○	○
TheorySig_QCDscale_VBF_VBFsel_ACC_HWW	○	
TheorySig_QCDscale_VH	○	○
TheorySig_QCDscale_bbH	○	
TheorySig_QCDscale_ggF_2j_VBFsel_HWW	○	
TheorySig_QCDscale_ggF_3j_VBFsel_HWW	○	
TheorySig_QCDscale_ggF_GGFsel_ACC_HWW	○	
TheorySig_QCDscale_ggF_mig01	○	
TheorySig_QCDscale_ggF_mig12	○	
TheorySig_QCDscale_ggF_mu	○	○

NP name	single Higgs	double Higgs
Theoretical uncertainties		
Signal uncertainties		
TheorySig_QCDscale_ggF_pTH120	○	
TheorySig_QCDscale_ggF_pTH60	○	
TheorySig_QCDscale_ggF_qm_t	○	
TheorySig_QCDscale_ggF_res	○	
TheorySig_QCDscale_ggF_vbf2j	○	
TheorySig_QCDscale_ggF_vbf3j	○	
TheorySig_QCDscale_ggH_pTH_GGF_HWW	○	
TheorySig_QCDscale_hh		○
TheorySig_QCDscale_tHW	○	
TheorySig_QCDscale_tHqb	○	
TheorySig_QCDscale_ttH	○	○
TheorySig_SIG_PS_bbbb		○
TheorySig_SIG_PS_bbtautau		○
TheorySig_SysHiggsNorm_bbtautau		○
TheorySig_SysTheoryDelta1_ggZH_VHbb	○	
TheorySig_SysTheoryDelta1_qqVH_VHbb	○	
TheorySig_SysTheoryDelta2_ggZH_VHbb	○	
TheorySig_SysTheoryDelta2_qqVH_VHbb	○	
TheorySig_SysTheoryPSUE_AZNLO_MPI_VHbb	○	
TheorySig_SysTheoryPSUE_AZNLO_Ren_VHbb	○	
TheorySig_SysTheoryPSUE_AZNLO_Var1_VHbb	○	
TheorySig_SysTheoryPSUE_AZNLO_Var2_VHbb	○	
TheorySig_SysTheoryPSUE_H7_VHbb	○	
TheorySig_SysTheoryQCDscaleDelta400_ggVH_VHbb	○	
TheorySig_SysTheoryQCDscaleDelta400_qqVH_VHbb	○	
TheorySig_SysVHNLOEWK_VHbb	○	
TheorySig_SysVHQCDscaleMbb_VHbb	○	
TheorySig_SysVHQCDscaleMbb_ggZH_VHbb	○	
TheorySig_SysVHQCDscalePTV_VHbb	○	
TheorySig_SysVHQCDscalePTV_ggZH_VHbb	○	
TheorySig_SysVHUEPSMbb_VHbb	○	
TheorySig_SysVHUEPSPTV_VHbb	○	
TheorySig_SysttHNorm_bbtautau		○
TheorySig_UEPS_AZNLO_ISR_HZZ	○	
TheorySig_UEPS_AZNLO_Var3c_HZZ	○	
TheorySig_UEPS_AZNLO_hard_HZZ	○	
TheorySig_UEPS_VBF	○	
TheorySig_UEPS_VH_channel_HGam	○	
TheorySig_UEPS_ggF	○	
TheorySig_UEPS_ggF_GGFsel_HWW	○	
TheorySig_UEPS_ggF_VBFsel_HWW	○	
TheorySig_UEPS_hh_VH_Htautau	○	

NP name	single Higgs	double Higgs
Theoretical uncertainties		
Signal uncertainties		
TheorySig_UEPS_hh_boost_VBFH_Htautau	○	
TheorySig_UEPS_hh_boost_ggH_Htautau	○	
TheorySig_UEPS_hh_vbf_VBFH_Htautau	○	
TheorySig_UEPS_hh_vbf_ggH_Htautau	○	
TheorySig_UEPS_lh_VH_Htautau	○	
TheorySig_UEPS_lh_boost_VBFH_Htautau	○	
TheorySig_UEPS_lh_boost_ggH_Htautau	○	
TheorySig_UEPS_lh_vbf_VBFH_Htautau	○	
TheorySig_UEPS_lh_vbf_ggH_Htautau	○	
TheorySig_UEPS_ll_VH_Htautau	○	
TheorySig_UEPS_ll_boost_VBFH_Htautau	○	
TheorySig_UEPS_ll_boost_ggH_Htautau	○	
TheorySig_UEPS_ll_vbf_VBFH_Htautau	○	
TheorySig_UEPS_ll_vbf_ggH_Htautau	○	
TheorySig_UEPS_ttH	○	
TheorySig_VBFH_MUR_MUF_Htautau	○	
TheorySig_VH_MUR_MUF_Htautau	○	
TheorySig_dQQPdf_bbyy		○
TheorySig_mtop_hh		○
TheorySig_r_bbH_ggH_HZZ	○	
TheorySig_ttH_varA14_ttHML	○	
TheorySig_ttH_varF_ttHML	○	
TheorySig_ttH_varRF_ttHML	○	
TheorySig_ttH_varR_ttHML	○	

NP name	single Higgs	double Higgs
Experimental uncertainties		
Luminosity uncertainties		
ATLAS_LUMI_1516_UNCOR	○	○
ATLAS_LUMI_1517_UNCOR	○	
ATLAS_LUMI_RUN2_CORR	○	○
ATLAS_r15_Luminosity_bbbb		○
ATLAS_r16_Luminosity_bbbb		○
Mass uncertainties		
ATLAS_MSS_lhchcMass	○	
Pile-up reweighting uncertainties		
ATLAS_PRW_DATASF	○	○
ATLAS_PRW_DATASF_HWW	○	
ATLAS_PRW_DATASF_Htautau	○	
ATLAS_PRW_DATASF_Rel21	○	
ATLAS_PRW_DATASF_Rel21_VHbb	○	
ATLAS_PRW_DATASF_bbyy		○
Electron uncertainties		
ATLAS_EL_EFF_ID_CorrUncertaintyNP11	○	
ATLAS_EL_EFF_ID_CorrUncertaintyNP12	○	
ATLAS_EL_EFF_ID_CorrUncertaintyNP13_HWW	○	
ATLAS_EL_EFF_ID_CorrUncertaintyNP14	○	
ATLAS_EL_EFF_ID_CorrUncertainty_NP6_HWW	○	
ATLAS_EL_EFF_ID_NONPROMPT_D0_Htautau	○	
ATLAS_EL_EFF_ID_SIMPLIFIED_UncorrUncertaintyNP12_HWW	○	
ATLAS_EL_EFF_ID_SIMPLIFIED_UncorrUncertaintyNP3	○	
ATLAS_EL_EFF_ID_SIMPLIFIED_UncorrUncertaintyNP4_HWW	○	
ATLAS_EL_EFF_ID_TOTAL_1NPCOR_PLUS_UNCOR	○	○
ATLAS_EL_EFF_ISO_TOTAL_1NPCOR_PLUS_UNCOR	○	○
ATLAS_EL_EFF_RECO_TOTAL_1NPCOR_PLUS_UNCOR	○	
ATLAS_EL_EFF_TRIG2015_TOTAL_Htautau	○	
ATLAS_EL_EFF_TRIG2016_TOTAL_Htautau	○	
ATLAS_EL_EFF_TRIG_TOTAL_1NPCOR_PLUS_UNCOR	○	○
Photon uncertainties		
ATLAS_PH_EFF_ID_Uncertainty	○	○
ATLAS_PH_EFF_ISO_Uncertainty	○	○
ATLAS_PH_SCALE_CONVEFFICIENCY	○	
ATLAS_PH_SCALE_CONVFAKERATE	○	
ATLAS_PH_SCALE_CONVRADIUS	○	
ATLAS_PH_SCALE_LEAKAGECONV	○	
ATLAS_PH_SCALE_LEAKAGEUNCONV	○	

NP name	single Higgs	double Higgs
Experimental uncertainties		
Electron and photon calibration uncertainties		
ATLAS_EG_RESOLUTION_ALL	○	○
ATLAS_EG_RESOLUTION_MATERIALCALO	○	
ATLAS_EG_RESOLUTION_MATERIALCRYO	○	
ATLAS_EG_RESOLUTION_MATERIALGAP	○	
ATLAS_EG_RESOLUTION_MATERIALIBL	○	
ATLAS_EG_RESOLUTION_MATERIALID	○	
ATLAS_EG_RESOLUTION_MATERIALPP0	○	
ATLAS_EG_RESOLUTION_PILEUP_Rel21	○	
ATLAS_EG_RESOLUTION_SAMPLINGTERM	○	
ATLAS_EG_RESOLUTION_ZSMEARING	○	
ATLAS_EG_SCALE_ALLCORR	○	○
ATLAS_EG_SCALE_E4SCINTILLATOR	○	
ATLAS_EG_SCALE_G4	○	
ATLAS_EG_SCALE_L1GAIN	○	
ATLAS_EG_SCALE_L2GAIN	○	
ATLAS_EG_SCALE_LARCALIB_EXTRA2015PRE	○	
ATLAS_EG_SCALE_LARCALIB_ETABIN0	○	
ATLAS_EG_SCALE_LARCALIB_ETABIN1	○	
ATLAS_EG_SCALE_LARELECUNCONV_ETABIN0	○	
ATLAS_EG_SCALE_LARELECUNCONV_ETABIN1	○	
ATLAS_EG_SCALE_LARUNCONVCALIB_ETABIN0	○	
ATLAS_EG_SCALE_MATCALO_ETABIN0	○	
ATLAS_EG_SCALE_MATCRYO_ETABIN1	○	
ATLAS_EG_SCALE_MATCRYO_ETABIN3	○	
ATLAS_EG_SCALE_MATCRYO_ETABIN7	○	
ATLAS_EG_SCALE_MATCRYO_ETABIN8	○	
ATLAS_EG_SCALE_MATID_ETABIN0	○	
ATLAS_EG_SCALE_MATID_ETABIN1	○	
ATLAS_EG_SCALE_MATID_ETABIN2	○	
ATLAS_EG_SCALE_MATPP0_ETABIN0	○	
ATLAS_EG_SCALE_MATPP0_ETABIN1	○	
ATLAS_EG_SCALE_PEDESTAL	○	
ATLAS_EG_SCALE_PS_BARREL_B12	○	
ATLAS_EG_SCALE_PS_ETABIN0	○	
ATLAS_EG_SCALE_PS_ETABIN3	○	
ATLAS_EG_SCALE_PS_ETABIN6	○	
ATLAS_EG_SCALE_PS_ETABIN8	○	
ATLAS_EG_SCALE_S12_ETABIN0	○	
ATLAS_EG_SCALE_S12_ETABIN1	○	
ATLAS_EG_SCALE_S12_ETABIN3	○	
ATLAS_EG_SCALE_TOPOCLUSTER_THRES	○	
ATLAS_EG_SCALE_WTOTS1	○	
ATLAS_EG_SCALE_ZEESYST	○	

NP name	single Higgs	double Higgs
Experimental uncertainties		
Muon uncertainties		
ATLAS_MUON_EFF_ISO_STAT_Rel21	○	
ATLAS_MUON_EFF_ISO_SYS_Rel21	○	
ATLAS_MUON_EFF_RECO_STAT_LOWPT_Rel21	○	
ATLAS_MUON_EFF_RECO_STAT_Rel21	○	
ATLAS_MUON_EFF_RECO_SYS_LOWPT_Rel21	○	
ATLAS_MUON_EFF_RECO_SYS_Rel21	○	
ATLAS_MUON_EFF_STAT	○	
ATLAS_MUON_EFF_SYS	○	○
ATLAS_MUON_EFF_SYS_LOWPT	○	
ATLAS_MUON_EFF_TTVA_SYS_Rel21	○	
ATLAS_MUON_EFF_TrigStat2015_Htautau	○	
ATLAS_MUON_EFF_TrigStat2016_Htautau	○	
ATLAS_MUON_EFF_TrigStatUncertainty	○	○
ATLAS_MUON_EFF_TrigSyst2015_Htautau	○	
ATLAS_MUON_EFF_TrigSyst2016_Htautau	○	
ATLAS_MUON_EFF_TrigSystUncertainty	○	○
ATLAS_MUON_ID	○	
ATLAS_MUON_ID_Rel21	○	
ATLAS_MUON_ISO_STAT	○	
ATLAS_MUON_ISO_SYS	○	
ATLAS_MUON_MS	○	
ATLAS_MUON_MS_Rel21	○	
ATLAS_MUON_SAGITTA_RESBIAS	○	
ATLAS_MUON_SAGITTA_RESBIAS_Rel21	○	
ATLAS_MUON_SAGITTA_RHO	○	○
ATLAS_MUON_SAGITTA_RHO_Rel21	○	
ATLAS_MUON_SCALE	○	
ATLAS_MUON_SCALE_Rel21	○	
ATLAS_MUON_TTVA_STAT	○	
ATLAS_MUON_TTVA_SYS	○	
Tau uncertainties		
ATLAS_TAU_EFF_ELEOLR_TRUEELE	○	○
ATLAS_TAU_EFF_ELEOLR_TRUEHADTAU	○	○
ATLAS_TAU_EFF_ID_HIGHPT		○
ATLAS_TAU_EFF_ID_HIGHPT_Htautau	○	
ATLAS_TAU_EFF_ID_HIGHPT_ttHML	○	
ATLAS_TAU_EFF_ID_TOTAL		○
ATLAS_TAU_EFF_ID_TOTAL_Htautau	○	
ATLAS_TAU_EFF_ID_TOTAL_ttHML	○	
ATLAS_TAU_EFF_RECO_HIGHPT	○	
ATLAS_TAU_EFF_RECO_TOTAL	○	○
ATLAS_TAU_EFF_TRIG_STATDATA2015	○	○
ATLAS_TAU_EFF_TRIG_STATDATA2016	○	○
ATLAS_TAU_EFF_TRIG_STATMC2015_Htautau	○	
ATLAS_TAU_EFF_TRIG_STATMC2016	○	○
ATLAS_TAU_EFF_TRIG_SYST2016		○
ATLAS_TAU_SF_TMID_L12Tau_ttHML	○	
ATLAS_TAU_TES_DET		○
ATLAS_TAU_TES_DET_Htautau	○	
ATLAS_TAU_TES_DET_ttHML	○	
ATLAS_TAU_TES_INSITU		○
ATLAS_TAU_TES_INSITU_Htautau	○	
ATLAS_TAU_TES_INSITU_ttHML	○	
ATLAS_TAU_TES_MODEL		○
ATLAS_TAU_TES_MODEL_Htautau	○	
ATLAS_TAU_TES_MODEL_ttHML	○	